ISSN 1811-1165 (Print)
ISSN 2413-2179 (Online)

EURASIAN PHYSICAL TECHNICAL JOURNAL

VOLUME 23, NO. 3(57), 2026

phtj.buketov.edu.kz

EURASIAN PHYSICAL TECHNICAL JOURNAL

p - ISSN 1811-1165
e - ISSN 2413-2179

Volume 23, No. 3(57), 2026

Journal Founder:

NON-PROFIT LIMITED COMPANY «KARAGANDA NATIONAL RESEARCH UNIVERSITY NAMED AFTER ACADEMICIAN YE.A. BUKETOV»

https://phtj.buketov.edu.kz

https://www.scopus.com/sourceid/21100920795

www.facebook.com/groups/1103109540750967

Registration Certificate No.4382-Zh, November 7, 2003.

Re-registration Certificate No.KZ32VPY00135738, November 28, 2025 issued by the Information Committee of the Ministry of Culture and Information of the Republic of Kazakhstan

Contact information:

Editorial board of EAPhTJ
(Build. 2, room 216)
Karaganda Buketov University
Universitetskaya Str.28, Karaganda,
Kazakhstan, 100024
Subscription index: 75240

Tel: +7(7212) 77-04-03
Fax: +7(7212) 35-63-98
E-mail: ephtj2021@gmail.com
ephtj@mail.ru

Signed to print 16.06.2026
Format 60x84 1/8. Offset paper.
Volume 20.38 p.sh. Circulation 300 copies.
Order No. 132.

Printed in the Publishing House of Karaganda National Research University named after academician Ye.A. Buketov

Tel. +7 (7212) 35-63-16.
E-mail: printed@karnu-buketov.edu.kz

EDITOR-IN-CHIEF
Sakipova S.E., Buketov Karaganda National Research University, Karaganda, Kazakhstan

SECTION EDITORS-IN-CHIEF

Physics & Astronomy
Miroshnichenko A.S., Department of Physics and Astronomy, University of North Carolina at Greensboro, North Carolina, USA

Engineering
Senyut V.T., Joint Institute of Mechanical Engineering of National Academy of Sciences of Belarus, Minsk, Belarus

Energy
Jakovics A., Institute of Numerical Modelling, University of Latvia, Riga, Latvia

Materials Science
Zeinidenov A.K., Buketov Karaganda National Research University, Karaganda, Kazakhstan

EDITORIAL BOARD
Aringazin A.K., L.N. Gumilyov Eurasian National University, Astana, Kazakhstan
Dzhumanov S., Institute of Nuclear Physics, Uzbekistan Academy of Sciences, Tashkent, Uzbekistan
Hançerlioğullari A., Kastamonu Üniversitesi, Kastamonu, Turkey
Ibrayev N.Kh., Institute of Molecular Nanophotonics, Buketov Karaganda National Research University, Karaganda, Kazakhstan
Kucherenko M.G., Director of the Laser and Information Biophysics Centre, Orenburg State University, Orenburg, Russia
Kuritnyk I.P., Department of Electronics and Automation, High school in Oswiecim, Poland
Kushpil S., Heavy Ion Group, Nuclear Physics Institute of the Czech Academy of Science, Řež near Prague, Czech Republic
Miau J.J., Department of Aeronautics and Astronautics, National Cheng Kung University, Tainan, Taiwan
Oikonomou V.K., Aristotle University of Thessaloniki, Thessaloniki, Greece
Saulebekov A.O., Kazakhstan Branch of Lomonosov Moscow State University, Astana, Kazakhstan
Shrager E.R., National Research Tomsk State University, Tomsk, Russia
Stoev M., South-West University «Neofit Rilski», Blagoevgrad, Bulgaria
Suprun T., Institute of Engineering Thermophysics of NASU, Kyiv, Ukraine
Trubitsyn A.A., Ryazan State Radio Engineering University, Ryazan, Russia
Volkov K.N., Kingston University, London, United Kingdom

TECHNICAL EDITOR
Kambarova Zh.T., Buketov Karaganda National Research University, Karaganda, Kazakhstan

© Buketov Karaganda National Research University, 2026

Eurasian Physical Technical Journal, 2026, Vol. 23, No. 3(57)

CONTENTS

PREFACE……..……..... 4

MATERIALS SCIENCE		
1	***Giniyatova Sh.G., Kozlovskiy A.L., Iskakov K., Shadiyar D., Uglov V.V., Borgekov D.B.*** Study of the influence of the type and energy of ions during irradiation on the change in the structural and mechanical properties of high-entropy AlNbTiVZr alloy…….…….....	5
2	***Toktarbaiuly O., Kydyrbay N.B., Zhazitov M.R., Tezekbay Y.Zh., Abduvalov A.Zh., Serikov T. M.*** Growth and Surface Structure of Fe Monolayers on Pt(110) …….……..	16
3	***Greshta V., Yar-Mukhamedova G.Sh., Imanbayeva A.K., Dzhus A., Zellele D.M.*** Selective degradation characteristics of silver-coated magnesium alloy biodegradable implants with silver cladding for osteosynthesis applications. …….…….…….…….....	28
4	***Ibrayev N.Kh., Amanzholova G.S., Aimagambetova A.A.*** Photonics of benz [c, d] indole-based polymethine dyes molecules and singlet oxygen sensitization..…...	37
5	***Sanchez Cornejo H.E., Kargin J.B., Afanasyev D.A., Guchenko S.A., Sagyndykova G.E., Zhangozin K.N., Bustamante Dominguez A., Celis Rojas S.R., Barnes C.H.W., De Los Santos Valladares L.*** Anisotropic microstrain and its relationship with the out-of-plane texture and the superconducting properties of YBCO films grown onto $SrTiO_3$ (100) and $LaAlO_3$ (100) substrates by chemical solution deposition……...	44
ENERGY		
6	***Atyaksheva A.V., Sarakeshova N.N., Rozhkova O.V. Zhaksylyk A.M., Zhumaliyeva A.K, Aitmagambetova M.B., Umirzakov R.A.*** Effect of oxygen addition on low-rank coal drying in a technology for volatile gas generation……..	54
7	***Min'kov L.L., Gimayeva N.R.*** The influence of thermostating temperature on the ignition and deformation dynamics of a cylindrical charge in a nozzle less propulsion device.…….……	64
8	***Alkina A.D., Kuatova A.S., Mekhtiyev A.D., Yurchenko A.V., Bainiyazov B.A.*** Investigation of the parameters of a hybrid-solar power plant for energy supply of remote autonomous consumers. ……..……..……..……..……..…….....	74
9	***Sakipova S.E., Smagulov Zh.K., Bekturganov Zh.S., Ismailov Zh.T., Kartbayeva, G.T., Duisenbayeva M.S., Ospanova D.A.*** Development of a bioreactor heating system using a ground-source heat pump…….....	86
ENGINEERING		
10	***Kulsartov T., Akhanov A., Askerbekov S., Shaimerdenov A., Chikhray Ye., Bugybay Zh.*** Modernization of a thermal desorption spectroscopy setup for high-sensitivity analysis of hydrogen and helium isotopes..……..……..……..…….....	94
11	***Kazhikenova S., Akhmetova S., Belomestny D.*** Modernization of the methodology and installation of triaxial compression for the study of rheological properties of dispersed media**.** ……..……..……..……..…….	103
12	***Turmaganbet U.K., Turlykozhayeva D.A., Akhtanov S.N., Temesheva S.A., Ussipov N.M., Tao M.*** Autonomous search and rescue drone with real-time YOLO Object Detection and GPS Navigation using Raspberry Pi 4. ……..……..……..……..…….	115
PHYSICS AND ASTRONOMY		
13	***Osang, J. E., Inyang, E. P., Valentine, N. H., Mopta, S. E., William, E. S., Amajama, J., & Ekechukwu, C.*** Spectroscopy and structural properties of heavy quarkonium systems…….....……..….	125

14	***Achkassova S.E., Vaidman N.L., Khokhlov S.A., Agishev A.T., Azhikenova A.S.*** Photometric variability of do Leo based on tess data. ……..……..……...……...	138
15	***Ratbay* A.*, Razina O., Tsyba P., Satbekova E.*** Cosmological evolution dynamics and Om(z) diagnostic in a scalar–fermion model with a generalized scale factor. ……..……...……..	144
16	***Kalambay M., Kuvatova D., Ishchenko M., Berczik P., Omarov Ch., Kusakin A.*** Could globularly clusters in the vicinity of the Galactic center have contributed stars to the nuclear star cluster in the past? ……..……...……	154

.

Dear authors and readers!
Dear colleagues!

As usual, in the Preface we inform the authors and readers about the latest significant achievements of the journal. Journal and author metrics in the Scopus database depend on citation counts; so, due to these, the CiteScore Tracker value reached 1.5 for the first time in August! This achievement confirms a significant step toward increasing the journal's international visibility, expanding its readership and author base, and strengthening its position within the global scientific community.

A significant event this summer was the invitation of a new member to the editorial board - Doctor of Physical and Mathematical Sciences *Konstantin Nikolaevich Volkov* – researcher of the Faculty of Engineering, Computing and the Environment, Kingston University, London. Professor Volkov K.N. is a highly qualified and respected expert in fields such as heat and mass transfer, turbulence, laminar-to-turbulent flow transition, two-phase flows, heat exchangers, computational fluid dynamics (CFD), numerical methods, and aerospace engineering (ih 19). We are confident that professional experience will contribute strengthening the journal's metrics and expanding international scientific collaboration.

In this issue the Materials Science section new, original research results on the properties of materials exposed to various influences are presented. Irradiation of the near-surface layers of the AlNbTiVZr alloy leads to changes in both structural and mechanical properties. Under ultra-high vacuum conditions, the formation of an ordered surface layer—or a moiré-type superstructure—was observed, resulting from the lattice mismatch between Fe and Pt(110). The enhanced efficacy and safety of biodegradable implants are attributed to the selective degradation characteristics of a magnesium–zinc–zirconium–neodymium alloy system featuring silver coatings. The efficiency of triplet-triplet energy transfer has been established, making the 2848SL derivative a promising agent for photodynamic therapy. Anisotropic micro-strains play a decisive role in the formation of the superconducting properties of YBCO films and influence their superconducting characteristics.

The "Energy" section presents the results of research aimed at solving current energy problems, such as: studying the effect of oxygen supply on the drying process of low-grade coals in the technology of their thermal processing; modeling the steady-state operation of a nozzleless jet engine with a cylindrical solid-propellant charge made of viscoelastic material; calculating the operating parameters of a hybrid wind-solar power plant for autonomous energy supply in a sharply continental climate; and assessing the thermal output of the external circuit of a ground-source heat pump.

The "Engineering" section presents the results of developing innovative research methods aimed at improving the efficiency of technical devices and technologies: modernizing a thermal desorption spectroscopy system to enhance the sensitivity of gas-phase mass spectrometry analysis; the determination of rheological and deformation characteristics of dispersed materials, specifically sand-clay molding mixtures; development of intelligent unmanned aerial vehicles with onboard computer vision to perform onboard human detection and GPS-based localization in real-time

"Physics and Astronomy" section are devoted to studying the patterns of complex interactions at the macroscopic level: the spectroscopy and structural properties of heavy quarkonium systems are investigated within the Varshni–Hellmann potential model; a photometric analysis of the cataclysmic variable star DO Leo; a cosmological model of an expanding Universe featuring a scalar-fermion interaction mediated by a Yukawa-type coupling; and the results of direct N-body simulations of three Milky Way bulge globular clusters (Terzan 2, Terzan 4, Terzan 5) that evolving in a time-varying galactic potential.

We hope the presented articles will not only be interesting but also useful in preparing new publications for researchers, teachers, graduate students, and postgraduates.

Please remember to cite the articles published in our journal.

And we look forward to seeing you among our readers and authors in the future.

With respect and hope for fruitful collaboration,
Editor-in-Chief, Professor Sakipova S.E.
September, 2026

EURASIAN PHYSICAL TECHNICAL JOURNAL

2026, Volume 23, No. 3 (57)

https://doi.org/10.31489/2026N3/5-15

Received: 28/03/2026 Revised: 17/08/2026 Accepted: 28/09/2026 Published online: 30/09/2026

Original Research Article

Open Access under the CC BY -NC-ND 4.0 license

UDC 53.043

STUDY OF THE INFLUENCE OF THE TYPE AND ENERGY OF IONS DURING IRRADIATION ON THE CHANGE IN THE STRUCTURAL AND MECHANICAL PROPERTIES OF HIGH-ENTROPY AlNbTiVZr ALLOY

Giniyatova Sh.G.[1,2], Kozlovskiy A.L.[1,2]*, Iskakov K.[1,2], Shadiyar D.[1], Uglov V.V.[3], Borgekov D.B.[1,2]

[1] NJSC L.N. Gumilyov Eurasian National University, Astana, Kazakhstan
[2] Institute of Nuclear Physics of the ARKAE, Almaty, Kazakhstan
[3] Belarusian State University, Minsk, Belarus
* *Corresponding author*: kozlovskiy.a@inp.kz

Abstract. *The main aim of this study is to identify the role of energy and type of incident ions during irradiation of the near-surface layers of the AlNbTiVZr alloy in alteration of the structural and mechanical properties, as well as to determine the role of accumulation of structural damage on the softening of the near-surface layer depending on the irradiation fluence. According to the data obtained, it was established that a change in the type of ions and the energy of ions leads to a growth in the degree of structural damage associated with volumetric swelling, while an increase in the energy of ions leads to an elevation in the degree of deformation distortions of the tensile type, caused by an increase in ionization losses and cascade displacements, which elevate the concentration of defects in the near-surface layer. It has been shown that the development of volumetric swelling processes and the accumulation of defective clusters are the main factors causing a decrease in hardness and deterioration of the mechanical characteristics of the irradiated material. The results obtained demonstrate that the type and energy of incident ions, as well as the irradiation fluence, have a determining effect on the kinetics of degradation of mechanical properties and radiation resistance of the near-surface layers of the alloy under study.*

Keywords: high-entropy alloys, radiation resistance, resistance to degradation, radiation defects, structural materials.

1. Introduction

In modern materials science, regarding the study of promising materials for new generation nuclear reactors, high-entropy alloys have occupied a special place in the past few years, a distinctive feature of which is a multicomponent composition, which includes five or more elements in similar atomic concentrations [1-3]. In this case, the use of close ratios of components in the composition leads to the formation of a high entropy of mixing, which in turn stabilizes simple crystalline structures through cationic substitution and changes the physical and mechanical properties of the alloys. Due to these effects arising in the structure of alloys, high-entropy alloys are considered one of the potential materials of the new generation, capable of operating under conditions of high temperatures, large neutron fluxes and exposure to nuclear fission fragments, as well as resistance to degradation processes upon contact with aggressive environments [4,5]. Unlike traditional alloys, in which one element is the main one and the others act as alloying additives, high-

entropy alloys lack a dominant component, in them, the equilibrium ratio of elements leads to the formation of a high configurational entropy of mixing, which determines the stability of the crystalline structure, as well as the emergence of a complex field of local stresses and energy barriers for the diffusion of atoms, which increases strength, ductility, thermal stability and resistance to external influences [6-8]. Another feature of high-entropy alloys is their resistance to the corrosive effects of aggressive environments, including water vapor, liquid metals, or molten salts, which makes high-entropy alloys potentially suitable for use in next-generation reactors operating on alternative coolants such as lead, sodium, or molten salts [9,10].

It should also be noted that in recent years, much attention in the study of the properties of high-entropy alloys has been paid to their resistance to the accumulation of radiation damage, as well as to assessment of the likelihood of the formation of long-lived radioactive isotopes in alloys after high-dose irradiation [11,12]. In this regard, to restrain these processes in the production of high-entropy alloys, elements with low activation, in particular, elements such as iron, chromium, vanadium, titanium, and tantalum, the use of which allows for a significant reduction in the level of radioactive waste and simplification of reactor decommissioning processes, are used [13-15]. High-entropy alloys play a significant role in thermonuclear energy, for installations such as ITER and DEMO, whose materials must withstand high thermal loads, intense neutron irradiation, and surface erosion upon contact with plasma [16,17]. In this case, much attention in this area is paid to high-temperature refractory high-entropy alloys based on tungsten, niobium, molybdenum and tantalum, which are considered as potential materials for the creation of divertors, plasma walls and other structural components of thermonuclear installations [18-20].

High-entropy alloys are also being considered as materials for next-generation nuclear fuel cladding due to their higher mechanical strength, oxidation resistance, and thermal stability compared to traditional zirconium alloys, which improves the safety of nuclear reactor operation and increases the burnout efficiency of nuclear fuel [21,22]. At the same time, despite the great prospects for the use of high-entropy alloys as structural and functional materials for nuclear and thermonuclear energy, the widespread introduction of these alloys today requires the search for and solution of a number of scientific and technological issues, the key of which is the assessment of the mechanisms of destruction and softening of the near-surface layers of alloys exposed to ionizing radiation. In particular, it is necessary to obtain new data on the mechanisms of defect formation and their evolution depending on variations in irradiation conditions, including exposure to various types of ionizing radiation, determine long-term structural stability and establish critical irradiation doses at which the degradation of the near-surface layers becomes irreversible and can lead to destabilization of the entire material.

In this regard, the main aim of this study is to identify the role of energy and type of incident ions during irradiation of the near-surface layers of high-entropy AlNbTiVZr alloy on the change in structural and mechanical properties, as well as to determine the influence of the accumulation of structural damage caused by irradiation on the softening processes depending on the irradiation fluence. Interest in this type of research is driven by the need to expand our understanding of the patterns of ion ranges of different masses and energies in materials, which is an important step in planning experiments on ion modeling of radiation effects, as well as in analysis of the stability of promising materials, including high-entropy alloys, to the effects of intense charged particle fluxes.

2. Materials and methods

A high-entropy alloy based on compounds of aluminum, niobium, titanium, vanadium and zirconium, obtained by spark sintering methods from metal powders mixed in equal proportions of components, was chosen as the object of research. The alloy sample was prepared by mixing the selected components in a stoichiometric ratio of 20 at. % and subsequently melting the mixture using the electric-arc remelting method in an argon atmosphere. The remelting process was repeated at least five times to ensure a uniform distribution of elements within the alloy.

X-ray structural analysis of the alloy samples was performed using a D8 Advance ECO diffractometer; X-rays were generated by a copper tube (Cu Kα wavelength = 1.54 Å). Diffraction patterns were recorded in Bragg-Brentano geometry over an angular range of $2\theta = 20–60°$ with a step size of 0.05°. Structural parameters were determined using Diffrac.EVA v.4.2 software. Parameter refinement involved comparing the results with reference values and identifying deviations caused by external factors, such as lattice distortions resulting from alloy fabrication methods or ion irradiation. According to X-ray phase analysis data, the phase composition of the alloy is characterized by a body-centered phase B2, enriched in aluminum and zirconium, as well as

inclusions in the form of Zr_5Al_3 and the Laves phase ZrAlV, the presence of which is due to their inclusion near the grain boundaries of the main phase, which leads to the creation of additional strengthening effects due to the formation of interphase boundaries and dislocation effects. The key reason for choosing the AlNbTiVZr alloy as the object of research is its belonging to the class of refractory high-entropy alloys, the combination of elements in which ensures the stability of the material during operation in the operating temperature range of 600 – 1000 °C, as well as possessing high heat resistance and oxidation resistance. The multicomponent composition of the AlNbTiVZr alloy leads to the creation of a large number of structural distortions of the crystal lattice, which in turn complicates the migration of point defects and slows down diffusion processes, thereby reducing the rate of accumulation of radiation damage and degradation of the alloy microstructure.

Modeling of radiation damage in the near-surface layers of the studied alloy samples was carried out at the DC-60 heavy ion accelerator located at the Astana branch of the Institute of Nuclear Physics of the Ministry of Energy of the Republic of Kazakhstan (Astana, Kazakhstan). Irradiation was carried out with O^+, Ar^+, Kr^+ and Xe^+ ions with energies of 28 MeV, 70 MeV, 145 MeV and 230 MeV, respectively. Irradiation fluences ranged from 5×10^{10} to 10^{14} ion/cm^2. Irradiation was carried out at room temperature. The choice of ion types for irradiation is determined by the need for a comprehensive study of the influence of the mass and energy of incident particles on the processes of formation and accumulation of radiation defects in the material. The use of ions with significantly different atomic masses makes it possible to reproduce various mechanisms of energy transfer in the crystal lattice and to evaluate the nature of structural changes that occur under radiation exposure.

The values of ionization losses, as well as changes in their profiles along the trajectory of ion movement in the near-surface layers of alloys at irradiation fluence growth, were determined using the SRIM Pro 2013 software code. The assessment results of changes in the profiles are shown in Figure 1a, reflecting the change in the values of ionization losses of ions along the trajectory, caused by the processes of elastic and inelastic interactions during the collision of ions with the crystal structure. As can be seen from the data presented, ionization losses during the interaction of incident ions with electrons, which are associated with the excitation and subsequent ionization of electrons and electron shells, play a dominant role in alteration of the structural features of the studied alloys during irradiation. Moreover, as the penetration depth increases, the role of electron ionization losses decreases, while the contribution of electronic stopping power and nuclear stopping power grows due to the increase in the concentration of elastic collisions of incident ions with atomic nuclei, which leads to their displacement from the nodes of the crystal lattice. The maximum ion range is about 10 – 14 μm, and it should be noted that alteration of the type and energy of ions does not make a significant difference in the maximum ion range, while alteration of the energy of ions plays a very important role in the value of ionization losses and the kinetics of their changes along the ion range.

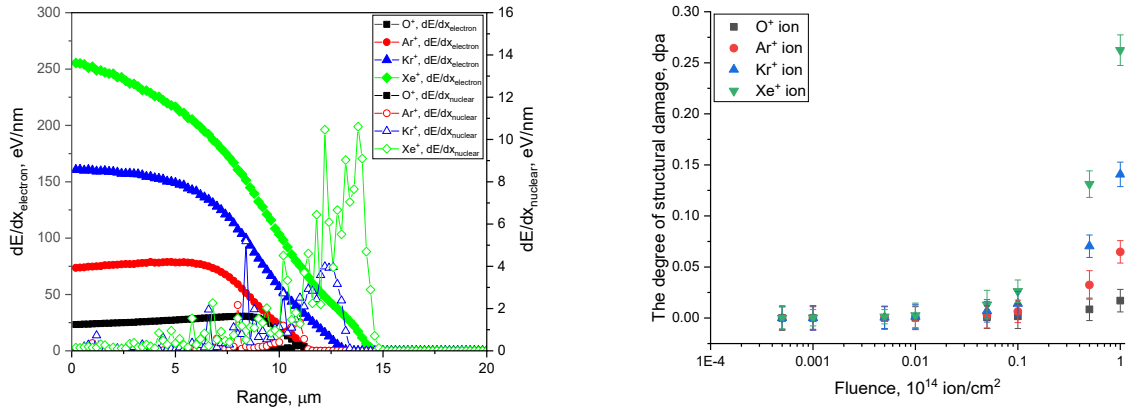
Table 1 shows the main characteristics of the interaction of incident ions with the crystalline structure of the alloy during irradiation, reflecting the values of ionization losses, as well as the ion range in the near-surface layers. Data for ionization loss values are given as a range of values observed at the maximum. For electron ionization losses, these values were estimated at an ion range of up to 5 μm, while for nuclear ionization losses, these values were determined based on the maximum achieved during the slowing down of incident ions and their deceleration, at which ion-nucleus interactions dominate.

Table 1. Calculation data for ionization losses and ion range

Parameter	Ion			
Type of ion	O^+	Ar^+	Kr^+	Xe^+
Energy of ion, MeV	28 MeV	70 MeV	145 MeV	230 MeV
Range of ion, μm	10.7 ± 0.2 μm	10.8 ± 0.3 μm	12.5 ± 0.2 μm	13.8 ± 0.4 μm
$dE/dx_{nuclear}$, eV/nm	0.2 – 0.3	1.1 – 1.3	2.5 – 3.9	10 – 11
$dE/dx_{electron}$, eV/nm	25 – 30	67 – 76	123 – 145	200 – 240

According to the presented data on the assessment results of ionization losses and ion range in the near-surface layers of alloys, it can be concluded that an increase in ion energy from 28 MeV for O^+ to 145 MeV and 230 MeV for Kr^+ and Xe^+ ions leads to a change in the ion range by no more than 2.0 – 3.0 μm, and in the case of Ar^+ ions with an energy of 70 MeV, the ion range is comparable to the range of O^+ ions. In this case, the change in the type of ions and interaction mechanisms has a clearly expressed dependence on the mass of

the ions and the initial energy. In this case, the analysis of the ionization loss values showed that in the case of heavy Kr^+ and Xe^+ ions, the ionization loss values are more than an order of magnitude higher than those of O^+ ions, which is due to the greater intensity of the interaction of incident heavy ions with the electron and nuclear subsystems, which leads to more intense slowing down of the ions. It should also be noted that lighter O^+ ions, due to the peculiarities of interaction with the electron and nuclear subsystem at lower energy, are able to penetrate to greater depths, due to lower values of ionization losses, especially when interacting with nuclei. According to the presented calculations, it can be concluded that the use of these types of ions allows the formation of a damaged area of approximately the same range in depth in alloy samples, which in turn can be used to describe the structural and mechanical changes in the near-surface layers.



a) b)

Fig. 1. Results of calculations using the SRIM Pro software code: a) Values of change in ionization losses along the trajectory of ions in the alloy; b) Dependence of the change in the value of atomic displacements for the studied ions upon collision and change in irradiation fluence

Figure 1b shows the results of calculations of the values of atomic displacements depending on the irradiation fluence, characterizing the number of displacements of atoms from the nodes of the crystal lattice as a result of the interaction of incident ions with the crystal structure of the target. To estimate the dpa values, the methodology described in [23] was used. Data are given for all types of considered ions used for irradiation of alloy samples depending on the irradiation fluence. A general analysis of the obtained values indicates that at low irradiation fluences (5×10^{10} - 5×10^{11} ion/cm^2) the degree of structural damage is extremely low and does not differ significantly depending on the type of ions used for irradiation. In this case, the observed effects are explained by the fact that at low irradiation fluences, a limited number of point defects are formed in the material, such as vacancies and interstitial atoms, which can recombine with each other, and the areas where these defects are formed are isolated from each other. At fluences above 10^{12} ion/cm^2, the differences between the effects of ions depending on their type and energy become more pronounced, which is explained by the fact that heavy ions have a greater mass and higher momentum, as a result of which they transfer more energy to the atoms of the crystal lattice during collisions. This leads to the formation of more intense displacement cascades and an increase in the number of radiation defects formed. At the same time, light ions such as oxygen lose more energy through ionization processes, which reduces the contribution of nuclear collisions and, accordingly, reduces the level of structural damage.

The determination of structural damage in the near-surface layer of the AlNbTiVZr alloy was carried out by the assessment of changes in the structural parameters of the main phase B2 and further calculation of changes in the structural damage degree based on changes in the crystal lattice volume in comparison with the results for the initial samples with a change in the irradiation fluence. To assess the influence of accumulated structural damage caused by irradiation with heavy ions of different energies on the change in the mechanical properties of alloys, as well as to identify the role of changes in ionization losses and structural damage on the degree of softening of damaged layers, a hardness assessment method was used.

Changes in sample hardness before and after testing were determined using an indentation method employing a Vickers diamond pyramid indenter. The load applied to the indenter was approximately 10 N, and the dwell time was about 15 seconds; the indenter was then moved a distance of approximately 30 μm, and the measurements were repeated. At least 20 indentations were performed on each irradiated alloy sample.

3. Results and discussion

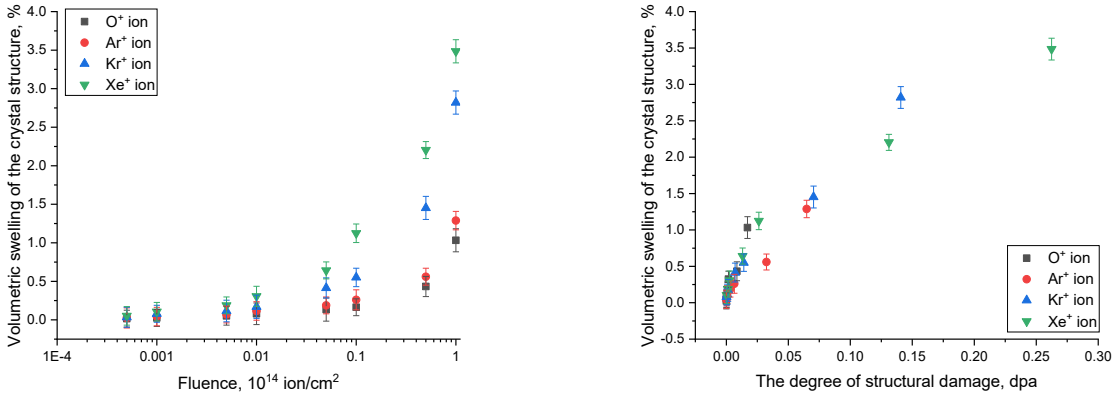
One of the key parameters characterizing the degree of influence of heavy ions on the crystal structure is the change in the volume of the crystal lattice of irradiated samples and its comparison with the results of the initial values. In this case, for cubic lattices, the change in the crystal lattice volume characterizes the overall deformation of the crystal structure, and the nature of the changes itself determines the type of deformation distortions caused by the processes of interaction of ions with the material. Also, the use of this parameter makes it possible to quantitatively estimate the degree of radiation-induced structural changes caused by the accumulation of deformation distortions, and the value itself for cubic types of crystalline structures is an integral characteristic of the deformation state, since the lattice parameters in cubic systems are the same in all directions, which means that an increase or decrease in the volume of the crystalline structure reflects a change in interatomic distances, as well as the total effect of radiation defects and their accumulation in the damaged layer.

Figure 2 shows the assessment results of the change in the degree of volumetric swelling of the crystal lattice caused by the accumulation of deformation distortions in the crystal structure, caused by the processes of interaction of incident ions with the target material. The choice of crystal lattice volumetric expansion as an evaluation parameter is based on the following assumptions. Structural damage resulting from the interaction of incident ions with the crystal structure causes distortion due to the formation and subsequent migration of defects and vacancies. In this instance, comparing the crystal lattice volumes of samples before and after irradiation makes it possible to assess the extent of structural change caused by external factors, while the nature of these changes allows for the identification of the type of deformation involved. According to the assessment of the data obtained, the increase in the crystal lattice volume for irradiated samples indicates the formation of tensile deformation stresses in the crystal structure caused by irradiation, the accumulation of which is associated with the formation of vacancies and their subsequent agglomeration and the formation of vacancy clusters. At the same time, the accumulation of vacancy defects leads to a growth in interatomic distances, which consequently leads to an elevation in the crystal lattice parameters. The very nature of changes in the value of volumetric swelling of the crystal lattice, shown in Figure 2a, indicates a cumulative effect caused by a change in the irradiation fluence, as well as the direct influence of the energy and type of incident ions on the degree of deformation distortions. In the case of lighter O^+ ions, changes in the volumetric swelling degree are most pronounced at fluences above 10^{13} ion/cm^2, while at irradiation with Kr^+ or Xe^+ ions, an intensive growth in the volumetric swelling degree is observed at fluences above $5\times10^{11} – 10^{12}$ ion/cm^2. In the case of irradiation with Ar^+ ions, the nature of changes in the degree of volumetric swelling is similar to the changes caused by irradiation with O^+ ions, but the degree of changes is somewhat higher. The dependencies obtained are a direct confirmation of the role of changes in the type and energy of ions in the deformation-induced distortion of the crystalline structure of the damaged layer. According to the data obtained, the higher the energy of the incident ions, the more intense the change in the volumetric swelling of the damaged layer, which is especially evident at high irradiation fluences.

In this case, an elevation in the irradiation fluence causes a reduction in the distance between structurally altered areas that arise along the trajectory of ion movement in the damaged layer, thereby increasing the density of damaged areas and their subsequent overlap. In this case, the size of the incident ions and their energy play a key role in the size of these regions with increased defectiveness, which in turn leads to the fact that the higher the energy of the ions, the larger the size of these regions, and accordingly the overlapping effect is achieved at lower irradiation fluence values. Also, according to the data presented in Table 1, a change in the type and energy of incident ions leads to an elevation in ionization losses, which, as a consequence, leads to a growth in the intensity of cascade displacements, and, as a consequence, an increase in the concentration of defects in the damaged area, which causes more intense distortions due to a higher density of defects and vacancies in the damaged layer. Based on the obtained data on the dependence of changes in the degree of volumetric swelling, and also taking into account the fact that the growth of deformation distortions occurs when structurally altered areas overlap, it is possible to draw a conclusion about critical fluences at which the nature of deformation processes changes and destabilization of the damaged layer grows.

In this case, at irradiation with O^+ or Ar^+ ions, the formation of overlapping defect regions is observed at fluences above 10^{13} ion/cm^2, while for heavy Kr^+ and Xe^+ ions, the overlapping of defect regions is observed at fluences above $5\times10^{11} – 10^{12}$ ion/cm^2, which in turn indicates a higher efficiency of heavy ions in the initiation of structural changes due to the accumulation of radiation-induced defects and vacancies. An

assessment of the characteristic sizes of defective areas, taking into account the obtained critical fluence values at which a sharp change in the volumetric swelling degree is observed and taking into account the assumption of a uniform distribution of these areas in the material, showed that for O^+ and Ar^+ ions, the average sizes of structurally altered areas are of the order of 3 – 5 nm, and for Kr^+ and Xe^+ ions, the characteristic sizes are of the order of 10 – 20 nm. In this case, the overlap of defective areas leads to the formation of continuous zones of increased defectiveness, which is accompanied by an increase in the density of deformation distortions of the crystal lattice due to the active accumulation of vacancies, the formation of vacancy clusters, which enhances the effect of local destabilization of the crystal structure of the near-surface layers. The overlap of such damaged regions is accompanied by an increase in the concentration of vacancy defects and the formation of vacancy clusters, nanopores and other defective structures, which are the main source of radiation-induced volumetric swelling. The accumulation of such defects leads to a local increase in interatomic distances and the formation of tensile deformations in the crystal lattice, which ultimately manifests itself in an increase in the volume of the material. It should also be noted that at high ion energies, the contribution of ionization energy losses associated with the excitation of the electronic subsystem of the material grows. This can lead to additional local energy disturbances in the structure of the material and enhance the processes of defect formation and atomic migration. In combination with nuclear collisions, such processes contribute to a more intense development of radiation damage and an increase in volumetric swelling, which is most clearly seen in the dependencies shown in Figure 2a for heavy Kr^+ and Xe^+ ions, for which the maximum change in the volumetric swelling value at a fluence of 10^{14} ion/cm^2 is 2.8 % and 3.5 %, respectively, while for samples irradiated with O^+ and Ar^+ ions, the maximum change in the volumetric swelling value is about 1.0 – 1.3 % at a fluence of 10^{14} ion/cm^2.



a) b)

Fig. 2. Results of the assessment of changes in structural properties: a) results of changes in volumetric swelling depending on irradiation fluence; b) results of changes in volumetric swelling depending on the damage degree

For a correct comparison of the degree of volumetric swelling caused by different types of ions during irradiation, the dependence of the change in the volumetric swelling value on the degree of structural damage caused by atomic displacements was plotted. The use of the atomic displacement parameter allows for an objective comparison of the results of irradiation with different ions, since this parameter considers not only the type and energy of the incident particles, but also the total density of defects arising during the collision of ions with the crystal structure of the target material. The need to use such a dependence is due to the fact that when irradiated with different ions, there are significant differences in the mechanisms of energy transfer to the material, the depth of particle penetration, and the nature of the formation of displacement cascades. Light ions, such as O^+, lose energy to a greater extent through ionization processes, interacting with the electron subsystem of the material. At the same time, heavier ions such as Kr^+ and Xe^+ have significantly greater mass and are able to initiate intense nuclear collisions, forming powerful cascades of atomic displacements. This leads to the formation of different concentrations of radiation defects even at the same irradiation fluence values. In this case, the construction of the dependence of volumetric swelling on the value of atomic displacements makes it possible to determine how effectively the formation of defects affects the change in the crystal lattice volume and the development of deformation distortions in the material. Analysis of the presented dependencies in Figure 2b showed a direct correlation between the change in the volumetric swelling

value and the value of atomic displacements caused by irradiation. According to the given dependencies, a change in the type of ions leads to more pronounced structural degradation due to an increase in atomic displacements caused by changes in ionization losses of ions and energy transfer mechanisms. In this case, heavy ions transfer more energy to the atoms of the target crystal lattice, which leads to the formation of more powerful displacement cascades and an increase in the concentration of vacancies, which leads to increased destabilization of the near-surface layer. Moreover, the evaluation of the obtained dependencies makes it possible to demonstrate more clearly the effect of alteration of the type and energy of ions during irradiation on the kinetics of destabilization of the near-surface layers associated with the accumulation and subsequent aggregation of vacancy defects arising as a result of irradiation. According to the presented dependencies, the ion energy growth leads to an increase in the processes of energy transfer to the electron subsystem, thereby increasing ionization electron losses (see the data presented in Table 1). For light ions, electron braking becomes the dominant mechanism of energy loss, which is accompanied by excitation and ionization of atoms, as well as a local increase in temperature in the ion passage area. These processes contribute to additional changes in the structure of the material and can lead to the formation of tensile deformation distortions in the crystal lattice.

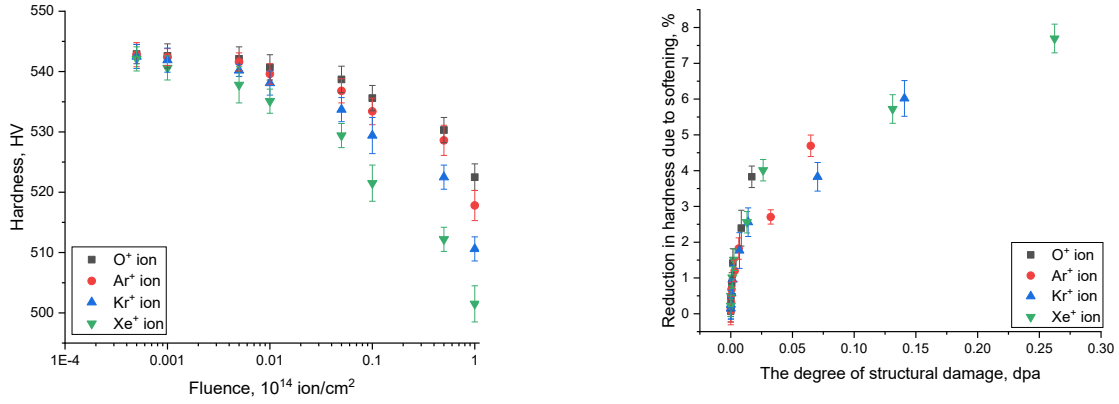
The occurrence of such distortions is associated with the accumulation of vacancies and the expansion of interatomic distances in damaged areas. As the ion energy grows, these effects intensify, leading to an increase in local stresses and an elevation in the crystal lattice deformation degree. As a result, a more pronounced change in the lattice parameters and an increase in the volume of material in the near-surface layer are observed. At high particle energies, the contribution of ionization losses becomes dominant. Electronic excitations can lead to local energy excitation of the lattice, which contributes to additional rearrangement of the material structure and can enhance the processes of defect formation and atomic migration.

The main mechanism that determines the degree of structural damage is nuclear deceleration of ions, associated with elastic collisions of incident particles with atoms of the crystal lattice. In such collisions, part of the ion energy is transferred to the atoms of the material, which can leave their positions at the nodes of the lattice. If the energy of the transmitted pulse exceeds the atom displacement threshold, Frenkel pairs, consisting of a vacancy and an interstitial atom, are formed. At high ion energies, such displacements can initiate cascades of atomic collisions, as a result of which one displaced atom knocks out other atoms from the lattice nodes. As a result, a region of local radiation damage with a high concentration of defects is formed, and in the case of heavy Kr^+ and Xe^+ ions, the sizes of these regions are significantly larger than for lighter O^+ and Ar^+ ions, which in turn leads to increased destabilization effects. The analysis of the obtained dependencies makes it possible to more clearly demonstrate the effect of the type and energy of ions on the kinetics of destabilization of the near-surface layers of the material. Heavy ions such as Kr^+ and Xe^+ cause more intense nuclear braking processes and form more powerful displacement cascades, which leads to accelerated accumulation of defects. As a result, there is an increase in the processes of vacancy clustering, pore formation and volumetric swelling growth, which ultimately leads to more pronounced structural degradation of the near-surface layer of the irradiated material.

Figure 3 reveals the assessment results of changes in the hardness of the studied alloy samples depending on the irradiation fluence. According to the data presented in Figure 3a, it is evident that at low irradiation fluences (below 10^{12} ion/cm^2), the changes in the hardness values of the near-surface layer are practically no different from the initial values, and the degree of change is no more than 0.2 – 0.5 % of the initial values. The obtained results indicate that in the case of failure to achieve the effect of overlapping defective areas in the damaged layer, changes in the structure of alloys due to the occurrence of point and vacancy defects do not have a significant effect on the change and destabilization of mechanical properties. With an increase in irradiation fluence above 10^{12} ion/cm^2, at which the formation of the effect of overlapping defective areas is observed for heavy ions, according to the presented data on changes in hardness, a reduction in values is observed, which indicates a decrease in the resistance of the material to plastic deformation caused by irradiation. The most pronounced change in hardness for samples irradiated with O^+ ions at a fluence of 10^{14} ion/cm^2 is approximately 520 – 525 HV, which, as a percentage relative to the initial values, is less than 4 %. In the case of irradiation with Ar^+ ions, the reduction in hardness at a fluence of 10^{14} ion/cm^2 is approximately 515 – 517 HV, which is less than 5 % of the initial values.

In the case of heavy Kr^+ and Xe^+ ions, the decrease in hardness at a fluence of 10^{14} ion/cm^2 is more pronounced than in the case of irradiation with light ions and is approximately 6 – 8 % of the initial values of the hardness of the alloys. This behavior is due to the fact that heavy ions transfer more energy to the atoms of the crystal lattice, forming more intense displacement cascades and increasing the concentration of vacancy

defects. In this case, the decrease in hardness is associated with the development of processes of volumetric swelling and the accumulation of defective clusters, which lead to a weakening of interatomic bonds and an increase in local tensile deformations in the crystal lattice. The overlapping of defective areas at high fluences contributes to the formation of zones of increased defectiveness, which leads to the softening of the near-surface layer of the material.



a) b)

Fig. 3. Results of the assessment of changes in the mechanical properties of alloys: a) results of changes in hardness depending on irradiation fluence; b) results of the assessment of the degree of hardness reduction during softening depending on the value of atomic displacements caused by irradiation

Figure 3b demonstrates the assessment results of the degree of hardness reduction during softening depending on the value of atomic displacements caused by irradiation. Analysis of the data obtained showed that an elevation in the structural damage degree leads to a gradual increase in the value of the reduction in hardness of the alloy under study. At small damage values (up to ~ 0.01 – 0.02 dpa), the reduction in hardness remains insignificant and amounts to less than 1 – 2 %, which indicates a weak influence of the initial accumulation of point defects on the mechanical properties of the material.

At this stage, most of the resulting vacancies and interstitial atoms can recombine without causing significant degradation of the structure. As the degree of damage increases to ~0.05 – 0.10 dpa, a more noticeable decrease in hardness, reaching approximately 2 – 3 %, is observed. This is due to an increase in the concentration of radiation defects and the onset of their clustering, which leads to local distortions of the crystal lattice and a decrease in the material's resistance to plastic deformation. At high damage values (~0.15 – 0.30 dpa), the reduction in hardness becomes most pronounced and can reach 6 – 8 %. In this area there is an active accumulation and aggregation of vacancy defects, the formation of defective clusters and local areas of disordered structure. The overlapping of displacement cascades leads to the formation of continuous zones of increased defectiveness, which contributes to the destabilization of the near-surface layer and its softening.

Also, analysis of the data obtained showed that the degree of hardness reduction depends on the type of incident ions. The most significant decrease in hardness is observed upon irradiation with heavy Xe^+ ions, for which, at maximum damage values (~0.27 dpa), the decrease in hardness reaches about 7 – 8 %. Slightly lower values are typical for Kr^+ ions, where the reduction in hardness is approximately 5 – 6 %. For Ar^+ ions, the hardness reduction value is at the level of 3 – 4 %, whereas when irradiated with light O^+ ions, the reduction in hardness remains minimal and does not exceed 2 – 3 %. The obtained dependences are explained by the fact that heavy ions transfer more energy to the atoms of the crystal lattice, forming more powerful displacement cascades and causing a more intense accumulation of radiation defects. As a result, the destabilization degree of the structure grows, which leads to a more pronounced softening of the material. Thus, the results presented show that the reduction in hardness is directly related to the radiation damage degree, and the intensity of material softening increases as dpa grows. In this case, the greatest influence on the change in mechanical properties is exerted by heavy Kr^+ and Xe^+ ions, which cause the most significant degradation of the structure of the near-surface layer.

4. Conclusion

Analysis of structural changes in the near-surface layer depending on the type of incident ions made it possible to estimate the onset of the formation of overlapping regions of defective inclusions in the damaged layer, as well as to qualitatively assess the sizes of these regions formed along the trajectory of ion movement in the material. According to the assessment, it was found that for light O^+ and Ar^+ ions the overlap of defective inclusions is observed at fluences above 10^{13} ion/cm^2, which makes it possible to conclude that the sizes of defective areas are of the order of 3 – 5 nm. For heavy Kr^+ and Xe^+ ions, the overlap of defective regions, which causes an increase in structural changes, is observed at fluences of the order of 5×10^{11} – 10^{12} ion/cm^2, which makes it possible to conclude that the sizes of defective regions as a result of the interaction of ions with the crystal structure are of the order of 10 – 20 nm, and the increase in size compared to light ions is due to the formation of more powerful displacement cascades and an elevation in the contribution of electronic stopping power and nuclear stopping power to structural changes caused by irradiation. The results obtained indicate that the type of incident ions and the irradiation fluence value determine the nature of the formation of the defective structure of the material, as well as the critical conditions under which the overlap of radiation-induced damaged areas begins. Moreover, heavy ions form larger damage zones and cause the overlap of defective areas at significantly lower fluences compared to light ions, which leads to more intense destabilization of the near-surface layer of the material.

Based on the data obtained, it can be concluded that during description of structural damage and changes in the mechanical properties of alloys irradiated with different ions, the most optimal parameter for comparison of changes caused by irradiation is the degree of damage, and not the irradiation fluence.

Studies on the assessment of the mechanical properties of alloys showed that ion irradiation leads to a gradual change in the mechanical properties of the near-surface layer of the alloy under study, expressed in a decrease in microhardness as the irradiation fluence and the structural damage degree grow. It has been established that the softening degree is directly related to the radiation damage value, characterized by the dpa parameter: at low damage values, changes in mechanical properties remain insignificant, whereas with an increase in the damage degree, a more pronounced reduction in hardness is observed. The greatest deterioration in mechanical characteristics was recorded during irradiation with heavy Kr^+ and Xe^+ ions, which is associated with the formation of more powerful displacement cascades and an increased concentration of vacancy defects in the crystal lattice. It is shown that the accumulation and subsequent aggregation of vacancy defects, as well as the overlap of damaged areas at high irradiation fluences, lead to increased deformation distortions of the crystal structure and destabilization of the near-surface layer of the material. Moreover, the development of volumetric swelling processes and the formation of defective clusters are the main factors causing a decrease in hardness and deterioration of the mechanical properties of the irradiated material.

Conflict of interest statement

The authors declare that they have no conflict of interest in relation to this research, whether financial, personal, authorship or otherwise, that could affect the research and its results presented in this paper.

CRediT Author statement

Giniyatova Sh.G. - conceptualization, resources, writing—original draft preparation; **Kozlovskiy A.L., Uglov V.V.** - methodology, validation, writing-review and editing; **Iskakov K.** - formal analysis; writing-original draft preparation; **Shadiyar D**. - formal analysis, visualization; **Borgekov D.B. –** supervision, methodology. All authors have read and agreed to the published version of the manuscript.

Statement on the use of Artificial Intelligence: The team of authors declares that they did not use artificial intelligence tools to process or analyze the data during the preparation of the article.

Data Availability Statement: The datasets used and/or analyzed during the current study available from the corresponding author on reasonable request.

Funding:

This research was funded by the Committee of Science of the Ministry of Science and Higher Education of the Republic of Kazakhstan (No. AP23489223).

References

1. Pickering, E. J., Carruthers, A. W., Barron, P. J., Middleburgh, S. C., Armstrong, D. E., & Gandy, A. S. (2021). High-entropy alloys for advanced nuclear applications. *Entropy*, *23*(1), 98. https://doi.org/10.3390/e23010098

2. Xiang, C., Han, E. H., Zhang, Z. M., Fu, H. M., Wang, J. Q., Zhang, H. F., & Hu, G. D. (2019). Design of single-phase high-entropy alloys composed of low thermal neutron absorption cross-section elements for nuclear power plant application. *Intermetallics*, *104*, 143-153. https://doi.org/10.1016/j.intermet.2018.11.001

3. Skakov, M. K., Baklanov, V. V., Nurpaissova, G. S., Akaev, A. S., Bekmuldin, M. K., & Toleubekov, K. O. (2024). Analysis of methods for simulating the decay heat in corium when modeling a severe accidents at nuclear power plant. *Eurasian Physical Technical Journal*, *21*(1), 47. https://doi.org/10.31489/2024No1/57

4. Shi, T., Lei, P. H., Yan, X., Li, J., Zhou, Y. D., Wang, Y. P., & Lu, C. Y. (2021). Current development of body-centered cubic high-entropy alloys for nuclear applications. *Tungsten*, *3*(2), 197-217. https://doi.org/10.1007/s42864-021-00115-4

5. Moschetti, M., Burr, P. A., Obbard, E., Kruzic, J. J., Hosemann, P., & Gludovatz, B. (2022). Design considerations for high entropy alloys in advanced nuclear applications. *Journal of Nuclear Materials*, *567*, 153814. https://doi.org/10.1016/j.jnucmat.2022.153814

6. Chakraborty, P., & Tewari, R. (2025). High-entropy alloys for nuclear applications. *Journal of Materials Science*, *60*(3), 1439-1453. https://doi.org/10.1007/s10853-024-10511-z

7. Cheng, Z., Sun, J., Gao, X., Wang, Y., Cui, J., Wang, T., & Chang, H. (2023). Irradiation effects in high-entropy alloys and their applications. *Journal of Alloys and Compounds*, *930*, 166768. https://doi.org/10.1016/j.jallcom.2022.166768

8. Yang, T., Guo, W., Poplawsky, J. D., Li, D., Wang, L., Li, Y., & Zinkle, S. J. (2020). Structural damage and phase stability of $Al_{0.3}$CoCrFeNi high entropy alloy under high temperature ion irradiation. *Acta Materialia*, 188, 1-15. https://doi.org/10.1016/j.actamat.2020.01.060

9. Kumar, N. K., Li, C., Leonard, K. J., Bei, H., & Zinkle, S. J. (2016). Microstructural stability and mechanical behavior of FeNiMnCr high entropy alloy under ion irradiation. *Acta Materialia*, *113*, 230-244. https://www.osti.gov/biblio/1256811

10. Zhang, L., Zhang, P., Li, N., Zhang, X., & Mei, X. (2024). Effects of single and simultaneous Fe, He ions irradiations on CoCrFeMnNi high entropy alloy. *Journal of Alloys and Compounds*, *994*, 174711. https://doi.org/10.1016/j.jallcom.2024.174711

11. Zdorovets, M. V., Kozlovskiy, A. A., Moldabayeva, G., Ivanov, I. A., & Konuhova, M. (2025). Radiation-induced degradation effects of optical properties of MgO ceramics caused by heavy ion irradiation. *Optical Materials: X*, 26, 100406. https://doi.org/10.1016/j.omx.2025.100406

12. Turdiyev, M. T., Kasenov, B. K., Nukhuly, A., Bekturganov, Zh. S., Kasenova, S. B., Sagintaeva, Z. I., & Kuanyshbekov, E. E. (2025). Thermodynamic and electrophysical properties of a new semiconductor based on oxides of rare-earth and transition metals. *Eurasian phys. tech. j.*, *22*(3 (53)), 36-47. https://doi.org/10.31489/2025N3/36-47

13. Moldabayeva, G. Z., Kozlovskiy, A. L., Kuldeyev, E. I., Syzdykov, A. K., & Bakesheva, A. (2024). Study of the effectiveness of corrosion resistance growth by application of layered AlN–TiO2 coatings. *Coatings*, 14(4), 373. https://doi.org/10.3390/coatings14040373

14. Kareer, A., Waite, J. C., Li, B., Couet, A., Armstrong, D. E. J., & Wilkinson, A. J. (2019). 'Low activation, refractory, high entropy alloys for nuclear applications'. *Journal of Nuclear Materials*, *526*, 151744. https://doi.org/10.1016/j.jnucmat.2019.151744

15. Wang, B., Yang, C., Shu, D., & Sun, B. (2023). A review of irradiation-tolerant refractory high-entropy alloys. *Metals*, *14*(1), 45. https://doi.org/10.3390/met14010045

16. Ferreirós, P. A., von Tiedemann, S. O., Parkes, N., Gurah, D., King, D. J. M., Norman, P., & Knowles, A. J. (2023). VNbCrMo refractory high-entropy alloy for nuclear applications. *International Journal of Refractory Metals and Hard Materials*, *113*, 106200. https://doi.org/10.1016/j.ijrmhm.2023.106200

17. Tong, Y., Velisa, G., Zhao, S., Guo, W., Yang, T., Jin, K., & Zhang, F. X. (2018). Evolution of local lattice distortion under irradiation in medium- and high-entropy alloys. *Materialia*, *2*, 73-81. https://doi.org/10.1016/j.mtla.2018.06.008

18. El Atwani, O., Vo, H. T., Tunes, M. A., Lee, C., Alvarado, A., Krienke, N., & Martinez, E. (2023). A quinary WTaCrVHf nanocrystalline refractory high-entropy alloy withholding extreme irradiation environments. *Nature Communications*, *14*(1), 2516. https://doi.org/10.1038/s41467-023-38000-y

19. Ge, G., Chen, F., Tang, X., Wang, Y., & Li, C. (2022). Irradiation damage versus lattice distortion in AlNbTiVCrx (x= 0, 0.5, 1) high-entropy alloys from first-principles calculations and irradiation experiments. *Journal of Nuclear Materials*, *563*, 153630. https://doi.org/10.1016/j.jnucmat.2022.153630

20. Kombaiah, B., Zhou, Y., Jin, K., Manzoor, A., Poplawsky, J. D., Aguiar, J. A., & Zhang, Y. (2023). Nanoprecipitates to enhance radiation tolerance in high-entropy alloys. *ACS Applied Materials & Interfaces*, *15*(3), 3912-3924. https://doi.org/10.1021/acsami.2c17540

21. Zong, Y., Hashimoto, N., & Oka, H. (2022). Study on irradiation effects of refractory bcc high-entropy alloy. *Nuclear Materials and Energy*, *31*, 101158. https://doi.org/10.1016/j.nme.2022.101158

22. Barron, P. J., Carruthers, A. W., Fellowes, J. W., Jones, N. G., Dawson, H., & Pickering, E. J. (2020). Towards V-based high-entropy alloys for nuclear fusion applications. *Scripta Materialia*, *176*, 12-16. https://doi.org/10.1016/j.scriptamat.2019.09.028

23. Egeland, G. W., Valdez, J. A., Maloy, S. A., McClellan, K. J., Sickafus, K. E., & Bond, G. M. (2013). Heavy-ion irradiation defect accumulation in ZrN characterized by TEM, GIXRD, nanoindentation, and helium desorption. *Journal of Nuclear Materials*, 435(1-3), 77-87. https://doi.org/10.1016/j.jnucmat.2012.12.025

Authors' information

Giniyatova, Sh. G. – Candidate of Physical and Mathematical Sciences, Professor, Lecturer and Researcher, Department of Nuclear Physics, New Materials and Technologies, L.N. Gumilyov Eurasian National University; Scopus Author ID: 8211979800; https://orcid.org/0000-0003-4990-1208

Kozlovskiy, A.L. – PhD, Professor, Lecturer and Researcher, Department of Nuclear Physics, New Materials and Technologies, L.N. Gumilyov Eurasian National University; Scopus Author ID: 55632118900; https://orcid.org/0000-0001-8832-7443; kozlovskiy.a@inp.kz

Iskakov, K. – PhD Candidate, Department of Nuclear Physics, New Materials and Technologies, L.N. Gumilyov Eurasian National University. https://orcid.org/0009-0008-6650-7986 iskakov.k@inp.kz

Shadiyar D. – 2nd year student of Electric power system, L.N. Gumilyov Eurasian National University, https://orcid.org/0009-0006-6083-7349, shadiyar_db@enu.kz

Uglov, V.V. – Doctor of Physical and Mathematical Sciences, Professor, Department of Solid State Physics and Nanotechnology, Belarusian State University; Scopus Author ID: 7005653968; https://orcid.org/0000-0003-1929-4996; uglov@bsu.by

Borgekov, D.B. – PhD, Director of the Astana Branch of the Institute of Nuclear Physics of the ARKAE RK, Researcher, Laboratory of Engineering Profile, L.N. Gumilyov Eurasian National University; Scopus Author ID: 56440218700; https://orcid.org/0000-0002-9727-0511; d.borgekov@inp.kz

EURASIAN PHYSICAL TECHNICAL JOURNAL

2026, Volume 23, No. 3 (57)

https://doi.org/10.31489/2026N3/16-27

Received: 01/04/2026 Revised: 02/09/2026 Accepted: 28/09/2026 Published online: 30/09/2026

Original Research Article

Open Access under the CC BY -NC-ND 4.0 license

UDC 53.043

GROWTH AND SURFACE STRUCTURE OF Fe MONOLAYERS ON Pt(110)

Toktarbaiuly O.[1,2]*, Kydyrbay N. B.[1,2], Zhazitov M. R.[1,2], Tezekbay Y. Zh.[1,2], Abduvalov A. Zh.[3], Serikov T. M.[4]

[1] Renewable Energy Laboratory, National Laboratory Astana, Nazarbayev University, Astana, Kazakhstan
[2] Institute of New Materials and Energy Technologies, Nazarbayev University, Astana, Kazakhstan
[3] School of Intelligent Systems, Astana IT University, Astana, Kazakhstan
[4] Buketov Karaganda National Research University, Karaganda, Kazakhstan
*Corresponding author: olzat.toktarbaiuly@nu.edu.kz

Abstract. *The structural evolution of Fe monolayers deposited on a Pt(110) surface was investigated under ultra-high vacuum conditions using scanning tunneling microscopy, low-energy electron diffraction, and Auger electron spectroscopy. A clean Pt(110) substrate exhibiting the characteristic (1×2) missing-row reconstruction was prepared by repeated cycles of argon ion sputtering, oxidation, and high-temperature annealing. Surface cleanliness and reconstruction were confirmed by Auger electron spectroscopy and low-energy electron diffraction, while scanning tunneling microscopy imaging revealed an anisotropic terrace–step morphology with atomic rows characteristic of the reconstructed Pt(110) surface. Fe monolayers were subsequently deposited on the clean substrate at room temperature by electron-beam evaporation. Auger electron spectroscopy measurements confirmed the presence of iron on the surface, together with minor carbon and oxygen contamination. Low-energy electron diffraction patterns recorded after Fe deposition showed a noticeable modification of the substrate diffraction features, indicating partial suppression of the original Pt(110)-(1×2) reconstruction. In addition, a sixfold diffraction feature observed at higher electron energy suggests the formation of an ordered overlayer or Moiré-type superstructure arising from the lattice mismatch between Fe and Pt(110). These results provide insight into the growth behavior and interface structure of Fe monolayers on reconstructed Pt(110), and establish a basis for future studies of iron oxide formation and redox transformations on this surface.*

Keywords: Fe growth; Pt(110); surface reconstruction; epitaxial growth.

1. Introduction

Metal-oxide interfaces play a central role in many areas of surface science, heterogeneous catalysis, corrosion, and nanostructured materials research [1–3] . Ultrathin oxide films grown on metallic substrates often exhibit structural, electronic, and catalytic properties that differ significantly from those of bulk oxides, making them valuable model systems for studying fundamental processes at the atomic scale [4–6]. In particular, well-defined oxide films supported on single-crystal metal surfaces provide an ideal platform for investigating the relationship between surface structure, chemical composition, and catalytic activity under controlled experimental conditions [7,8].

Metal surfaces, particularly noble metals, have long served as model substrates for investigations of thin film growth and surface reactions because they combine high chemical stability with well-defined

crystallographic structures [9,10]. Among noble metal substrates, platinum occupies a particularly important position due to its broad technological relevance in heterogeneous catalysis and its strong interaction with a wide range of adsorbates, metals, and oxide species. platinum surfaces are especially attractive due to their technological relevance in catalysis and their ability to support a variety of adsorbates and thin film structures [11,12]. Within the family of low-index platinum surfaces, Pt(110) has attracted special interest because of its pronounced structural anisotropy and its tendency to reconstruct under vacuum conditions. among the low-index platinum surfaces, Pt(110) has received considerable attention because of its pronounced surface reconstruction and anisotropic atomic structure [13,14].Under ultra-high vacuum (UHV) conditions, the clean Pt(110) surface reconstructs into a stable (1×2) missing-row structure [15,16]. In this reconstruction, every second atomic row along the (110) direction is removed, resulting in parallel atomic rows separated by troughs along the (001) direction [17,18]. As a result, the reconstructed surface displays a strongly anisotropic morphology composed of terraces, atomic rows, and step edges, which can act as preferential sites for adsorption, nucleation, and subsequent thin film growth [19].

A thorough examination of the structural and electronic characteristics of reconstructed Pt(110) surface has been done through different techniques such as low-energy electron diffraction (LEED), scanning tunneling microscopy (STM), and Auger electron spectroscopy (AES). [20]. Iron oxide thin films grown on metal substrates have attracted significant attention due to their complex structural behavior and important catalytic properties[20,21]. Iron oxides are widely used in applications such as environmental catalysis, oxidation reactions, and magnetic materials [22,23]. When grown as ultrathin films on metal surfaces, iron oxides can form a variety of structural phases depending on deposition conditions, oxygen exposure, and annealing temperature [24,25]. These systems therefore provide valuable model platforms for investigating oxide growth mechanisms, surface reconstructions, and redox processes at the nanoscale [1]. The Fe/Pt interface is particularly interesting because of the lattice mismatch between iron and platinum, which can lead to the formation of Moiré superstructures and other complex surface morphologies during film growth.

Previous studies have shown that the deposition of iron on noble metal substrates may result in different growth modes, including island formation, layer-by-layer growth, or mixed growth mechanisms depending on experimental conditions. Furthermore, exposure of iron films to oxygen can lead to the formation of various iron oxide phases, whose structural and electronic properties depend strongly on film thickness and substrate interactions. Understanding the oxidation and reduction behavior of iron oxide films on metal substrates is important for clarifying the stability and transformation mechanisms of these systems under reactive environments. Repeated oxidation–reduction cycles may significantly modify the morphology, composition, and surface structure of oxide films. Investigating these processes at the atomic scale is therefore essential for gaining deeper insight into the dynamics of oxide formation and reduction on metal surfaces.

In the present work, the growth and redox cycling of iron oxide films on a Pt(110) surface are investigated using a combination of scanning tunneling microscopy (STM), low-energy electron diffraction (LEED), and Auger electron spectroscopy (AES). A clean reconstructed Pt(110) surface is first prepared and characterized under ultra-high vacuum conditions. Subsequently, iron monolayers are deposited on the substrate, and their structural properties are analyzed. The system is then subjected to controlled oxidation and thermal annealing cycles to study the formation and reduction of iron oxide films. Attention is given to the evolution of surface morphology, structural ordering, and growth mechanisms during the oxidation–reduction cycling process.

2.Materials and Methods

2.1 Ultra-High Vacuum System

All experiments were carried out in an ultra-high vacuum (UHV) chamber equipped with facilities for surface preparation and analysis. The base pressure of the system was maintained at approximately 6.4^{-10} Torr during the experiments. The chamber was equipped with low-energy electron diffraction (LEED), Auger electron spectroscopy (AES), and scanning tunneling microscopy (STM) for structural and chemical characterization of the surface.

2.2 Sample Preparation

The experiments were performed using a single-crystal Pt(110) sample with a diameter of 10 mm, corresponding to a geometric surface area of approximately 78.5 mm². Prior to measurements, the surface was cleaned using repeated cycles of argon ion sputtering, oxidation, and thermal annealing. Sputtering was carried

out using an Ar^+ ion beam for approximately 20 minutes with a beam current of about 2 μA and an argon pressure of approximately 10 Pa.

Following sputtering, the sample was exposed to oxygen at a pressure of about 10 Pa for approximately 2 hours to remove residual carbon contamination from the surface. After the oxidation step, the sample was heated to approximately 480 °C and subsequently annealed at temperatures up to 1000 K. This procedure allowed carbon and oxygen contaminants to react and desorb from the surface, resulting in a clean Pt(110) surface. The cleanliness and structural ordering of the surface were verified by AES and LEED measurements. A well-defined (1×2) reconstruction characteristic of the Pt(110) missing-row structure was observed after the cleaning procedure.

2.3 Surface Characterization

Auger electron spectroscopy (AES) was used to determine the elemental composition of the surface and to monitor the presence of carbon, oxygen, and iron during the experiments. Characteristic Auger peaks corresponding to carbon and oxygen were used to evaluate surface contamination during the cleaning process.

Low-energy electron diffraction (LEED) measurements were performed to investigate the surface crystallographic structure and reconstruction of the Pt(110) surface. Diffraction patterns were recorded at different electron energies to confirm the formation of the (1×2) reconstructed surface.

Surface morphology and atomic-scale structure were examined using scanning tunneling microscopy (STM). STM measurements were performed in constant-current mode under UHV conditions. Typical tunneling parameters corresponded to a tunnel barrier of 3–4 eV. STM images were acquired to investigate the terrace structure, atomic rows, and step morphology of the reconstructed Pt(110) surface.

2.4 Iron Deposition

Fe was deposited on the clean Pt (110) surface at room temperature using an electron-beam evaporator. The deposition rate and nominal film thickness were controlled using a calibrated quartz crystal thickness monitor. The deposited Fe coverage corresponded to a few monolayers (ML), with an effective thickness of approximately 0.18 nm (1.8 Å) per Fe monolayer used for estimating the nominal coverage. After deposition, the surface was characterized using AES and LEED to confirm the presence of iron and to examine the structural changes induced by the deposited Fe atoms.

2.5 Oxidation and Reduction Cycles

Following iron deposition, the Fe/Pt(110) system was subjected to controlled oxidation and thermal annealing cycles to study the formation and reduction of iron oxide monolayers. Oxidation of the surface was performed by exposing the sample to oxygen under controlled conditions. Subsequent thermal annealing was used to induce reduction processes and modify the surface structure. The structural evolution of the surface during these oxidation–reduction cycles was monitored using AES, LEED, and STM measurements. Attention was given to changes in surface morphology, diffraction patterns, and chemical composition to understand the growth behavior of iron oxide monolayers and their transformation during repeated cycling processes.

3. Results and Discussion

3.1 Structure of the Clean Pt(110) Surface

It is a well-known fact that clean Pt(110) surface reconstructs into stable structure known as (1x2) missing row type. The crystallographic properties of the surface are given below. A top view of an fcc(110) crystal is shown in Figure 1. The surface consists of closed-packed rows in the [1-10] direction, separated by large distances in the [001] direction.

Along the [001] direction of a (1x2) missing-row reconstructed fcc(110) surface the structure repeats every four distances $d=a/\sqrt{2}$ (where a=2.77A denotes the bulk nearest-neighbor distance for platinum). Note that d is the smallest distance between atomic rows along the [001] direction if the second and deeper layers are considered. the completely arranged (1x2) arrangement, the period of 4d corresponds to a phase difference value of 2π. There exists a total of four distinguishable nonequivalently sublattice structures. Using them, it is possible to create three kinds of displacements represented by: $n\pi/2$ where n is represented by 1,2 or 3. The obtained shifts can be separated into two classes. The first-class defects having phase difference of π, 3π,… [Figures 2(b) and 2(c)] do not change the average height of surface level. The other class of defects causes a

phase shift of π/2 or 3π/2 and are necessarily correlated with the surface step [Figures 2(d) and 2(e)]. In cases when the defects belong only to the first class, phase shift of π, 3π,… , the surface fully preserves its flat appearance. Depending on the defects at the surface, two completely distinct scenarios can happen: either surface becomes non-planar or remains planar.

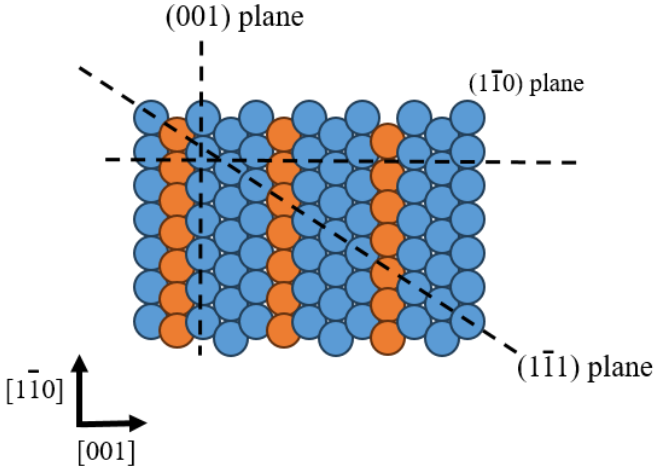


Fig. 1. Schematic top view of the fcc Pt(110) surface showing the atomic arrangement and crystallographic directions. The close-packed atomic rows run along the [110] direction, while the [001] direction corresponds to the spacing between rows. The orientations of the (001), (110), and (111) crystallographic planes relative to the surface are indicated.

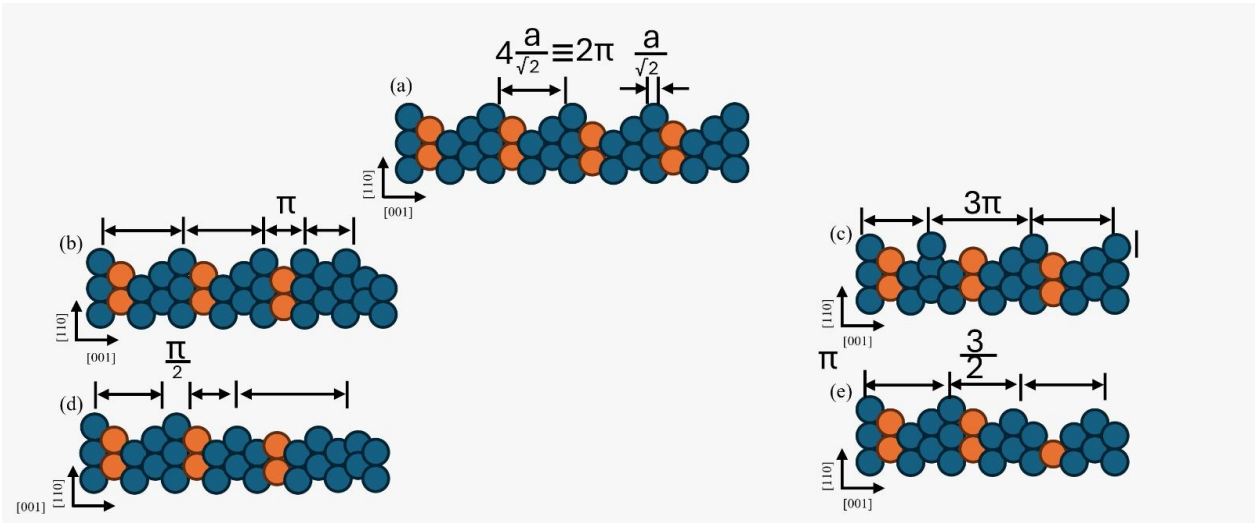


Fig. 2. Side view of the (1×2) reconstructed fcc(110) surface: (a) ideal surface with 4d periodicity along [001]; (b, c) antiphase domain walls with phase shifts of π and 3π; (d, e) surface steps with phase shifts of π/2 and 3π/2.

Figure 2 shows the (1×2) reconstructed fcc (110) surface in a side view with its surface characteristics. As illustrated in Fig. 2(a), the surface has a period of 4d along the [001]. This represents the missing-row mechanism. Here, the phase difference of 2π can be attributed to the distance between the two equivalent lattice sites on the ideal reconstructed surface and gives rise to the fundamental periodicity level in the surface system.

Two major types of surface defects are identified. The first flaw occurs in antiphase domain walls as indicated in Fig. 2(b) and Fig. 2(c). The phase difference in this case is either π or 3π. However, it must be noted that these domain boundaries do not change the height of the surface as they represent simple movements of the reconstructed rows.

The second type of defect corresponds to surface steps, as shown in Fig. 2(d) and Fig. 2(e). The phase shift for this type of defect is π/2 and 3π/2, and there is a change in the mean surface level by a single interlayer spacing. In contrast to the antiphase domain walls, the step defects involve a structural phase shift and a vertical shift of the surface. As can be seen from Fig. 2(a-e), the reconstructed Pt(110)-(1×2) surface accommodates

different types of defects by specific phase relationships, and this may play a significant role in the surface morphology and influence the Fe growth processes.

The anisotropic morphology observed for the Pt(110) surface originates primarily from the intrinsic (1×2) missing-row reconstruction of the clean surface. The reconstruction results from the removal of every second atomic row from the outermost layer along the [001] direction, producing parallel close-packed Pt rows separated by troughs. This structural arrangement gives rise to a pronounced anisotropy in the surface morphology and creates nonequivalent sites, including terraces, troughs, and step edges.

The formation of the ordered anisotropic surface proceeds through several stages. First, Ar^+ ion sputtering removes adsorbed contaminants and disrupts the outermost surface layers. Subsequent exposure to oxygen promotes the conversion and removal of residual carbon-containing species during the following thermal treatment. During high-temperature annealing, surface diffusion and atomic rearrangement become sufficiently pronounced to restore the thermodynamically stable Pt(110)-(1×2) missing-row reconstruction. Thus, the final anisotropic terrace–trough morphology is not produced directly by ion sputtering but results from the reconstruction and ordering of the Pt surface during the subsequent thermal treatment.

3.2 Structural Characterization of the Fe/Pt(110) Interface

The Pt (110) surface has been widely studied using techniques such as Low Energy Electron Diffraction (LEED), Auger Electron Spectroscopy (AES), and Scanning Tunneling Microscopy (STM), among others. In the present study, AES was used to study the Pt (110) surface. The study revealed that carbon and oxygen were present on the surface. To obtain a clean surface, Ar^+ ion bombardment coupled with an oxidation treatment was used. Subsequently, the sample was flashed, which caused the carbon-oxygen species to react, leading to desorption from the Pt (110) surface as depicted in Figure 3.

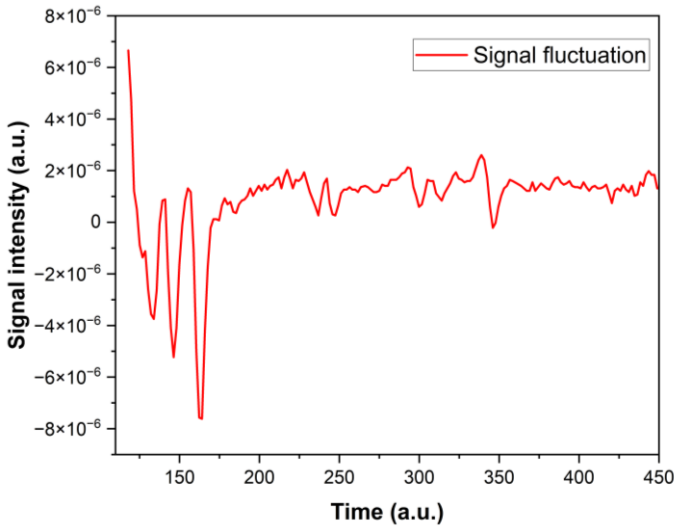


Fig. 3. Temporal evolution of the C KLL Auger signal intensity during the cleaning procedure of the Pt(110) surface. The initial transient region and subsequent quasi-stationary region are indicated.

The temporal evolution of the AES signals shown in Fig. 3–Fig. 5 provides information on the changes occurring at the Pt(110) surface during the cleaning procedure. In particular, the characteristic C KLL and O KLL Auger signals shown in Fig. 3 and Fig. 4, respectively, reflect changes in the surface concentrations of carbon- and oxygen-containing species during Ar^+ ion sputtering, oxidation, and subsequent thermal treatment. The initial transient response corresponds to the stage in which the surface composition and experimental conditions are changing. With continued cleaning and thermal treatment, the intensities of the signals associated with surface contaminants decrease and approach a quasi-stationary level. The stabilized response observed in Fig. 5 indicates that the surface composition and experimental conditions have reached a relatively stable state. The decrease in the C and O Auger signal intensities in Fig. 3 and Fig. 4, respectively, is interpreted as a reduction in the surface concentrations of carbon- and oxygen-containing species. However, the stabilization of the AES signal alone is not considered sufficient evidence of complete surface cleaning. The cleanliness and structural ordering of the Pt(110) surface were therefore evaluated using the combined AES, LEED, and STM results.

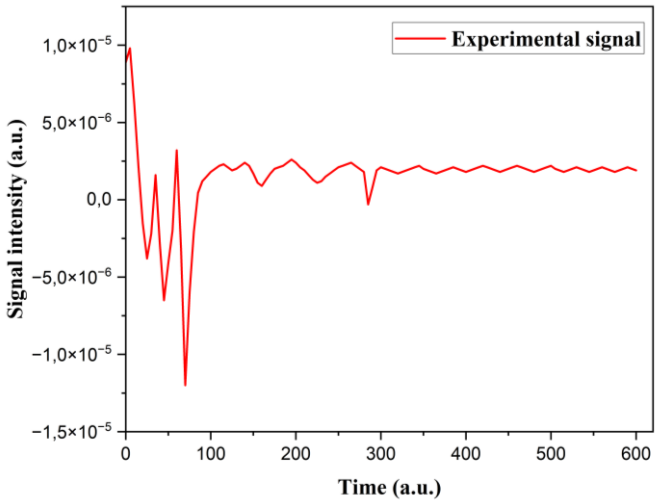


Fig. 4. Temporal evolution of the O KLL Auger signal intensity during the cleaning and annealing treatment of the Pt(110) surface. The transient and quasi-stationary regions are indicated.

The reduced C and O signals observed in Fig. 3 and Fig. 4, together with the well-defined Pt(110)-(1×2) LEED pattern in Fig. 6 and the ordered terrace–step morphology observed by STM in Fig. 7–Fig. 9, provide complementary evidence for effective removal of the major surface contaminants. The observed changes in the AES signals may result from the combined effects of Ar^+ ion bombardment, oxidation, thermal treatment, desorption of volatile surface species, and stabilization of the surface under UHV conditions. Therefore, the temporal evolution of the AES signals shown in Fig. 3–Fig. 5 is considered together with the final AES, LEED, and STM characterization when assessing the surface cleanliness and structural ordering.

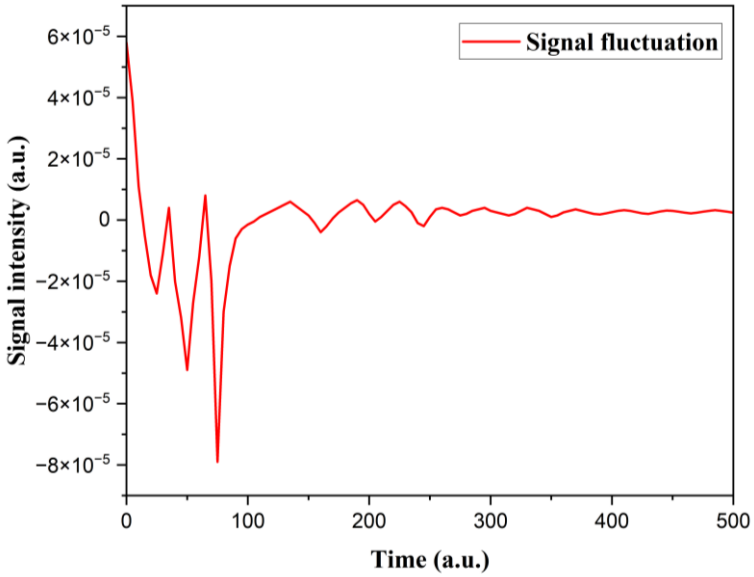


Fig. 5. Temporal evolution of the selected AES signal intensity associated with the Pt(110) surface after the cleaning procedure, showing the transition from the initial transient regime to a stable quasi-stationary state.

The structural arrangement of the Pt(110) surface and the effect of Fe deposition were investigated using low-energy electron diffraction (LEED). The LEED patterns recorded at different primary electron energies are presented in Fig. 6(a–d): (a) and (b) correspond to the clean Pt(110) surface at electron energies of 76 and 84 eV, respectively, while (c) and (d) show the corresponding patterns after Fe deposition at 82 and 92 eV. Following the annealing and flashing treatment, the clean Pt(110) surface exhibits well-defined and regularly arranged diffraction spots, confirming the formation of a well-ordered crystalline surface and indicating the successful removal of significant surface impurities. The patterns obtained at 76 and 84 eV (Fig. 6(a,b)) are qualitatively similar, demonstrating that the overall surface structure remains unchanged with variation in the

primary electron energy, although the relative intensities of the diffraction spots vary due to the energy dependence of the electron scattering process. The characteristic (1×2) features associated with the missing-row reconstruction of Pt(110) are clearly observed for the clean surface.

After Fe deposition, the characteristic (1×2) features become substantially less distinct [Fig. 6(c)], indicating that the Fe overlayer partially suppresses or modifies the long-range order of the Pt(110) missing-row reconstruction. At a primary electron energy of 92 eV (Fig. 6(d)), a distinct hexagonal diffraction pattern is observed. The appearance of six-fold symmetry indicates the formation of an ordered Fe overlayer with a periodicity different from that of the underlying Pt(110) substrate. This behavior can be associated with the development of a Moiré-type surface superstructure resulting from the lattice mismatch between the Fe overlayer and the Pt(110) surface. Thus, the LEED results demonstrate that Fe deposition modifies the reconstructed Pt(110) surface while simultaneously promoting the formation of an ordered overlayer structure.

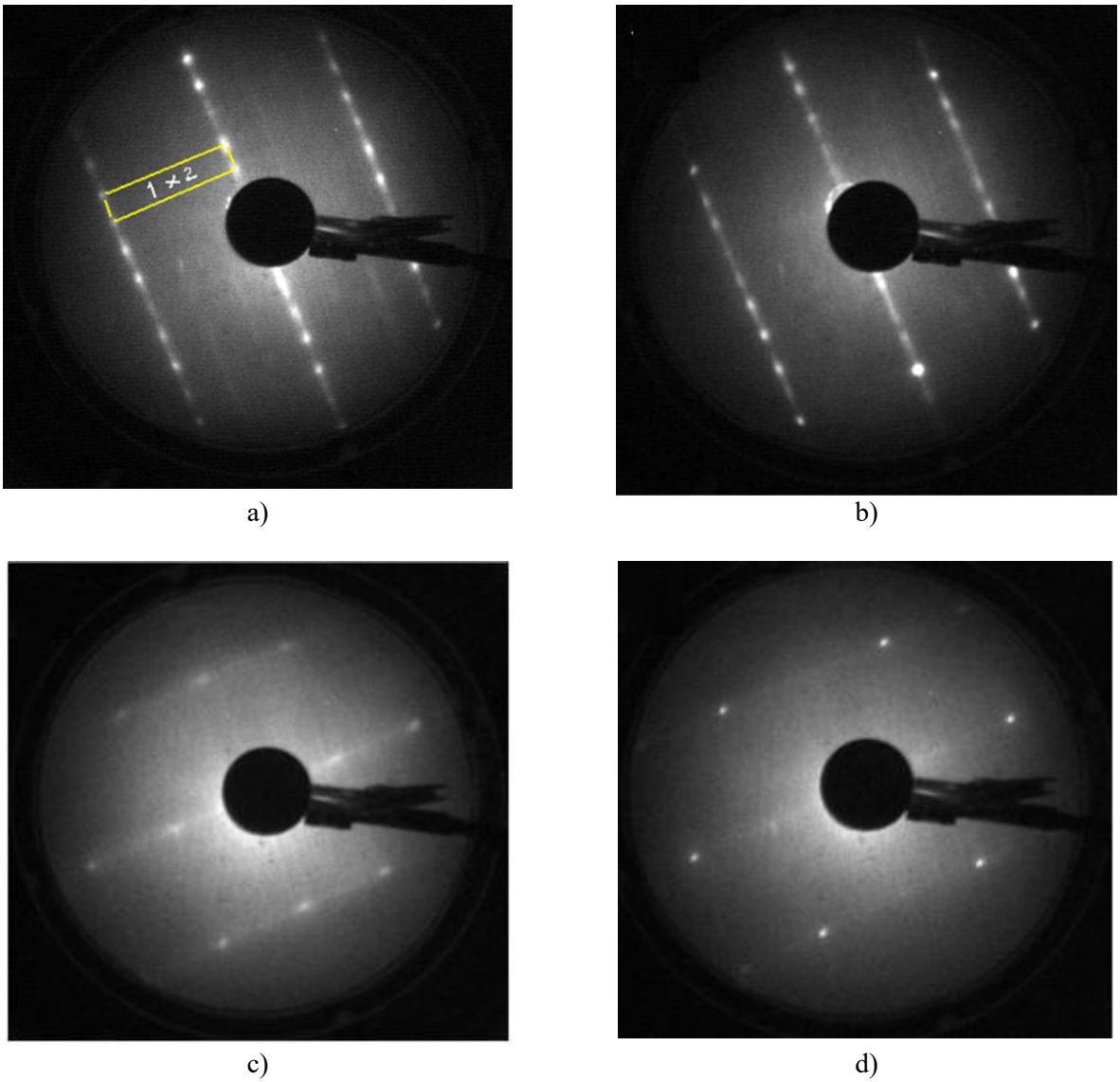
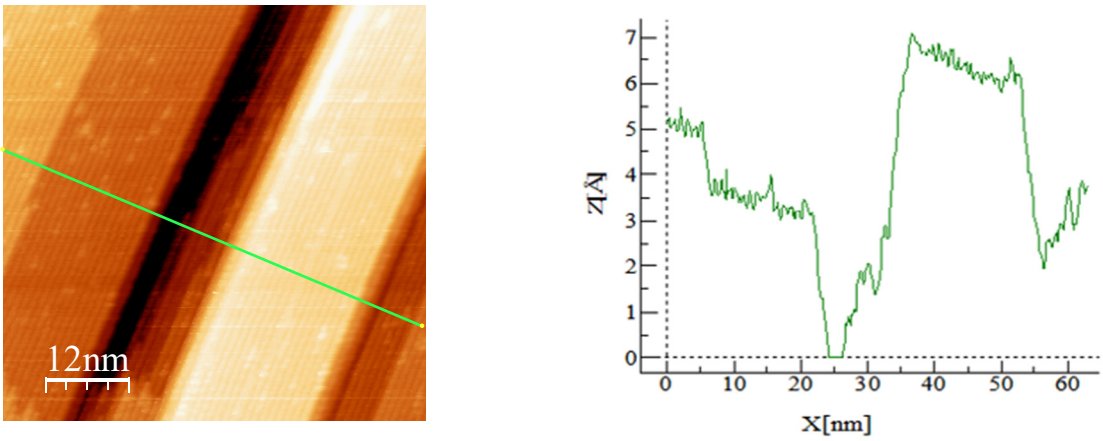


Fig. 6. LEED patterns obtained from the Pt(110) surface and Fe/Pt(110) system at different electron energies after annealing and flashing: (a) clean Pt(110), E_0 = 76 eV; (b) clean Pt(110), E_0 = 84 eV; (c) Fe/Pt(110), E_0 = 82 eV; and (d) Fe/Pt(110), E_0 = 92 eV. Fe deposition partially suppresses the missing-row reconstruction, while the hexagonal pattern in (d) indicates the formation of an ordered Fe overlayer.

Figure 7 shows a STM top view of the clean Pt(110) surface following the preparation process. As indicated in Fig. 7(a), it is evident that the surface is well ordered with features that correspond to the missing-row reconstructed Pt(110)-(1×2) surface. The presence of long-range features on the surface indicates that the surface is anisotropic in nature. This is due to the presence of atomic rows and troughs on the surface that result from the missing-row reconstruction. The STM image in Fig. 7(a) indicates that the surface is well

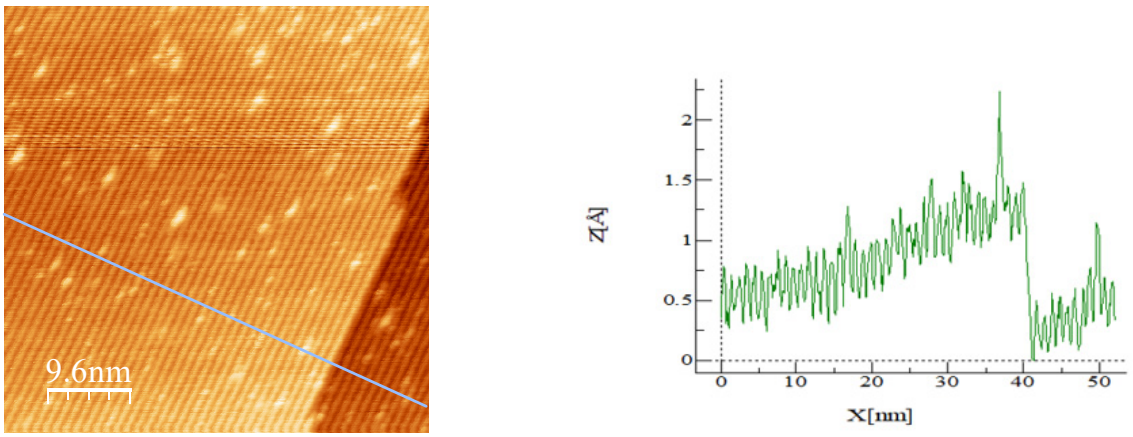
ordered at long range. However, there is also evidence of step features on the surface, which is characteristic of the missing-row reconstructed surface. The line profile in Fig. 7(b), which is indicated by the green line in Fig. 7(a), indicates that there is significant height variation on the surface. This is due to the presence of features on the surface that result in step features. The presence of the terrace-step configuration in Fig. 7(a,b) reveals that the cleaning-annealing process was effective in creating a well-structured surface, which is essential for further experimental work on Fe film depositions. The presence of terraces is also significant in Fe film growth and oxidation.



a) b)

Fig. 7. STM image of the reconstructed Pt(110) surface: (a) topography showing long-range order with step features and (b) line profile along the green line in (a), showing the terrace-step height variation. The well-structured surface confirms the effectiveness of the cleaning-annealing process.

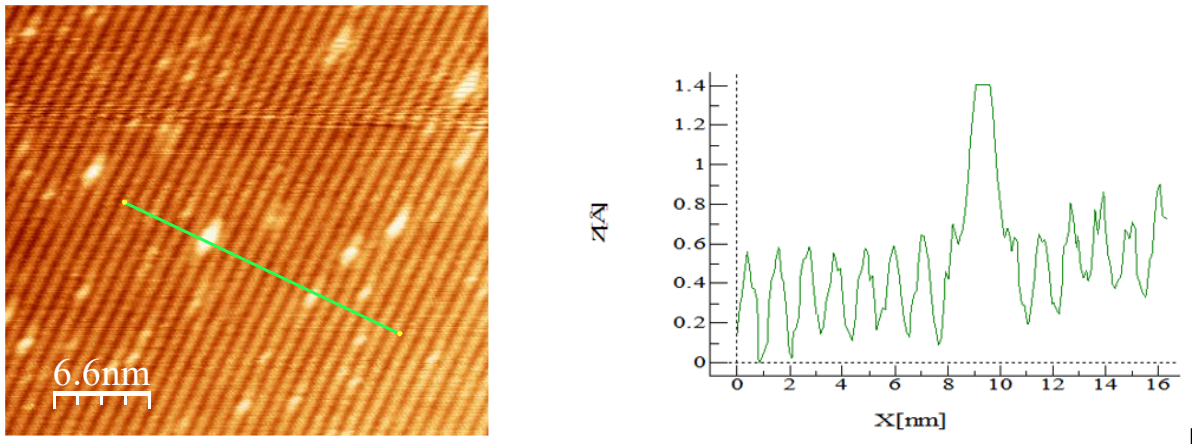
Figure 8 displays a constant current STM image of a reconstructed area of the Pt(110) surface that possesses a (1×2) reconstruction, as well as a cross-sectional profile of the reconstructed area. As seen in Fig. 8(a), the surface features a well-ordered area characterized by rows of atomic features that are characteristic of the missing row reconstructed Pt(110)-(1×2) surface. In addition to the well-ordered rows of atomic features, a well-defined step-like feature appears near the right-hand side of the reconstructed area. As seen in Fig. 8(b), the cross-sectional profile taken along the line shown in Fig. 8(a), a well-defined step appears on the surface, indicating a step-like feature on the reconstructed area of the Pt(110)-(1×2) surface. The height difference of the step appears to be around 1.4 Å, characteristic of a monoatomic step that separates terraces on the reconstructed surface. In addition, a finer corrugation, characterized by a height of approximately 0.85 Å, appears superimposed on the step profile.



a) b)

Fig.8. Constant-current STM image of (1×2) areas on the missing-row reconstructed Pt(110) surface: (a) 48 nm × 48 nm topography; (b) cross-section along the line in (a), showing a downward step.

The presence of well-ordered terraces and well-defined step edges in Fig. 8a,b implies that the Pt(110) substrate was in a very well-prepared condition after the cleaning process. The step edges are believed to be of prime importance during the process of Fe deposition because they might be used as nucleation centers for the deposited atoms. Figure 9 displays a high-resolution STM image of the reconstructed Pt(110) surface together with the corresponding cross-sectional profile taken perpendicular to the atomic rows along the [$1\bar{1}0$] direction. As shown in Fig. 9(a), the STM image clearly reveals the characteristic row structure of the reconstructed Pt(110)-(1×2) surface. In addition to the well-defined row structure, several bright features are observed, which can be attributed to surface adsorbates, such as oxygen- and carbon-containing species. The line profile presented in Fig. 9(b), taken along the direction indicated in Fig. 9(a), reveals the surface corrugation perpendicular to the atomic rows and confirms the periodicity associated with the Pt(110)-(1×2) reconstruction. The measured corrugation reaches approximately 0.8 Å, which is consistent with the characteristic row structure of the reconstructed Pt(110) surface. These observations confirm that the substrate is well ordered and suitably prepared for subsequent thin-film deposition experiments. Following preparation and characterization of the clean Pt(110) substrate, Fe thin films were deposited at room temperature using an electron-beam evaporator. The thickness of the deposited Fe films was monitored and calibrated using a quartz crystal thickness monitor. The resulting Fe/Pt(110) surfaces were subsequently characterized by Auger electron spectroscopy (AES) and low-energy electron diffraction (LEED) to evaluate their surface chemical composition and structural ordering.



a) b)

Fig.9. Large-scale STM image of the Pt(110) surface: (a) 33 nm × 29 nm topography; (b) cross-section along the line in (a), indicating the corrugation normal to the [110] rows.

The differentiated AES spectrum obtained after Fe deposition exhibits pronounced features in the 550–730 eV energy range, which are characteristic of iron Auger transitions and confirm the successful formation of an Fe overlayer on the reconstructed Pt(110) surface, as shown in Fig. 10.

In addition, weak signals attributed to carbon and oxygen are observed in Fig. 10, indicating minor residual contamination and/or partial oxidation of the deposited film. Prior to Fe deposition, AES measurements of the clean Pt(110) substrate showed almost no detectable oxygen or carbon, demonstrating that these species became more evident only after Fe deposition. This behavior, as illustrated in Fig. 10, is consistent with the higher chemical reactivity of Fe compared with Pt, which makes the deposited layer more susceptible to adsorption of residual gases under UHV conditions.

The presence of an O Auger signal after Fe deposition should not be attributed exclusively to surface contamination. Because Fe is considerably more reactive toward oxygen than Pt, the observed oxygen signal may also originate from partial oxidation of the deposited Fe layer by residual oxygen-containing species under the experimental conditions. Therefore, the O signal observed after Fe deposition is interpreted as a possible combination of residual oxygen-containing adsorbates and partial oxidation of the Fe overlayer.

The LEED observations provide a basis for further investigation of the Fe/Pt(110) interface and its evolution during oxidation and reduction. Scanning tunnelling microscopy (STM) is being employed to characterize the surface morphology of the Fe overlayer at the nanoscale, with particular emphasis on its growth mode, including the possible formation of islands and other interface-related structures. Further

experiments will focus on the oxidation of Fe/Pt(110) to produce iron oxide films, followed by characterization using Auger electron spectroscopy (AES) and LEED. Subsequent thermal annealing will be used to induce oxygen desorption and reduction of the iron oxide surface, while AES, LEED, and STM will be employed to monitor the associated structural, compositional, and morphological changes.

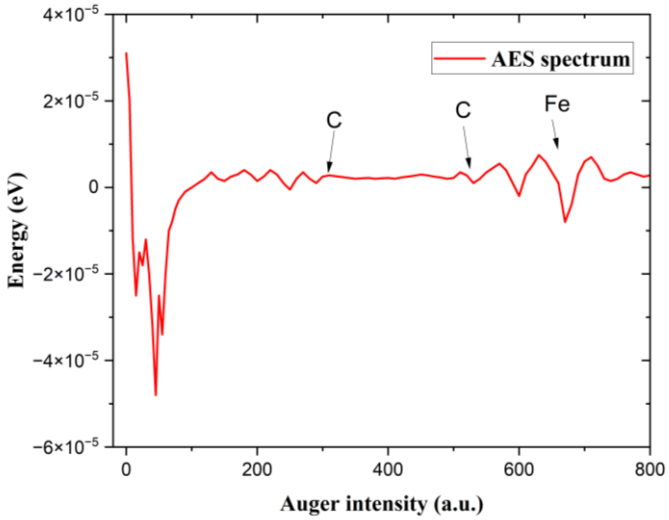


Fig. 10. Auger electron spectrum (AES) of a Fe monolayer deposited on the Pt(110) surface. The spectrum indicates the presence of iron with small contributions from carbon and oxygen, suggesting minor surface contamination.

These experiments will provide further insight into the growth and stability of iron oxide films on reconstructed Pt(110), their behavior during repeated oxidation–reduction cycles, and the morphological evolution associated with the reduction process.

4. Conclusion

In this study, the growth and structural evolution of Fe overlayers on a Pt(110) surface were investigated under ultra-high-vacuum (UHV) conditions using a combination of Auger electron spectroscopy (AES), low-energy electron diffraction (LEED), and scanning tunneling microscopy (STM). The clean Pt(110) surface, exhibiting the characteristic (1 × 2) missing-row reconstruction, was prepared through repeated cycles of Ar^+ ion sputtering, oxidation, and annealing. AES confirmed the effective removal of carbon- and oxygen-containing contaminants, while LEED demonstrated the formation of a well-ordered reconstructed surface. STM revealed the characteristic step-and-terrace morphology of Pt(110), with atomic rows oriented along the corresponding crystallographic directions. The observed step structure and surface corrugation were consistent with the expected morphology of the missing-row reconstruction.

The deposition of Fe onto the reconstructed Pt(110) surface was confirmed by AES through the appearance of Fe-related signals. Following Fe deposition, LEED revealed modifications of the characteristic Pt(110) reconstruction, together with additional diffraction features attributed to the formation of a Moiré-type superstructure. These observations demonstrate that Fe deposition significantly modifies the structural ordering of the Pt(110) surface and results in the formation of a well-defined Fe/Pt(110) interface. The structural characterization performed in the present study establishes Fe/Pt(110) as a suitable model system for investigating the subsequent formation and evolution of iron oxide on a metallic substrate.

Future experiments will focus on the controlled oxidation of the Fe overlayer under UHV conditions. The resulting iron oxide phases will be characterized using AES, LEED, and STM to determine their chemical composition, crystallographic structure, and surface morphology. Particular attention will be paid to the effects of Fe coverage, oxygen exposure, and annealing temperature on oxide formation and structural ordering. These studies will provide insight into the oxidation behavior and structural evolution of Fe/Pt(110) interfaces and contribute to a better understanding of model metal–oxide interfaces relevant to surface chemistry, catalysis, and oxidation–reduction processes.

Conflict of interest statement
The authors state that they do not have any form of conflict of interest concerning their research, whether it is financial, personal, related to authorship and so on, that might interfere with the research itself, and results mentioned in this article.

CRediT author statement
Toktarbaiuly O.: Investigation and Supervision; **Kydyrbay N.B.:** Conceptualization, Writing – original draft; **Zhazitov M.R**..: Methodology, Writing - review & editing; **Tezekbay Y.Zh**.: Investigation & Validation; **Abduvalov A.Zh.:** Data curation, Formal analysis; **Serikov T.M.:** Visualization; Review and Editing. The final manuscript has been approved, and it has been perused by all authors.

Statement on the use of Artificial Intelligence.
During the preparation of this manuscript, artificial intelligence tools were used solely for language editing and grammatical improvement.

Data Availability Statement
The data are available upon reasonable request from the authors.

Funding

The funding for this research has been provided by the Science Committee at the Ministry of Science and Higher Education (MHES) of the Republic of Kazakhstan under Grant No. AP23488359.

References

1. Somorjai, G. A., & Li, Y. (2010). *Introduction to surface chemistry and catalysis* (2nd ed.). John Wiley & Sons. https://www.wiley-vch.de/en/areas-interest/natural-sciences/introduction-to-surface-chemistry-and-catalysis-978-0-470-50823-7
2. Freund, H.-J., Kuhlenbeck, H., & Staemmler, V. (1996). Oxide surfaces. *Reports on Progress in Physics, 59*(3), 283–347. https://doi.org/10.1088/0034-4885/59/3/002
3. Campbell, C. T. (1997). Ultrathin metal films and particles on oxide surfaces: Structural, electronic and chemisorptive properties. *Surface Science Reports, 27*(1–3), 1–111. https://doi.org/10.1016/S0167-5729(96)00011-8
4. Freund, H.-J., & Pacchioni, G. (2008). Oxide ultra-thin films on metals: New materials for the design of supported metal catalysts. *Chemical Society Reviews, 37*(10), 2224–2242. https://doi.org/10.1039/B718768H
5. Diebold, U. (2003). The surface science of titanium dioxide. *Surface Science Reports, 48*(5–8), 53–229. https://doi.org/10.1016/S0167-5729(02)00100-0
6. Wintterlin, J., & Bocquet, M.-L. (2009). Graphene on metal surfaces. *Surface Science, 603*(10–12), 1841–1852. https://doi.org/10.1016/j.susc.2008.08.037
7. Vlieg, E., Robinson, I. K., & Kern, K. (1990). Relaxations in the missing-row structure of the (1×2) reconstructed surfaces of Au(110) and Pt(110). *Surface Science, 233*(3), 248–254. https://doi.org/10.1016/0039-6028(90)90636-M
8. Sowa, E. C., Van Hove, M. A., & Adams, D. L. (1988). The missing-row model for the reconstructed Pt(110)-(1×2) surface: A LEED intensity analysis showing multilayer distortions. *Surface Science, 199*(1–2), 174–182. https://doi.org/10.1016/0039-6028(88)90406-2
9. McIntyre, B. J., Salmeron, M., & Somorjai, G. A. (1993). In situ scanning tunneling microscopy study of platinum (110) in a reactor cell at high pressures and temperatures. *Journal of Vacuum Science & Technology A, 11*(4), 1964–1968. https://doi.org/10.1116/1.578531
10. Minca, M., Penner, S., Loerting, T., Menzel, A., Bertel, E., Zucca, R., & Redinger, J. (2007). Chemisorption of hydrogen on the missing-row Pt(110)-(1×2) surface. *Topics in Catalysis, 46*(1–2), 161–167. https://doi.org/10.1007/s11244-007-0326-4
11. Fery, P., Moritz, W., & Wolf, D. (1988). Structure determination of the (1×2) and (1×3) reconstructions of Pt(110) by low-energy electron diffraction. *Physical Review B, 38*(11), 7275–7284. https://doi.org/10.1103/PhysRevB.38.7275
12. Doná, E., Cordin, M., Deisl, C., Bertel, E., Franchini, C., Zucca, R., & Redinger, J. (2009). Halogen-induced corrosion of platinum. *Journal of the American Chemical Society, 131*(8), 2827–2829. https://doi.org/10.1021/ja809674n
13. Pedersen, T. M., Li, W.-X., & Hammer, B. (2006). Structure and activity of oxidized Pt(110) and α-PtO_2. *Physical Chemistry Chemical Physics, 8*(13), 1566–1574. https://doi.org/10.1039/B515166J
14. Pendry, J. B. (1974). Low-energy electron diffraction. In *Interaction of atoms and molecules with solid surfaces* (pp. 201–211). Springer. https://doi.org/10.1007/978-1-4684-8777-0_7
15. Briggs, D., & Seah, M. P. (Eds.). (1990). *Practical surface analysis, Volume 1: Auger and X-ray photoelectron spectroscopy* (2nd ed.). John Wiley & Sons. ISBN 0-471-92081-9.
16. Chen, C. J. (2021). *Introduction to scanning tunneling microscopy*. Oxford University Press. https://academic.oup.com/book/41125
17. Bode, M. (2003). Spin-polarized scanning tunnelling microscopy. *Reports on Progress in Physics, 66*(4), 523–582. https://doi.org/10.1088/0034-4885/66/4/203

18. Spiridis, N., Wilgocka-Ślęzak, D., Freindl, K., Figarska, B., Giela, T., Młyńczak, E., & Korecki, J. (2012). Growth and electronic and magnetic structure of iron oxide films on Pt(111). *Physical Review B, 85*(7), Article 075436. https://doi.org/10.1103/PhysRevB.85.075436

19. Ritter, M., Ranke, W., & Weiss, W. (1998). Growth and structure of ultrathin FeO films on Pt(111) studied by STM and LEED. *Physical Review B, 57*(11), 7240–7247. https://doi.org/10.1103/PhysRevB.57.7240

20. Lewandowski, M., Pabisiak, T., Michalak, N., Miłosz, Z., Babačić, V., Wang, Y., Korecki, J., & Kiejna, A. (2018). On the structure of ultrathin FeO films on Ag(111). *Nanomaterials, 8*(10), Article 828. https://doi.org/10.3390/nano8100828

21. Shipilin, M., Lundgren, E., Gustafson, J., Zhang, C., Bertram, F., Nicklin, C., & Merte, L. R. (2017). Fe oxides on Ag surfaces: Structure and reactivity. *Topics in Catalysis, 60*(6–8), 492–502. https://doi.org/10.1007/s11244-016-0714-8

22. Soldemo, M., Niu, Y., Zakharov, A., Lundgren, E., & Weissenrieder, J. (2015). A well-ordered surface oxide on Fe(110). *Surface Science, 639*, 13–19. https://doi.org/10.1016/j.susc.2015.04.008

23. Seidel, P., Pomp, S., Schwarz, F., & Sterrer, M. (2025). Stability and dissolution of single-crystalline iron oxide thin films in electrochemical environments. *Surface Science, 751*, Article 122621. https://doi.org/10.1016/j.susc.2024.122621

24. Venables, J. A. (1994). Atomic processes in crystal growth. *Surface Science, 299–300*, 798–817. https://doi.org/10.1016/0039-6028(94)90698-X

25. Brune, H. (1998). Microscopic view of epitaxial metal growth: Nucleation and aggregation. *Surface Science Reports, 31*(4–6), 125–229. https://doi.org/10.1016/S0167-5729(99)80001-6

AUTHORS' INFORMATION

Toktarbaiuly, Olzat. – Ph.D., National Laboratory Astana, Nazarbayev University, Astana, Kazakhstan; ORCID iD: 0000-0003-4594-3435; olzat.toktarbaiuly@nu.edu.kz

Kydyrbay, Nazerke S. – Master (Sci.), National Laboratory Astana, Nazarbayev University, Astana, Kazakhstan; ORCID iD: 0009-0002-6067-7817; nazerke.kydyrbay@nu.edu.kz

Zhazitov, Mergen R. – National Laboratory Astana, Nazarbayev University, Astana, Kazakhstan; ORCID iD: 0009-0008-3494-1067; olzat.toktarbaiuly@nu.edu.kz

Tezekbay, Yerbolat Zh. - Master (Sci.), National Laboratory Astana, Nazarbayev University, Astana, Kazakhstan, Kazakhstan; ORCID iD: 0000-0001-7479-6898; yerbolat.tezekbay@nu.edu.kz

Abduvalov, Alshyn Zh. - Ph.D., Associate Professor, School of Intelligent Systems, Astana IT University, Astana,

Kazakhstan ORCID iD: 0000-0003-4252-8674; alshyn.abduvalov@astanait.edu.kz

Serikov, Timur M. – Ph.D., Associate Professor, Buketov Karaganda National Research University Karaganda, Kazakhstan; ORCID iD: 0000-0003-4302-9674; serikov-timur@mail.ru

EURASIAN PHYSICAL TECHNICAL JOURNAL

2026, Volume 23, No. 3 (57)

https://doi.org/10.31489/2026N3/28-36

Received: 01/06/2026 Revised: 25/08/2026 Accepted: 28/09/2026 Published online: 30/06/2026

Original Research Article

Open Access under the CC BY -NC-ND 4.0 license

UDC 539.216.2:620.193:669.721: 615.46

SELECTIVE DEGRADATION CHARACTERISTICS OF SILVER-CLAD MAGNESIUM ALLOY BIODEGRADABLE IMPLANTS WITH FOR OSTEOSYNTHESIS APPLICATIONS

Greshta V.[1], Yar-Mukhamedova G.Sh.[2], Imanbayeva A.K.[2]*, Dzhus A.[1], Zellele D.M.[2]

[1] Zaporizhzhia Polytechnic National University, Zaporizhzhia, Ukraine
[2] Farabi University, Almaty, Kazakhstan
*Corresponding author: akmaral@physics.kz

Abstract. *Biodegradable implants present significant challenges that hinder their widespread clinical application despite their potential benefits. Key issues include inconsistent degradation rates, insufficient mechanical strength, and the risk of inflammatory responses. These challenges must be addressed to enhance the efficacy and safety of biodegradable implants. This study focuses on the selective degradation behavior of a magnesium-zinc-zirconium-neodymium alloy coated with a silver layer of 200-300 and 500 nm in thickness. The material is proposed for manufacturing biodegradable implants intended for bone fracture treatment. According to the results of potential-dynamic studies of samples in the Ringer-Locke solution, it was found that its corrosion potential was -1.444 and -1.466 V, and the corrosion current density was 0.5012 and 0.3981 mA/cm², respectively. The observed corrosion behavior of the studied samples is attributed to the distinctive characteristics of selective degradation occurring in areas of localized corrosion damage. It was shown that the surface of the corrosion damage of a sample with a coating thickness of 500 nm was enriched with zinc. For the sample with a 200-300 nm coating, the localized corrosion area also became enriched in zinc, while the remaining elements dissolved in the following sequence: magnesium, zirconium, silver, and neodymium.*

Keywords: selective degradation, biodegradable implant, corrosion, osteosynthesis, Ringer-Locke solution, magnesium alloys, silver coating.

1. Introduction

The development of biodegradable implants has gained considerable attention in modern orthopedics and traumatology due to their ability to provide temporary mechanical support during bone healing and subsequently degrade, eliminating the need for a second surgical removal. Despite the advantages, current biodegradable implant materials – especially those based on magnesium (Mg) – face critical limitations, including uncontrolled degradation rates, insufficient mechanical strength, and a lack of antibacterial properties, which may compromise long-term clinical outcomes [1, 2].

Conventional orthopedic implants made from titanium or stainless steel are mechanically robust but remain permanently in the body unless surgically removed, which introduces risks such as infection, stress shielding, and complications from secondary surgery. On the other hand, biodegradable polymers often lack the mechanical strength required for load-bearing applications. Thus, there is a strong demand for new-generation biodegradable materials that cannot only degrade in a controlled manner but also provide adequate mechanical support and prevent post-operative infections [3,4].

Magnesium alloys have emerged as promising candidates due to their biocompatibility, as Mg and its alloys are naturally present in the human body and play a vital role in various biological processes [3-9]. Unlike traditional implant materials, Mg alloys degrade over time within the body, negating the need for surgical removal as well as the degradation products are generally non-toxic and can be metabolized. Furthermore, the elastic modulus of Mg alloys is closer to that of natural bone compared to other metallic implant materials such as stainless stell and titanium alloys reducing the risk of stress shielding, a phenomenon where the implant bears too much of the load leading to bone resorption and weakening [3-9].

Nonetheless, one of the key challenges remains controlling the corrosion and degradation rate in physiological environments to ensure mechanical integrity during the healing period; rapid loss of strength or volume due to hydrogen evolution and premature degradation must be addressed through alloying, microstructure control and surface treatments. Extensive efforts have been made to enhance their corrosion resistance and mechanical performance through alloying, grain refinement via severe plastic deformation and the application of surface coatings [10-12]. For example, the work by Yousefpour et al. [13] demonstrated enhanced corrosion control and mechanical integrity in Mg-based implants via tailored microstructures and surface engineering. However, achieving both corrosion control and antibacterial functionality remains a challenge. To address these shortcomings, this study investigates a novel magnesium-zinc-zirconium-neodymium (NZ30K) alloy, further alloyed with silver (Ag) to form an NZ30K+ Ag alloy, and modified with a silver cladding layer. Silver, well known for its broad spectrum of antibacterial activity, has gained attention as a functional addition to Mg-based alloys. The inclusion of Ag serves a dual purpose: enhancing mechanical properties and introducing antibacterial activity through the release of silver ions (Ag^+) ions during degradation [14-16]. Previous studies have demonstrated that Ag addition into biodegradable Mg-based alloys can provide antibacterial activity while also affecting their corrosion and degradation behaviour [17,18]. Furthermore, silver cladding not only boosts surface antimicrobial performance but also offers a means to influence the corrosion behaviour and degradation profile of the underlying alloy.

The NZ30K alloy was studied because the magnesium matrix ensures biodegradability, while zinc, zirconium, and neodymium contribute to microstructural stability and mechanical properties. The addition of silver is intended to provide an additional antibacterial effect and modify the corrosion behavior. Compared to conventional biodegradable Mg-Zn and Mg-Ca alloys, the studied system combines multicomponent alloying with a silver-containing surface layer. This allows for the evaluation of the influence of both bulk composition and surface modification on localized corrosion.

Understanding the selective degradation behavior of such a composite system is critical for tailoring degradation kinetics to match bone healing timelines. Therefore, this research focuses on the selective degradation characteristics of NZ30K+Ag alloy implants with silver cladding of varying thickness (200-300 nm and 500 nm) in Ringer-Locke solution. The results aim to guide the development of next generation biodegradable implants that address the current limitations in orthopedic applications by combining mechanical integrity, antibacterial protection and controlled biodegradability.

2. Materials and methods

NZ30K magnesium alloy samples, alloyed with Ag, were produced by smelting in an aging process [17], [19]. Cylindrical samples measuring 12 mm in diameter and 30 mm in length were prepared. The chemical composition of the samples was determined using the X-ray spectral method using the Scanning electron microscope EVO-40XVP, ZEISS, with INCA Energy 350 microanalysis system (Oxford) EHT=12.00 kV, as summarized in Table 1. The elemental composition is given as it was obtained from the instrument's software. These values are used to characterize the nominal composition of the alloy being analyzed.

Table 1. Chemical composition of the NZ30K+Ag alloy of the studied samples

Alloy	**Content of chemical elements, wt. %**				
	Mg	Zn	Zr	Nd	Ag
NZ30K+Ag	95.57	0.69	0.86	2.79	0.09

The samples of the alloy under study were clad with a layer of silver 200-300 and 500 nm thick using a 600 mA DC magnetron sputtering system (DXT-450) equipped with a circular source and a target with Ag (50 mm in diameter) in a gas discharge. The vacuum chamber of the system was a cylinder with an internal diameter and height of 500 mm cylindrical samples made of silver-alloyed NZ30K (Table 1) were chemically

degreased and cleaned by ultrasonication in a hot ethanol bath for 10 minutes and dried in warm air. Then they were mounted on a rotating (9 Hz) fixture located 90 mm from the sputtering source. Before deposition of the silver coating, air was evacuated the chamber using a diffusion oil pump to achieve a residual pressure of 1-10^{-3} Pa. The samples were ion-etched at a bias potential of 1000 V for 15 minutes at a pressure of 1.5 Pa. An unbalanced magnetron, supplied from, was used in a 600 mA DC mode at 400 V. The silver coating was applied at a constant magnetron power of 240 W and a substrate bias voltage of 100 V. The argon pressure in the deposition chamber was 1.0 Pa. The time of silver deposition on the surface of the studied magnesium alloy was 5 and 15 minutes for coating thicknesses of 200-300 and 500 nm. Two coating thicknesses were selected to evaluate the influence of the silver layer thickness on the corrosion behavior of the alloy under the same deposition conditions.

Corrosion tests of silver-clad samples were carried out in a Ringer-Locke solution (an aqueous solution of un-distilled water with the following chemical reagents, procured from Beijing Chemical Works, in mg/l: NaCl - 9; $NaHCO_3$; $CaCl_3$; KCl 0.2; CHO_{6126} - 1) at a temperature of 20±1°C.

The establishment of a stationary value of the corrosion potential E_{corr} on the tested samples on the PN-2MK-10A potentiostat in automatic mode has been recorded. The polarization curves were plotted on this potentiostat after the corrosion potential was established on them, and then the potentials of the samples were shifted in the forward and reverse directions at a scan rate of 1 mV/s. The surfaces of corrosion damage on the samples on a JSM6360 scanning electron microscope with a JED-2300 energy dispersive microanalyzer has been researched. The characteristic features of the selective degradation of NZ30K+Ag alloy components in local corrosion damage were studied using the calculated selective degradation coefficients Z_{Zn}, Z_{Zr}, Z_{Nd}, and Z_{Ag}, which were calculated by the formula:

$$Z_{(\mathrm{Zn,Zr,Nd,Ag})} = \frac{\Delta(\mathrm{Zn, Zr, Nd, Ag}) \times \mathrm{Mg}}{\Delta\mathrm{Mg} \times (\mathrm{Zn, Zr, Nd, Ag})},$$

where Δ(Zn, Zr, Nd, Ag) is the difference between the content of Zn, Zr, Nd, Ag in the alloy before testing and in localized corrosion damage, wt. %. Mg is magnesium content in NZ30K+Ag alloy, wt. %. ΔMg is the difference between the Mg content in the alloy before testing and in localized corrosion damage, wt. %. Zn, Zr, Nd, Ag are the content of Zn, Zr, Nd and Ag in the alloy before testing. Depletion of the element under study relative to Mg occurs at $Z > 1$. Relative depletion occurs at $Z = 1$. $Z < 1$ indicates that the element is depleted less rapidly than Mg or is relatively enriched in the analyzed region.

3. Results and discussion

The metallographic analysis of the surface of a localized pitting corrosion on an NZ30K+Ag alloy sample, clad with a silver layer 200-300 nm thickness, revealed a distinctive microrelief pattern. This microrelief is characteristic of the selective degradation observed in steels and alloys at anode regions (Figure 1). In particular, corrosion pores, channels (Figures 1(a) and (b)) and tunnels (Figures 1(c) and (d)) have been observed. At the same time, corrosion degradation of the alloy in the vicinity of the intermetallic inclusion was recorded in (Figures 1(a) and (b)). Selective corrosion is caused by local heterogeneity in the alloy's composition and structure. This promotes preferential dissolution near defects and intermetallic inclusions. Further hydrolysis of the corrosion products and chlorides accumulation in these areas can acidify the local environment and accelerate the formation of pits, pores, channels, and corrosion tunnels.

This is attributed [20] to defects in the alloy structure in these places and the increased porosity of oxide films formed as a result of vacancy coagulation during the solid-phase diffusion of alloy components between the solid solution and the inclusion. An acidic chloride-containing environment that accumulates in corrosion damage due to the hydrolysis of corrosion products often leads to intensive growth of corrosion products by the mechanisms inherent in pitting [21-22]. Under such conditions, corrosion losses from pitting decrease with an increase in the specific magnetic susceptibility of steels and alloys [23].

The chemical composition of the alloy surface in the pitting corrosion formed as a result of contact corrosion between the alloy and the coating in the Ringer-Locke solution by energy dispersive microanalysis has been determined (Figure 1(a)), Table 2. An analysis of the data presented in Tables 1 and 2 indicate a reduction in the content of Mg from 95.57 wt.% (Table 1) down to 94.23 wt.% (Table 2), Zn from 0.69 wt.% (Table 1) to 0.37 wt.% (Table 2) and Nd from 2.79 wt.% (Table 1) to zero (Table 2). Conversely, Zr content

increased from 0.86 wt.% (Table 1) to 1.04 wt. % (Table 2). This led to the selective degradation of metals in the pitting corrosion (Figure 1(a)).

The characteristic features of this process were evaluated by the coefficients of selective degradation (Z) of zinc, zirconium, neodymium, and silver, calculated according to the above formula, using the data from Tables 1 and 2. The calculated coefficients Z_{Zn}, Z_{Zr}, Z_{Nd}, and Z_{Ag} for the spectrum 1 location (Figure 1(a)) are given in Table 3. According to the data from Table 3, the values were found to be greater than one. This showed that Zn, Zr, Nd, and Ag dissolved from the surface of the pitting corrosion more intensively than magnesium. In addition, the higher the value of the Z coefficients, the more intense the degradation of the chemical element from the surface of the corrosion damage. Under these conditions, it can be noted that the degradation rate of the components of the NZ30K+Ag alloy increased in the following order: Mg, Zr, Zn, Ag, Nd. Compared with the initial alloy composition, the analysed region of pitting corrosion showed enrichment in Zr and depletion in Mg, Zn, and Ag. The oncoming solid-phase diffusion of Zr, Zn, and O atoms in the surface layers of the localized corrosion damage suggests increased formation of oxygen-containing corrosion products or oxide species, since a sufficiently high oxygen content (4.36 wt. %) was found from Table 2. In addition, it is known [24, 25], about the ability of Zn and Zr to form dense oxide films on the surface of magnesium alloys that can resist corrosion, including in the Ringer-Locke solution. At the same time, it should be noted that the degradation of solid solutions with a high content of electronegative component is mainly accompanied by surface reorganization by solid-phase diffusion [25].

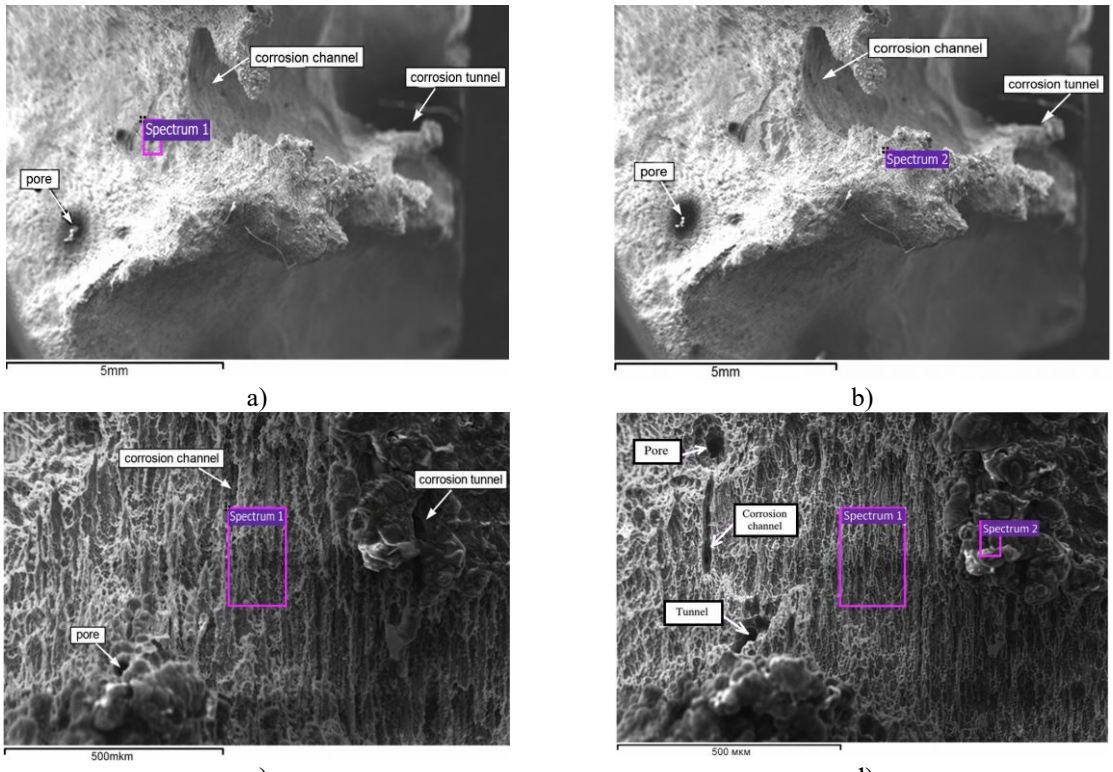


Fig.1. SEM micrographs and localized analysis areas of corrosion damage surfaces of a sample made of NZ30K+Ag alloy clad with a silver layer 200-300 nm thick. (a) Damage 1, spectrum 1. (b) Damage 1, spectrum 2. (c) Damage 2, spectrum 1. (d) Damage 2, spectrum 2.

Table 2. Chemical composition of the surface of localized corrosion damage of a sample clad with a silver layer of 200-300 nm thickness (Figure 1)

No.	Localized corrosion damage to the sample	Content of chemical elements, wt. %					
		Mg	Zn	Zr	Nd	Ag	O
1	Figure 1(a)	94.23	0.37	1.04	0.00	0.00	4.36
2	Figure 1(b)	90.66	0.42	0.63	0.00	1.94	6.25
3	Figure 1(c)	90.10	0.69	1.13	0.81	0.04	7.24
4	Figure 1(d)	77.31	0.53	0.53	0.00	2.01	19.62

Table 3. Coefficients of selective degradation of Zn (Z_{Zn}), Zr (Z_{Zr}), Nd (Z_{Nd}), and Ag (Z_{Ag}) metals on the surface of localized corrosion damage of a sample of silver clad with a thickness of 200...300 nm

No.	Localized corrosion damage to the sample	Coefficients of selective degradation of metals from localized corrosion damage			
		Z_{Zn}	Z_{Zr}	Z_{Nd}	Z_{Ag}
1	Figure 1(a)	25.9	11.7	55.9	55.9
2	Figure 1(b)	7.6	5.2	19.5	40.2
3	Figure 1(c)	0.0	5.5	12.4	9.8
4	Figure 1(d)	1.2	2.2	5.2	60.9

Research outlined in study [25] highlights that the selective degradation of metals from alloys facilitates solid-phase diffusion and characterized by critical potentials. At these potentials, significant reorganization of the surface layers occurs, resulting in the formation of pores, corrosion tunnels, and pitting. These surface changes increase the material's defectiveness and significantly reduce its corrosion resistance. Such damage was found on the surface of localized corrosion damage of a sample made of NZ30K+Ag alloy clad with a silver layer 200-300 nm thick (Figure 1), so its corrosion potential E_{corr} -1.444 V, established during electrochemical tests (Table 4), was critical for these processes. Under these conditions, the corrosion current density i_{corr} was quite high, 0.5012 mA/cm^2, which correlates with the nature of the corrosion fracture of the sample. It should be noted that the coefficients of the Tafel equation for the anodic b_a = 0.113 and cathodic b_k = -0.110 reactions are close (Table 4). However, the coefficient b_k is 0.003 less than b_a. This indicates that the activation energy of the cathodic reaction is higher [26]. This may be the reason for the slowdown in the corrosion degradation of the alloy.

Table 4. Electrochemical parameters of the studied samples of NZ30K+Ag alloy clad with a layer of silver in Ringer-Locke solution

No.	Coating thickness, nm	Corrosion potential, E_{corr}	Corrosion current density, i_{corr}, mA/cm^2	Tafel coefficients	
				$b_к$	b_a
1	200-300	-1.444	0.5012	-0.110	0.113
2	500	-1.466	0.3981	-0.113	0.103

The energy dispersive analysis of the surface of the test sample in the aforementioned pitting corrosion (Figure 1(b), spectrum 2) showed that its chemical composition changed significantly, particularly, the content of Mg and Zr decreased down to 90.66 and 0.63 wt. %, respectively (Table 2). This determined the nature of the selective degradation of metals in the corrosion damage. From the analysis of the data in № 2 of Table 2, it can be noted that the intensity of degradation of alloy components in it increased in the following order: Mg, Zr, Zn, Nd, and Ag. Under such conditions, the surface of the corrosion damage (Figure 1(b), spectrum 2) was enriched with Mg and depleted in Zr, Zn, Nd, and Ag. The observed redistribution of elements may involve surface diffusion processes associated with selective dissolution, as reported for metal alloys undergoing dealloying [24]. In contrast to spectrum 1 (Figure 1(a)), the intensity of selective degradation of these chemical elements was much lower, since its selective degradation coefficients were less than № 1.2 (Table 3). This trend led to the formation of a denser oxide film at the site of spectrum 2 (figure 1(b)), since the oxygen content here was 1.4 times higher than in spectrum 1 (Figure 1(a) and Table 2).

It was found that the content of Mg in another pitting corrosion on the surface of the sample clad with a silver layer 200-300 nm thick (Figure 1 c) decreased, and Zn, Zr, and Nd increased relative to its content on the surface (Figures 1(a) and (b)), № 1, 2 (Table 2). It should be noted that the Ag content decreased by 48.5 times. This contributed to a significant decrease in the coefficients of selective degradation $Z_{Zn,}$ $Zr_{Nd,Ag}$ №3 from table 3. The analysis of these coefficients showed that the intensity of degradation of alloy components in the pitting corrosion spectrum 1 from Figure 1(c) increased in the following order: Zn, Mg, Zr, Ag, and Nd. This caused the enrichment of its surface with Zn and the depletion of Mg, Zr, Ag, and Nd. Under such conditions, the solid-phase diffusion of Zn atoms was directed to the nanovolume of the alloy, and Mg, Zr, Ag, and Nd to the surface of the pitting corrosion. The accumulation of Zn in the surface layers contributed to the formation of self-protective oxide films in this area, since the oxygen content here increased up to 7.24 wt. % of № 3 (Table 2). However, in the upper left corner (Figure 1(b)), pores, corrosion channels, and tunnels were found, which, according to [24], may be due to the selective degradation of the alloy components Mg and Nd with the most electronegative values of the standard electrode potential. At the same time, the corrosive

medium in the pores could be acidified due to the hydrolysis of corrosion products, which caused its development into localized corrosion damage of the alloy up to 100 μm in size (upper left corner of Figure 1(c)), which grew by mechanisms inherent in pitting corrosion [26].

A decrease in the content of Mg, Zn, Zr, and Nd and an increase in Ag up to 2.01 wt. % were found on the surface of the pitting corrosion located 200 μm to the right of spectrum 1 (Figure 1(c)). % spectrum 2 Figure 1(d). This affected its selective degradation coefficients, № 4 of Table 2. From the analysis of these coefficients, it can be noted that the intensity of corrosion degradation of alloy components increased in the following order: Mg, Zn, Zr, Nd, and Ag. Thus, it turns out that the surface of the localized corrosion damage was enriched with Mg and depleted in Zn, Zr, Nd, and Ag. This compositional redistribution may be associated with selective dissolution and possible solid-state redistribution of alloying elements of Mg atoms into the alloy nanovolume, and Zn, Zr, Nd, and Ag to the surface of the localized corrosion damage. Summarizing the above, it can be noted that the NZ30K+Ag alloy sample clad with a 200-300 nm silver layer underwent intense contact and crevice corrosion with the formation of localized corrosion damage, where the alloy components dissolved selectively.

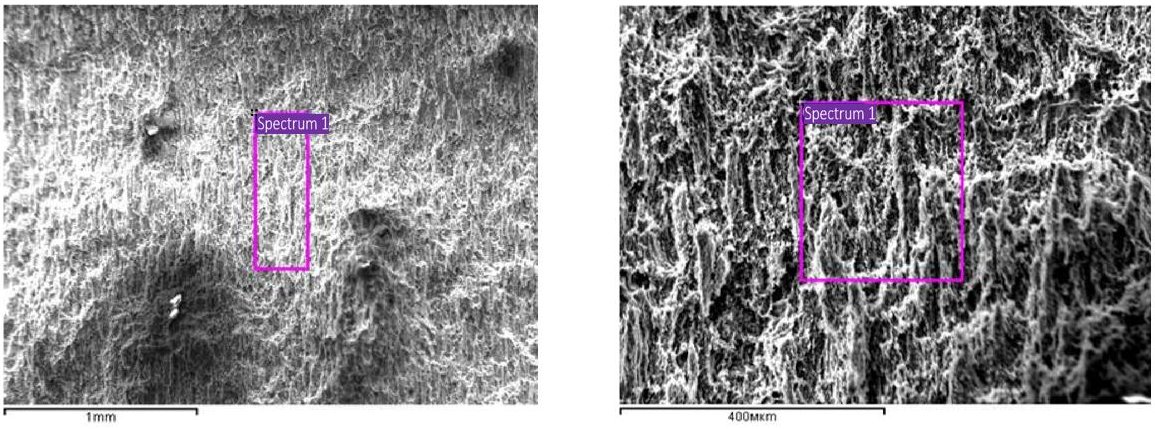
Table 5. Chemical composition of the surface of localized corrosion damage of a sample clad with a silver layer of 500 thickness (Fig. 2)

No.	Localized corrosion damage to the sample	Content of chemical elements, wt. %					
		Mg	Zn	Zr	Nd	Ag	O
1	Figure 2(a)	89.53	0.54	3.6	1.39	0.0	4.94
2	Figure 2(b)	90.76	0.52	0.0	0.0	2.68	6.04

Table 6. Coefficients of selective degradation of Zn (Z_{Zn}), Zr (Z_{Zr}), Nd (Z_{Nd}) and Ag (Z_{Ag}) from the surface of localized corrosion damage of a 500-thick silver clad sample (Fig. 2)

No.	Localized corrosion damage to the sample	Coefficients of selective degradation of metals from localized corrosion damage			
		Z_{Zn}	Z_{Zr}	Z_{Nd}	Z_{Ag}
1	Figure 2(a)	3.4	50.4	7.9	15.8
2	Figure 2(b)	0.58	19.9	19.9	619.8

In particular, the surface of the corrosion damage was mainly enriched with Mg, and in some areas with Zn, but severely depleted in Nd and, especially, Ag. The latter have the most negative (Nd = -2.7V) and positive (Ag = +0.799V) values of the standard electrode potential, which could be the reason for the acceleration of solid-phase diffusion of Nd atoms to the surface of corrosion damage by silver. A sample of NZ30K+Ag alloy clad with a 500 nm thick silver layer was also subjected to contact and crevice corrosion. According to the results of energy dispersion analysis of the surface of localized corrosion damage (Figure 2(a)), it was found that the content of Mg, Zn, Nd, and Ag decreased and Zr increased (Tables 1 and 5).



a) b)

Fig. 2. SEM micrographs and localized analysis areas of corrosion damage of a sample of NZ30K+Ag alloy clad with a 500 nm thick silver layer. (a) Spectrum 1. (b) Spectrum 2.

The values in Tables 2 and 5 correspond to individual EDS measurements performed at the regions marked in Figures 1 and 2 and therefore represent local chemical compositions rather than surface-averaged

values. Analysis of the coefficients of selective degradation of alloy components (Table 6) showed that they dissolved in the following order: Mg, Zn, Nd, Ag, and Zr. This resulted in the enrichment of the surface of corrosion damage with Mg and the depletion of Zn, Nd, Ag, and Zr, which caused its solid-phase diffusion to its surface, and Mg atoms in the opposite direction. It should be noted that on the surface of the corrosion damage of the sample, localized degradation of the alloy in the vicinity of intermetallic inclusions was also detected (Figure 2(a)) and the microrelief is inherent in the selective degradation of steels and alloys, as mentioned above. Under such conditions, the corrosion potential E_{corr} = -1.466V and the corrosion current density i_{corr} = 0.3981 mA/cm^2 were established on the surface of the sample (table 4). Thus, the potential E_{corr} of the sample was 0.022 V negative, and i_{corr} was 0.1031 mA/cm^2 less than that of the sample with a coating thickness of 200-300 nm.

Zr and Nd were not detected on the surface (Figure 2(b) and Table 5), but the content of Ag and oxygen increased. The initial Ag content of the alloy was very low (0.09 wt%, Table 1), while local EDS analysis revealed 2.68 wt% Ag (Table 5). This increase is most likely due to the presence of residual silver coating or localized accumulation of Ag-containing corrosion products. This influenced the nature of the selective degradation of the alloy components; particularly, it was found that the intensity of its degradation in the local corrosion damage increased in the following sequence: Zn, Mg, Zr, Nd, and Ag. Under such conditions, the surface became enriched with Zn while experiencing a depletion of Mg, Zr, Nd, and Ag. This redistribution triggered the solid-phase diffusion of Zn atoms into the alloy's nanovolume, with Mg, Zr, Nd, and Ag migrating in the opposite direction. The solid-phase diffusion of Mg atoms, as the main component of the NZ30K+Ag alloy with a high negative value of the standard electrode potential (-2.363V), contributed to the formation of nonequilibrium vacancies that coagulated into pores [27] (Figure 2(b)). Acidified corrosion products accumulated in them [25], which formed corrosion tunnels due to leakage from the pores under the influence of gravity. This tendency was observed in work [26] on heat exchanger plates subjected to pitting and crevice corrosion.

In summary, it can be noted that the sample of NZ30K+Ag alloy coated with a 500 nm thick layer of silver was subjected to contact and crevice corrosion. The intensity of its corrosion destruction was lower than that of the sample with a coating thickness of 200-300 nm. This is due to the above characteristic features of its selective degradation in longitudinal corrosion damage.

4. Conclusions

NZ30K+Ag alloy samples with silver coatings of 200-300 and 500 nm thickness were tested for contact and crevice corrosion in Ringer-Locke solution. Potentiodynamic polarization tests revealed corrosion potentials (E_{corr}) of -1.444 V and -1.466 V, and corrosion current densities of 0.5012 and 0.3981 mA/cm^2, respectively. These values reflect the alloys susceptibility to selective degradation during localized corrosion.

The surface analysis of corrosion-damaged areas indicated that for the 200-300 nm coated samples, the sequence of selective degradation followed either Mg, Zr, Zn, Nd, Ag or Mg, Zn, Zr, Nd, Ag, with Mg enrichment observed in the affected regions. For the 500 nm coating, the selective degradation sequence depended on the analyzed localized corrosion region. For Figure 2(a), the sequence was Mg, Zn, Ag, Zr, whereas for Figure 2(b) it was Zn, Mg, Zr, Nd, and Ag.

Further surface characterization revealed Zn enrichment in localized corrosion zones of 200-300 nm coatings, with degradation proceeding as Zn, Mg, Zr, Ag, and Nd. For the 500 nm coatings, the sequence was Zr, Mg, Nd, Zn, and Ag. These degradation patterns are characteristic of progressive localized corrosion and suggest concurrent repair and stabilization processes occurring at the corrosion sites.

Conflict of interest statement
The authors confirm that they have no conflicts of interest – financial, personal, authorship-related, or any other – that could influence this research or the results presented in this paper.

CRediT author statement:
Conceptualization: Greshta V. and Yar-Mukhamedova G.; Formal analysis: Imanbayeva A., Zelele D., and Dzhus A.; Validation: Imanbayeva A. and Dzhus A.; Writing – original draft: Greshta V., Yar-Mukhamedova G., and Zelele D.; Writing – review & editing: Greshta V., Imanbayeva A., Zelele D., and Yar-Mukhamedova G.; Supervision: Yar-Mukhamedova G.

Statement on the use of Artificial Intelligence.
The authors declare that no artificial intelligence tools were used to generate scientific content, results, or conclusions of this article.

Data Availability Statement
The data that support the findings of this study are available upon reasonable request from the corresponding author.

References

1 Li, H., Zheng, Y., and Qin, L. (2014). Progress of biodegradable metals. *Prog. Nat. Sci. Mater. Int.*, *24*(5), 414–422. https://doi.org/10.1016/j.pnsc.2014.08.014

2 Cui, L.-Y., Li, X.-T., Zeng, R.-C., Li, S.-Q., Han, E.-H., & Song, L. (2017). In vitro corrosion of Mg–Ca alloy: The influence of glucose content. *Frontiers of Materials Science, 11*(3), 284–295. https://doi.org/10.1007/s11706-017-0391-y

3 Liu, Y., Yin, J., & Zhu, G. (2025). Advances in magnesium-based biomaterials: Strategies for enhanced corrosion resistance, mechanical performance, and biocompatibility. *Crystals, 15*(3), Article 256. https://doi.org/10.3390/cryst15030256

4 Sharma, S. K., Gajević, S., Sharma, L. K., Pradhan, R., Miladinović, S., Ašonja, A., & Stojanović, B. (2024). Magnesium-Titanium Alloys: A Promising Solution for Biodegradable Biomedical Implants. *Materials*, *17*(21), 5157. https://doi.org/10.3390/ma17215157

5 Saberi, A., Baltatu, M. S., & Vizureanu, P. (2024). Recent Advances in Magnesium–Magnesium Oxide Nanoparticle Composites for Biomedical Applications. *Bioengineering*, *11*(5), 508. https://doi.org/10.3390/bioengineering11050508

6 Sezer, N., Evis, Z., Kayhan, S. M., Tahmasebifar, A., & Koç, M. (2018). Review of magnesium-based biomaterials and their applications. *Journal of Magnesium and Alloys, 6*(1), 23–43. https://doi.org/10.1016/j.jma.2018.02.003

7 He, M., Chen, L., Yin, M., Xu, S., & Liang, Z. (2023). Review on magnesium and magnesium-based alloys as biomaterials for bone immobilization. *Journal of Materials Research and Technology*, *23*, 4396–4419. https://doi.org/10.1016/j.jmrt.2023.02.037

8 Wang, H., Qiang, L., Mi, X., Wang, T., & Xu, X. (2023). Additive manufacturing of degradable magnesium alloys and their application in orthopedic implants. *Digital Medicine*, *9*(3), Article e00008. https://doi.org/10.1097/DM-2023-00008

9 Thirugnanasambandam, A., Mohankumar, A., Reddy Botta, R. P., Chong, W. W. F., Thangamani, G., & Gupta, M. (2024). Hydroxyapatite reinforced magnesium alloy composites using the ultrasonic-assisted rheo-squeeze casting technique: Microstructural and mechanical performance evaluation for bone fixture applications. *Crystals*, *14*(7), Article 667. https://doi.org/10.3390/cryst14070667

10 Muradov, A. D., Mukashev, K. M., Yar-Mukhamedova, G. S., & Korobova, N. E. (2017). Impact of silver metallization and electron irradiation on the mechanical deformation of polyimide films. *Technical Physics*, *62*(11), 1692–1697. https://doi.org/10.1134/s1063784217110226

11 Sagyndykov, A. B., Kalkozova, Z. K., Yar-Mukhamedova, G. S., & Abdullin, K. A. (2017). Fabrication of nanostructured silicon surface using selective chemical etching. *Technical Physics*, *62*(11), 1675–1678. https://doi.org/10.1134/s106378421711024x

12 Wang, J., Zhang, Z., Zhang, Y., Jin, L., & Sheng, L. (2022). Experimental measurement on the phase equilibria of the Mg–Ag–Cu ternary system at 350 and 400 °C. *Journal of Magnesium and Alloys*, *10*(2), 449–457. https://doi.org/10.1016/j.jma.2020.12.019

13 Yousefpour, F., Jamaati, R., & Aval, H. J. (2022). Synergistic effects of hybrid (HA+Ag) particles and friction stir processing in the design of a high-strength magnesium matrix bio-nano composite with an appropriate texture for biomedical applications. *Journal of the Mechanical Behavior of Biomedical Materials*, *125*, Article 104983. https://doi.org/10.1016/j.jmbbm.2021.104983

14 Niwas, R., & Kumar, V. (2025). Synergic effect of nano sized ceramic powder of titanium dioxide and silver on AZ91D composites fabricated by friction stir processing. *Ceramics International*, *51*(1), 1259–1270. https://doi.org/10.1016/j.ceramint.2024.11.106

15 Greshta, V., Shalomeev, V., Dzhus, A., & Mityaev, M. (2023). Study of the influence of silver alloying on the microstructure and properties of magnesium alloy NZ30K for implants in osteosynthesis. *New Materials and Technologies in Metallurgy and Mechanical Engineering*, (2), 14–19. https://doi.org/10.15588/1607-6885-2023-2-2

16 Golovakha, M. L., Neryanov, Y. M., Ivchenko, D. V., & Kudievsky, A. V. (2016). *General issues of traumatology and orthopedics: Study guide for practical classes* (2nd ed.). Zaporizhzhia State Medical University.

17 Chowdeswarihalli Narayanappa, C., Nagappan, B., Vignesh, P., & Thirugnanasambandam, A. (2024). Enhancing biocompatibility and antibacterial activity of Mg/HA (magnesium-hydroxyapatite) composites with silver nanoparticles for orthopedic implant applications. *Proceedings of the Institution of Mechanical Engineers, Part E: Journal of Process Mechanical Engineering*, Article 09544089241281544. https://doi.org/10.1177/09544089241281544

18 Feng, Y., Zhu, S., Wang, L., Chang, L., Hou, Y., & Guan, S. (2018). Fabrication and characterization of biodegradable Mg-Zn-Y-Nd-Ag alloy: Microstructure, mechanical properties, corrosion behavior and antibacterial activities. *Bioact Mater.* 3(3), 225-235. https://doi.org/10.1016/j.bioactmat.2018.02.002

19 Greshta, V. L., Narivskyi, O., Dzhus, A., Vynar, V., Yar-Mukhamedova, G., Mukashev, K., Beissen, N., Mussabek, G., Imanbayeva, A.K., Zelele, D., Atchibayev, R., Kemelzhanova, A. (2024). Corrosion behavior of magnesium alloys NZ30K and NZ30K alloyed with silver in a model solution of the osteosynthesis process. *Eurasian phys. tech. j.*, *21*(3), 29–36. https://doi.org/10.31489/2024NO3/29-36

20 Narivs'kyi, O. E. (2007). Influence of the heterogeneity of AISI-321 steel on its pitting in chloride-containing media. *Materials Science*, *43*(2), 256–264. https://doi.org/10.1007/s11003-007-0029-9

21 Narivs'kyi, O. E. (2023). Corrosion behavior of austenitic steels in chloride-containing media during the operation of plate-like heat exchangers. *Physical Sciences and Technology*, *10*(2), Article 06. https://doi.org/10.26577/phst.2023.v10.i2.06

22 Yang, Z., Dong, H., Han, Y., Zhang, Y., Li, P., & Feng, Y. (2024). The growth behavior and mechanisms of pitting corrosion on super 13Cr martensitic stainless-steel surfaces at different diameter-to-depth ratios. *Coatings*, *14*(4), Article 435. https://doi.org/10.3390/coatings14040435

23 Zelele, D. M., Rutkowska-Gorczyca, M. (2024). Electrochemical synthesis and functional properties of metal and alloy-based composition coatings. *Recent Contributions to Physics*, *1*(88), 41–48. https://doi.org/10.26577/RCPh.2024v88i1a06

24 Fritz, J. D., Pickering, H. W. (1991). Selective anodic dissolution of Cu–Au alloys: TEM and current transient study. *Journal of the Electrochemical Society*, *138*(11), 3209–3218. https://doi.org/10.1149/1.2085394

25 Narivs'kyi, O.E. (2005). Corrosion fracture of platelike heat exchangers. *Materials Science*, *41*(1), 122–128. https://doi.org/10.1007/s11003-005-0140-8

26 Narivskyi, O.E., Belikov, S.B., Subbotin, S. A., Pulina, T.V. (2021). Influence of chloride-containing media on the pitting resistance of AISI 321 steel. *Materials Science*, *57*(2), 291–297. https://doi.org/10.1007/s11003-021-00544-z

27 Pickering, H. W. (1983). Characteristic features of alloy polarization curves. *Corrosion Science*, *23*(10), 1107–1120. https://doi.org/10.1016/0010-938x(83)90092-6

AUTHORS' INFORMATION

Greshta, Viktor – Candidate of Technical Sciences, Professor, Rector of Zaporizhzhya Polytechnic National University, Ukraine; Scopus Author ID: 55944039900; https://orcid.org/0000-0002-4589-6811; greshtaviktor@gmail.com

Yar-Mukhamedova, Gulmira Sharipovna – Doctor of Phys. and Math. Sciences, Professor, Al-Farabi Kazakh National University, Almaty, Kazakhstan; Scopus Author ID: 6505954975; https://orcid.org/0000-0001-5642-3481; gulmira-alma-ata@mail.ru

Imanbayeva, Akmaral Karimovna – Candidate of Phys. and Math. Sciences, Researcher, Al-Farabi Kazakh National University; Almaty, Kazakhstan; Scopus Author ID: 15054326000; https://orcid.org/0000-0001-9900-9782; akmaral@physics.kz

Dzhus, Anna - PhD student, Senior Lecturer, Department of Physical Materials Science, Zaporizhzhya Polytechnic National University, Ukraine; Scopus Author ID: 58722586900; https://orcid.org/0000-0002-6474-0732; anna_92@ukr.net

Zellele, **Daniel M.** – PhD, Researcher, Bahir Dar University, Ethiopia; Al-Farabi Kazakh National University, Kazakhstan; Scopus Author ID: 59399902800; https://orcid.org/0009-0003-1085-5264; danayermukhamed92@gmail.com

EURASIAN PHYSICAL TECHNICAL JOURNAL

2026, Volume 23, No. 3 (57)

https://doi.org/10.31489/2026N3/37-43

Received: 25/07/2026 Revised: 15/08/2026 Accepted: 28/09/2026 Published online: 30/09/2026

Original Research Article

Open Access under the CC BY -NC-ND 4.0 license

UDC 538.9, 539.2

PHOTONICS OF BENZ [C, D] INDOLE-BASED POLYMETHINE DYES MOLECULES AND SINGLET OXYGEN SENSITIZATION

Ibrayev N.Kh., Amanzholova G.S.*, Aimagambetova A.A.

Institute of Molecular Nanophotonics, Buketov Karaganda National Research University, Karaganda, Kazakhstan

*Corresponding author: gulnur_as@inbox.ru

Abstract. *This study presents a comparative study of the photophysical properties of the basic polymethine dye bcd based on benz[c,d]indole and its modified derivative 2848SL. Replacing the phenyl groups (Ph) at the nitrogen atoms with butyl radicals (Bu), as well as introducing phenylmercapto groups (-SPh) into the 2848SL molecule, improves electron conjugation, resulting in a bathochromic shift of the absorption and fluorescence maxima to the near-IR region. This modification was found to increase the lifetime of the triplet state from 21.1 to 33.2 μs and leads to an increase of the quantum yield of singlet oxygen generation $O_2(^1\Delta_g)$ to 0.10. The obtained results confirm the effectiveness of triplet-triplet energy transfer, making the 2848SL derivative a promising agent for photodynamic therapy.*

Keywords: benz[c,d]indole, polymethine dyes, intersystem crossing, triplet state, singlet oxygen, photodynamic therapy.

1. Introduction

The development of organic photosensitizers in the near-infrared (IR) range is a key challenge in modern biophotonics and photodynamic therapy (PDT) for cancer [1-3]. The key requirement for such molecules is the ability to effectively absorb light within the «therapeutic transparency window of biological tissues» (700–1100 nm) and possess a high quantum yield of singlet oxygen generation ($O_2(^1\Delta_g)$) [1,4].

The main method for shifting the absorption bands of polymethine dyes (PD) to the long-wavelength region of the spectrum is the lengthening of the polymethine chain [5]. However, such an increase of chain length causes a violation of the uniformity of the charge distribution in the dye chromophore. That leads to strong nucleophilic solvation in liquid and polymeric media. Such solvation causes a decrease in the absorption intensity in the near-IR range of the spectrum [6]. In addition, the lengthening of the polymethine chain leads to a decrease of the photostability and thermal stability of the dyes [5]. A real breakthrough in this area is the use of the heterocyclic ring of benz[c,d]indole. Due to the rigid, developed aromatic π-system, it provides a bathochromic shift of up to 800–1000 nm with a minimal chain length, while maintaining high extinction and stability of the molecule [1].

A fundamental spectral feature of all benz[c,d]indole derivatives is their extremely low fluorescence quantum yields (φ), which do not exceed a few percent [7]. Until recently, it was believed that the benz[c,d]indole residue merely enhances bond order heterogeneity and vibronic interactions, converting all excitation energy into heat. This undoubtedly opens up possibilities for photothermal therapy.

By analogy with classical heterocyclic systems, the rigid π-system of the benz[c,d]indole nucleus forms a spatially closed electron circuit – a conditional «loop». According to modern quantum chemical concepts [8], the peculiarities of π-electron delocalization in such a circuit during the optical transition determine the specific overlap of the wave functions of the singlet and triplet states. The resulting effective configurational perturbations dramatically enhance the spin-orbit interaction in the molecule. This weakens the quantum-mechanical prohibition on changes in multiplicity and sharply increases the rate constant of intersystem crossing (k_{ISC}) between the singlet (S_1) and triplet (T_1) levels [9-13].

Thus, the energy of the absorbed quantum of light is not simply wasted on heating the medium, but is effectively accumulated in the long-lived triplet level (T_1) of the dye. Since the triplet state of the dye molecule is capable of interacting energetically and according to the laws of spin conservation with the ground triplet state of molecular oxygen ($O_2(^3\Sigma_g^-)$), efficient energy transfer occurs. The result of this process is the sensitization of $O_2(^1\Delta_g)$.

This paper presents the spectral and luminescence characteristics of benz[c,d]indole-based PDs and evaluates their potential as agents for generating $O_2(^1\Delta_g)$.

2. Materials and methods

To establish the «structure – property» relationship, a comparative analysis of two systems was carried out: the basic symmetric dye bcd and the modified derivative 2848SL, which were synthesized at the Institute of Organic Chemistry of the National Academy of Sciences of Ukraine (Kyiv). The chemical structures of the benz[c,d]indole polymethine dyes studied in the work are shown in Fig. 1.

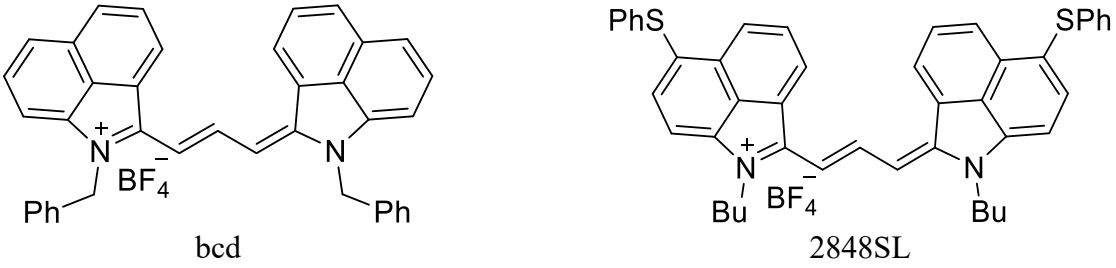


Fig.1. Structural formulas of the studied benz[c,d]indole PDs

The structural differences between the base dye bcd and the derivative 2848SL include the substitution of phenyl groups (Ph) at the nitrogen atoms of the indole cores with butyl radicals (Bu) and the introduction of electron-donating phenylmercapto groups (-SPh) into the heterocyclic core structure. These changes of the chemical structure provide more efficient conjugation of the π-system in the 2848SL molecule. That explains the observed bathochromic shift of the absorption and fluorescence maxima to the near-IR region compared to the base compound bcd.

Ethanol was used as the liquid medium. The dye concentration in the ethanol solutions was 10^{-5} mol/L. Measurements were performed in quartz cuvettes with a 10 mm optical path length. Electronic absorption spectra of the solutions and films were recorded in the spectral range of 200–1100 nm on a Cary 300 automated dual-beam spectrophotometer (Agilent). Fluorescence spectra were measured on a CaryEclipse spectrofluorimeter (Agilent). The kinetics of triplet state deactivation and singlet oxygen phosphorescence were studied on an FLS 1000 stationary spectrometer (Edinburgh Instr.). A tunable laser system (SolarLS) was used as a source of pulsed photoexcitation. It consisted of a solid-state Nd:YAG laser LQ529 and a parametric light generator OPO LP604 with the following output radiation parameters: pulse energy up to 47 mJ and a repetition rate of 10 Hz. The formation of $O_2(^1\Delta_g)$ was confirmed by direct recording of its emission at 1270 nm. Mathematical analysis, deconvolution, and approximation of the experimental decay curves with multiexponential functions were performed using the Fluoracle software package (Edinburgh Instr.).

The quantum yield (Φ_Δ) of $O_2(^1\Delta_g)$ generation was determined using the relative method [14] according to the formula:

$$\Phi_\Delta(x) = \Phi_\Delta^{st} \cdot \left(\frac{S_x}{S_{st}}\right) \cdot \left(\frac{f_{st}}{f_x}\right) \cdot \left(\frac{P_{st}}{P_x}\right) \quad (1)$$

where S_x and S_{st} – integrated phosphorescence intensities of $O_2(^1\Delta_g)$ at a wavelength of 1270 nm for the sample under study and the standard, respectively; f_x and f_{st} – fractions of light absorbed by the sample and the standard at the excitation wavelength (f=1–10^{-D}, where D is the optical density); P_x and P_{st} – excitation laser power during measurements of the sample and the standard; Φ_Δ^{st} – $O_2(^1\Delta_g)$ quantum yield for the standard compound. Rose Bengal (RB) was used as the standard [15,16]. Measurements of $O_2(^1\Delta_g)$ phosphorescence decay kinetics were performed at room temperature in an open cuvette (1 cm) to allow free access of oxygen. The integrated intensity was calculated by numerically integrating the experimental decay curves using the trapezoidal rule in OriginPro 8.0 software [17].

3. Results and discussion

A preliminary analysis of the electronic absorption and fluorescence spectra of compound bcd confirmed that the incorporation of the rigid benz[c,d]indole heterocyclic core, possessing the developed aromatic π-system, provides substantial shifts of the electronic transitions into the near-IR region without the need to lengthen the polymethine chain [1,18]. That is consistent with the well-known ability of a number of heterocyclic terminal groups (4-pyrylium, 4-thiopyrylium, and benz[c,d]indole) to shift the absorption and emission bands of cyanine dyes deep into the near-IR region owing to the nature of the terminal fragment [19]. Measurements showed that the main absorption band of the dye lies in the 600-800 nm region and has an asymmetric shape, characteristic of polymethine dyes, with a gentle rise and a vibrational maximum at the short-wavelength edge. In the UV region of the spectrum, a declining absorption curve was recorded in the 250-500 nm region (Fig. 2).

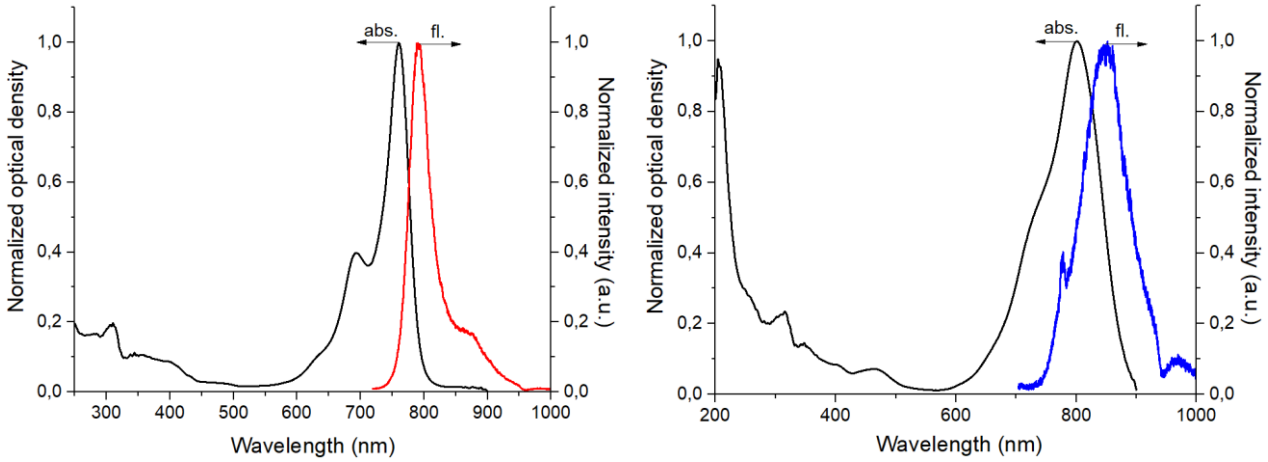


Fig.2. Absorption and fluorescence spectra of PD bcd (a) and 2848SL (b) in solution (ethanol, 10^{-5} mol/L)

The fluorescence spectra of PD bcd are almost mirror-symmetrical to their absorption spectra. In solution, the absorption band maximum of PD bcd is at 760 nm with a shoulder at approximately 690 nm. The fluorescence band maximum is at 790 nm.

The incorporation of a phenylmercapto group (-SPh) into the benz[c,d]indole core shifts the absorption and fluorescence bands of PD into the near-IR region [18]. Replacing the phenyl groups on the nitrogen atoms with butyl groups alleviates steric hindrance. In the case of bcd, phenyl groups disrupt the planarity of the chromophore and partially interrupt conjugation along the chain; in contrast, the butyl groups in 2848SL do not interfere in this way, resulting in a more planar molecule and more effective conjugation, which further enhances the bathochromic shift. Thus, the shift in the absorption maximum from 760 to 800 nm and the fluorescence maximum from 790 to 830 nm results from the combined effect of the electronic influence of the –SPh group and improved molecular conjugation achieved by replacing Ph with Bu.

To study the dynamics of triplet states and singlet-triplet annihilation processes, the dyes were embedded in a solid polyvinyl butyral (PVB, 7.5%) matrix. The delayed fluorescence (DF) kinetic curves of the studied compounds are shown in the Fig. 3. As can be seen from the graphs, a characteristic increase of luminescence intensity is observed for both compounds, followed by monoexponential decay. Calculation of the triplet state

lifetimes revealed significant differences between the samples. The triplet state lifetime for the base bcd dye is 21.1±0.7 μs, while for the modified 2848SL compound, it increases to 33.2±0.8 μs. The increased triplet lifetime in the 2848SL derivative indicates more effective protection of the triplet level from nonradiative deactivation, which is ensured by a change in the molecular structure. The observed DF indicates the presence of long-lived triplet states of the dye.

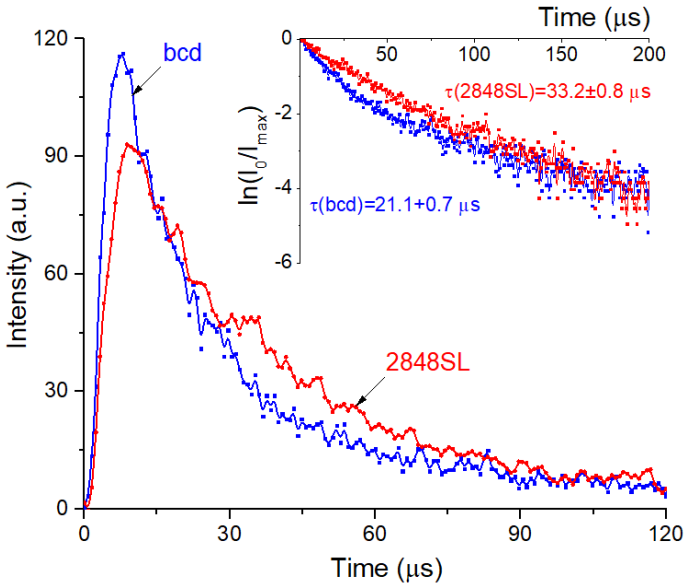


Fig.3. Kinetics of the DF of bcd and 2848SL dyes in PVB films (7.5%) at atmospheric pressure

To quantitatively assess the photosensitizing capacity, the $O_2(^1\Delta_g)$ phosphorescence decay kinetics was recorded at a wavelength of 1270 nm under pulsed laser excitation (Fig. 4). Comparative analysis showed that the photosensitizing activity of the dye 2848SL significantly exceeds that of the base compound bcd.

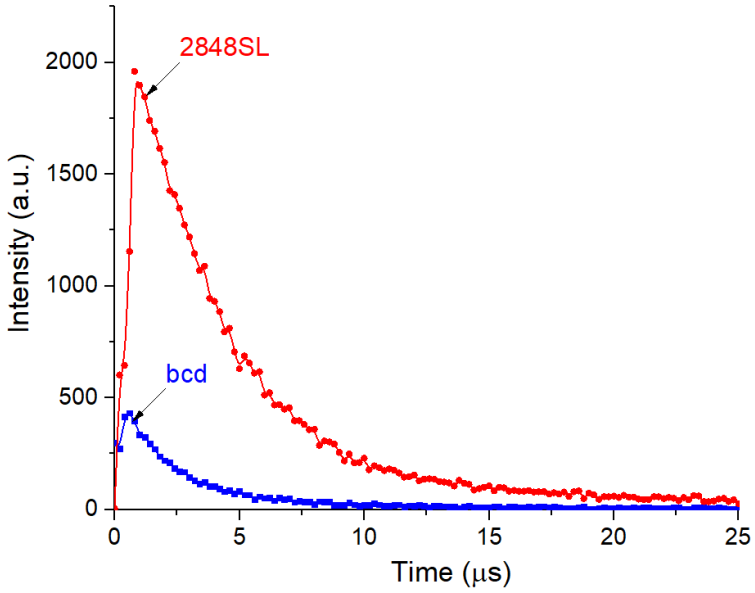


Fig.4. Decay kinetics of $O_2(^1\Delta_g)$ sensitized by dyes bcd and 2848SL in ethanol, C=10^{-5} mol/L

Kinetic analysis allowed us to determine the lifetime τ and quantum yields Φ_Δ of $O_2(^1\Delta_g)$ for both systems. When excited at 760 nm, the bcd dye demonstrated a lifetime of 4.22±0.57 μs and Φ_Δ=0.02. In turn, for the 2848SL dye, when excited at 800 nm, the lifetime was 7.08±0.9 μs and Φ_Δ=0.10. The higher signal intensity and increased values of these parameters in the presence of 2848SL indicate the efficiency of photoinduced energy transfer processes in this system [20].

The obtained experimental data indicate that $O_2(^1\Delta_g)$ is generated due to energy transfer from the dye to $O_2(^3\Sigma_g^-)$. When dye triplets collide with oxygen molecules, the quintet, triplet, and singlet states of the collision complex $[T\ldots{}^3\Sigma_g^-]^{1,3,5}$ are formed (reaction 2). For the singlet, the decay reaction with the formation of the S_0 state of the dyes and $O_2(^1\Delta_g)$ is spin-allowed.

$$T + O_2(^3\Sigma_g^-) \rightarrow [T\ldots{}^3\Sigma_g^-]^{1,3,5} \rightarrow S_0 + O_2(^1\Delta_g) \quad (2)$$

This interaction facilitates overcoming the spin inhibition during the collision of a triplet-excited dye with an oxygen molecule in its ground triplet state. As a result, an efficient energy transfer occurs, accompanied by a change in the spin state of the oxygen molecule and the generation of its $O_2(^1\Delta_g)$.

$O_2(^1\Delta_g)$ molecules, emitting phosphorescence, deactivate into the ground state of $O_2(^3\Sigma_g^-)$:

$$^1\Delta_g \rightarrow {}^3\Sigma_g^- + h\upsilon_{Phos} \quad (3)$$

Thus, the obtained results confirm that the studied benz[c,d]indole dyes effectively sensitize $O_2(^1\Delta_g)$ due to triplet-triplet energy transfer, that makes them promising agents for photodynamic therapy.

4. Conclusion

This study presents a comparative study of the photophysical properties of the benz[c,d]indole polymethine dyes bcd and 2848SL. It was experimentally demonstrated that the introduction of a phenylmercapto group (-SPh) and butyl substituents into the 2848SL structure leads to a bathochromic shift of the absorption and fluorescence bands to the near-IR region (absorption maximum at 800 nm, fluorescence maximum at 830 nm), that corresponds to the «therapeutic window» of biological tissues.

Measurements of the delayed fluorescence kinetics revealed an increase of the triplet state lifetime from 21.1±0.7 μs for bcd to 33.2±0.8 μs for 2848SL, indicating more effective protection of the triplet level from nonradiative deactivation.

Oxygen phosphorescence detection at 1270 nm confirmed $O_2(^1\Delta_g)$ generation. For the bcd dye, upon excitation at 760 nm, the $O_2(^1\Delta_g)$ lifetime was 4.22±0.57 μs with a quantum yield of Φ_Δ=0.02, while for 2848SL, upon excitation at 800 nm, these parameters increased to 7.08±0.9 μs and Φ_Δ=0.10.

Thus, structural modification of benz[c,d]indole dyes provides the targeted enhancement of the triplet channel and significantly increases the efficiency of $O_2(^1\Delta_g)$ sensitization. The 2848SL dye exhibits higher photosensitizing activity than the parent bcd, making it a promising agent for photodynamic therapy and photocatalysis.

The obtained results demonstrate the potential of benz[c,d]indole derivatives for combined photodynamic and photothermal therapy, owing to a combination of near-IR absorption, effective generation of $O_2(^1\Delta_g)$ and the predominance of thermal relaxation over fluorescence – features that enable a dual mechanism of action that is innovative for this class of compounds.

Conflict of interest statement

The authors declare that they have no known financial or personal conflicts of interest that could influence the results of the work presented in this article.

CRediT author statement

IbrayevN.Kh.: Writing – review & editing, Resources, Project administration, Methodology, Conceptualization. **Amanzholova G.S.:** Writing – original draft, Visualization, Validation, Investigation, Data curation. **Aimagambetova A.A.:** Visualization, Validation, Investigation.

Statement on the use of Artificial Intelligence.

During the preparation of this manuscript, artificial intelligence tools were used solely for language editing and grammatical improvement. No AI tools were used to generate scientific content, analysis, results, or conclusions.

Data Availability Statement

The data are available upon reasonable request from the authors.

Funding

This work was supported by the Committee of Science of the Ministry of Science and Higher Education of the Republic of Kazakhstan under Grant No. AP23490195.

References

1 Bricks, J.L., Kachkovskii, A.D., Slominskii, Yu.L., et al. (2015). Molecular design of near infrared polymethine dyes: A review. *Dyes and Pigments*, 121, 238–255. https://doi.org/10.1016/j.dyepig.2015.05.016

2 Dereje, D.M., Pontremoli, C., Moran Plata, M.J., et al. (2022). Polymethine dyes for PDT: recent advances and perspectives to drive future applications. *Photodiagnosis and Photodynamic Therapy*, 21, 397-419. https://doi.org/10.1007/s43630-022-00175-6

3 Ishchenko, A.A., & Syniugina, A.T. (2023). Structure and photosensitizer ability of polymethine dyes in photodynamic therapy: A review. *Theoretical and Experimental Chemistry,* 58(6), 373–401. https://doi.org/10.1007/s11237-023-09754-9

4 Polishchuk, V., Filatova, M., Rusanov, E., et al. (2022). Trianionic 1,3,2-Dioxaborine- Containing Polymethines: Bright Near-Infrared Fluorophores. *Chemistry – A European Journal,* 28(70), e202202168. https://doi.org/10.1002/chem.202202168

5 Tolmachev, A.I., Slominskii, Yu.L., & Ishchenko, A.A. (1998). New cyanine dyes absorbing in the NIR region. *New Infrared Dyes for High Technology Applications.NATO ASI Series.3. High Technology,* 52, 385-415. https://doi.org/10.1007/978-94-011-5102-3_19

6 Ishchenko, A. A., Derevyanko, N. A., Zubarovskii, V. M., et al. (1985). Influence of length of the polymethine chain on width of absorption bands of symmetric cyanine dyes.*Theoretical and Experimental Chemistry,* 20(4), 415-422. https://doi.org/10.1007/BF00516576

7 Derevyanko, N.A., Ishchenko, A.A., & Kulinich, A.V. (2020). Deeply coloured and highly fluorescent dipolar merocyanines based on tricyanofuran. *Physical Chemistry Chemical Physics,* 22(5), 2748-2762. https://doi.org/10.1039/C9CP05827C

8 Drexhage, K. H. (1976). Fluorescence Efficiency of Laser Dyes. *Journal of Research of the National Bureau of Standards – A. Physics and Chemistry,* 80A(3), 421-428. https://doi.org/10.6028/jres.080A.044

9 Voiciuk, V., Redeckas, K., Derevyanko, N.A., et al. (2014). Study of photophysical properties of a series of polymethine dyes by femtosecond laser photolysis. *Dyes and Pigments,* 109, 120–126. https://doi.org/10.1016/j.dyepig.2014.05.012

10 Kulinich, A.V., Ishchenko, A.A., Chibisov, A.K., et al. (2014). Effect of electronic asymmetry and the polymethine chain length on photoprocesses in merocyanine dyes. *Journal of Photochemistry and Photobiology A: Chemistry,* 274, 91-97. https://doi.org/10.1016/j.jphotochem.2013.09.016

11 Redeckas, K., Voiciuk, V., Ishchenko, A.A., et al. (2018). Dark states of symmetric polymethine dyes revealed by pump–dump–probe spectroscopy. *Lithuanian Journal of Physics,* 58(4), 346-357. https://doi.org/10.3952/physics.v58i4.3879

12 Ishchenko, A.A., Kurdyukova, I.V., Bogdanovich, M.V., et al. (2021). Electronic structure and spectral-fluorescent properties of thiopyrylo-4-tricarbocyanine laser dyes. *Optics and Spectroscopy,* 129(8), 926-934. https://doi.org/10.1134/S0030400X21070080

13 Rüttger, F., Mindt, S., Golz, C., et al. (2019). Isomerization and dimerization of indocyanine green and a related heptamethine dye. *European Journal of Organic Chemistry,* 2019(30), 4791-4796. https://doi.org/10.1002/ejoc.201900715

14 Bregnhøj, M., & Ogilby, P.R. (2026). Quantum yield standards for the photosensitized production of singlet oxygen in water. *Physical Chemistry Chemical Physics,* 28(26), 15768-15790. https://doi.org/10.1039/D6CP01739H

15 Szewczyk, G., & Mokrzyński, K. (2025). Concentration-dependent photoproduction of singlet oxygen by common photosensitizers. *Molecules,* 30 (5), 1130. https://doi.org/10.3390/molecules30051130

16 Wilkinson, F., Helman, W.P., & Ross, A.B. (1993). Quantum Yields for the Photosensitized Formation of the Lowest Electronically Excited Singlet State of Molecular Oxygen in Solution. *Journal of Physical and Chemical Reference Data* 22(1), 113-262. https://doi.org/10.1063/1.555934

17 OriginLab Corporation, Originpro 8.0; Originlab Corporation, Northampton, MA, USA, 2007.

18 Ishchenko, A.A. (1994). Structure and Spectral-Luminescent Properties of Polymethine Dyes [in Russian]. Kyiv: Naukova Dumka, 232 p.

19 Henary, M., Paranjpe, S., & Owens, E.A. (2013). Synthesis and applications of benzothiazole containing cyanine dyes. *Heterocyclic Communications,* 19 (2), 1-11. https://doi.org/10.1515/hc-2013-0012

20 Kanofsky, J. R., & Sima, P. D. (2000). Structural and environmental requirements for quenching of singlet oxygen by cyanine dyes. *Photochemistry and Photobiology,* 71(4), 361-368. https://doi.org/10.1562/0031-8655(2000)0710361SAERFQ2.0.CO2

AUTHORS' INFORMATION

Ibrayev, Niyazbek - Doctor of Physico-Mathematical Sciences, Professor, Institute of Molecular Nanophotonics, Buketov Karaganda National Research University, Karaganda, Kazakhstan; SCOPUS Author ID: 9333698600; Web of Science Researcher ID: C-2957-2015; https://orcid.org/0000-0002-5156-5015; niazibrayev@mail.ru

Amanzholova, Gulnur - PhD, Senior Researcher, Institute of Molecular Nanophotonics, Buketov Karaganda National Research University, Karaganda, Kazakhstan; SCOPUS Author ID: 57204729767; Web of Science Researcher ID: U-6122-2018; https://orcid.org/0000-0002-0201-2692; gulnur_as@inbox.ru

Aymagambetova, Amina - Master, Junior Researcher, Institute of Molecular Nanophotonics, Buketov Karaganda National Research University, Karaganda, Kazakhstan; SCOPUS Author ID: 59365258300; https://orcid.org/0009-0002-2414-9005; fiz.tekh@mail.ru

EURASIAN PHYSICAL TECHNICAL JOURNAL

2026, Volume 23, No. 3 (57)

https://doi.org/10.31489/2026N3/44-53

Received: 08/07/2026 Revised: 18/08/2026 Accepted: 28/09/2026 Published online: 30/09/2026

Original Research Article

Open Access under the CC BY -NC-ND 4.0 license

UDC 538.945.91; 621.785

ANISOTROPIC MICROSTRAIN AND ITS RELATIONSHIP WITH THE OUT-OF-PLANE TEXTURE AND THE SUPERCONDUCTING PROPERTIES OF YBCO FILMS GROWN ONTO $SrTiO_3$ (100) AND $LaAlO_3$ (100) SUBSTRATES BY CHEMICAL SOLUTION DEPOSITION

Sanchez Cornejo H.E.[1]*, Kargin J.B.[2], Afanasyev D.A.[3], Guchenko S.A.[3], Sagyndykova G.E.[2], Zhangozin K.N.[4], Bustamante Dominguez A.[1], Celis Rojas S.R.[5], Barnes C.H.W.[6], De Los Santos Valladares L.[2,6]*

[1] Major National University of San Marcos, Lima, Peru
[2] Institute of Physical and Technical Sciences, L.N. Gumilyov Eurasian National University, Astana, Kazakhstan
[3] Buketov Karaganda National Research University, Karaganda, Kazakhstan
[4] «TSK Vostok» LLP, Astana, Kazakhstan
[5] National University of Barranca, La Florida, University Campus, Barranca, Peru
[6] Cavendish Laboratory, Department of Physics, University of Cambridge, Cambridge, United Kingdom
Corresponding authors: henry.sanchez@unmsm.edu.pe

Abstract. *The anisotropic microstrain and its relationship with the out-of-plane texture and superconducting properties of $YBa_2Cu_3O_{7-\delta}$ (YBCO) films grown onto $SrTiO_3$ (100) and $LaAlO_3$ (100) single-crystal substrates by the chemical solution deposition sol-gel technique are considered. X-ray diffraction analysis present (00l) reflections from the YBCO phase in both films, with c-axis grain fraction values of 88% and 81% for the $SrTiO_3$ and $LaAlO_3$, respectively. The ω-scan measurements around the (005) reflection reveal a multi-layer structure for both films: three sub-layers with Δω = 0.35 °, 0.83 ° and 1.0 ° for YBCO/$SrTiO_3$, and two sub-layers with Δω = 0.45° and 2.0° for YBCO/$LaAlO_3$. Microstructural analysis using Debye-Scherrer and Williamson-Hall methods indicates that the YBCO films exhibit significant anisotropic microstrain, with the strain state being more homogeneous on $LaAlO_3$ than on $SrTiO_3$. The superconducting properties show a strong dependence on microstrain: The YBCO film on $LaAlO_3$ exhibit a higher onset critical temperature ($T_{C(Onset)} \approx 92$ K) compared to that grown onto $SrTiO_3$ ($T_{C(Onset)} \approx 78$ K), despite the latter having a higher degree of c-axis texture. This work demonstrates that anisotropic microstrain plays a dominant role in determining the superconducting properties of YBCO films grown by the chemical solution deposition technique, highlighting that structural texture alone is not the only factor governing superconducting performance.*

Keywords: superconductivity, anisotropic microstrain, out-of-plane texture, sol-gel, chemical solution deposition.

1. Introduction

The discovery of high-temperature superconductors (HTS) in complex oxides such as the cuprates has enormously increased the interest in growing epitaxial thin films of a wide range of transition metal oxides displaying remarkable functional properties [1, 2]. Among these materials, $YBa_2Cu_3O_{7-\delta}$ (YBCO) has emerged as one of the most promising candidates for technological applications due to its ability to transport high critical current densities at the boiling point of liquid nitrogen (77 K). However, the strongly anisotropic nature of

YBCO, characterized by a short coherence length and a large anisotropy in their physical properties, imposes requirements on the films microstructure to achieve optimal superconducting performance. From this, the anisotropy is an intrinsic factor that dictates the magnetic properties of YBCO, thus having a great impact for many applications [3]. The anisotropy of YBCO makes it necessary to use epitaxial layers with biaxial texture, i.e., with good out-of-plane and in-plane orientation, to achieve critical current densities ($J_C(B,T)$) higher than 10^6 A/cm² at 77 K [3, 4]. In thin films, texture refers to the relative ordering of crystallites to a particular direction of growth, called the texture axis [4, 5]. Out-of-plane texture, which refers to the orientation of the crystallographic axes with respect to the substrate normal, is particularly crucial due determines the alignment of the superconducting CuO_2 planes. A high uniaxial texture, where the grains grow with their *c*-axis perpendicular to the substrate, is essential for maximizing current transport [6]. Contrariwise, the presence of *a*-axis oriented grains or the formation of 90° grain boundaries can strongly deteriorate the critical currents and therefore the potential applications [7]. Quantifying the degree of texture in YBCO layers is commonly achieved by various experimental techniques, such as X-ray diffraction (XRD), pole figure analysis, ω-scans (rocking curves), Raman spectroscopy and electron microscopy [8].

Chemical solution deposition (CSD), and in particular the sol-gel method, has emerged as a low-cost and highly scalable alternative for the fabrication of YBCO superconducting films [9, 10]. Unlike vacuum deposition techniques, CSD does not require expensive equipment and offers precise control over stoichiometry and microstructure [11]. Among the advantages of the fluorine-free sol-gel method are the stability of the precursor solution, a denser film microstructure, and the elimination of HF formation during processing [12, 13]. The combination of sol-gel chemistry with deposition techniques such as ink-jet printing offers significant advantages, including reduced waste of the precursor solution, production in long lengths, and the possibility of switching from depositing a coating to a multifilamentary superconductor [14]. This makes the CSD route an attractive option for the industrial production of coated conductors [15]. Moreover, these solution processes provide better homogeneity and composition control than other techniques like sputtering or MOCVD, and can render easiness of coating on substrates with various shapes and forms by simple techniques such as dip coating.

Despite the advances in the growth of YBCO films, there is a gap in the quantitative understanding of how out-of-plane texture, microstrain, and anisotropic microstrain together influence the superconducting properties. Most studies have focused on texture characterization, but few have systematically addressed how structural inhomogeneities, such as the microstrain generated during growth, affect the superconducting properties [10, 16]. The microstrain in the crystallites can affect the width of the diffraction peaks and is therefore a crucial parameter that must be considered in an accurate microstructural analysis [17]. Furthermore, the stress between the substrate and the YBCO lattice significantly affects the in-plane and out-of-plane orientations, as well as the growth parameter window [18]. Understanding this relationship is essential for optimizing growth conditions and maximizing superconducting performance. In particular, the correlation between uniaxial texture and anisotropic microstrain has been scarcely explored, despite its importance for confirming the high ordering of the CuO_2 superconducting planes [3, 6].

From this, the aim of the present work is to investigate the anisotropic microstrain and its relationship with the out-of-plane texture and the superconducting properties of YBCO films grown on $SrTiO_3$ (100) and $LaAlO_3$ (100) single-crystal substrates by the chemical solution deposition (CSD) sol-gel technique. The out-of-plane texture was analysed by X-ray diffraction technique, where rocking curves (ω-scans) around the (005) reflection provide information about the degree of inclination of the *c*-axes of the superconducting grains with respect to the growth direction. The microstrain and crystallite size were evaluated using both the Debye-Scherrer and Williamson-Hall methods to separate the contributions of crystallite size and lattice strain to the peak broadening, enabling a detailed analysis of the microstrain anisotropy. The superconducting properties were correlated with the out-of-plane texture parameters ($\Delta\omega$) and the microstrain (ε).

2. Experimental Methodology

The superconducting YBCO films were prepared by a chemical solution deposition (CSD) followed by thermal treatments, according to the procedure reported elsewhere [10, 20]. In brief, for a solution containing 1.5 g of YBCO 1.3487gr of Cu acetate (Cu $(OOCCH_3)_2 \cdot H_2O$), 0.7613 g of Y acetate (Y $(OOCCH_3)_3 \cdot 4H_2O$) and 1.1502 g of Ba acetate (Ba $(OOCCH_3)_2$) were reacted. The acetates were mixed and completely dissolved in a solution of ethanol (C_2H_5OH) and oxalic acid ($H_2C_2O_4$) (ratio 1:1). Subsequently, the solution left to decant 12 h in a matrix of oxalic acid and ethanol alcohol, subjected to a magnetic stirrer at 250 rpm to ensure a correct

homogeneity in the mixture. The resulting product is a precursor solution comprising of oxalates of Y, Ba and Cu in a colloidal matrix of oxalic acid. These oxalates were then deposited onto substrates of strontium titanate (SrTiO3) (100) and lanthanum aluminate ($LaAlO_3$) (100) by using a Fisher pipette. The sample was immediately dried at 40 °C in order to remove volatile elements. This process was repeated 7 times.

The crystallization and epitaxial growth of the YBCO layer was achieved by *ex situ* heat treatments, as represented in Fig. 1. The film was heated and sintered at 860 °C in a tubular furnace (LENTON LTF-PTF Model 16/610) in oxygen atmosphere for 12h, and subsequently re-oxygenated at 600 °C. The furnace was programmed to anneal and to quench the sample at the same ratio (1 °C/min).

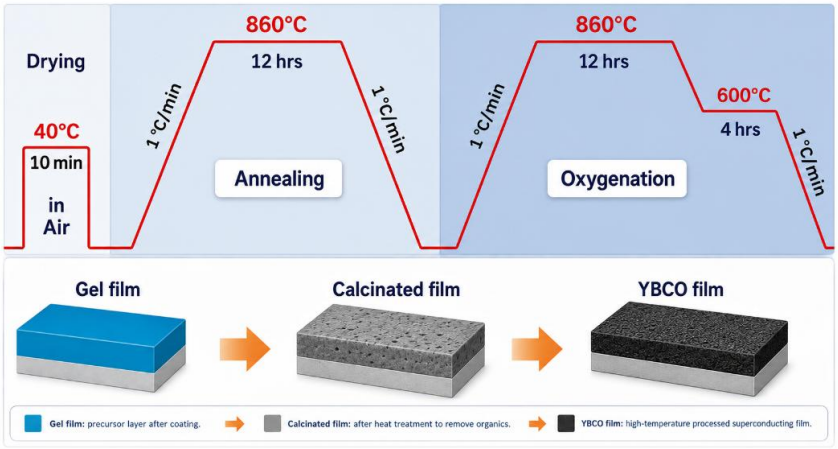


Fig.1. Schematic representation for the *ex-situ* heat treatments performed on CSD YBCO films on $LaAlO_3$ and $SrTiO_3$ substrates. The slow heating rate (1 ºC/min) released volatile hydrocarbons. The YBCO superconducting films are obtained after oxygenating the samples at 860 ºC.

The crystallization of the sample was studied by X-ray diffraction (XRD). The data were collected from 8º to 80º (0.04º step) using a powder universal diffractometer Bruker D8 with Cu $K_\alpha 1$ radiation (λ =1.54056 Å). The texture analysis was achieved by Rocking Curves measurements around the reflection (005) 2θ = 38.72 ° with 0.02 ° (ω) step and time step 6 seconds by 15° to 23° intervals. The surface morphology of the film was inspected using a NIKON ME600L optical microscope. Magnetic measurements were performed using a Quantum Design DC-MPMS-SQUID magnetometer equipped with a 7 T superconducting magnet. The superconducting transition temperature T_C was determined from temperature-dependent measurements of the magnetization $M(T)$ under H_{ext} = 100 and 500 Oe.

3. Results and discussion

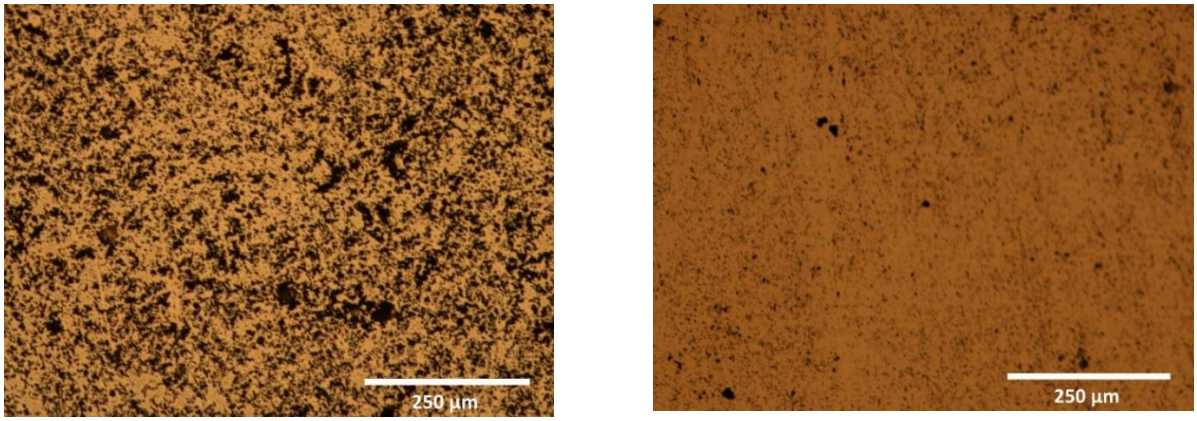
Figure 2 shows the surface morphology of the YBCO films on $SrTiO_3$ and $LaAlO_3$ substrates obtained by the oxalate CSD route and after oxygenation at 860 ºC. The results reveal that the samples consist on granular films where the YBCO grains are uniformly dispersed over the substrates surface and forming small groups.

Figure 3 shows the XRD patterns of the annealed YBCO films on $SrTiO_3$ and $LaAlO_3$ substrates obtained by CSD. The presence of the peaks (003), (004), (005), (006) and (007) reveal epitaxial growth in the c-direction or texture axis. The strong reflections (black in colour) (100), (200) and (300) correspond to the $SrTiO_3$ and $LaAlO_3$ substrates. The Y_2BaCuO_5 (Y211), CuO and Y_2O_3 are also detected as secondary phases. The Y211 phase (PDF card 78-1719 [3]) is detected by the reflections around 25.92°, 30.40°, 40.96° and 61.52°. The CuO phase might be present due to inhomogeneities in the starting precursor solution [3]. This phase is observed in relative minor amount with reflections around 27.72° (just observed on YBCO/STO sample) and 35.56°. Whereas, the Y_2O_3 reflections are around 58.32° and 68.08°.

The out-of-plane texture of the formed films was analysed from the fraction of c-axis orientation, f_s, by using Eq. (1):

$$\frac{I^{005}}{I^{200}} = \frac{f_c . I^{005}_{stand}}{(1 - f_c) I^{200}_{stand}} \quad (1)$$

where, I_{Stand} is the standard intensity obtained for randomly oriented samples (PDF card 40-159 [3]).



a) b)

Fig.2. Optical microscope images of the YBCO film on (a) $SrTiO_3$ and (b) $LaAlO_3$ substrate, obtained by CSD and annealing. The images are 5× magnified.

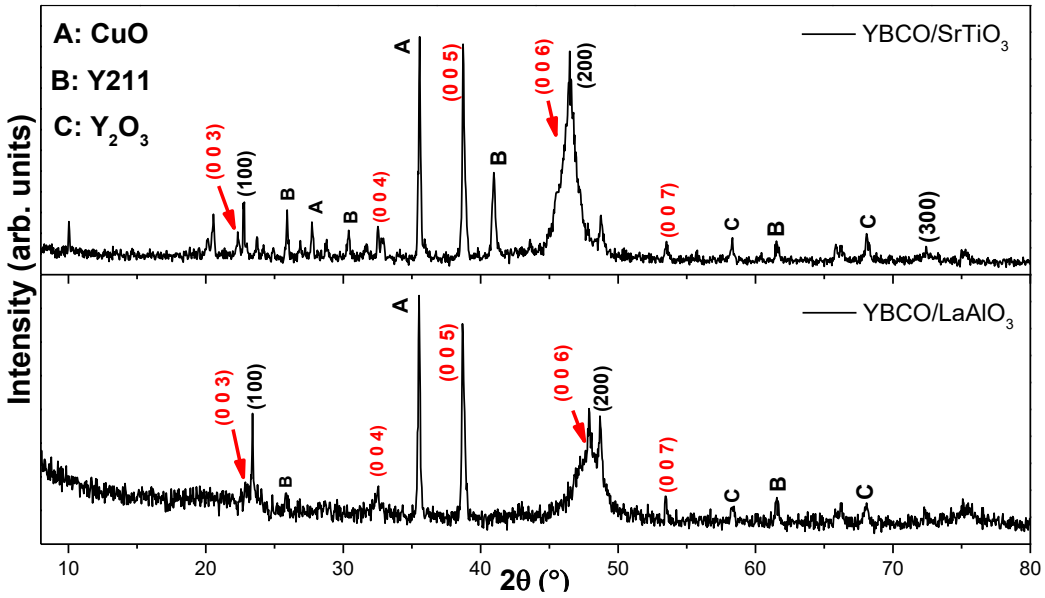


Fig.3. XRD pattern of an annealed YBCO film on $SrTiO_3$ (top) and $LaAlO_3$ (bottom) substrate obtained by CSD.

We obtain f_s = 0.88 and 0.81 for the YBCO onto $SrTiO_3$ and $LaAlO_3$ substrates, respectively. Therefore, 88% of the superconductor phase in the YBCO on $SrTiO_3$ and 81% on $LaAlO_3$ followed the preferential orientation given by the substrate. These values have been achieved since the lattice constant of both substrates are quite similar to that of YBCO orthorhombic. Thus, a higher percentage of out-of-plane textured grains better are obtained for YBCO on $SrTiO_3$ than on $LaAlO_3$.

3.1 Microstructural Analysis: Crystallite Size and Microstrain.

To evaluate the microstructural parameters, a first approximation of the crystallite size D was obtained using the Debye-Scherrer equation [3, 21], neglecting peak broadening caused by residual stress:

$$D = \frac{K\lambda}{\beta_{corr} \cos \theta_{hkl}} \tag{2}$$

Here, D is the average crystallite size (hereinafter $D_{Scherrer}$), λ is the wavelength of the applied X-ray, θ_{hkl} is the Bragg's angle, β_{corr} is the instrumentally corrected full width at half maximum (FWHM) in radians, and K = 0.916 is the Scherrer constant [21]. The obtained $D_{Scherrer}$ values are summarized in Table 1.

However, microstrain within the crystallites also contributes to peak broadening [22], requiring a more accurate analysis. From this, the Williamson Hall method was used to simultaneously determine the lattice strain (ε) and the crystallite size (in following D_{WH}) using the equation [22]:

$$\beta_{corr}\cos\theta = \frac{K\lambda}{D_{WH}} + 4\varepsilon\sin\theta \quad (3)$$

The lattice strain (ε) was obtained from the slope of the linear fit of $\beta_{hkl}\cos\theta$ vs $4\sin\theta$ plots for the main diffraction peaks, while the intercept $K\lambda/D_{WH}$ yields the volume-weighted crystallite size (D_{WH}). The WH data are listed in Table 1, while Williamson-Hall plots and microstructural parameters obtained results are summarized in Figure 4.

Table 1. Main diffraction peaks and both Debye-Scherrer and Williamson Hall analysis data.

Sample	Phase	(hkl)	2θ (°)	θ (°)	β_{obs}	β_{obs} (rad)	β_{inst} (rad)	β_{sample} (rad)	βcosθ (rad)	4sinθ	$D_{scherrer}$ (nm)	$\overline{D}_{scherrer}$ (nm)
YBCO/STO	YBCO	(004)	30.40	15.20	0.22	0.003839	0.002094	0.00322	0.00311	1.048	48.0	47.2
		(005)	38.72	19.36	0.20	0.003491	0.002268	0.00266	0.00251	1.327	58.1	
		(006)	46.60	23.30	0.28	0.004887	0.002443	0.00423	0.00388	1.582	36.6	
		(007)	53.52	26.76	0.25	0.004363	0.002792	0.00335	0.00299	1.799	46.2	
	Y211	(102)	25.92	12.96	0.16	0.002792	0.002094	0.00185	0.00180	0.896	83.6	55.5
		(112)	30.40	15.20	0.16	0.002792	0.002094	0.00185	0.00179	1.048	83.6	
		(321)	40.96	20.48	0.32	0.005585	0.002443	0.00502	0.00470	1.400	30.8	
		(330)	61.52	30.76	0.40	0.006981	0.002792	0.00640	0.00550	2.048	24.2	
	CuO	(110)	27.72	13.86	0.16	0.002792	0.002094	0.00185	0.00180	0.958	83.6	110.8
		(002)	35.56	17.78	0.145	0.002531	0.002268	0.00112	0.00107	1.221	138	
	Y_2O_3	(440)	58.32	29.16	0.36	0.006283	0.002792	0.00563	0.00492	1.946	27.5	27.8
		(622)	68.12	34.06	0.36	0.006283	0.002967	0.00554	0.00459	2.242	28.0	
YBCO/LAO	YBCO	(004)	30.48	15.24	0.24	0.004188	0.002094	0.00363	0.00350	1.051	42.6	43.2
		(005)	38.74	19.37	0.22	0.003839	0.002268	0.00309	0.00292	1.328	50.0	
		(006)	46.60	23.30	0.28	0.004887	0.002443	0.00423	0.00388	1.582	36.6	
		(007)	53.48	26.74	0.26	0.004538	0.002792	0.00357	0.00319	1.798	43.4	
	Y211	(102)	25.80	12.90	0.16	0.002792	0.002094	0.00185	0.00180	0.892	83.6	45.1
		(330)	58.44	29.22	0.36	0.006283	0.002792	0.00563	0.00492	1.950	27.5	
		(303)	61.56	30.78	0.40	0.006981	0.002792	0.00640	0.00550	2.049	24.2	
	Y_2O_3	(622)	68.08	34.04	0.36	0.006283	0.002967	0.00554	0.00459	2.241	28.0	28.0

The Debye-Scherrer crystallite sizes ($D_{scherrer}$) for the YBCO phase in the films on $SrTiO_3$ and $LaAlO_3$ are 47.2 nm and 43.2 nm, respectively (Table 1). This difference, although modest, indicates that the YBCO grains are slightly larger on the $SrTiO_3$ substrate. This is somewhat surprising given that $LaAlO_3$ has the smaller lattice mismatch magnitude (-0.83%) compared to $SrTiO_3$ (+1.35%). The larger crystallite size on STO may therefore be attributed to other factors beyond the lattice mismatch, such as differences in surface energy, interfacial chemistry, and nucleation kinetics between the two substrates. For the Y211 secondary phase, the average $D_{scherrer}$ values are 55.5 nm (STO) and 45.1 nm (LAO), while CuO (only in STO) shows a larger size of ~111 nm and Y_2O_3 exhibits the smallest and most consistent size (~28 nm) on both substrates.

The Williamson-Hall analysis, which separates the contributions of crystallite size and microstrain, yields significantly larger crystallite sizes (D_{WH}) for YBCO: 85.2 nm (STO) and 81.0 nm (LAO), estimated from the intercept. This discrepancy between $D_{scherrer}$ and D_{WH} is attributed to the presence of microstrain, which contributes to the peak broadening and is accounted for in the WH method. The microstrain values (ε) obtained from the slopes of the WH plots are 0.0275% for YBCO on STO and slightly lower for LAO (~0.025%), while the Y211 phase exhibits similar strain values (~0.0275%). Notably, the lower strain in the YBCO phase on LAO, despite its poorer texture, suggests that the strain is not the main factor limiting the out-of-plane texture; rather, the lattice mismatch and the substrate-film interface quality play a more critical role.

A crucial aspect of this analysis is the anisotropic nature of the microstrain. The orthorhombic structure of YBCO gives rise to different strain contributions along the crystallographic axes, which are not captured by the uniform deformation model (UDM) commonly used in WH analysis. Additionally, the oriented growth of the YBCO phase promotes the appearance of anisotropic microstrain. The linearity of the WH fits, as indicated by the R^2 values, is reasonable for the secondary phase Y211 (0.776 and 0.991 for STO and LAO, respectively) but poor for YBCO (0.059 for STO and 0.0004 for LAO). This poor linearity for YBCO is a direct consequence of the anisotropic microstrain present in the orthorhombic lattice, where the strain is not isotropic but rather distributed differently along the a-, b- and c-axes.

In contrast, the no-oriented growth structure of Y211 (orthorhombic) allows a better linear fit, indicating that the strain in this secondary phase is more isotropic and well described by the UDM. The low R^2 for YBCO also reflects the fact that the peak broadening in this phase is not purely dominated by size and strain effects, but also by the presence of structural defects and the strong texture, which introduce additional strain anisotropy. The good agreement between the $D_{scherrer}$ and D_{WH} for the Y211 phase (55.5 nm and 81.4 nm on STO; 45.1 nm and 77.8 nm on LAO) suggests that the strain contribution in this secondary phase is relatively uniform and well described by the UDM. The larger WH size indicates that the crystallites are less strained than the YBCO matrix, which is consistent with their formation as isolated precipitates during the thermal treatment [23].

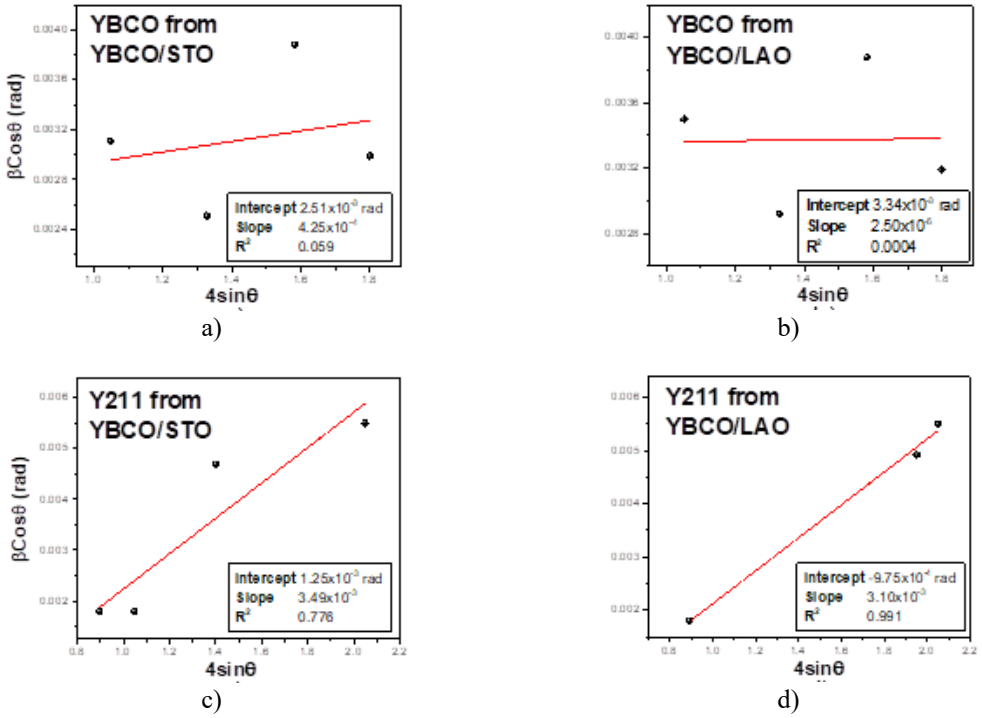


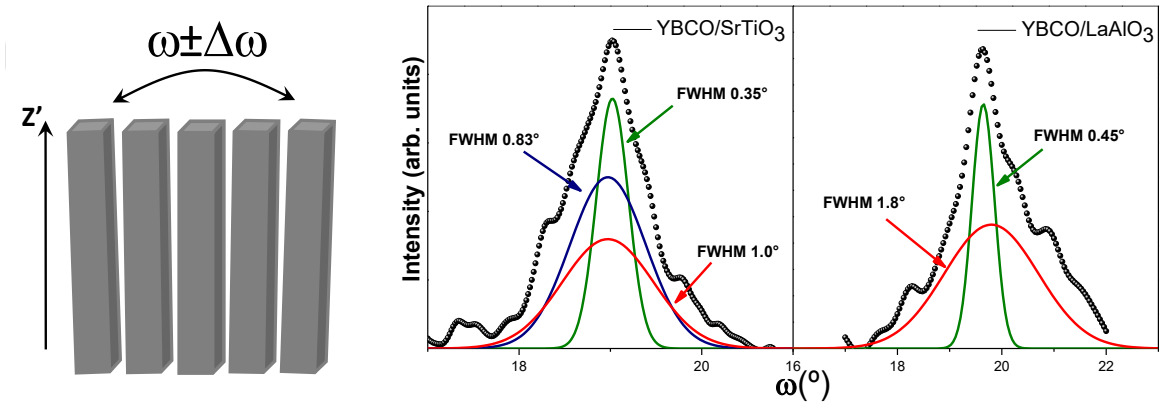
Fig.4. Williamson Hall plots of YBCO phase from a) YBCO/STO and b) YBCO/LAO samples; W-H plots from Y211 phase from and c) Y211/STO and d) Y211/LAO samples.

The anisotropic microstrain analysis reveals that the YBCO films on both substrates exhibit significant strain heterogeneity, which directly influences the superconducting properties. The STO substrate, with a larger lattice mismatch (+1.35%), induces a higher tensile strain in the YBCO lattice compared to the LAO substrate (-0.83%). This higher strain on STO leads to a higher density of structural defects and oxygen disorder, which ultimately affects the superconducting transition temperature (T_C). Conversely, the lower strain on LAO favours an optimal oxygen ordering and a higher hole doping level in the CuO_2 planes, thereby promoting a higher T_C despite the lower degree of c-axis texture (f_s = 0.81 for LAO vs 0.88 for STO). This highlights that the anisotropic microstrain, rather than the out-of-plane texture alone, plays a dominant role in determining the superconducting properties of these films.

3.2 Out-of-plane texture: Rocking curves

The out-of-plane texture was analysed by rocking curves XRD around the (005) reflection. This reflection was chosen because its intensity is higher than the other (00l) reflections and also because its position in XRD plot (around 2θ = 38.72º) is far away from any other reflection from the substrate (in particular the (200) reflection). The Figure 5 shows the results for the two films and the Δω values are listed in Table 2. The FWHM (full width half maximum) value of the Rocking curve provides relevant information about the degree of inclination of the c-axes of the superconducting grains with respect to the normal of the plane substrate.

Each Gaussian function provides different Δω values meaning that the films consist on multilayers of YBCO of different texture [7]. Since the texture of the films is strongly influenced by the substrate, the smaller Δω values in each sample should correspond to layers close to the YBCO/substrate interface, whereas high Δω values represent textures of layers close to the surface of the film.



a) b) c)

Fig.5. (a) The rocking curve is a measure of the degree of inclination in the grains with respect to the normal of the substrate (z'). (b) Rocking curves measurements corresponding to the (005) reflection for YBCO/STO. Is observed the presence of three textured groups of YBCO crystallites with different inclination angles values (Δω); (c) RC measurement of the YBCO/$LaAlO_3$ sample where two textured layers groups are observed.

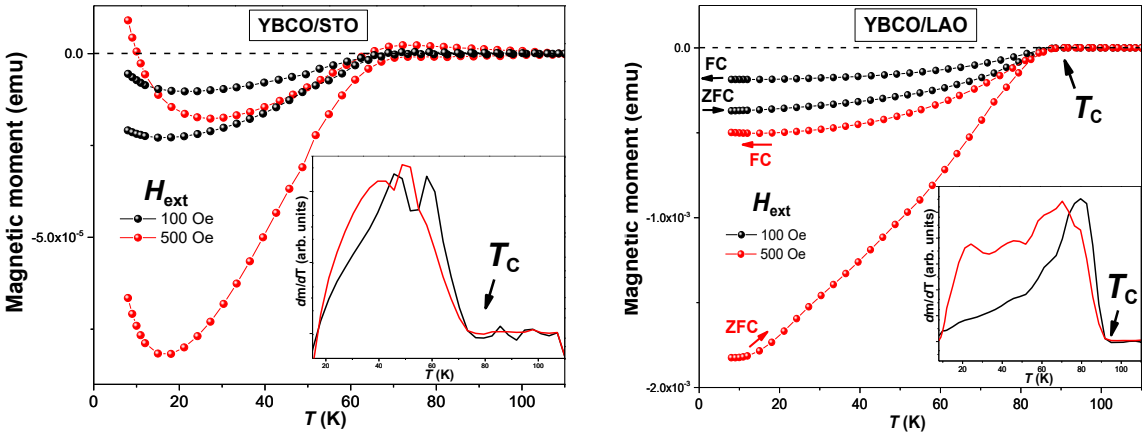
Table 2. f_s values and Full width at the half maximums (FWHM, Δω) of the rocking curves corresponding to the reflection (005) for YBCO films obtained by the oxalate CSD route on $SrTiO_3$ and $LaAlO_3$ substrates and after oxygenation at 860 ºC.

	Lattice constant mismatch (Δa)	f_s	Δω
YBCO/STO	+1.35	0.88	0.35° (Close to the film/ substrate interface)
			0.83° (Intermediate YBCO crystallites group)
			1.0° (Close to the surface)
YBCO/LAO	-0.83	0.81	0.45° (Close to the film/ substrate interface)
			2.0° (Close to the surface)

Note that the sample deposited on $LaAlO_3$ presents only two layers with different texture although the inner layer presents the poorest texture (with Δω =0.45º) compared to those from the other samples. Despite the YBCO film deposited on $SrTiO_3$ contains three layers with different texture, the texture of its inner layer is the best (Δω =0.35º).

3.3 Superconducting properties: Correlation with Texture and Microstrain

The temperature dependence of the magnetic moment (Fig. 6) reveals a marked difference in the superconducting properties of the YBCO films on $SrTiO_3$ and $LaAlO_3$. The sample grown on LAO exhibits a sharp diamagnetic transition with an onset critical temperature $T_{C(Onset)} \approx 92$ K, while the film on STO shows a significantly lower $T_{C(Onset)} \approx 78$ K. This notable difference is attributed to the combined effect of out-of-plane texture and anisotropic microstrain. The LAO substrate, with a smaller lattice mismatch (-0.83%), induces a lower strain state in the YBCO lattice, resulting in a more homogeneous distribution of strain and a lower density of structural defects. This lower strain favours an optimal oxygen ordering and a higher hole doping level in the CuO_2 planes, thereby promoting a higher T_C. On the other hand, the relative larger tensile strain imposed by the STO substrate (+1.35%) introduces a higher density of structural defects and oxygen disorder, which effectively suppresses T_C to 78 K. Interestingly, although the STO substrate yields a higher degree of c-axis texture (f_s = 0.88) compared with the LAO (f_s = 0.81) and a slightly larger crystallite size (47.2 nm and 43.2 nm for STO and LAO, respectively), the final T_C is more strongly influenced by the anisotropic microstrain and the resulting oxygen stoichiometry than by the purely structural texture. This finding highlights the critical role of microstrain anisotropy in determining the superconducting performance of YBCO films. A distinctive feature observed in the ZFC curve of the YBCO/STO sample is a clear increase in the magnetic moment below 15 K, indicating a paramagnetic contribution that superimposes on the diamagnetic signal. This low-temperature paramagnetic tail is not observed in the YBCO/LAO sample, suggesting a higher concentration of magnetic secondary phases in the YBCO/STO film. As confirmed by the XRD analysis (Fig. 3 and Table 1), the YBCO/STO sample exhibits a larger relative abundance of CuO and Y211 phases. Both of these secondary phases contain magnetic Cu^{2+} ions: CuO is antiferromagnetic below 230 K but retains a net paramagnetic or weak ferromagnetic moment at very low temperatures, while Y211 is known to exhibit antiferromagnetic correlations that can give rise to a Curie-type paramagnetic response.



a) b)

Fig.6. Temperature dependence of the magnetic moment for YBCO films grown on (a) STO and (b) LAO substrates, measured under H_{ext} = 100 and 500 Oe (ZFC and FC modes). The insets show the first derivative of the ZFC curves, highlighting the onset critical temperature.

The presence of these magnetic contributions, particularly at temperatures below 15 K, competes with the Meissner shielding, reducing the effective diamagnetic moment and making the ZFC branch less negative. This effect also complicates the precise determination of the lower critical field and the shielding fraction for the STO sample.

4. Conclusion

The anisotropic microstrain and its relationship with the out-of-plane texture and the superconducting properties of YBCO films grown by chemical solution deposition onto $SrTiO_3$ and $LaAlO_3$ substrates were investigated. The structural and textural analysis revealed that both films exhibit epitaxial growth in the *c*-direction, with a higher fraction of *c*-axis oriented grains on $SrTiO_3$ (88%) compared to $LaAlO_3$ (81%). The ω-scans further demonstrated that the films are composed of multiple sub-layers with distinct out-of-plane textures, indicating a complex growth mode influenced by the substrate. The YBCO/STO film exhibited three textured sub-layers with $\Delta\omega$ values of 0.35°, 0.83°, and 1.0°, while the YBCO/LAO film showed two sub-layers with $\Delta\omega$ = 0.45° and 2.0°. This multilayer structure reflects the evolution of the texture from the substrate interface to the film surface, where the best texture is achieved near the interface. A crucial finding emerged from the microstructural analysis using both Debye-Scherrer and Williamson-Hall methods, which revealed the presence of significant anisotropic microstrain in the YBCO films. The poor linearity of the Williamson-Hall fits for the YBCO phase (R^2 = 0.059 for STO and 0.0004 for LAO), in contrast to the excellent linearity for the secondary Y211 phase (R^2 = 0.776 for STO and 0.991 for LAO), is a direct consequence of the anisotropic strain distribution in the orthorhombic YBCO lattice. This indicates that the strain is not isotropic but varies along the crystallographic axes, which is a critical factor influencing the properties of the film. The microstrain values obtained were 0.0275% for YBCO on STO and slightly lower (~0.025%) for LAO, with the Y211 phase exhibiting similar strain values (~0.0275%). The lower strain on LAO, despite its poorer texture, suggests that the lattice mismatch and substrate-film interface quality play a more critical role in determining the strain state than the out-of-plane texture alone.

The superconducting properties were found to be strongly correlated with the anisotropic microstrain rather than with the out-of-plane texture alone. The YBCO film on LAO, despite having a lower degree of *c*-axis texture (f_s = 0.81), exhibited a significantly higher onset critical temperature ($T_{C(Onset)} \approx$ 92 K) compared to the film on STO ($T_{C(Onset)} \approx$ 78 K). This is attributed to the lower lattice mismatch of LAO (-0.83%) inducing a more homogeneous strain distribution and a lower density of structural defects, which favor optimal oxygen ordering and hole doping in the CuO_2 planes. Conversely, the larger tensile strain imposed by the STO substrate (+1.35%) introduces a higher density of structural defects and oxygen disorder, effectively suppressing T_C. Additionally, the presence of a paramagnetic upturn at low temperatures in the YBCO/STO sample, attributed to magnetic secondary phases (CuO and Y211), further confirms the higher degree of structural and chemical inhomogeneity in this film. This study shows that anisotropic microstrain is a crucial

parameter that governs the superconducting performance of CSD-derived YBCO films. While achieving a high degree of out-of-plane texture is important, minimizing anisotropic microstrain through appropriate substrate selection or strain engineering is essential for optimizing the superconducting properties.

Conflict of interest statement
The authors declare that they have no conflict of interest in relation to this research, whether financial, personal, authorship or otherwise, that could affect the research and its results presented in this paper.

CRediT author statement
Sanchez Cornejo H.E.: Software; Investigation; Writing – review & editing; **Kargin J.B.:** Data curation; Formal analysis; **Afanasyev D.A., Guchenko S.A.:** Validation, Writing – original draft; **Sagyndykova G.E., Zhangozin K.N.:** Formal analysis; Visualization; **Bustamante Dominguez A.:** Funding acquisition, Writing – original draft; **Celis Rojas S.R., Barnes C.H.W.:** Conceptualization, Methodology; **De Los Santos Valladares L.:** Supervision, Resources. The final manuscript was read and approved by all authors.

Statement on the use of Artificial Intelligence.
The authors declare that no artificial intelligence tools were used to generate scientific content, results, or conclusions of this article.

Data Availability Statement
The data are available upon reasonable request from the authors.

Funding

This work has been supported by the Peruvian Agency of Science CONCYTEC-PROCIENCIA through grant No. PE501088281-2024-PROCIENCIA. The work in Barranca, Peru, has been supported by a collaboration agreement between the University of Cambridge and the National University of Barranca (Contract number RG92973).

This research has been funded by the Science Committee of the Ministry of Science and Higher Education of the Republic of Kazakhstan (Grant No. AP23488258).

References

1 Wu, M. K. Ashburn, J.R., Torng, C.J., Hor, P.H., Meng, R.L., Gao, L., Huang, Z.J., Wang, Y.Q., & Chu C.W. (1987). Superconductivity at 93 K in a New Mixed-Phase Y-Ba-Cu-O Compound System at Ambient Pressure. *Phys. Rev. Lett.*, 58, 908–910. https://doi.org/10.1103/PhysRevLett.58.908

2 Bednorz, J. G., Müller, K. A. (1986). Possible high Tc superconductivity in the Ba:La:Cu:O system. *Z. Phys. B Condens. Matter*, 64, 189–193. https://doi.org/10.1007/BF01303701

3 Cornejo, H.S., De Los Santos Valladares, L., Barnes, C.H. Moreno, N.O., & Domínguez, A.B. (2020). Texture and magnetic anisotropy of $YBa_2Cu_3O_{7-x}$ film on MgO substrate. *J.Mater.Sci. Mater. Electron.*, 31, 21108–21117. https://doi.org/10.1007/s10854-020-04623-w

4 Puig, T., Puig, M.A., Mestres, N., van Seijen, H., Alzina, F., Gonzalez, J., Obradors, X., Graafsma, H., Usoskin, A., & Freyhardt, H.C. (2001). Texture analysis of coated conductors by micro-Raman and synchrotron X-ray diffraction. *Mat. Res. Soc. Symp.*, 659, II5.6.1 https://doi.org/10.1557/PROC-659-II5.6

5 Vermeir, P., Cardinael, I., Bäcker, M., Schaubroeck, J., Schacht, E., Hoste, S. & Van Driessche, I. (2004). Fluorine-free water-based sol-gel deposition of highly epitaxial $YBa_2Cu_3O_{7-\delta}$ films. *Supercond. Sci. Technol.*, 22, 075009. http://dx.doi.org/10.1088/0953-2048/22/7/075009

6 Wu, C., Zhao, G., Fang, P., Wang, S., & Zhang, Y. (2017). An All Sol-Gel Process for the Heteroepitaxial Growth of $YBa_2Cu_3O_{7-x}$/$LaNiO_3$/$YBa_2Cu_3O_{7-x}$ Tri-layer. *Coatings,* 7(5), 62. https://doi.org/10.3390/coatings7050062

7 Zanetti, S.M., Leite, E.R., Longo, E., & Varela, J.A. (2001). Preparation of ferroelectric bi-layered thin films using the modified polymeric precursor method. *Mater. Res.,* 4, 3, 157–162. https://doi.org/10.1590/S1516-14392001000300003

8 Obradors, X., Puig, T., Ricart, S., Coll, M., Gazquez, J., Palau, A., & Granados-Garcia, X. (2012). Growth, nanostructure and vortex pinning in superconducting $YBa_2Cu_3O_7$ thin films based on trifluoroacetate solutions. *Supercond. Sci. Technol.*, 25, 123001. http://dx.doi.org/10.1088/0953-2048/25/12/123001

9 Gross, M.E., Hong, M., Liou, S., & Gallagher, P.K. (1988). Versatile New Metalorganic Process for Preparing Superconducting Thin Films. *Appl. Phys. Lett.*, 52, 160–162. https://doi.org/10.1063/1.99038

10 Zalamova, K., Romà, N., Pomar, A., Morlens, S., Puig, T., Gázquez, J., Carrillo, A., Sandiumenge, F., Ricart, S., Mestres, N., & Obradors, X. (2006). Smooth Stress Relief of Trifluoroacetate Metal-Organic Solutions for $YBa_2Cu_3O_7$ Film Growth. *Chem. Mater.,* 18 (25): 5897–5906. https://doi.org/10.1021/cm061556+

11 Araki, T., & Hirabayashi, I. (2003). Review of a chemical approach to $YBa_2Cu_3O_{7-x}$-coated superconductors-metalorganic deposition using trifluoroacetates. *Supercond. Sci. Technol.*, 16, R71–R94. http://doi.org/10.1088/0953-2048/16/11/R01

12 Lian, J., Yao, H., Shi, D., Wang, L., Xu, Y., Liu, Q., & Han, Z. (2003). Structural characterization of epitaxial YBCO thin films prepared by a fluorine-free sol-gel method for coated conductors. *Supercond. Sci. Technol.*, 16, 838. http://doi.org/10.1088/0953-2048/16/8/302

13 Pop, C., Barusco, P., Vlad, R., Queralto, A., Gupta, K., Almog, B., Saraf, A., Deutscher, G., Granados, X., Puig, T., & Obradors, X. (2022). High critical current solution derived $YBa_2Cu_3O_7$ films grown on sapphire. *Supercond. Sci. Technol.*, 35, 054007. https://doi.org/10.1088/1361-6668/ac5be9

14 Van Driessche, I., Feys, J., Vermeir, P., & Lommens, P. (2012). Ink-jet printing of $YBa_2Cu_3O_7$ superconducting coatings and patterns from aqueous solutions. *J. Mater. Chem.,* 22, 3717–3726. https://doi.org/10.1557/opl.2012.812

15 Izumi, T., Yoshizumi, M., Miura, M., Sutoh, Y., Nakanishi, T., Nakai, A., Ichikawa, Y., Yamada, Y., Goto, T., Yajima, A., Aoki, Y., Hasegawa, T., & Shiohara, Y. (2008). Research and development of reel-to-reel TFA-MOD process for coated conductors. *Physica C*, 468, 1527–1530. https://doi.org/10.1016/j.physc.2008.05.270

16 Sánchez-Valdés, C. F., Puig, T., & Obradors, X. (2015). In situ study through electrical resistance of growth rate of trifluoroacetate-based solution-derived $YBa_2Cu_3O_7$ films. *Supercond. Sci. Technol.*, 28, 024006. https://doi.org/10.1088/0953-2048/28/2/024006

17 Palmer, X., Pop, C., Eloussifi, H., Villarejo, B, Roura, P., Farjas, J., Calleja, A., Palau, A., Obradors, X., Puig, T., & Ricart, S. (2016). Solution design for low-fluorine trifluoroacetate route to $YBa_2Cu_3O_7$ films. *Supercond. Sci. Technol.*, 29, 024002. http://dx.doi.org/10.1088/0953-2048/29/2/024002

18 Zhou, X., Chen, J., Huang, R., Li, M., Liu, Zh., & Cai, Ch. (2025). In-plane and out-of-plane orientations of YBCO and their correlation with a/b-axis twin structures. *Ceram. Int.*, 51, 1, 1326–1338. https://doi.org/10.1016/j.ceramint.2024.11.112

19 Domínguez, A.B., De Los Santos Valladares, L., Cornejo, H.S., Osorio-Anaya, A.M., Santibañez, J. F., Sovero, L.S., & Barnes, C.H.W. (2021). $YBa_2Cu_3O_7$ films grown onto $SrTiO_3$ and YSZ substrates by chemical solution deposition of trifluoroacetates. *J. Electroceram.,* 47, 15–22. https://doi.org/10.1007/s10832-021-00256-5

20 Domínguez, A.B., Osorio-Anaya, A.M., De Los Santos Valladares, L., Carhuancho, H., González, G. J.C., Cernicchiario, G., Feijoo Levano, J.A. (2006). Synthesis of YBa2Cu3O7-δ using oxalate precursor and sol-gel method. *Advances in Science and Technology,* 47, 37-42. https://doi.org/10.4028/www.scientific.net/AST.47.37

21 Sanchez Cornejo, H., Dominguez, A.B, Holmes, S.N., Seo, J.W., Albino Aguiar, J., Silva, V.A.J., Barnes, C.H.W., & De Los Santos Valladares, L. (2025). Vortex dynamics study on an uniaxially textured YBCO/MgO superconducting film from magnetic measurements. *Supercond. Sci. Technol*., 38, 035028. https://doi.org/10.1088/1361-6668/adb6d8

22 Dadras, S., & Davoudiniya, M. (2018). Analysis of YBCO high temperature superconductor doped with silver nanoparticles and carbon nanotubes using Williamson–Hall and size–strain plot. *Physica C: Superconductivity and its applications,* 548 116–118. https://doi.org/10.1016/j.physc.2018.02.022

23 Kargin, J., Sanchez Cornejo, H.E., Zhangozin, K., Zhanabergenov, T., Kassymkhanov, Zh., Seo, J., Holmes, S.N., & Barnes, C.H.W., Albino Aguiar J., De Los Santos Valladares L. (2024). Manometric determination of the oxygen diffusion coefficients in $YBa_2Cu_{3-y}Fe_yO_{6+x}$. *Journal of Superconductivity and Novel Magnetism,* 37 1965–1975 https://doi.org/10.1007/s10948-024-06796-5

AUTHORS' INFORMATION

Sanchez, Cornejo H.E – Doctoral candidate of Physics; Ceramics and Nanomaterials Laboratory, Faculty of Physical Science, Major National University of San Marcos, Lima, Peru. https://orcid.org/0000-0002-6211-165X; henry.sanchez@unmsm.edu.pe

Kargin, J.B. - Candidate of Physical and Mathematical Sciences, Professor, L.N. Gumilyov Eurasian National University, Astana, Kazakhstan; https://orcid.org/0000-0002-1027-6428; kargin_db@enu.kz

Afanasyev, D.A. - Ph.D, Professor, Buketov Karaganda National Research University, Karaganda, Kazakhstan; https://orcid.org/0000-0002-0437-5315; a.d.afanasyev2@gmail.com

Guchenko, S.A. – Master (Sci.), Research Fellow, Buketov Karaganda National Research University, Karaganda, Kazakhstan; https://orcid.org/0000-0002-9954-5478; guchen@mail.ru

Sagyndykova, G.E. - Candidate of Physical and Mathematical Sciences, Senior Lecturer, L.N. Gumilyov Eurasian National University, Astana, Kazakhstan; https://orcid.org/0000-0001-5792-8799, gsagyndyk75@gmail.com

Zhangozin, K.N. - Candidate of Physical and Mathematical Sciences, Associate Professor, Leading Researcher of TSK-Vostok LLP, Astana, Kazakhstan; https://orcid.org/0000-0003-1234-0486; 4kzh@mail.ru

Bustamante, Dominguez, A. – PhD, Principal Professor, Major National University of San Marcos, Lima, Peru; https://orcid.org/0000-0001-5892-3500, abustamanted@unmsm.edu.pe

Celis, Rojas S.R.- Master (Sci.), Professor, National University of Barranca, Peru, https://orcid.org/0000-0002-1438-5373, rcelis@unab.edu.pe

Barnes, C.H.W- PhD, Professor, Cavendish Laboratory, Department of Physics, University of Cambridge, Cambridge, Ununited Kingdom https://orcid.org/0000-0001-7337-7245, chwb101@cam.ac.uk

De Los Santos, Valladares, L. – PhD, Research Associate at the Cavendish Laboratory, Department of Physics, University of Cambridge, UK; Visiting Professor, L.N. Gumilyov Eurasian National University, Astana, Kazakhstan, https://orcid.org/0000-0001-5930-9916 , ld301@cam.ac.uk

EURASIAN PHYSICAL TECHNICAL JOURNAL

2026, Volume 23, No. 3 (57)

https://doi.org/10.31489/2026N3/54-63

Received: 29/04/2026 Revised: 11/09/2026 Accepted: 28/09/2026 Published online: 30/09/2026

Original Research Article

Open Access under the CC BY -NC-ND 4.0 license

UDC 53.043

EFFECT OF OXYGEN ADDITION ON LOW-RANK COAL DRYING IN A TECHNOLOGY FOR VOLATILE GAS GENERATION

Atyaksheva A.V.[1]*, Sarakeshova N.N.[1], Rozhkova O.V.[1,2], Zhaksylyk A. M11, Zhumaliyeva A.K.[1], Aitmagambetova M.B.[1] Umirzakov R.A.[1]

[1] Energy Institute of S. Seifullin, Kazakh Agrotechnical Research University, Astana, Kazakhstan
[2] AO «PolyTechPark», Almaty, Kazakhstan
Corresponding author: sahsa77@mail.ru

Abstract. The article presents the results of oxygen addition effect at the low-rank coal drying in the coal heat treatment technology. *Drying, as one of the stages of the technology, is carried out by diffusion method, using an oxygen addition in a quantity of 2%. The results of the study show the possibility of intensifying moisture removal by the proposed method at the expense of intensifying oxidation processes in diffusion conditions of porous body. Coal has effective and closed porosity. The increased concentration of oxygen in air creates conditions for intensifying oxidation reactions in the effective porosity. In the matrix of the porous body of coal, heat is emitted and temperatures rise. Quantity of the heat produced by the low-temperature reaction of oxygen in coal elements (≈1.24·10^{25} W) allows to increase the temperature of the total mass of coal approximately to the 60°C. Due to the increase in temperature, the dynamic pressure in the flow through the open porosity increases (≈ 6.18·10^{-3}Pa). As a sequence, the static pressure is reduced to negative value (down to negative 100 Pa) in closed pores. The reduction of external pressure alters the gas equilibrium, which leads to the effect of destruction of capillary condensate and promotes moisture release. The final mass fraction of H_2O as a result of diffusion method of drying when the oxygen content of the air is raised during the drying process for 1 hour in a range from≈ 2.9 to 5.8 %.*

Keywords: coal, oxygen, diffusion drying, porosity, static pressure.

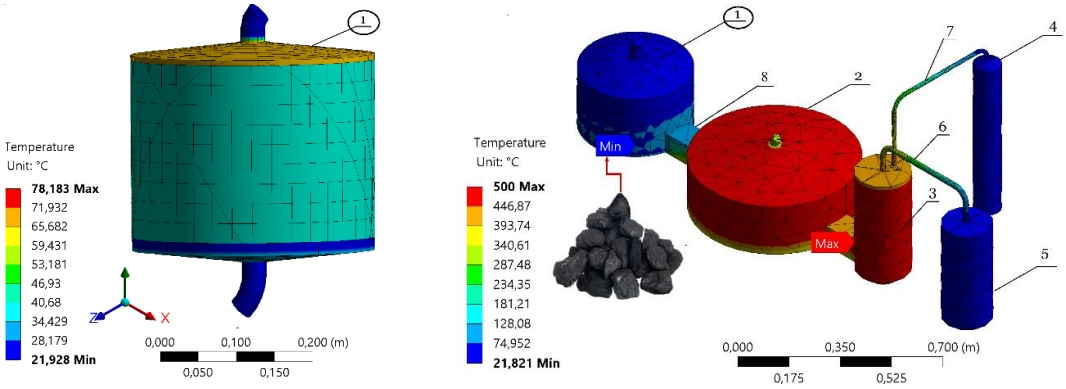
1. Introduction

The trend of development of clean coal technologies not only in Kazakhstan, but also worldwide requires finding simple solutions to obtain economically and environmentally attractive methods. In this direction, the effect could be achieved by using domestic coal reserves in the technology of the releasing volatile gases. Typically, gas generation technologies are taking stage by stage, including drying processes, processes of the thermal treatment and the releasing of the volatile gases [1,2]. Drying is one of the most responsible steps in the preparation of low-rank coals, because of the significant moisture coal content. However, such coals are highly efficient for pyrolysis, gasification and liquefaction [3], where careful preparation of the coal to processes is required. Today, well-proven coal preparation technologies with effective moisture removal, such as «evaporative drying technologies, rotary-drying, fluidized-bed drying, hot oil immersion drying, as well as non-evaporative drying technologies such as hydrothermal drying, mechanical/thermal drying, etc.», are

summarized in many sources but they [4,5] have significant shortcoming - the electric energy consumption in dryers per 1 kg of H_2O removed in a range from 300 kJ to 11000 kJ. In the direction of reducing energy costs, drying technologies are being developed for gasification using the filtration method with the use of «combined mechanical extrusion-hot air/microwave drying» taking into account slow oxidation and increased temperature [6]. Technologies have an economic advantage over the above, but are limited to an initial moisture content of up to 50%. Slow oxidation with rising temperatures within the porous coal will cause changes in all system parameters, including fragmentary changes in pore structures. The paper [7] presents studies on fragmentary changes and changes in the morphology of low-rank coals with increased temperature due to slow oxidation process in a diffusion. The authors show that the influence of the surface porous structure of coal on the oxidation process is determined by the movement of oxygen through open pores during oxygen adsorption due to increased concentration with subsequent intensification of reaction kinetics. At the same time, the authors of works [8-10] present the evolution of functional groups of different types of coal, including low rank, and the formation of volatile substances at low temperatures (up to 30°C) oxidation of alkynes, alkenes, etc. their high reactive capacity and corresponding rise in temperature from oxygen reactions. On this basis, it can be argued that in coal, as in the thermodynamic system, heat and mass exchange processes occur which do not exclude removal of moisture from the "coal-drying chamber" system. This assumption was taken as the basis of studies on the possibility of drying intensification by diffusion when using an oxygen additive in the diffusion stream. The aim of the study is to determine coal efficiency of drying by diffusion, taking into account the addition of oxygen for intensification of drying during thermal treatment of low-rank coal.

2. Material and Methods

The object of the study is a coal-drying chamber (fig.1.a) for the generating volatile gases technology (fig.1.b) and presented in more detail in [10,11] for release of CH_4, CO, H_2 in coal gasification process. In the studies, a method based on the simulation of the movement of continuous medium and discrete phase was used to determine the final moisture of coal as a porous body in the pattern of the coal-drying chamber. The drying chamber has a volume 0,0359m^3 and the surface area 1,0824 m^2. The pattern is scalable for pilot coal gas generation technology. Drying is carried out by the flow of the rising air, with the addition of oxygen in the amount of 2% of the air volume, supplied at a rate of 0.8 m/s during 1 hour through perforated openings into the coal matrix in mass 48.4 kg.



1 – coal-drying chamber; 2 – isothermal heating chamber; gas generation chamber; 4 – inert gas delivery capacity; 5 – volatile gases collection and storage capacity; 6 – volatile gas transport pipeline; 7 – inert gas pipeline; 8 – coal transporter.

Fig.1. Physico-mathematical pattern of the thermal coal treatment installation for the release of volatile gases: a – pattern of the technology; b – pattern of coal-drying chamber in technology.

The gas generation technology from coal presented (fig. 1.b) is implemented through energy activation of the element-element bonds of coal during the three main stages: drying, isothermal heating; release of volatile combustible gases [11]. The challenge of the technology is to create optimal conditions at each stage to maximize the release of the volatile gases from coal. Drying of coal involves preparing the coal with parameters that have the greatest positive effect on the subsequent process in the isothermal chamber. The scientific novelty of the research is to determine the effect of the addition of 2% oxygen to air during the drying

stage of low-grade coal through diffusion in a ball chamber of heat treatment technology. Low-rank Coke weakly sintering coal (Kazakhstan, Ekibastuz Deposit) was used as the material under investigation, corresponding to the classification of Coal Mv (coals with mechanical viscosity), the physico-mechanical characteristics were obtained experimentally in [10], which as a porous body are presented in the table. 1 and represented in [11,12].

Table1. Analytical properties of coal MV

Density, [kg/m^3]	Isotropic thermal conductivity, [W/m C°]	Specific heat, [J/kg °C]	Transmissivity, [s]	Pore volume, [m^3/kg]	Mass, [kg]
1100	0.32	1200	0.7	0.0067	76.5

To achieve the objective of assessing the effect of oxygen-added drying with the diffusion method on water removal intensity, tasks must be performed:

1. To analyze the oxygen addition (2%) in the air composition on the effect of the increase in coal temperature and dynamic diffusion flow pressure;

2. To analyze the drying intensity of coal depending on the increase in dynamic pressure and the occurrence of negative static pressure.

To solve these problems, simulation of the diffusion drying process through a coal matrix was used in the Ansys Academic Research CFD environment using the engineering modules «Flow through a porous media» and «Species transport», which allows the forecasting and control of moisture flows in relation to temperature, static, dynamic pressure, chemical reactions, species… etc. As boundary conditions, the "velocity inlet" conditions at the inlet of the drying chamber and the "pressure outlet" conditions at the outlet in a given area of geometry are taken into account, as presented in table 2 and the properties of coal and air according to tables 1 and 3.

Table 2. Boundary conditions

Velocity magnitude, [m/s]	Turbulent intensity, [%]	Turbulent viscosity ratio	Temperature, [K]	Backflow total temperature, [K]	Mass inlet fraction O_2	Mass outlet fraction O_2	Initial moisture, [%]
0.8	5	5	290	300	0.23	0,21	60

Table 3. Physical properties of airant

Density, [kg/m^3]	Specific heat, [J/kg·K]	Thermal conductivity, [W/m·K]	Viscosity, [kg/m·s]	Molecular weight, [kg/k·mol]	Standart state entropy, [J/kgmol·K]	Turbulent dissipation rate, [J/kgmol·K]
1.225	1006.43	0.0242	1.7894e-05	28.966	194336	0.007468

Table 4. Physical properties of coal

Density, [kg/m^3]	Specific heat, [J/kg·K]	Thermal conductivity, [W/m·K]	Initial temperature, [K]	Permeability, [мD]	Pore volume, (m^3/kg)
1100	802.3	0.243	290	28.966	0.00036

The computational grid parameters accepted for calculation with independent similarity are shown in Table 5. Analysis of the grid independence shows a discrepancy in the size of cells 2 times not more than 3 percent. Dynamic mesh selection for drying chamber is shown in figure 2.

Table 5. Mesh parameters

Target skewness	Inflation option			Mesh metric Element quality		Mesh metric Element quality		Pinch tolerance [m]	Sizing	
									nodes	elements
0.000009	Transition ratio	Max layers	Grows rate	Min [m]	Max [m]	Everage [m]	Standard deviation			
	0.272	40	1.2	2.0354e-0004	1m	0.57015	0.00376	3.117e-0.04	4178330	2307966

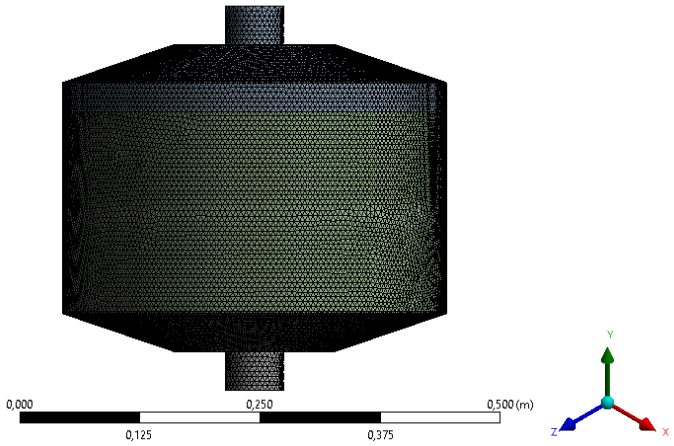


Fig.2. Dynamic mesh selection for drying chamber

In addition, under the conditions of oxygen transfer to porous space, it is necessary to take into account the parameters of the model of the porous medium. Table 6 presents the body coal porous zone conditions. Таблица 6. Porous zone conditions.

Table 6. Body coal porous zone conditions

Relative velocity resistance	Viscous resistance (Inverse absolutely permeability) in all directions [$1/m^2$]	Effective diffusion coefficient [m^2/s]	Effective thermal conductivity, [W/m·K]
Viscous resistance	3.45e+13	$4.8 \cdot 10^{-9}$	0.243

In the simulation, a kinetic-diffusive scheme of coal oxidation under self-heating is used In the simulation, a kinetic-diffusive scheme of coal oxidation under self-heating was used «Viscous Standard k-e (2-eqn) in the realizable k-epsilon model and standard wall functions. The drying time was based on the "Pseudo Time step" value of 1 second with 3,000 operations, which corresponds to the 50 min drying process.

3. Results and discussion

3.1 Analysis results and discussion of oxygen addition (2%) in the air composition on the effect of the increase in coal temperature and dynamic diffusion flow pressure.

To predict the increase in temperature and dynamic pressure of the diffusion flow in an effective coal of internal heating is due to an increase in oxygen concentration and intensification of the kinetics of reactions with heat release [13]. Low-rank coals have a developed, both open and closed porosity, which creates heterogeneity of properties such as heat conductivity, heat capacity, density, etc., in the coal matrix that determine the conditions for the intensity of oxidation reaction kinetics at a given velocity. In turn, temperature causes a change in dynamic pressure directly related to the velocity of the diffusion flow. The kinetic model of internal heating in a coal layer can be represented by the following dependencies, according to [14]:

$$(1-\varepsilon)C_c\rho_c\frac{\partial T_{ox}}{\partial t}=\frac{\partial}{\partial x}\left(\lambda\frac{\partial T_{ox}}{\partial x}\right)+Q_c k(T_{ox})C_c, \quad (1)$$

where T_{ox} (K), C_c (KJ/kg), ρ_c(m^3/kg), λ_c, Q_c is relatively concentration and temperature of oxygen, heat capacity and density of coal, heat of oxygen reaction with coal elements; k is oxygen diffusion coefficient and ε is temperature coefficient of oxygen sorption rate; λ – thermal conductivity of coal efficient coefficient (W/mK).

Temperature coefficient of oxygen sorption rate, taking into account the unevenness of the velocity distribution [15]:

$$\varepsilon\frac{\partial C}{\partial t}=\frac{\partial}{\partial x}\left[D_{ox}\frac{\partial C_c}{\partial x}\right]-k(T_{ox})C_c, \quad (2)$$

and

$$k(T_{ox})=k_0+E(T_{ox}-T_0), \quad (3)$$

where E is activation energy for the low-rank coal presented is 1 -11 kcal/mole; ε is kinetic ratio of oxygen concentration change in layer is equal $\frac{C}{C_0}$.

The concentration of oxygen at the coal surface will be determined by its air content, taking into account convective heat exchange between coal and air. If the oxygen concentration in the supplied air is considered constant, then the system can be supplemented by boundary conditions:

$$\lambda\frac{\partial T_{ox}(0,t)}{\partial x}=\alpha\left(T_{ox}[0,T]\right)-T_0 \quad (4)$$
$$C[0;T]=C_{0x}$$
$$T[x;0]=T_{0x}$$

The intensity of convective heat exchange between coal and oxygen-containing air under given geometric conditions is determined by a number Nu, directly dependent on the heat exchange coefficient α (heat transfer coefficient (W/m^{2}K)), the geometric characteristics of the drying installation and the coefficient of thermal conductivity of coal. At the same time, the oxygen diffusion process in the coal layer is carried out at a given concentration, so as an initial boundary conditions it is decided on the stationary equation of the change in oxygen concentration under diffusion conditions:

$$C[x;0]=C_{ox}\exp\left(-x\sqrt{k/D_{ox}}\right) \quad (5)$$

The maximum heat reaction in the coal is observed on the surface at the highest possible concentration of oxygen. Due to the heat conductivity of coal, which directly depends on density and porosity, layers will be heated deep down according to the temperature gradient direction. On this basis it can be written:

$$T_c[x,t]\to T_{ox};x\to\infty$$
$$C_{ox}[x,t]\to 0;x\to\infty$$

Simulation showed (fig. 3. a, b) that in the process of diffusion drying zones with maximum mass fraction of oxygen (fig. 3.a) are formed, reaching 0.23 in which there is a maximum can be increase in temperature to 348 K (fig. 4) due to the emission of heat C_c = 1.24 ·10^{-25} W (fig. 3.b). But at the same time, the maximum coal temperature does not exceed the low-grade coals' self-ignition temperatures (t ≈ 130°C – 150°C). Average temperature by volume of coal during drying when the initial air temperature is set T = 18°C, consists of t ≈ 60°C. In addition, an amount of CO_2 is generated during the self-heating process, which determines whether the risk of self-ignition can be reduced.

As noted above, chemical reactions in a given temperature range occur through the reaction of oxygen to coal. Of course, the concentration of oxygen on the surface of coal plays a major role, and the addition of active oxygen will help to accelerate the oxidation process and increase temperature and pressure. The line graph presented in fig. 4 shows the dependence of temperature rise, heat reaction, oxygen concentration and dynamic pressure. Fig. 4 shows that the proposed method gradually increases coal temperature from 291 K to 355 K in different zones of the coal matrix throughout the drying process. The oxidation reaction begins with a mass fraction of oxygen on the coal surface $\approx 1.42 \cdot 10^{-3}$ $O_{2/}$ per one kg of air, corresponds to the mean value of heat reaction $C_c \approx 0.62 \cdot 10^{-24}$ W.

The maximum amount of heat reaction by the flow of oxygen approximately C_c consists of $\approx 1.24 \cdot 10^{-25}$ at the mass fraction of the oxygen $O_2 \approx 1.42 \cdot 10^{-3}$ O_2/ per one kg of air. The dynamic pressure growth rate in the flow reaches $P_d \approx 6.18 \cdot 10^{-3}$ Pa.

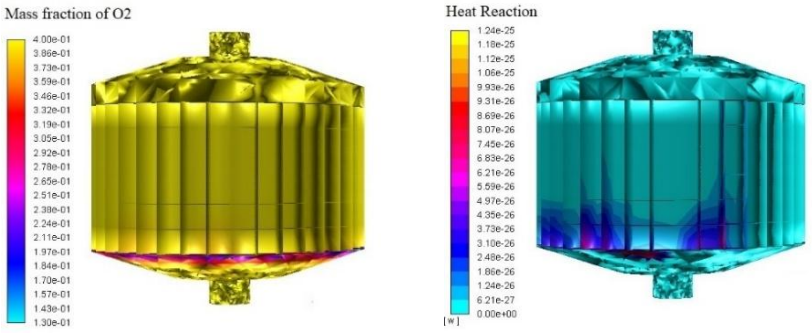


Fig.3. O_2 mass fraction and heat of oxygen reaction with coal during the diffusion drying process: a – O_2 mass fraction; b – heat of oxygen reaction with coal.

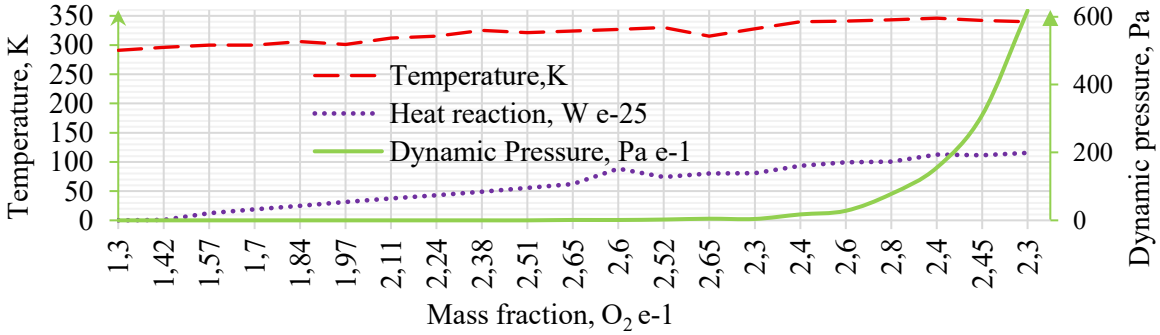


Fig.4. Dependence of temperature rise, heat reaction on the surface oxygen concentration of coal and dynamic pressure.

3.2 Analysis results and discussion of the drying intensity of coal depending on the increase in dynamic pressure and the occurrence of negative static pressure.

The intensity of the drying n process is determined by the total transport of moisture through the coal body during the process. According to the theory of heat mass exchange, the total water transfer through a porous body under diffusion conditions is defined as [15 -21]:

$$G_i = \int_F \left(j_F \cdot n_F\right) dF, \tag{7}$$

where n_F is normal vector to the surface; $j_F = f(x; y; z; \tau)$ is the flow of matter.

The density of the flow of matter (moisture) is defined by both a molecular and a convective component that occurs in this process:

$$j = j_{diff} \cdot j_{conv} = -\rho D gradm \cdot \rho mv, \tag{8}$$

where is D the diffusion coefficient of a two-component mixture consisting of water and air.

The external mass exchange is characterized by the intensity of the flow emitted from a wet coal surface, according to Dalton's Law of the partial pressure:

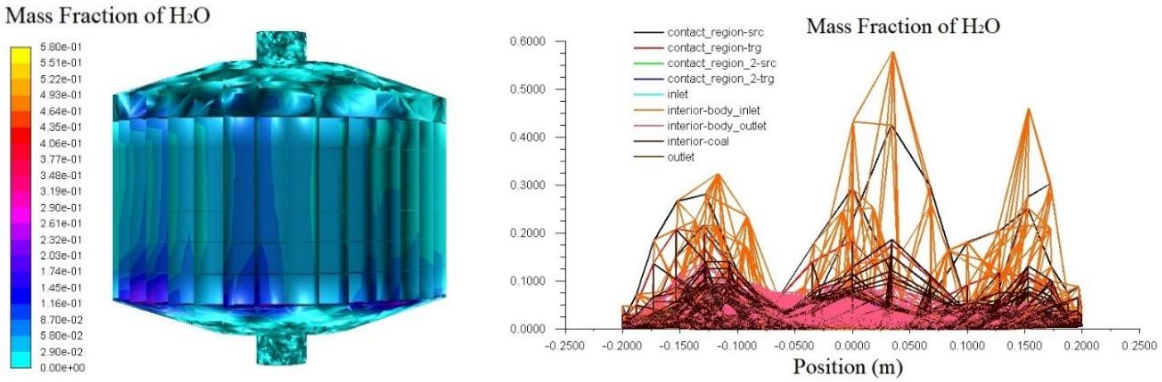
$$g_i = \alpha^{/}\left(\phi P_n - \left(\phi P_c\right)\right)dF, \tag{9}$$

where $\alpha^{/}$ is the moisture coefficient, which depends on the hydrodynamic conditions of the environment; ϕ is coefficient taking into account the reduction of the water vapour above the surface of coal partial pressure (interior body coal).

$$\phi = 0.091 \cdot 10^{\frac{293}{t_c+273}}, \tag{10}$$

where t_c is temperature of environment.

Fig. 5. a ,b shows the model of drying in a diffusion chamber, taking into account at least 23% oxygen content. According to fig. 5 (a), the mass moisture fraction in the respective coal zones may vary from 0.60 (at the interior body inlet) to 0.01 (at the interior body outlet) during drying. According to figure 5 (b), maximum mass fraction on the perimeter of the chamber is observed at the exit from the drying chamber and on the surface of the coal (interior body coal and interior body outlet). On the interior body outlet mass fraction of water consists of no more than ≈ 0.02. At the same time, at the inlet of the coal-drying chamber (interior body inlet) mass fraction of water consists of for about ≈ 0.06. The calculation model is based on the initialization and calculation of the activity of all chamber zones during the process in the total mass of coal, taking into account the total moisture. (Wet basis model)



a b

Fig.5. Mass fraction of H_2O release during the diffusion drying process: a – in common; b – on the perimeter of the chamber.

According to the abovementioned equations (7 - 9), a significant influence on the intensity of the removal of moisture from the low-grade coal matrix is caused by the magnitude of the dynamic pressure when the temperature changes accordingly [20, 21]. Low-rank coals have a closed porosity, with moisture that can exceed more than 40%. Taking into account the Kelvin's equation for a model of pore-containing matrix drying [22], Knudsen's diffusion law, and also considering the gas permeability of an unconsolidated porous medium [23] and the above represented equations (7 - 10) the water rate equation for drying low-rank coal can be presented:

$$J_w = -4\pi\varepsilon \frac{DT^{0.75}\left(P_d - P_s\right)}{RP_d} M, \tag{11}$$

where T is the medium temperature (K), R is the equilibrium gas constant, M is molar mass of water.

Figure 6 shows a line graph of the dehumidification in the coal matrix as a function of static, dynamic pressure and temperature.

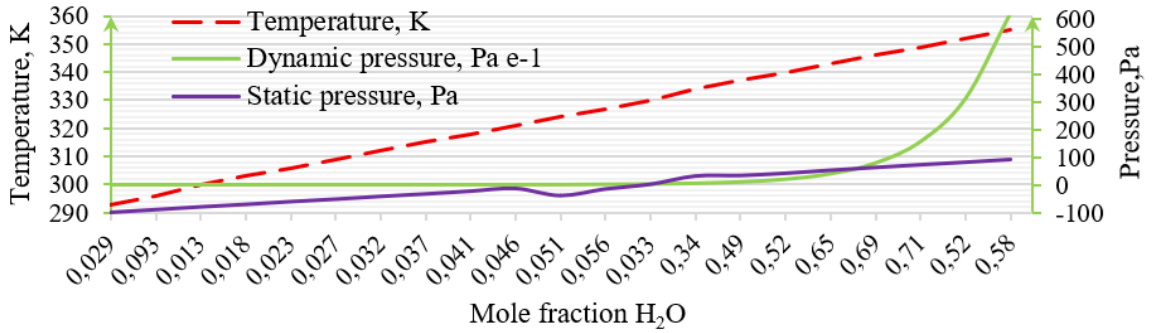


Fig.6. Dependence H_2O mole fraction from dynamic pressure and absolute temperature during the diffusion drying process.

The intensity of moisture (H_2O) release in the process increases significantly with increasing dynamic pressure in a range from $P_d \approx 2\%$ to 65% under conditions of the negative static pressure $P_s \approx$ -100 before it became positive. It is suggested that, the changing in pressure alters the gas Kelvin's equilibrium, which leads to the effect of destruction of capillary condensate and promotes moisture release [24]. Thus, it can be argued that diffusion drying with the addition of 2% active oxygen has a positive effect on drying intensity. In addition, the self-heating effect of coal at a temperature increase of up to 60 °C also has a positive impact on further heat treatment of low-rank coal. To confirm the effectiveness of this method compared to vacuum drying, the final moisture content results obtained in this study (#2) were compared with the results (#1) obtained from experimental low-grade coal formation in a ball pit diffusion chamber - dryer in the vacuum of identical gasification technology. [24-27] and presented in Table 4.

Table 7. Comparison of the simulation and experimental data of vacuum drying

Experimental group	Average density [kg/m^3]	Static Pressure [Pa]	Average final moisture [%]
#1	980	≈ -0.025	≈5.17
#1	950	≈ -0.102	≈1.03
#1	917	≈ -0.475	≈2.37
#1	1000	≈ -0.475	≈2.38
#1	1100	≈ -0.478	≈2.38
# 2	1100	≈ -0.100	≈2.9 – 5.8

Comparative analysis of results showed that the active addition of oxygen during low-rank coal drying promotes drying intensification in a similar way to the conditions for creating diffusional dryers when creating vacuum even at higher coal density.

4. Conclusion

Evaluating of the oxygen addition at the low-rank coal drying in the heat treatment technology in amount of 2% shows, that intensification of moisture removal occurs along the chain «increase in oxygen concentration – reaction with heat release – rise in temperature – increase in dynamic pressure – decrease static pressure to negative», which leads to conditions that promote internal moisture output from coal. At this:

1. The results of analysis of the influence of the addition of oxygen in the amount of 2% in the air composition on the effect of the increase in coal temperature showed the possibility of increasing the temperature of coal from 291 K to 355 K in different zones of the coal matrix due to intensification of oxidation reactions in zones of concentration increase oxygen from ≈ $1.42 \cdot 10^{-3}$ O_2/per kg of coal.

2. The results of analysis of coal drying intensity relative to temperature rise and dynamic and static pressure change showed that it is possible to dry coal with an initial humidity of 60% when moisture is finally removed to 2,9 - 5.8% due to reduced pressure contributing to the release of moisture.

Conflict of interest statement
The authors declare that they have no conflict of interest in relation to this research, whether financial, personal, authorship or otherwise, that could affect the research and its results presented in this paper.

CRediT author statement
Atyaksheva A.V., Sarakeshova N. N., Rozhkova O. V., Zhumaliyeva A.K.: Conceptualization, Data Curation, Writing Original Draft; Methodology. **Zaksylyk A.M., Aitmagambetova M.B., Umirzakov R. A.:** Investigation, Software, Writing Review & Editing, Supervision. The final manuscript was read and approved by all authors.

Statement on the use of Artificial Intelligence.
During the preparation of this manuscript, artificial intelligence tools were used solely for language editing and grammatical improvement.

Data Availability Statement
The data are available upon reasonable request from the authors.

Funding
This study was carried out with the financial support of the Science Committee of the Ministry of Science and Higher Education of the Republic of Kazakhstan, PSF BR34637474 (IRN) "Development and implementation of innovative domestic technologies for the capture and decontamination of flue gases in coal-fired power plants with integrated solutions for decarbonization and utilization of carbon dioxide."

References

1 Li, Q., & Zhang, J. (2017). Coal gasification. *Multiphase Reactor Engineering for Clean and Low-Carbon Energy Applications*, 65-118. https://doi.org/10.1002/9781119251101.ch3

2 Zhang, Z., Yi, B., Sun, Z., Zhang, Q., Feng, H., Hu, H., ... & Zhao, C. (2021). Reaction process and characteristics for coal char gasification under changed CO_2/H_2O atmosphere in various reaction stages. *Energy*, *229*, 120677. https://doi.org/10.1016/j.energy.2021.120677

3 Karthikeyan, M., Zhonghua, W., & Mujumdar, A. S. (2009). Low-rank coal drying technologies—current status and new developments. *Drying Technology*, *27*(3), 403-415. https://doi.org/10.1080/07373930802683005

4 Rao, Z., Zhao, Y., Huang, C., Duan, C., & He, J. (2015). Recent developments in drying and dewatering for low rank coals. *Progress in Energy and Combustion Science*, *46*, 1-11. https://doi.org/10.1016/j.pecs.2014.09.001

5 Li, M., Liu, M., Xu, C., Wang, J., & Yan, J. (2023). Thermodynamic and sensitivity analyses on drying subprocesses of various evaporative dryers: a comparative study. *Energy*, *284*, 128571. https://doi.org/10.1016/j.energy.2023.128571

6 Deng, J., Qu, G., Ren, S., Wang, C., Su, H., Yuan, Y., & Wang, J. (2024). Effect of water soaking and air drying on the thermal effect and heat transfer characteristics of coal oxidation at the low-temperature oxidation stage. *Energy*, *288*, 129705. https://doi.org/10.1016/j.energy.2023.129705

7 Cai, J., Yu, Z., Yang, S., Tang, J., Ma, Z., Xie, X., & Hu, X. (2023). Fractal characteristics of coal surface structure during low-temperature oxidation and its effect on oxidizability. *Energy*, *284*, 128526. https://doi.org/10.1016/j.energy.2023.128526

8 Zhang, L., Wen, C., Li, S., & Yang, M. (2024). Evolution and oxidation properties of the functional groups of coals after water immersion and air drying. *Energy*, *288*, 129709. https://doi.org/10.1016/j.energy.2023.129709

9 Taraba, B., Rudolf, P., & Václav, S. (2011). Calorimetric investigation of chemical additives affecting oxidation of coal at low temperatures. *Fuel processing technology,* 92(3), 712-715. https://doi.org/10.1016/j.fuproc.2010.12.003

10 Ybray, S. Report on the research internship at the Institute of Coal Chemistry and Chemical Materials Science of the Federal Research Center for Coal and Coal Chemistry, Siberian Branch of the Russian Academy of Sciences (SB RAS). 2022 s.54. Available at: https://portal.kazatu.kz/e-books/index.php

11 Atyaksheva A., Dashevskaya A., Mergalimova A., Ybray S., Aitmagambetova M., Umirzakov R., Sultanbek, Z. (2025). Evaluating of the sudden heat impact on volatile gases release during the gasification process of weakly grade metamorphized coal. *Eastern-European Journal of Enterprise Technologies,* 3(6 (135)). https://doi.org/10.15587/1729-4061.2025.331223

12 Mergalimova, A., Atyaksheva, A., Ybray, S., & Seitzhapparov, N. (2024). Identification of the low-rank coals thermal heating behavior. *Eastern-European Journal of Enterprise Technologies*, 128(6). https://doi.org/10.15587/1729-4061.2024.299538

13 Suprun, T. (2022). Local approach to improve the aerodynamic characteristics of the final drying process. *Eurasian Physical Technical Journal*, *19*(2 (40)), 65-70. https://doi.org/10.31489/2022No2/65-70

14 Atyaksheva, A. V., Atyaksheva, A. D., Ryvkina, N. V., Yermekov, M. T., Rozhkova, O. V., & Smagulov, A. S. (2022). Effectiveness analysis of Maikuben brown coal combustion in the heating boiler "Kamkor-300". *Journal of Physics: Conference Series,* 2211 (1), 012003). https://doi.org/10.1088/1742-6596/2211/1/012003

15 Zheng, C., Yao, Q., Li, X., Hudson-Edwards, K., Shan, C., Shang, X., & Li, Y. (2022). Experimental investigation of mechanical characteristics of coal samples at different drying temperatures. *Drying Technology*, *40*(16), 3483-3495. https://doi.org/10.1080/07373937.2022.2060999

16 Mekhtiyev, A. D., Sarsikeyev, Y. Z., Atyaksheva, A. V., Atyaksheva, A. D., Gerassimenko, T. S., & Alkina, A. D. (2021). Method of preventing deposits on the inner surface of circulating water pipelines of ferroalloy electric furnace cooling systems. *Metalurgija*, *60*(3-4), 321-324. https://hrcak.srce.hr/file/372263

17 Feng, G., Niu, X., Liao, J., Han, Y., Bai, Z., & Li, W. (2019). Correlation between drying behaviors of brown coal and its pore structures. *Energy & Fuels*, *33*(7), 6027-6037. https://doi.org/10.1021/acs.energyfuels.9b00657

18 Baubek, A., Atyaksheva, A., Zhumagulov, M., Kartjanov, N., Plotnikova, I., & Chicherina, N. (2021). Complex studies of the innovative vortex burner device with optimization of design. *Progress in Material Science and Engineering,* 139-153. Cham: Springer International Publishing. https://doi.org/10.1007/978-3-030-68103-6_13

19 Zhang, Z., & Zhang, S. (2022). A new moisture control method: Analysis of dynamic changes of temperature and moisture in coal particles during drying. *Energy Reports*, *8*, 4170-4181. https://doi.org/10.1016/j.egyr.2022.03.033

20 Ganzhara, V.I., Atyaksheva, A.V., Zhakishev, B.A., Belov, M.N., Stepakhin, A.S., Los', V.V. (2002). Light and super-light gravel materials on basis of ash-slag mixtures formed during hydraulic removal. *Stroitel'nye Materialy*, 10, 22 – 24, Article EID: 2-s2.0-0036921238.

21 Dostiyarov, A., Sarakeshova, N., & Yamanbekova, A. (2024). The result of the investigation of a new micromodule gas burner with a sudden expansion at the outlet. *Eastern-European Journal of Enterprise Technologies*, 129(8). https://doi.org/10.15587/1729-4061.2024.303636

22 Maalal O., Prat M., & Lasseux D. (2021). Pore network model of drying with Kelvin effect. *Physics of Fluids*, 33(2). https://doi.org/10.1063/5.0035651

23 Reinecke, S. A., & Sleep, B.E. (2002). Knudsen diffusion, gas permeability, and water content in an unconsolidated porous medium. *Water Resources Research*, *38*(12), 16-1-16-5. https://doi.org/10.1029/2002WR001278

24 Wen, Y., Liao, J., Liu, X., Wei, F., & Chang, L. (2017). Removal behaviors of moisture in raw lignite and moisturized coal and their dewatering kinetics analysis. *Drying Technology*, *35*(1), 88-96. https://doi.org/10.1080/07373937.2016.1160246

25 Rong, L., Song, B., Yin, W., Bai, C., & Chu, M. (2017). Drying behaviors of low-rank coal under negative pressure: Kinetics and model. *Drying technology*, *35*(2), 173-181. https://doi.org/10.1080/07373937.2016.1164712

26 Wang H., Dlugogorski B. Z., Kennedy E. M. (2003). Coal oxidation at low temperatures: oxygen consumption, oxidation products, reaction mechanism and kinetic modelling. *Progress in energy and combustion science*, 29(6), 487-513. https://doi.org/10.1016/S0360-1285(03)00042-X

27 Rong, L., Xiao, J., Wang, X., Sun, J., Jia, F., & Chu, M. (2020). Low-rank coal drying behaviors under negative pressure: Thermal fragmentation, volume shrinkage and changes in pore structure. *Journal of Cleaner Production*, *272*, 122572. https://doi.org/10.1016/j.jclepro.2020.122572

AUTHORS' INFORMATION

Atyaksheva, Alexandra Vladimirovna – Associate Professor, PhD (Tech), Energy Institute of S. Seifullin Kazakh Agrotechnical Research University, Astana, Scopus Author ID: 57204188485, https://orcid.org/0000-0003-2523-3890; sahsa77@mail.ru

Sarakeshova, Nurbubi Nurkenovna – PhD, Head of the Educational Programs Group Thermal Power Engineering, Energy Institute, S.Seifullin Kazakh Agrotechnical Research University, Astana, Scopus Author ID: 58640264400, https://orcid.org/0009-0007-9362-7740, n.sarakeshova@kazatu.edu.kz

Rozhkova, Olga Vladimirivna – Professor, Doctor of Chemical Sciences, Academician of the National Academy of Natural Sciences of the Republic of Kazakhstan, Energy Institute of S. Seifullin Kazakh Agrotechnical Research University, JSC «PolyTechPark», Astana, Scopus ID: 57197747892, https://orcid.org/0000-0001-8163-7035; rozhkova.o@stsolutions.kz

Zhaksylyk, Akbota Meirambekovna – Senior lecture, Energy Institute of S. Seifullin Kazakh Agrotechnical Research University, Astana, Scopus ID: 60214592400, https://orcid.org/0000-0002-1441-586X; b_meyrambek@mail.ru.

Zhumaliyeva Altynai Kairbekovna – Senior lecture, Master of Technical Sciences, Energy Institute, S. Seifullin Kazakh Agrotechnical Research University, Astana, https://orcid.org/0000-0002-0342-1869; zhumaliyeva1990@list.ru

Aitmagambetova Maralgul Borambaevna – Doctoral student, researcher, Energy Institute, S. Seifullin Kazakh Agrotechnical Research University, Astana, Scopus ID: 57226317403 https://orcid.org/0000-0002-0342-1869 aiti.mb@yandex.kz

Umirzakov Ruslan Abildaevich – Doctoral student, researcher, Energy Institute, S. Seifullin Kazakh Agrotechnical Research University, Astana, Scopus ID: 57208883904 https://orcid.org/0000-0002-3047-9046; ars_uran@mail.ru

EURASIAN PHYSICAL TECHNICAL JOURNAL

2026, Volume 23, No. 3 (57)

https://doi.org/10.31489/2026N3/64-73

Received: 13/05/2026 Revised: 15/08/2026 Accepted: 28/09/2026 Published online: 30/09/2026

Original Research Article

Open Access under the CC BY -NC-ND 4.0 license

UDC 533.6.011, 621.453, 519.63

THE INFLUENCE OF THERMOSTATTING TEMPERATURE ON THE IGNITION AND DEFORMATION DYNAMICS OF A CYLINDRICAL CHARGE IN A NOZZLELESS PROPULSION DEVICE

Min'kov L.L.[1]*, Gimayeva N.R.[2]

[1] National Research Tomsk State University, Tomsk, Russia
[2] Moscow Aviation Institute, Moscow, Russia
*Corresponding author: lminkov@ftf.tsu.ru

Abstract. *This article presents the results of numerical simulation of the transition to steady-state operation of a nozzle less propulsion device (NPD) with a cylindrical viscoelastic solid propellant charge. The study was performed in a two-dimensional axisymmetric formulation, taking into account the coupled interaction of viscous compressible combustion products and a deformable charge. The viscoelastic behavior of the propellant is described using Prony series and the Williams-Landel-Ferry temperature-time shift function. It was found that an increase in the initial thermostatting temperature of the charge reduces its ignition time and decreases the initial shear modulus, which leads to a more than twofold increase in surface movement. It is shown that low initial temperatures lead to a decrease in propellant chamber pressure, while an increase in temperature by 115 °C increases the maximum pressure by 25 atm. The convergence of the numerical solution on three computational grids is assessed.*

Keywords: nozzle less propulsion device, viscoelastic charge, ignition of the charge, coupled simulation.

1. Introduction

Nozzle less propulsion devices (NPD) are of considerable interest for use in the launch stages of integral rocket-ramjet systems due to their high reliability, structural simplicity, no need for detachable nozzle equipment, and reduced requirements for thermal protection [1–3]. Based on a simplified physical mathematical model proposed in [4] for analyzing the intra chamber processes of the NPD, the following was established. The outlet cylindrical shape section results in 14% momentum loss compared to classical propulsion device. At the same time, the formation of a conical outlet charge channel section can contribute to an increase in the efficiency of the NPD, on condition that the reduction in the active combustion surface area remains relatively small. The observed deformation of the solid propellant charge due to significant pressure differences in the channel during the initial section of the NPD operation creates a risk of instability in the functioning of the propulsion device due to the mutual influence of deformation and gas-dynamic processes. To ensure a reliable assessment of the design's performance, it is crucial to conduct coupled modeling of gas dynamics and stress-strain state.

The viscoelastic properties of modern mixed solid propellant (the time dependence of the shear and elastic modules) significantly influence the assessment of the stress-strain state of the charge. In [5], a modeling of

the dynamic response of the SP charge to the initial load from the pressure increase was carried out using a quasi-static elastic analysis; taking into account the viscoelastic properties of the HTPB (transient analysis).

It was found that the first method gives overestimated response values relative to the second. An analysis of a solid propellant charge viscoelastic behavior of an NPD under the action of a gas-dynamic load during the initial period of its operation under various thermostatting conditions charge, assuming that the channel surface ignites instantly, was conducted in [6]. It was shown that an increase in the charge thermostatting temperature of the solid propellant leads to a decrease in the maximum pressure in the NPD combustion chamber due to an increase in the cross-sectional area of the channel.

In the work [7-9] an analysis was carried out of the two-pulse solid rocket engine starting operation. The study is based on the joint solution of: a system of three-dimensional non-stationary equations for a viscous heat-conducting gas; a system of equations of the mechanics of deformable solids; the heat transport equation – for calculating the propellant surface temperature. It is shown that for a 0.9 m charge in length and a channel diameter of 0.08 m, in case of rigid fixation of the nozzle block, with an increase in pressure from 0.1 MPa to 23.6 MPa, the amplitude of longitudinal oscillations of the charge surface can reach 10 mm, and lateral – 3 mm. In the paper [10], a viscoelastic structural analysis was performed to evaluate the influence of the insert properties on the distribution of stresses and strains along the insert/fuel interface in a solid-propellant propulsion device. The analysis was conducted based on a simplified two-dimensional axisymmetric model using the Ansys software package. The results showed that during the initial period of engine operation, under the influence of a load caused by an increase in pressure, the stresses along the interface increase with an increase in the initial modulus of elasticity and decrease with an increase in its Poisson's ratio.

The aim of this work is to study the influence of thermostatting conditions on the cylindrical viscoelastic charge of a solid propellant behavior under the action of a gas-dynamic load in NPD during the period when the engine reaches a steady-state operating mode, taking into account the gradual ignition of the solid propellant charge surface.

2. Physical statement of the problem

Figure 1 shows a cutout of a model nozzleless engine. The engine consists of a cylindrical solid propellant charge 1 attached to the engine body 2, an igniter 3, and a combustion chamber 4, which is initially closed by a plug 5. The left end surface and the cylindrical surface 6 of the charge are the surfaces capable of combustion. The right end surface 7 is armored. Combustion products entering from the combustion surface flow out through the boundary 8 after the plug is opened.

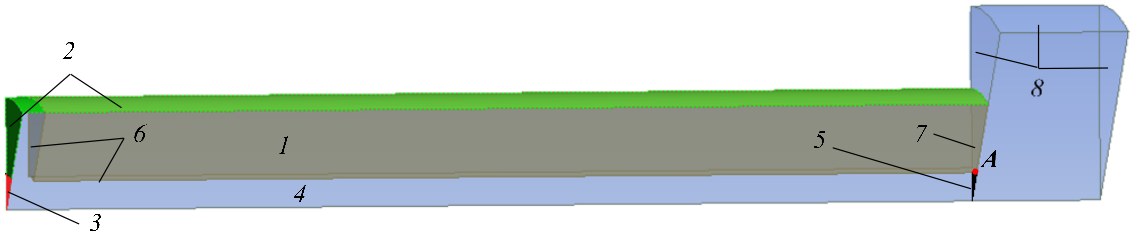


Fig.1. Sectional view of a model nozzleless engine: 1 – SP charge, 2 – housing, 3 – igniter device, 4 – combustion chamber, 5 – plug, 6 – combustion surface, 7 – inert surface, 8 – outlet boundary; A – control point

It is assumed that, at the initial moment, igniter 3 is triggered, the combustion products of which enter the combustion chamber filled with air and heat the surface of the charge 6 through convective, conductive, and radiant heat exchange. The igniter operates for a time t_{ig}, ensuring a mass flow equal to G_{ig}. After the charge surface temperature reaches the ignition temperature, mass and energy begin to flow from the combustion surface into the combustion chamber. After the pressure on the plug surface exceeds the breakdown pressure p_d, combustion products flow out of the combustion chamber.

The combustion products are assumed to be a three-component viscous compressible gas, with unsteady flow. The solid propellant charge is taken to be a visco-hyperelastic body, which is deformed under the action of the gas-dynamic load arising from the combustion products, altering the combustion surface. This, in turn, causes a change in the combustion chamber pressure, leading to a change in the charge's stress-strain state.

3. System of equations for the stress-strain state of a charge

To describe the effects of hyperelasticity, the Neo-Hooke model is used, and to describe the effects of viscoelasticity, the generalized Maxwell model is used, in which the relaxation modules of elasticity are approximated by Prony series [11].

Mass conservation equation

$$\frac{d\rho_s}{dt} + \rho_s \nabla_k V_{s,k} = 0\,, \tag{1}$$

Equation of motion for particle

$$\rho_s \frac{d^2 u_{s,i}}{dt^2} = \nabla_k \sigma_{s,ki}\,, \tag{2}$$

where $u_{s,i}$ – the movement of a particle inthe medium; $V_{s,i} = \frac{du_{s,i}}{dt}$ – the velocity of the movement of the particles in the medium.

Finite strain tensor

$$\varepsilon_{s,ij} = \frac{1}{2}\left(\nabla_i u_{s,j} + \nabla_j u_{s,i} + \nabla_i u_{s,k} \nabla_j u_{s,k}\right), \tag{3}$$

The relationship between stresses and strains for a visco-hyperelastic body is:

$$\sigma_{s,ij} = 2\int_0^t G(t-\tau)\frac{d}{d\tau}\left(\frac{1}{J}F_{ik}\cdot\frac{\partial w_D\left(\bar{I}_1\right)}{\partial C_{kl}}\cdot F_{lj}^T\right)d\tau + \delta_{ij}\int_0^t K(t-\tau)\frac{d}{d\tau}\left(\frac{\partial w_V(J)}{\partial J}\right)d\tau\,, \tag{4}$$

$$w_D\left(\bar{I}_1\right) = \frac{\bar{I}_1 - 3}{2}\,, \tag{5}$$

$$w_V(J) = (J-1)^2\,, \tag{6}$$

where $G(t)$ – is the relaxation shear modulus; $K(t)$ – is the relaxation volume modulus, $\bar{I}_1 = I_1/J^{2/3}$; $I_1 = \lambda_1^2 + \lambda_2^2 + \lambda_3^2$; $\lambda_1^2, \lambda_2^2, \lambda_3^2$ – eigenvalues of matrices $C_{ij} = F_{ki}F_{kj}$, $F_{ij} = \partial x_i/\partial X_j$ – are the components of the strain gradient tensor, $J = \det\left(F_{ij}\right)$.

The dependence of relaxation modules on time is approximated by Prony series [11]:

$$G(t) = G_0 g(t)\,,\ K(t) = \frac{2(1+\nu)}{3(1-2\nu)}G_0 g(t) \tag{7}$$

$$g(t) = \alpha_0 + \sum_{i=1}^{n}\alpha_i \exp\left(-\frac{t}{a(T)\tau_i}\right), \tag{8}$$

where α_i and τ_i – are the coefficients of the Prony series; $a(T)$ – is the temperature-time shift function; G_0 – is the initial shear modulus; ν – is the Poisson's ratio, $g(t)$ – is the relative relaxation modulus.

The temperature-time shift function $a(T)$ according to the Williams-Landel-Ferry model [12] has the form:

$$\log a(T) = \frac{a_1\left(T - T_0\right)}{a_2 + T - T_0}\,, \tag{9}$$

4. System of equations for the viscous compressible gas flow

To describe the flow of combustion products in the combustion chamber, the Navier-Stokes equations for a multi-component compressible heat-conducting gas are used.

Continuity equation

$$\frac{\partial \rho_g}{\partial t} + \frac{\partial \rho_g V_{g,k}}{\partial x_k} = S_\rho, \tag{10}$$

Mass conservation equation of ignition gas

$$\frac{\partial \rho_g \xi_{ig}}{\partial t} + \frac{\partial \rho_g \xi_{ig} V_{g,k}}{\partial x_k} = \frac{\partial}{\partial x_k}\left(\rho_g D_{ig} \frac{\partial \xi_{ig}}{\partial x_k}\right), \tag{11}$$

Mass conservation equation of propellant gas

$$\frac{\partial \rho_g \xi_{pr}}{\partial t} + \frac{\partial \rho_g \xi_{pr} V_{g,k}}{\partial x_k} = \frac{\partial}{\partial x_k}\left(\rho_g D_{pr} \frac{\partial \xi_{pr}}{\partial x_k}\right) + S_\rho, \tag{12}$$

Mass fractions conservation equation

$$\xi_{ig} + \xi_{pr} + \xi_{air} = 1, \tag{13}$$

Momentum equation

$$\frac{\partial \rho_g V_{g,i}}{\partial t} + \frac{\partial \rho_g V_{g,i} V_{g,k}}{\partial x_k} = -\frac{\partial p}{\partial x_i} + \frac{\partial \tau_{g,ik}}{\partial x_k}, \tag{14}$$

Energy conservation equation

$$\frac{\partial \rho_g e_g}{\partial t} + \frac{\partial \rho_g V_{g,k} h_g}{\partial x_k} = \frac{\partial}{\partial x_k}\left(\lambda_g \frac{\partial T_g}{\partial x_k} + \tau_{g,ik} V_{g,i}\right) + a \int_0^{4\pi} I(r_i, s_i) d\Omega - 4a\sigma T_g^k + S_E, \tag{15}$$

Radiative intensity transfer equation

$$\frac{\partial I(r_i, s_i) s_k}{\partial x_k} + (a + \sigma_s) I(r_i, s_i) = an^2 \frac{\sigma T^4}{\pi} + \frac{\sigma_s}{4\pi} \int_0^{4\pi} I(r_i, s_i) d\Omega, \tag{16}$$

where $e_g = \frac{1}{k-1}\frac{p}{\rho_g} + \frac{V_g^2}{2}$ – the total internal energy of the gas; $h_g = e_g + \frac{p}{\rho_g}$ – the total enthalpy of the gas; $V_g^2 = \sum_{k=1}^{3} V_{g,k}^2$ – the square of the velocity vector; $\tau_{g,ik}$ – the viscous stress tensor, $\mu_g\left(\frac{\partial V_{g,i}}{\partial x_k} + \frac{\partial V_{g,k}}{\partial x_i} - \frac{2}{3}\delta_{ik}\frac{\partial V_{g,j}}{\partial x_j}\right)$; t – time; x – the spatial coordinate; p – the pressure; V – the velocity; k – the specific heat ratio at constant pressure to the specific heat capacity at constant volume for a gas mixture; ξ_{ig} – ignition gas mass fraction, is the mass fraction of the fuel gas, ξ_{air} – the mass fraction of air, a – the radiation absorption coefficient, σ – the Stefan-Boltzmann constant, $5.67 \cdot 10^{-8}$W/(m^{2}K^4), σ_s – the scattering coefficient, n – the refractive index, s_i – the components of the radiation direction vector, r_i – the components of the position vector, Ω – the solid angle, S_ρ, S_E – the specific mass gain and energy gain due to propellant combustion, respectively.

Equation of state

$$p = \rho_g T_g \sum_{j=1}^{3} \xi_j R_j \,, \tag{17}$$

where $R_j = R_y / M_j$, R_y – the universal gas constant; M_j – the molar mass of the *j*th component.

In this formulation of the problem, the burning surface is replaced by a solid wall, and the mass gain and energy gain of gases is modeled through source terms in the continuity equation (10), in the propellant gas mass conservation equation (12), and in the energy conservation equation (15) [13]: $S_\rho = \rho_T u_{01} p^{\nu_1} \delta(x_k; R_k)$, $S_E = c_{p,pr} T_p S_\rho$, where R_k – the function describing the combustion surface; $c_{p,pr}$ – the specific heat capacity of the propellant gas at constant pressure, ρ_T – the fuel density. $u_{01} = u_0 \exp(\beta T_{g,0})$ – the fuel combustion rate at 1 atm [14], u_0 – the pre-exponential factor, β – the coefficient of sensitivity of the combustion rate to the initial temperature $T_{g,0}$, $\nu_1 = \nu_{ref} + k_\nu (T_{g,0} - T_{ref})$ – the exponent in the combustion rate law, k_ν – the temperature coefficient, ν_{ref}, T_{ref} – the reference values of the exponent and the initial temperature, T_p – the propellant combustion temperature, $\delta(x_k; R_k)$ – Dirac delta function.

4. Boundary conditions

For a solid body: plane of symmetry: $u_{s,nn} = 0$ – equality to zero of normal displacements; condition of fixing: $u_{s,i} = 0$ – displacements in all directions are equal to zero.

For gas: non-deformable solid wall: $V_{g,k} = 0$; igniter: $\rho_g V_{g,n} = G_{ig} \eta\ t_{ig} - t$, $T = T_{ig}$, $\xi_{ig} = 1$, $\xi_{pr} = 0$ where $\eta\ t$ – Heaviside function; deformable solid wall, propellant: $\rho_g V_{g,n} = G_{ig} \eta\ t_{ig} - t$, $T = T_{ig}$, $\xi_{ig} = 1$, $\xi_{pr} = 0$; channel outlet: $p = p_n$ – at subsonic flow the pressure is equal to the environmental pressure; plane of symmetry: $V_{g,n} = 0$, $\frac{\partial \varphi}{\partial n} = 0$, $\varphi = \rho_g, \xi_{ig}, \xi_{pr}, V_{g,\tau 1}, V_{g,\tau 2}, p$. The interface between the surface of a solid and a gas:

$\sigma_{s,nn} = -p + \tau_{g,nn}$ – equality of normal stresses in propellant and gas; $\sigma_{s,n\tau_1} = \tau_{g,n\tau_1}$, $\sigma_{s,n\tau_2} = \tau_{g,n\tau_2}$ – equality of shear stresses in propellant and gas; $V_{s,i} = V_{g,i}$ – equality of the movement speeds of propellant and gas particles. $I = \frac{1}{\pi}\left[n^2 \varepsilon_w \sigma T_w^4 - (1 - \varepsilon_w) \int_0^{4\pi} I \cdot s_n d\Omega \right]$, where ε_w – wall emissivity.

The propellant surface temperature is determined from the solution of an ordinary differential equation obtained by the method of integral relations using an approximation of the temperature profile inside the propellant by a third-order parabola [15]

$$\frac{dT_w}{dt} = \frac{4}{3} \frac{q_w^2}{\lambda_T \rho_T c_T} \frac{(T_g - T_w)}{(T_w - T_{wn})(2T_g - T_w - T_{wn})}, \tag{18}$$

with the initial condition: $T_w|_{t=0} = T_{wn}$, where q_w – the heat flow from the gas to the propellant surface, λ_T – the propellant thermal conductivity coefficient, c_T – the propellant specific heat capacity coefficient

5. Numerical technique

The computational domain is a sector of a cylindrical domain, fig. 1, in which the angle between the section planes drawn along the axis is 10°. For the numerical solution of the system equations (1)–(9) describing the stress-strain state of the charge, the finite element method with linear shape functions for eight-point hexagonal elements was used. The numerical solution of the system equations describing the flow of

combustion products (10)–(17) was performed using the Patankar method on a grid with hexagonal cells using an implicit upwind scheme of second-order accuracy in spatial variables for the convective terms of the equations and first-order accuracy in time. The implementation of these methods was carried out in the Ansys computing package in the Workbench environment using the Transient Structural and Fluent modules, respectively, data exchange between them was carried out using the System Coupling module. At each time step, 20 iterations were performed solving the system of hydrodynamic equations. At each stage of load-displacement coupling, 5 iterations were performed. The time step size was chosen to be 10^{-5} s, and the end time was 0.1 s. The ordinary differential equation (18) was solved using Euler's method.

6. The discussion of the results

For the numerical solution of the problem, the following parameter values were adopted. The charge length is 125 cm, web thickness is 7 cm, the charge channel radius is 4 cm, the gap width between the left ends of the combustion chamber and the charge is 1 cm, the width and height of the areas to the right of the charge are 19 cm and 21 cm, respectively. The thermophysical parameters of the combustion products are given in Table 1, the characteristics of the solid propellant are given in Table 2, the Prony series coefficients for the model propellant at a temperature of 20°C are given in Table 3 [16], the initial shear modules depending on temperature and Poisson's ratio are given in Table 4, the coefficients of the temperature-time shift function are given in Table 5 [17].

Table 1. Thermophysical properties.

Properties	Air	Gas from solid propellant	Gas from the ignition device
Specific heat, J/(kg·K)	1006	1900	800
Molar weight, kg/kmol	29	24	55
Dynamic viscosity, Pa·c	$1.79\cdot10^{-5}$	$8\cdot10^{-5}$	$4\cdot10^{-5}$
Thermal conductivity, W/(m·K)	0.0242	0.25	0.1

Table 2. Solid propellant properties.

Pre-exponential factor, u_0, mm/s	2.309	Combustion temperature, K	2900
Sensitivity coefficient, β, K^{-1}	$2.972\cdot10^{-3}$	Propellant density, kg/m^3	1700
Temperature coefficient, k_T, K^{-1}	$-1.5\cdot10^{-4}$	Thermal conductivity, W/(m·K)	0.6
Reference indicator, ν_{ref}	0.41	Specific heat capacity, J/(kg·K)	1400
Reference initial temperature, T_{ref}, K	343	Ignition temperature, K	600

Table 3. Prony series coefficients for propellant.

i	α_i	τ_i, c
0	0.0486666	
1	0.0114570	$5\cdot10^{-6}$
2	0.0055763	$5\cdot10^{-5}$
3	0.2436390	$1\cdot10^{-4}$
4	0.2486060	$2.5\cdot10^{-4}$
5	0.1022000	$5\cdot10^{-4}$
6	0.1285610	$1\cdot10^{-3}$
7	0.0833416	$2.5\cdot10^{-3}$
8	0.0551554	$5\cdot10^{-3}$
9	0.0537361	$1.5\cdot10^{-2}$
10	0.0190610	$5\cdot10^{-2}$

Table 4. Initial values of the shear modulus and Poisson's ratio.

T, °C	G_0, MPa	ν
–45	90	0.4999
20	50	
70	30	

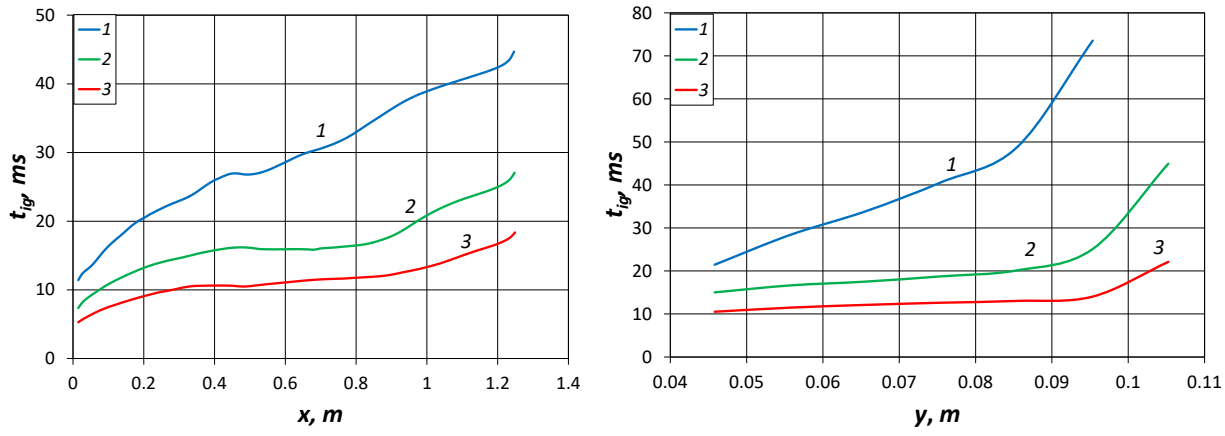
Table 5. Coefficients of the function a(T), equation (9).

a_1, [-]	–5.4
a_2, K	770.27
T_0, K	293

The absorption coefficient of gas mixture radiation was taken to be 80 m^{-1} [18]. As estimates show [6], by the time of 0.1 s the relative shear modulus reaches its lowest value of ~0.0487, (equation (8)), which is practically independent of the propellant temperature in the range from –45°C to +70°C. Therefore, further calculations were carried out up to the specified time.

Figure 2 shows the effect of the initial temperature on the ignition front propagation across the charge surface. Increasing the initial temperature leads to a decrease in the ignition time of the charge surface, with

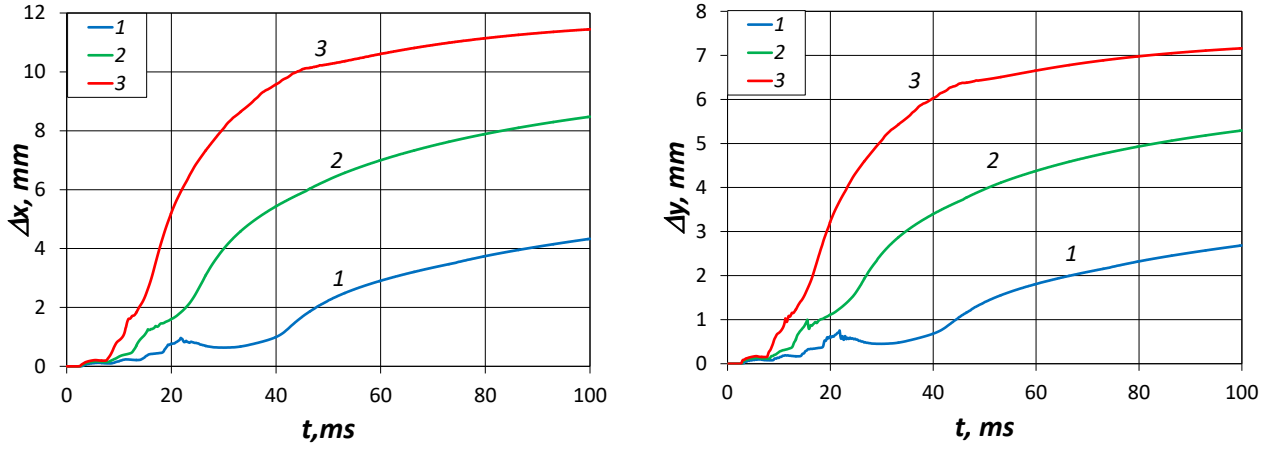
complete ignition of the end surface occurring much later than that of the cylindrical surface. The increase in the slope of the ignition curve for the end surface, fig. 2b, is due to the trapping of relatively cold gas at the dead end of the gap, resulting in an increase in the time it takes for the charge surface to warm up to ignition temperature. It should be noted that the thermal error in calculating the ignition time, which was due to the time step used in solving equation (18), amounted to approximately 3 ms.



a) *b*)

Fig.2. Dependence of surface ignition time on coordinate: *a* – cylindrical surface, *b* – end surface; *1* – T_0 = –45°C, *2* – T_0 = 20°C, *3* – T_0 = 70°C.

Low initial shear modulus values, typical for propellants with high thermostatting temperatures, lead to large displacements of the propellant surface, fig. 3. Reducing the shear modulus from 90 MPa to 30 MPa caused by high thermostatting temperatures resulted in a more than twofold increase in the displacement of point A from the equilibrium position, both axially and radially. The non-monotonic behavior of the curves up to the 20–30 ms time point is due to the operation of the igniter and the failure of the plug, which lead to significantly non-stationary processes in the combustion chamber.



a) *b*)

Fig.3. Dependence of the control point movement on time: *a* – longitudinal coordinate, *b* – radial coordinate; *1* – T_0 = –45°C, *2* – T_0 = 20°C, *3* – T_0 = 70°C.

Low initial charge temperatures lead to low pressures in the combustion chamber. Increasing the initial temperature by 115 degrees increases the maximum pressure by 25 atm, which is associated with an increase in the propellant combustion rate with increasing initial temperature. The dependence of the combustion rate on the initial temperature has a greater influence on the increase in pressure in the combustion chamber than the dependence of the elastic modulus on the initial temperature, when lower values of the elastic modulus lead to an increase in the cross-sectional area of the channel and a subsequent decrease in pressure [6].

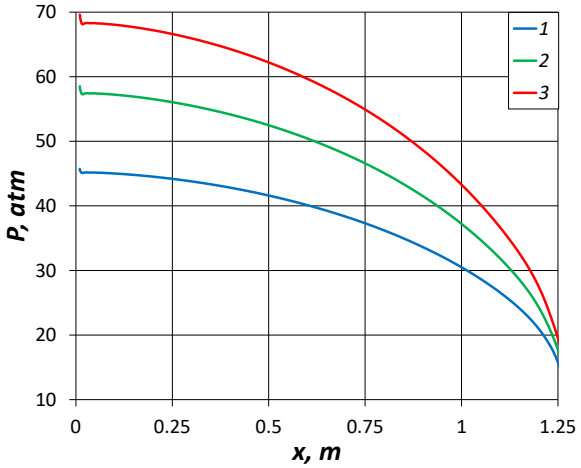


Fig.4. Pressure distribution on the combustion surface at the time of 0.1 s:
1 – T_0 = –45°C, 2 – T_0 = 20°C, 3 – T_0 = 70°C.

To study the convergence of the numerical solution, calculations were performed on three meshes, the parameters of which are given in Table 6. The number of elements and cells in the rotationally direction was equal to 1, which corresponds to an axisymmetric approximation. The calculations were performed with a time step of 10^{-5} s.

Table 6. Mesh parameters for convergence study.

Mesh name	Cell size along the x-axis and y-axis, mm	Number of cells in the gas region	Number of elements in the charge region
Mesh №1	10	1074	875
Mesh №2	5	4296	3500
Mesh №3	2.5	17184	14000

Convergence of the numerical solution is verified using the L_2 norm $\|\vec{x}\| = \sqrt{\frac{1}{n}\sum_{i=1}^{n} x_i^2}$. The convergence condition requires satisfying the inequality

$$\|\vec{u}_{h/2} - \vec{u}_{h/4}\| < \|\vec{u}_h - \vec{u}_{h/2}\|, \tag{19}$$

where $\vec{u}_h$ is the numerical solution vector obtained on the mesh 1 with step size h, $\vec{u}_{h/2}$ is that on the mesh 2, and $\vec{u}_{h/4}$ is that on the mesh 3. Table 7 presents the norms of the differences between solutions obtained on successive meshes for the pressure distribution along the channel axis at t = 100 ms, the dependence of the cylindrical surface ignition time on the longitudinal coordinate, and the radial displacement of point A over time. As the table shows, the convergence condition (19) is satisfied for all key parameters.

Table 7. Norms of the differences between numerical solutions on successive grids

$\vec{u}_h$	$\|\vec{u}_h - \vec{u}_{h/2}\|$	$\|\vec{u}_{h/2} - \vec{u}_{h/4}\|$
P, atm	0.705	0.297
t_{ign}, ms	4.185	2.365
Δy, mm	0.319	0.197

The pressure distribution along the charge combustion surface at a time of 100 ms is shown in fig. 5. Curve 1 corresponds to mesh №1, curve 2 – mesh №2, and curve 3 – mesh №3.

Fig. 6 shows the effect of the computational mesh on the dependence of the ignition time of a cylindrical charge surface on the longitudinal coordinate for propellant with an initial shear modulus of 70 MPa (T_0 = 20°C).

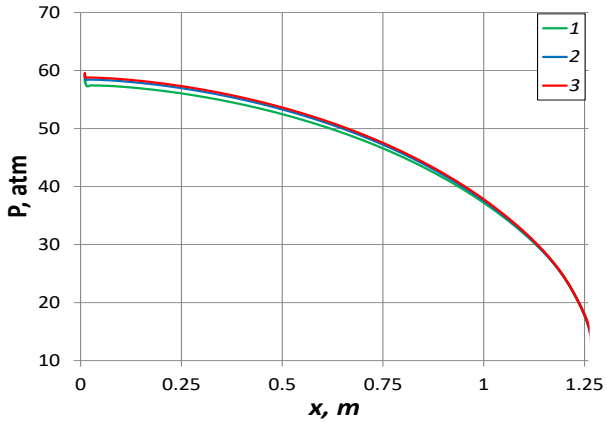


Fig.5. The effect of the mesh on the pressure distribution along the channel axis:
1 – mesh №1, *2* – №2, *3* – №3; T_0 = 20°C.

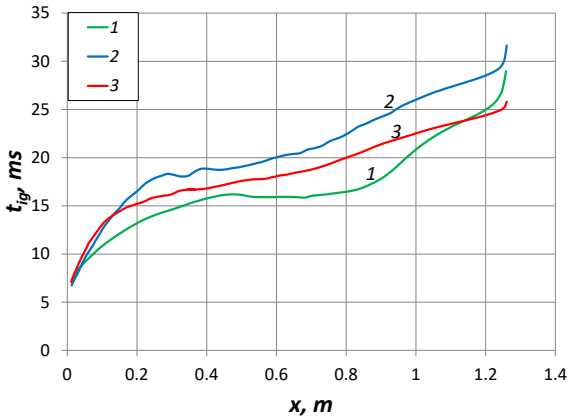


Fig.6. The effect of the mesh on the dependence of the ignition time on the longitudinal coordinate:
1 – mesh №1, *2* – №2, *3* – №3; T_0 = 20°C

7. Conclusions

The conducted study demonstrates the critical dependence of the dynamics of the NPD reaching a steady-state mode on the initial temperature of charge thermostatting. Increasing the temperature accelerates surface ignition but significantly reduces the propellant's shear modulus, which causes deformations (axial and radial) to more than double. This creates a risk of engine instability due to changes in the channel geometry. The two competitive effects determine combustion chamber pressure: an increase in the combustion rate as the propellant heats up (increasing pressure) and an increase in the flow area due to material softening (decreasing pressure). Practical NPD design requires considering not only the gas dynamics but also the viscoelastic properties of the propellant over a wide temperature range (from –45°C to +70°C). The obtained results can be used to optimize operating conditions and improve the reliability of nozzleless propulsion devises.

Conflict of interest statement
The authors declare that they have no conflict of interest in relation to this research, whether financial, personal, authorship or otherwise, that could affect the research and its results presented in this paper.

CRediT author statement
Minkov L.L.: Conceptualization, Methodology; ; **A.Gimayeva N.R.**:Investigation, Data Curation, Writing Original Draft. The final manuscript was read and approved by all authors.

Statement on the use of Artificial Intelligence.
The authors declare that no artificial intelligence tools were used to generate scientific content, results, or conclusions of this article.
Data Availability Statement
The data are available upon reasonable request from the authors.

Acknowledgements

This work was financially supported by the Ministry of Education and Science of the Russian Federation (state assignment No. FSWM-2025-0012).

References

1 Yanovskiy, L.S., Ed., Aref'ev, K.Yu, Milyokhin, Yu. M., Sorokin, V.A., & Gusev, C.A. (2020). *Ramjet engines on energy-intensive condensed materials*. TsIAM, Moscow, 197 p. https://rusneb.ru/catalog/000199_000009_010495374/?ysclid= mu3r0sxm1i797515443 [in Russian]

2 Milyokhin, Yu.M., Burskly, G.V., Lavrov, G.S., Popov, V.S., & Sadovnichiy, D.N. (2018). *Energetics and internal ballistics of solid rocket motors.* Nauka, Moscow, 358 p. https://search.rsl.ru/ru/record/ 01009779112 [in Russian]

3 Minkov, L., & Gimayeva, N. (2024). Effect of Two-Phase Flow on the Fuel Grain Ignition and its Departure from the Cartridge Case. *Eurasian Physical Technical Journal*, 21, 1(47), 84–92. https://doi.org/10.31489/2024No1/84-92

4 Gany, A., & Aharon, I. (2012). Internal Ballistics Considerations of Nozzleless Rocket Motors. *Journal of Propulsion and Power*, 15(6), 866–873. https://doi.org/10.2514/6.1995-2735

5 Chyuan, S.W. (2003). Dynamic analysis of solid propellant grains subjected to ignition pressurization loading. *Journal of Sound and Vibration*, 268, 465–483. https://doi.org/10.17223/19988621/98/11

6 Min'kov, L.L., Gimaeva, N.R., & Dil', D.V. (2025). Numerical study of the transition to a steady-state operating mode of a nozzleless propulsion system with a viscoelastic cylindrical charge. *Vestnik Tomskogo gosudarstvennogo universiteta. Matematika i mekhanika*, 98, 120–135. https://doi.org/10.17223/19988621/98/11

7 Li, Q., Liu, P., & He, G. (2015). Fluid–solid coupled simulation of the ignition transient of solid rocket motor. *Acta Astronautica*, 110, 180–190. https://doi.org/10.1016/j.actaastro.2015.01.020

8 Li, Y., Chen, X., Xu, J., Zhou, C., & Musa, O. (2018). Three-dimensional multi-physics coupled simulation of ignition transient in a dual pulse solid rocket motor. *Acta Astronautica*, 146, 46–65. https://doi.org/10.1016/j.actaastro.2018.01.058

9 Guo, X., Zhang, J.T., Zhang, M., Liu, L.S., Zhai, P.C., & Zhang, Q.J. (2016). Effects of liner properties on the stress and strain along liner/propellant interface in solid rocket motor. *Aerospace Science and Technology*, 58, 594–600. https://doi.org/10.1016/j.ast.2016.09.020

10 Marple, S.L., Jr. (1987). Digital spectral analysis: with applications. Prentice Hall, Englewood Cliffs, 492 p. https://openlibrary.org/books/OL2716295M/Digital_spectral_analysis

11 Williams, M.L., Landel, R.F., & Ferry, J.D. (1955). The Temperature Dependence of Relaxation Mechanisms in Amorphous Polymers and Other Glass-forming Liquids. *Journal of the American Chemical Society*, 77, 3701–3706. https://doi.org/10.1021/ja01619a008

12 Minkov, L.L., Shrager, E.R., & Kiryushkin, A.E. (2016). Two approaches for simulating the burning surface in gas dynamics. *Key Engineering Materials*, 685, 114–118. https://doi.org/10.4028/www.scientific.net/KEM.685.114

13 Rashkovskiy, S.A., Milekhin, Y.M., & Fedorychev, A.V. (2016). Correlation of parameters in the burning rate law and its influence on intraballistic characteristics of a rocket motor. *Combustion, Explosion, and Shock Waves*, 52(4), 427-438. https://doi.org/10.1134/S0010508216040067

14 Goodman, Th.R. (1964). Application of Integral Methods to Transient Nonlinear Heat Transfer. *Advances in Heat Transfer*, 1, 51–122. https://doi.org/10.1016/S0065-2717(08)70097-2

15 Xu, J., Chen, X., Wang, H., Zheng, J., & Zhou, C. (2014). Thermo-damage-viscoelastic constitutive model of HTPB composite propellant. *International Journal of Solids and Structures*, 51, 3209–3217. https://doi.org/10.1016/j.ijsolstr.2014.05.024

16 Adel, W.M., & Liang, G.Z. (2017). Analysis of Mechanical Properties for AP/HTPB Solid Propellant under Different Loading Conditions. *World Academy of Science, Engineering and Technology*, 11(12), 1906–1910. https://doi.org/10.5281/zenodo.1314893

17 Milekhin, Y.M., Kluchnikov, A.N., Popov, V.S., & Pelipas, N.D. (2014). Calculation of the unsteady internal ballistic parameters of the transition of a solid rocket motor to steady-state operation using the method of characteristics. *Combustion, Explosion, and Shock Waves*, 50(6), 676-688. https://doi.org/10.1134/S0010508214060094

AUTHORS' INFORMATION

Minkov, Leonid Leonidovich - Doctor of Phys. - Math. Sciences, Professor, Mathematical Physics Department, Physics Engineering Faculty, Tomsk State University, Tomsk, Russian Federation; ORCID ID: 0000-0001-6776-6375; lminkov@ftf.tsu.ru

Gimayeva, Nataliya Radikovna. - Post graduate student, Physics Engineering Faculty, National Research Tomsk State University, Tomsk, Russian Federation; ORCID ID: 0009-0006-9662-6818; natalia.gimaeva@inbox.ru

EURASIAN PHYSICAL TECHNICAL JOURNAL

2026, Volume 23, No. 3 (57)

https://doi.org/10.31489/2026N3/74-85

Received: 21/04/2026 Revised: 27/08/2026 Accepted: 28/09/2026 Published online: 30/09/2026

Scientific Review Article

Open Access under the CC BY -NC-ND 4.0 license

UDC 53.06; 621.31

INVESTIGATION OF THE PARAMETERS OF A HYBRID WIND–SOLAR POWER PLANT FOR ENERGY SUPPLY OF REMOTE AUTONOMOUS CONSUMERS

Alkina A.D., Kuatova A.S.*, Mekhtiyev A.D., Yurchenko A.V., Bainiyazov B.A.

Karaganda Technical University named after Abylkas Saginov, Karaganda, Kazakhstan
Tomsk Polytechnic University, Tomsk, Russia
Corresponding author: anarkuatova2019@gmail.com

Abstract. *This study investigates the operating parameters of a hybrid wind–solar power plant for autonomous electricity supply in the sharply continental climate of central Kazakhstan. The plant consisted of a 600 W wind turbine, four 200 W photovoltaic panels, a 12 V battery and a charge controller, the load being separated between alternating-current and direct-current circuits. Field measurements were carried out continuously during 2025 near Karaganda. The measured generation varied seasonally from 4.0 to 6.7 kWh/day, giving an annual output of 1993 kWh, the winter minimum falling to the level of the winter load. The monthly photovoltaic and wind outputs proved strongly anti-correlated, the Pearson coefficient being −0.81, which quantifies the seasonal complementarity of the two resources. A sizing criterion based on the coefficient of variation of the monthly generation and on a seasonal reserve factor is proposed. Raising the wind capacity to 1000 W while reducing the array to two 200 W panels lowers the coefficient of variation from 16.4 to 6.3 % and raises the December output from 4.0 to 5.5 kWh/day. Direct supply of the direct-current loads without inversion saves 25.8 % of the energy delivered to them and 18.9 % at plant level.*

Keywords: solar energy, hybrid power system, photovoltaic panels, autonomous power supply, seasonal generation, renewable energy, seasonal complementarity, direct-current distribution

1. Introduction

Currently, renewable energy sources are developing actively in Kazakhstan: their share of electricity generation exceeded 7 % in 2025 against less than 1 % ten years earlier [1, 2]. The country ranks ninth in the world by territory and has a low population density among 20.5 million inhabitants [3]. One of the directions of development of its energy sector is the creation of decentralised supply systems for remote consumers of ultra-low power, without which the development of agriculture, of new lands and of small business in such areas is impossible [4]. Due to the long distances of power transmission lines, considerable energy losses arise, and the construction of new lines is costly and, in some cases, may not pay for itself even after 25 years [5]. Developing renewable sources at the point of consumption removes this obstacle and makes it possible to use remote farmland and pastures [6]. According to open sources, the average duration of sunshine in Kazakhstan is 2200 to 3000 hours per year and the annual solar radiation per unit area is 1100 to 1900 kWh/m², the mean incident power on the Earth's surface being 110 to 190 W/m² and the radiation increasing from north to south from 4100 to 5300 MJ/m² [7].

The climate of the country is sharply continental almost everywhere. In the south there are many clear days in summer, high air temperatures and little precipitation through the year; in central and northern Kazakhstan there are fewer sunny days in winter, the winds are strong and the peak temperatures fall to –40 °C for short periods. In the west the Caspian Sea moderates the frosts although the winter winds are strong, and in the east the climate is more humid with winters as cold as in the north. The Kyzylorda region has the greatest solar potential, with 3100 hours of sunshine and about 2000 kWh/m² per year, while the potential of the country as a whole is estimated at up to 2.5 billion kWh [8].

Photovoltaic capacity of up to 50 000 MW per year is planned or already under construction [9]. Whereas solar panels are more promising for the southern regions, hybrid plants combining wind turbines with solar panels can be implemented in central Kazakhstan, where such a combination operates more efficiently in a sharply continental climate and exploits the wind potential during the winter season [10]. Northern and central Kazakhstan contain a significant amount of land suitable for agriculture. About 50 % of the territory has wind speeds of 4 to 5 m/s at a height of 30 m, the highest potential being in the Caspian region and in northern and southern Kazakhstan [11]. In central Kazakhstan the annual mean wind speed is 4 to 6 m/s, which is not always sufficient for high-capacity industrial turbines [12]. There are nevertheless several dozen locations with steady winds; at Osakarovka a wind plant of 150 MW consisting of 21 turbines of 7.7 MW each is under construction [13]. The highest wind speeds occur in January and February, in summer the mean speed decreases by half, and gusty and occasionally hurricane-force winds are characteristic of the region.

In addition to large wind turbines, low-capacity wind generators can be used in combination with solar panels. A mobile version can also be used for private livestock farms. This article presents the results of research on a hybrid wind–solar power plant (HWSPP) for energy supply to remote autonomous consumers, which is planned to be used in rural areas in the future.

Published studies of hybrid wind–solar systems in Kazakhstan are predominantly resource or policy assessments made at the level of national and regional energy balances [4]. Experimental data for installations of ultra-low rated power operated continuously for a full year under a sharply continental climate remain scarce [13]. Design recommendations are usually formulated as an approximately equal distribution of wind and photovoltaic capacities, without an explicit criterion linking the capacity ratio to the seasonal uniformity of generation [14]. The present work reports a full year of field measurements, quantifies the seasonal complementarity of the resources at the site, and formulates such a criterion.

2. Methods of research

Figure 1 shows a photograph of the hybrid wind–solar power plant designed to supply energy to remote autonomous consumers. The plant was installed on a 40-foot shipping container used as a utility and storage facility by the emergency service of the Fedorov Reservoir, Karaganda. The solar panels were mounted on a frame of shaped metal profiles and oriented to the south, with no tilt adjustment and no sun-tracking system throughout the research period. The wind generator was mounted on a mast of steel pipe at a height of 9 m above the ground and is equipped with a tail vane for orientation into the wind flow.

The panels were kept in a fixed position throughout the study period in order to ensure consistent measurement conditions. The effect of a manually adjustable tilt, corrected twice a year for the winter and summer positions, is evaluated quantitatively in Section 3, and a slotted bracket allowing this adjustment has been included in the design of the next prototype.

Figure 2 presents a schematic diagram of the configuration of the plant. It consists of a high-speed three-blade wind turbine with a synchronous electrical generator 1 and silicon solar panels 2, all connected in parallel at the same nominal voltage of 12 V. The generator 1 and the panels 2 are connected to a charge controller 3 and thence to a battery 4. The three-phase alternating current of the generator is converted to direct current by a full-wave rectifier with six diodes.All generated energy was stored in the battery (4) and supplied to consumers located inside the 40-foot shipping container via two 12 V direct current lines. The charge controller (3), battery (4), and inverter (5) were also placed inside the container. The distance from the power source to the most remote consumer inside the container did not exceed 10 m. In close proximity to the container, there is a caretaker’s house (an insulated container), where two people reside year-round.

To simplify the plant and reduce the overall electrical energy losses, 12 V direct-current lines were adopted, which eliminated the need for a common voltage inversion and for an alternating-current network with unnecessary conversions. A 200 Ah lead-acid battery from a truck served as the storage unit, and a 2 kW inverter was switched on only for appliances operating solely on alternating current, such as a microwave oven,

a low-power welding inverter, a drill and an angle grinder. Consumers able to work on 12 V direct current, including a water heater, lighting lamps, a laptop and charging units for various devices, were connected through DC/DC converters. Separating the load by current type and connecting the direct-current consumers directly to the line reduced energy losses by up to 30 % [14].



Fig. 1. Photograph of the experimental hybrid wind–solar power plant

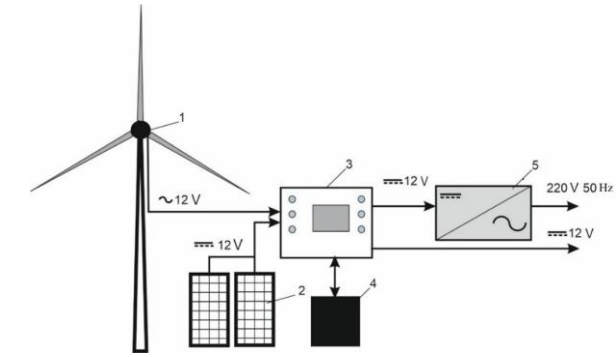


Fig. 2. Schematic diagram of the experimental hybrid wind–solar power plant

The experiment ran continuously throughout 2025 at an average annual load of 3 kWh/day, reaching 4 kWh/day in autumn and winter and falling to 2 kWh/day in summer and spring. The plant comprises four 200 W solar panels and one 600 W wind turbine, both manufactured in China; Table 1 gives the number of energy sources and the average electrical load by season. A conventional automotive-type lead-acid battery was selected primarily for its low cost and local availability. Under the regular deep-discharge cycles and the low ambient temperatures, down to −40 °C, typical of the region, the usable capacity and service life of such a battery are considerably lower than the manufacturer-rated values obtained under standard conditions. Alternatives that are more resistant to temperature and to cycling, namely valve-regulated gel and lithium iron phosphate cells, are compared with it in Table 7 of Section 3.

Table 1. Information on the number of energy sources and the average electrical load by season

Season	Wind Turbine Type Turbines (600 W each)	Number of Wind Turbines (600 W each)	Solar Panel Type/Power	Number of Solar Panels (200 W each)	Average Electrical Load by Season, kWh/day
Spring, summer	HY – 600	1	Solar panels type HH-POLY – 200 W	4	2
Autumn, winter	HY – 600	1	Solar panels type HH-POLY -200 W	4	4

Table 2 presents the characteristics of the solar panels used in the field experiments. The delivery package does not include a mounting frame, a DC 12 V to AC 220 V / 50 Hz inverter, or a battery. Table 3 presents the characteristics of the wind generator used in the field experiments. The delivery package does not include a mast, a 24–220 V inverter, or a battery.

Table 2. Characteristics of the HH-POLY – 200 W solar panel

Parameter	**Units**	**Value and Description**
Rated power	W	200
Nominal voltage	V	12
Material		Polycrystalline silicon
Declared efficiency (according to the datasheet)	%	18 at cell level; 16.8 at module level, calculated from the overall dimensions
Number of cells	pcs	64
Overall dimensions	mm	1530*780*30
Weight	kg	14
Country of manufacture		China

Table 3. Characteristics of the HY–600 wind generator

Parameter	Units	Value and Description
Number of blades	pcs	3
Rotor diameter	m	2,5
Maximum peak power of the wind generator	W	700
Rated power of the wind generator	W	600
Installation height	m	9 (standard delivery mast 6 m; a 9 m mast was used in the experiment)
Number of phases of the permanent magnet synchronous generator	pcs	3
Output voltage	V	12\24
Starting wind speed	m/s	2,5
Wind speed at which the wind generator reaches 100% power	m/s	8
Wind generation range	m/s	3 - 25
Operating rotor rotational speed	rpm	450
Service life	years	15
Axis of rotation		Horizontal
Wind orientation		Mechanical
Transmission of generated current to the controller		Via slip rings
Country of manufacture		China

The research was carried out under the climatic conditions of Karaganda in central Kazakhstan, a zone with a sharply continental climate and significant temperature fluctuations, where hot summers and cold winters create a number of difficulties for the operation of renewable sources [15]. The geographical coordinates are 49°48′ N and 73°07′ E, and the field experiments were performed at a test site in the area of the Fedorov Reservoir. Figure 3 shows a map indicating the settlements and the location of the city. The annual number of sunshine hours is about 2300 and the average solar radiation intensity about 1300 kWh/m² per year. The panels were installed in a fixed position without a tracking system and oriented to the south, at a zenith angle of 50° and an azimuth of 180°, the total surface area being 4.8 m². A single lead-acid battery of 200 Ah and 12 V served as the storage system, capable of autonomous operation for 14 hours in summer and 7 hours in winter.

Figure 4 presents a schematic electrical diagram of the HWSPP. In addition to the main equipment previously described in Figure 2, it also shows the measuring and control instruments that were used to obtain experimental data. The sources of electrical energy are a three-phase synchronous generator 1 with a rectifier 2, whose maximum peak power is 700 W and nominal power 600 W, the output voltage being selectable between 12 and 24 V, with 12 V chosen. The energy source also includes four solar panels 3, whose number remained unchanged throughout the experiment. All sources are connected through two 12 V direct-current lines to a charge controller 6. Each line carries a combined digital voltmeter 4 and ammeter 5 in a single housing with an LED display, used for real-time monitoring of the source parameters without data storage.

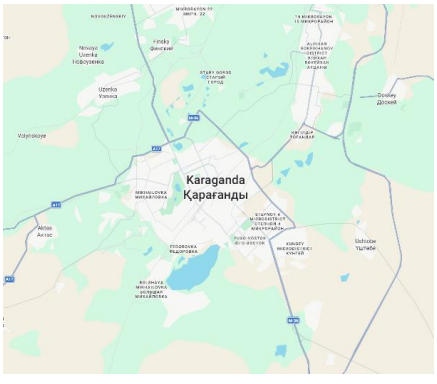


Fig. 3. Map indicating settlements and the location of the city

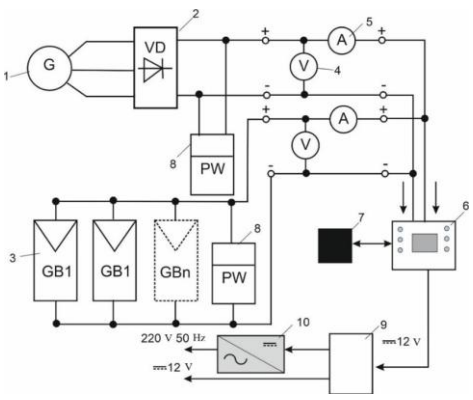


Fig. 4. Schematic electrical diagram of the HWSPP.

Electrical energy from sources 1 and 3 is supplied to the charge controller 6 and stored in the battery 7, from which it is delivered to consumers through a 12 V direct-current line. To record the generated energy, digital ATORCH DC power detectors 8 were used, capable of storing data and transmitting them over the internet to a server; each source had its own detector, so that the energy of the wind turbine and of the panels was measured separately. The energy then passes to a distribution unit 9 dividing it into two 12 V lines, one feeding an inverter 10 for loads with inductive characteristics and the other delivering direct current directly. The measuring instruments used are listed in Table 4.

Table 4. Measuring instruments

Name	Parameters	Resolution	Accuracy	Country of manufacture
Digital combined voltmeter and ammeter	Measurement of current and voltage. DC 0–100 V with a 100 A shunt and a 0.28-inch LED display	0.01 A; 0.01 V	±2%	China
Laser non-contact tachometer Victor DM6234P	Measurement of wind turbine rotational speed in the range of 2.5–99999 rpm	0.1 rpm	±(0.5% + 1)	China
Infrared pyrometer ADA TemPro 650 Hygro A00658	Temperature measurement in the range from –50 to +650 °C	0.1 °C	±1.5%	China

To measure current, voltage and power and to account for the generated electrical energy, a digital ATORCH DT3010 DC power detector made in China was used, with a measurement accuracy of ±1 %, a voltage range of 0 to 300 V DC and a current range of 0 to 100 A at resolutions of 0.05 V and 0.05 A, an energy range of 0 to 10 kWh at a resolution of 0.01 Wh and a temperature range of –10 to 99 °C at a resolution of 1 °C.



a *b*

Fig. 5. ATORCH DT3010 wattmeter: (a) front view; (b) rear view with connection diagram

The appearance of the detector is shown in Figure 5: a monochrome liquid-crystal display and a control button on the front side, and the connection diagram to the electrical network with three terminals on the back of the housing. The seasonal uniformity of generation was evaluated by two dimensionless indicators calculated from the twelve-monthly mean values of daily generation Ei. The first is the coefficient of seasonal non-uniformity

$$k_s = E_{max} / E_{min} , \quad (1)$$

and the second is the coefficient of variation of the monthly series

$$CV = \sigma^E / \bar{E} , \quad (2)$$

where σ^E is the standard deviation of the twelve monthly means and $\bar{E}$ is their arithmetic mean. The reliability of supply was characterised by the seasonal reserve factor

$$k_r = E_{min} / L_v , \quad (3)$$

where L_v is the average daily load in the autumn and winter period.

A configuration was considered acceptable when k_r was not lower than 1.2, which leaves a margin for the consecutive calm and overcast days that monthly means do not resolve.

The extent to which the two resources compensate each other over the year was quantified by the Pearson linear correlation coefficient between the monthly series of photovoltaic and wind generation

$$r_{pv} = \Sigma\,(E_{pv,i} - \bar{E}_{pv})(E_{v,i} - \bar{E}_{v}) \,/\, [\Sigma\,(E_{pv,i} - \bar{E}_{pv})^2 \cdot \Sigma\,(E_{v,i} - \bar{E}_{v})^2]^{1/2}\,, \quad (4)$$

a negative value of which indicates seasonal complementarity of the resources. This indicator is widely used in the joint planning of wind and photovoltaic capacities and permits a direct comparison of the results obtained at the test site with published data for other regions [19].

The saving obtained by supplying the direct-current loads without inversion was determined by comparing the energy withdrawn from the battery in two supply schemes for the same useful load. In the conventional scheme the whole load passes through the inverter and the direct-current appliances are then fed through mains adapters, so that the energy withdrawn per day is

$$W_a s = E_э s \,/\, (\eta_{inv} \cdot \eta_{aэ}) + E_a s \,/\, \eta_{inv} + P_0\,\tau\,, \quad (5)$$

whereas in the scheme adopted in this work the direct-current appliances are fed from the 12 V line through a DC/DC converter and the energy withdrawn is

$$W_э s = E_э s \,/\, (\eta_э s \cdot \eta_l) + E_a s \,/\, \eta_{inv} + P_0\,\tau_{on}\,, \quad (6)$$

where $E_э$s and E_as are the daily energy demands of the direct-current and alternating-current appliances, η_{inv}, $\eta_{aэ}$ and $\eta_э$s are the efficiencies of the inverter, of the mains adapters and of the DC/DC converter, η_l accounts for the ohmic loss in the 12 V line, P_0 is the no-load power of the inverter and τ is the time during which the inverter remains energised.

The loss factor of the line was calculated as $\eta_l = 1 - I^2R/P$ with $R = 2l\rho/S$ the loop resistance of a copper cable of length $l = 10$ m and cross-section $S = 4$ mm². The efficiencies were taken as $\eta_{inv} = 0.78$ at the part load characteristic of this plant, $\eta_{aэ} = 0.85$ and $\eta_э s = 0.92$, and the no-load power of the inverter as 8 W, these values being consistent with the measured data for low-voltage direct-current distribution reported in [20]. The expected generation of the proposed configuration, shown in Figure 9, was obtained by applying the measured monthly wind resource to the power curve of a 1000 W wind generator with a rotor diameter of 3.2 m against 2.5 m for the machine tested, the swept area being 1.64 times larger at the same cut-in speed of 2.5 m/s, and by scaling the measured photovoltaic generation in proportion to the installed capacity. The result exceeds by 8 to 14 % the value given by proportional scaling of the rated power, which is reported below as a conservative bound.

3. Results and Discussion

Figure 6 shows the average values of the electrical energy generated by the solar panels, kWh/day, against the month of the year. The values are averaged over the 30 or 31 days of each month: every day was recorded on the server as a separate value of the energy generated over 24 hours, and the values were summed and divided by the number of days automatically by the server software. Depending on the weather, the daily deviations ranged from 0.1 to 2 kWh/day. The graph in Figure 6 reflects only the energy generated by the four HH-POLY 200 W solar panels. Figure 7 presents, by the same processing method, the average daily generation of the HY–600 wind turbine over the twelve months of continuous operation; some days of each month were nearly windless and others had high generation, but the averaged value was used throughout.

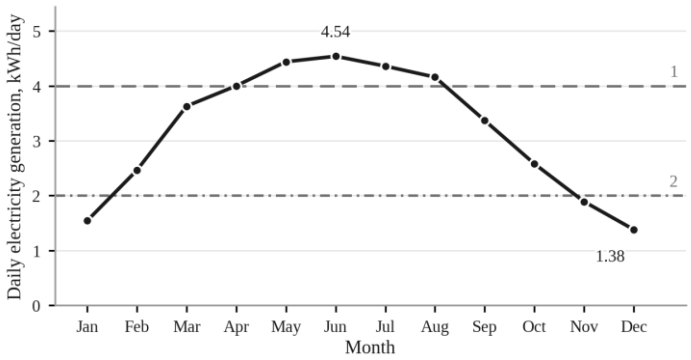


Fig. 6. Graph of the obtained average values of the electrical energy generated by solar panels, kWh/day.
1 – Average electrical load in winter and autumn, kWh/day; 2 – Average electrical load in summer and spring, kWh/day.

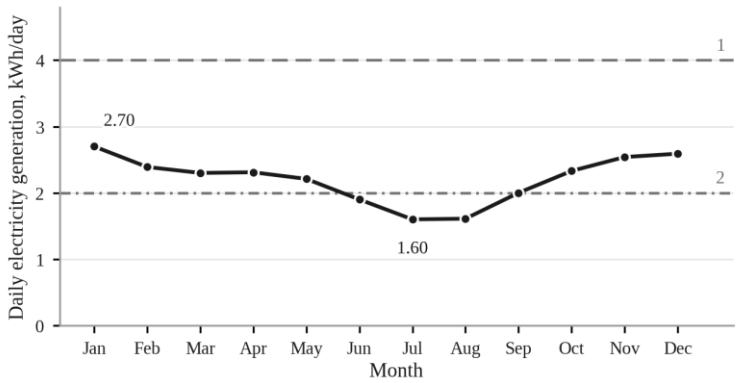


Fig. 7. Graph of the obtained average values of the electrical energy generated by the wind turbine, kWh/day. Average electrical load: 1 – in winter and autumn; 2 – in summer and spring.

Comparison of Figures 6 and 7 shows that the resources are in seasonal opposition: photovoltaic generation peaks at 4.54 kWh/day in June and falls to 1.38 kWh/day in December, whereas wind generation peaks at 2.70 kWh/day in January and falls to 1.60 kWh/day in July. The Pearson coefficient between the two monthly series, from equation 4, is −0.81, which indicates a strong seasonal complementarity at the test site and is more negative than the range from −0.3 to −0.6 usually reported for continental sites of the middle latitudes [19]. The coefficient of variation is 35.2 % for the photovoltaic component and 15.6 % for the wind component, so the wind resource is the more uniform of the two over the year.

Figure 8 shows the total electrical energy generated by the plant over the year by the wind turbine and the solar panels together. The proposed configuration converts solar radiation more efficiently during the summer period, while in the winter season more energy is supplied by the wind turbine. In the summer months the plant operates with a surplus, the generation exceeding the consumer demand by more than 4 kWh/day.

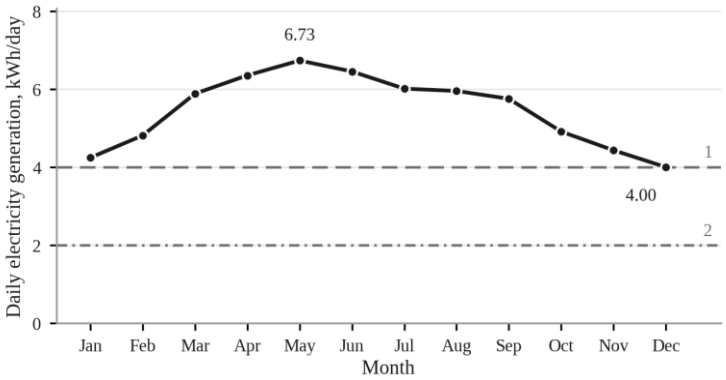


Fig. 8. Graph of the total amount of electrical energy generated by the HWSPP over the year, kWh/day. 1 – Average electrical load in winter and autumn, kWh/day; 2 – Average electrical load in summer and spring, kWh/day.

Integration of the measured monthly means over the year gives 1167.7 kWh for the photovoltaic array and 805.0 kWh for the wind generator, that is 1993.4 kWh for the plant, or 5.46 kWh/day on average. The specific yield of the array is 1460 kWh per kilowatt and the capacity factor of the wind generator is 15.3 %. The photovoltaic share of the annual output is 58.6 %, but it falls to 40.9 % in the three winter months and rises to 70.9 % in the three summer months, which follows directly from the fixed tilt. The coefficient of seasonal non-uniformity from equation 1 is 1.683 and the coefficient of variation from equation 2 is 16.4 %. The lowest monthly value, 4.00 kWh/day in December, coincides with the winter load of 4 kWh/day, so that the reserve factor from equation 3 falls to 1.00: the plant covers the load in the monthly mean but retains no margin for consecutive calm and overcast days and no surplus for restoring the battery.

The excess energy can be used for water heating, for various equipment and electric tools, for repair work with a small welding inverter, or for driving an electric pump to irrigate crops grown close to the source [16]. In the winter months the monthly mean generation falls to the level of the winter load itself, so that the seasonal reserve factor drops to unity; the plant does not enter a deficit in the monthly balance, but any sequence of calm and overcast days immediately leads to an emergency operating mode in which part of the consumers

has to be disconnected, and the battery cannot be brought back to a full state of charge [17]. For central Kazakhstan the most rational solution for remote autonomous consumers of low power is therefore a hybrid plant in which the capacities are matched to the seasonal structure of the resources rather than distributed equally.

The experiment showed that with one 600 W wind turbine and four 200 W solar panels a relatively balanced operation of the plant cannot be achieved. With this configuration the summer load can be raised to 5 or 6 kWh/day, but in December and January there is a risk of an emergency operating mode [18]. After theoretical calculation and analytical forecasting, it is proposed to use a 1000 W wind turbine, or two units of 500 W, together with two 200 W solar panels. Figure 9 presents the results of the numerical modelling of the expected generation. To place the results with respect to published work, the measured indicators were compared with those reported for hybrid installations of comparable and of larger rated power, as shown in Table 5. The capacity factor of 15.3 % obtained at a hub height of 9 m is consistent with the 12 to 18 % reported for small wind machines at continental sites with mean wind speeds of 4 to 6 m/s [16]. The specific photovoltaic yield of 1460 kWh per kilowatt exceeds the values normally quoted for northern Kazakhstan, which is explained by the high proportion of clear days in the cold season and by the low module temperature. The essential difference from published configurations concerns the wind share of the installed capacity: in [13] and [15] the capacities are distributed approximately equally, whereas at a site with a complementarity coefficient of −0.81 the uniformity of generation is governed by a wind share close to 70 %.

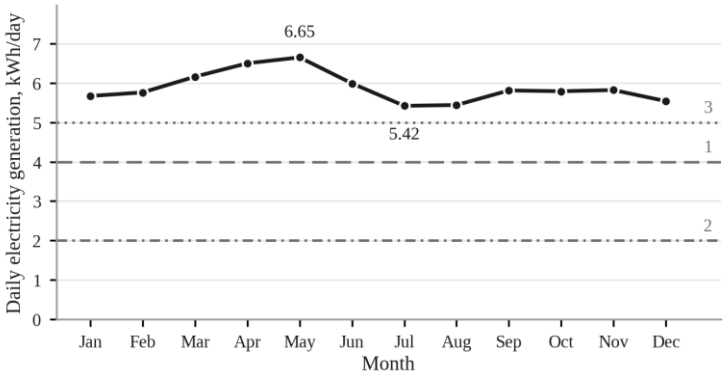


Fig. 9. Results of numerical modeling of the analytical forecast of the expected volume of electrical energy generation. 1 – Average electrical load in winter and autumn, kWh/day; 2 – Average electrical load in summer and spring, kWh/day; 3 – Total load regardless of the season, kWh/day.

Table 5. Comparison of the results obtained with published data on hybrid wind–solar systems

Source	Object and rated power	Wind share of installed capacity, %	Type of data	Key reported indicator
[13]	Hybrid wind–solar complex	≈ 50	Calculation	Equal distribution of capacities recommended
[14]	Wind–solar plant with diesel generators	40–60	Optimisation	Composition governed by the diesel share
[15]	Principles of construction of hybrid plants	≈ 50	Analytical	Equal distribution of capacities recommended
[16]	Review of hybrid wind–solar systems	various	Review	No site-specific sizing criterion
This work, tested	600 W wind + 800 W PV	43	Field measurement, 12 months	CV 16.4 %; December output 4.00 kWh/day; reserve factor 1.00
This work, proposed	1000 W wind + 400 W PV	71	Forecast from the measured series	CV 6.3 %; December output 5.54 kWh/day; reserve factor 1.39

The recommendation to provide a seasonally adjustable tilt was examined quantitatively. For the latitude of 49.8° N the biannual optimum angles are about 65° for the cold season and 35° for the warm one, against the fixed 50° used. Raising the tilt from 50 to 65° in December increases the beam component at solar noon by 7.7 % and the ground view factor from 0.125 to 0.202 at a snow albedo of 0.7, while the sky view factor falls from 0.821 to 0.711; an isotropic-sky calculation at a diffuse fraction of 0.5 gives a net gain of 6.8 % in the plane-of-array irradiation, raising the December output of the array from 1.38 to 1.47 kWh/day, the annual gain of 3 to 4 % agreeing with data for European sites at the same latitude [22]. At plant level the effect is small: since the array supplies only 34.5 % of the December output, the monthly minimum rises from 4.00 to 4.06 kWh/day, by 1.6 %, whereas rebalancing the capacities raises it to 5.54

kWh/day, by 38.5 %. Seasonal adjustment is therefore an inexpensive measure requiring a slotted bracket and two operations per year, but it cannot by itself remove the seasonal imbalance.

The saving obtained by supplying the direct-current loads at 12 V without inversion was evaluated from equations 5 and 6 for the measured load composition, in which appliances able to operate directly on direct current account for about 70 % of the annual consumption. For the same useful load the conventional scheme withdraws 4.415 kWh/day from the battery against 3.276 kWh/day for the scheme adopted here, a saving of 25.8 % of the energy delivered to those appliances and of 18.9 % at plant level; the value of 30 % quoted earlier is an upper bound reached only when the inverter works below 10 % of its rated power and stays energised around the clock. The transition to a low distribution voltage also has an unfavourable side: at a mean current of 9.72 A the ohmic loss in a copper cable of 4 mm² cross-section over a 10 m run reaches 8.27 W, that is 7.1 % of the transmitted power against less than 0.1 % at 220 V, so the admissible length of the line here does not exceed 15 m, beyond which 24 or 48 V becomes preferable [20]. The advantage of direct-current distribution as such, one to two percentage points of overall efficiency, is far smaller, since the saving arises mainly from the elimination of two conversion stages [21].

The technical indicators of the two configurations are collected in Table 6. The uniform year-round load that the tested configuration can carry is limited by its December output to 4 kWh/day, whereas the proposed configuration carries 5 kWh/day while retaining a seasonal reserve factor of 1.39, and its annual generation is 7.7 % higher, 2146 against 1993 kWh, despite the photovoltaic array being halved. The gain therefore comes not from an increase in the installed capacity but from matching the capacity ratio to the seasonal structure of the resources at the site.

The choice of the storage unit was reconsidered in the light of the operating conditions. The starter lead-acid battery is not intended for cyclic duty: under regular discharge to 50 % of capacity and at the winter temperatures inside the container, corrosion of the positive grid, sulphation and stratification of the electrolyte develop rapidly, and the service life predicted by weighted ampere-hour throughput models falls to two or three years against five to twelve for stationary OPzS cells [23]. Three options are compared in Table 7. Lithium iron phosphate cells give a usable depth of discharge of 80 % against 50 % and a cycle life about ten times longer, but must not be charged below 0 °C without an integrated heater, which in central Kazakhstan requires a management system with self-heating. Valve-regulated gel cells tolerate cyclic duty and temperatures down to −30 °C far better than starter batteries, need no maintenance and extend the replacement interval to five or six years; for an unheated container the gel battery is therefore recommended as the base option, and lithium iron phosphate with a heated management system where maintenance visits are difficult.

Table 6. Technical indicators of the configurations examined

Indicator	Unit	Tested 600 W + 800 W	Proposed 1000 W + 400 W
Annual generation	kWh	1993	2146
Minimum monthly mean generation	kWh/day	4.00	5.42
Coefficient of seasonal non-uniformity k_s	–	1.683	1.227
Coefficient of variation of monthly generation	%	16.4	6.3
Seasonal reserve factor in December k_r	–	1.00	1.39
Uniform year-round load supplied reliably	kWh/day	4.0	5.0

Table 7. Comparison of storage options for the proposed configuration

Indicator	Starter lead-acid	Valve-regulated gel	Lithium iron phosphate
Nominal capacity at 12 V, Ah	200	200	150
Usable depth of discharge, %	50	50	80
Usable energy, kWh	1.20	1.20	1.54
Cycle life at the stated depth of discharge	300–400	600–800	3000–4000
Minimum charging temperature, °C	−20	−30	0 without an integrated heater
Expected replacement interval, years	2–3	5–6	10

The measurements cover a single calendar year, which is the principal limitation of this work. The representativeness of 2025 was assessed against the long-term climatic characteristics of the site: the annual sunshine duration of about 2300 hours and the mean wind speed of 4 to 6 m/s at a height of 30 m correspond to the long-term normals for central Kazakhstan [12], and the measured capacity factor and specific yield lie within the expected ranges. With an interannual variability of wind energy production whose normalised interquartile range has a median of about 3.4 % and reaches 13.5 % at the least favourable sites [24], and a variability of the annual solar irradiation of 4 to 6 %, the December output lies between 3.5 and 4.5 kWh/day for the tested configuration and between 4.8 and 6.3 kWh/day for the proposed one, so the conclusion on the winter reserve holds over the whole interval. The conservative estimate by proportional scaling gives 4.76 kWh/day and a coefficient of variation of 6.7 %. Monitoring will continue for at least three further years with hourly recording of the load profile.

4. Conclusions

The scientific novelty of the study lies in the following:

- a circuit solution has been developed and tested in the field in which the load of an autonomous plant is separated between an alternating-current circuit and a direct-current circuit, the appliances able to operate on direct current being fed from the 12 V bus without inversion, and the annual dependences of the electrical parameters of the plant operating under this solution have been obtained from continuous measurements and are presented in Figures 6 to 8; the saving has been quantified as 25.8 % of the energy delivered to the direct-current appliances and 18.9 % at plant level, while the ohmic loss of the 12 V line, 7.1 % over a 10 m run, bounds the admissible length of that line at 15 m and defines the field of application of the solution;

- for the first time for the conditions of central Kazakhstan, the Karaganda region, the seasonal complementarity of the wind and solar resources has been quantified from a continuous year of field measurements, the Pearson correlation coefficient between the monthly photovoltaic and wind outputs being −0.81, which is markedly more negative than the values from −0.3 to −0.6 usually reported for continental sites of the middle latitudes;

- a reproducible criterion for selecting the ratio of the installed wind and photovoltaic capacities has been formulated, in which the ratio is chosen so as to minimise the coefficient of variation of the monthly generation subject to a seasonal reserve factor of not less than 1.2; applied to the measured series, this criterion gives a wind share of about 70 % of the installed capacity, whereas the approximately equal distribution of capacities recommended in earlier work gives a coefficient of variation 2.6 times higher, 16.4 % against 6.3 %;

- the effect of a seasonal adjustment of the tilt of the photovoltaic panels has been evaluated quantitatively against the rebalancing of the installed capacities, and it has been shown that for a plant with this capacity ratio the adjustment raises the December output by only 1.6 % against 38.5 % obtained by rebalancing, which establishes the order in which the two measures should be applied.

The practical significance of the work lies in the fact that the proposed configuration, a 1000 W wind turbine or two 500 W units together with two 200 W solar panels, allows:

- raising the minimum monthly mean generation in December from 4.00 to 5.54 kWh/day and the seasonal reserve factor from 1.00 to 1.39, and reducing the coefficient of variation of the monthly generation from 16.4 to 6.3 %;

- raising the uniform year-round load that can be supplied reliably from 4 to 5 kWh/day;

- halving the number of photovoltaic modules and the area of the mounting frame, which lowers the snow and wind load on the supporting structure and the labour of clearing snow from the array, while the generation in the winter months nevertheless increases.

Thus, the results of the study confirm the feasibility of widespread application of hybrid wind–solar systems of ultra-small and small capacity for decentralized power supply in rural and remote areas of central and northern Kazakhstan. Optimization of the ratio between wind and solar generation, taking into account regional climatic characteristics, can significantly improve the uniformity of generation and the reliability of supply of such systems, contributing to the development of agriculture, small business, and the development of new lands.

The principal limitation is the duration of the observations, one calendar year; its representativeness has been verified against the long-term climatic normals of the site and the published interannual variability of the resources, and the conclusions hold over the resulting interval. Monitoring is to be continued for at least three further years with hourly recording of the load profile. For an unheated container a valve-regulated gel battery is recommended instead of the starter battery used, since it extends the replacement interval from two or three to five or six years.

Conflict of interest statement

The authors declare that they have no conflict of interest in relation to this research, whether financial, personal, authorship or otherwise, that could affect the research and its results presented in this paper.

CRediT author statement

Kuatova A.S.: research, writing — original draft; **Alkina A.D.**: conceptualization, writing — review and editing; **Mekhtiyev A.D.**: research, writing — review and editing; **Bainiyazov B.A.**: research, formal analysis; **Yurchenko A.V.**: visualization, writing — review and editing. The final manuscript was read and approved by all authors.

Statement on the use of Artificial Intelligence.
The authors declare that no artificial intelligence tools were used to generate scientific content, results, or conclusions of this article

Data Availability Statement
The data that support the findings of this article are openly available.

References

1 Karatayev, M., Hall, S., Kalyuzhnova, Y., & Clarke, M.L. (2016). Renewable energy technology uptake in Kazakhstan: Policy drivers and barriers in a transitional economy. *Renewable and Sustainable Energy Reviews*, 66, 120–136. https://doi.org/10.1016/j.rser.2016.07.057

2 KAZENERGY. (2019). *The National Energy Report 2019*. Astana, Kazakhstan. Available at: https://www.kazenergy.com/upload/document/energy-report/NationalReport19_en.pdf

3 Xenarios, S., Darke, W., & Bekturganov, N. (2024). Clean energy challenges and innovation opportunities in Kazakhstan. *Environmental Research Communications*, 6(8), 085005. https://doi.org/10.1088/2515-7620/ad87b5

4 Karatayev, M., & Clarke, M. L. (2016). A review of current energy systems and green energy potential in Kazakhstan. *Renewable and Sustainable Energy Reviews*, 55, 491–504. https://doi.org/10.1016/j.rser.2015.10.078

5 Zhakiyev, N., Burkhanova, D., Nurkanat, A., Zhussipkaliyeva, S., Sospanova, A., & Khamzina, A. (2025). Green energy in grey areas: The financial and policy challenges of Kazakhstan's energy transition. *Energy Research & Social Science*, 124, 104046. https://doi.org/10.1016/j.erss.2025.104046

6 Temirgaliyeva, N., & Junussova, M. (2020). Renewable Electricity Production and Sustainability of the National and Regional Power Systems of Kazakhstan. *International Journal of Energy Economics and Policy*, 10(3), 58–67. https://doi.org/10.32479/ijeep.9150

7 Koshim, A., Karaca, F., & Clarke, M. L. (2015). Current Energy Resources in Kazakhstan and the Future Potential of Renewables: *A Review. Energy Procedia*, 59, 97–104. https://doi.org/10.1016/j.egypro.2014.10.354

8 Akbulut, A., Seker, O., Ozcan, S., & Beycioğlu, G. (2025). Energy, exergy and enviro-economic analysis of a hybrid energy plant utilizing biogas and solar technologies in the Almaty region, Republic of Kazakhstan. *Energy Strategy Reviews*, 11, 101118. https://doi.org/10.1016/j.cscee.2025.101118

9 Darke, W., Xenarios, S., & Zhakiyev, N. (2025). From fossil fuels to renewables: Analysing efficacy and impact of auctions to attract investment in resource-rich Kazakhstan. *Energy Strategy Reviews*, 53, 101470. https://doi.org/10.1016/j.esr.2025.101470

10 Zereshkian, S., & Mansoury, D. (2023). Solar-wind hybrid energy system to supply electricity for offshore oil and gas platforms in the Caspian Sea: A case study. *The Journal of Engineering*, 2023(6), e12239. https://doi.org/10.1049/tje2.12239

11 Xu, J., Assenova, A., & Erokhin, V. (2018). Renewable Energy and Sustainable Development in a Resource-Abundant Country: Challenges of Wind Power Generation in Kazakhstan. *Sustainability*, 10(9), 3315. https://doi.org/10.3390/su10093315

12 Karatayev, M., & Hall, S. (2020). Establishing and comparing energy security trends in resource-rich exporting nations (Russia and the Caspian Sea region). *Resources Policy*, 68, 101746. https://doi.org/10.1016/j.resourpol.2020.101746

13 Aliev, A. K., Dyusenov, K. M., Sednin, A. V., & Baimukhamedov, M. F. (2024). Development of a Hybrid Wind-Solar Energy Complex. *Proceedings of the University*, 1(94), 436–443. https://doi.org/10.52209/1609-1825_2024_1_436 [in Russian]

14 Lavrik, A. Yu., Zhukovsky, Yu. L., Lavrik, A., & Buldysko, A. D. (2020). Features of the optimal composition of a wind-solar power plant with diesel generators. *Power Engineering: Research, Equipment, Technology,* 22(1), 10–17. https://doi.org/10.30724/1998-9903-2020-22-1-10-17 [in Russian]

15 Dzendzerskii, V. A., Zhitnik, N. E., Plaksin, S. V., Pogorelaya, L. M., & Burak, I. I. (2007). Principles of Designing Hybrid Wind-Solar Power Systems. *Elektrotekhnika ta elektroenergetika,* (1), 67-72. [in Russian]

16 Roy, P., He, J., Zhao, T., & Singh, Y. V. (2022). Recent Advances of Wind-Solar Hybrid Renewable Energy Systems for Power Generation: A Review. *IEEE Open Journal of the Industrial Electronics Society*, 3, 81–104. https://doi.org/10.1109/OJIES.2022.3144093

17 Boute, A. (2020). Regulatory stability and renewable energy investment: The case of Kazakhstan. *Renewable and Sustainable Energy Reviews,* 121, 1009673. https://doi.org/10.1016/j.rser.2019.109673

18 Kumar, R. (2025). Renewable Energy Future: Can Large-Scale Solar and Wind Energy Projects in Kazakhstan and Uzbekistan Reduce Dependence on Fossil Fuels and Alter the Region's Energy Geography? *International Journal of Research Studies on Environment, Earth, and Allied Sciences*, 2(4), 14–17. https://doi.org/10.5281/zenodo.17590177

19 Han, S., Zhang, L., Liu, Y., Zhang, H., Yan, J., Li, L., Lei, X., & Wang, X. (2019). Quantitative evaluation method for the complementarity of wind–solar–hydro power and optimization of wind–solar ratio. *Applied Energy,* 236, 973–984. https://doi.org/10.1016/j.apenergy.2018.12.059

20 Khan, H. A., & Siraj, K. (2020). DC distribution for residential power networks – A framework to analyze the impact of voltage levels on energy efficiency. *Energy Reports*, 6, 944–951. https://doi.org/10.1016/j.egyr.2020.04.018

21 Haroon, A., Gelani, H. E., Tahir, H., & Manzoor, H. U. (2025). DC vs. AC distribution: Revealing the efficiency advantage of DC in today's energy landscape. *PLOS ONE*, 20(5), e0318444. https://doi.org/10.1371/journal.pone.0318444

22 Machidon, D., & Istrate, M. (2023). Tilt angle adjustment for incident solar energy increase: A case study for Europe. *Sustainability,* 15(8), 7015. https://doi.org/10.3390/su15087015

23 Dufo-López, R., Cortés-Arcos, T., Artal-Sevil, J. S., & Bernal-Agustín, J. L. (2021). Comparison of lead-acid and Li-ion batteries lifetime prediction models in stand-alone photovoltaic systems. *Applied Sciences*, 11(3), 1099. https://doi.org/10.3390/app11031099

24 Pryor, S. C., Shepherd, T. J., & Barthelmie, R. J. (2018). Interannual variability of wind climates and wind turbine annual energy production. *Wind Energy Science*, 3(2), 651–665. https://doi.org/10.5194/wes-3-651-2018

AUTHORS' INFORMATION

Alkina, Aliya – Candidate of Technical Sciences, Senior Lecturer, Department of Energy Systems, Karaganda Technical University named after Abylkas Saginov, Karaganda, Kazakhstan; Scopus Author ID: 57160184600; https://orcid.org/0000-0003-4879-0593; alika1308@mail.ru

Kuatova, Anar S. – Doctoral student, Department of Power Supply, S. Seifullin Kazakh Agrotechnical Research University, Astana, Kazakhstan; Scopus Author ID: 58613717500; https://orcid.org/0000-0001-8972-1346; anarkuatova2019@gmail.com

Mekhtiyev, Ali D. – Candidate of Technical Sciences, Professor, Member of the Board, Vice-Rector for Research, Karaganda Technical University named after Abylkas Saginov, Karaganda, Kazakhstan; Scopus Author ID: 57219935782; https://orcid.org/0000-0002-2633-3976; barton.kz@mail.ru

Yurchenko, Aleksey V. – Doctor of Technical Sciences, Professor, Tomsk Polytechnic University, Tomsk, Russia; Scopus Author ID: 55308619600; https://orcid.org/0000-0002-7854-5495; niipp@inbox.ru

Bainiyazov, Bakhtybek A. – Candidate of Technical Sciences, Head of the Educational Programs Group in Electric Power Engineering, S. Seifullin Kazakh Agrotechnical Research University, Astana, Kazakhstan; Scopus Author ID: 57194235483; https://orcid.org/0000-0002-1103-2329; bainiyazov69@mail.ru

EURASIAN PHYSICAL TECHNICAL JOURNAL

2026, Volume 23, No. 3 (57)

https://doi.org/10.31489/2026N3/86-93

Received: 27/02/2026 Revised: 15/08/2026 Accepted: 28/09/2026 Published online: 30/09/2026

Original Research Article

Open Access under the CC BY -NC-ND 4.0 license

UDC 53.097; 539.893

DEVELOPMENT OF A BIOREACTOR HEATING SYSTEM USING A GROUND-SOURCE HEAT PUMP

Sakipova S.E., Smagulov Zh.K.*, Bekturganov Zh.S., Ismailov Zh.T., Kartbayeva G.T., Duisenbayeva M.S., Ospanova D.A.

Buketov Karaganda National Research University, Karaganda, Kazakhstan

*Corresponding author: smagul@mail.ru

Abstract: *The article presents an evaluation of the performance of a ground-source heat pump system designed to maintain a specific temperature regime within a biogas bioreactor. The novelty and distinctive feature of the installation lie in its use of renewable thermal energy sources. For the first time, a system with an external ground-source heat pump circuit consisting of four boreholes with copper U-shaped tubes through which the coolant circulates has been developed. The system's design, operating principle, and technical specifications are described. An assessment of the thermal energy output, accounting for the efficiency characteristic of the external circuit of a ground-source heat pump is shown.*

Keywords: bioreactor, borehole, ground-source heat pump, heat pump, thermal efficiency.

1. Introduction

In the context of global climate change and depletion of natural resources, the transition to sustainable energy sources such as biogas is becoming a necessary condition for ensuring energy security and environmental sustainability. Indeed, a significant portion of industrial and household organic waste can serve as feedstock for the production of biogas and biomethane, paving the way for one of the most promising and vital trends in the evolution of the modern energy sector [1-9].

Biomethane and biogas, produced through the anaerobic digestion of organic waste (manure, sewage sludge, food waste, agro-industrial by-products, biological residues, etc.), possess significant energy value, as they can be used as fuel or for the generation of electricity and heat. The environmentally safe processing of agricultural waste to produce biogas makes it possible to minimize carbon emissions, reduce dependence on fossil fuels, and cut operating costs [10]. Producing biogas from waste as an effective solution for mitigating negative environmental impacts represents a significant step toward adopting renewable energy sources and establishing a sustainable global energy system [2, 7]. Along with agricultural waste, kitchen waste from catering establishments also serves as a promising substrate for decentralized biogas production, facilitating the implementation of circular economy principles and providing a cost-effective solution to energy supply and waste management issues on university campuses [6]. It is essential to adopt advanced anaerobic digestion technologies that optimize traditional digestion systems at wastewater treatment plants and waste processing facilities. These innovations—such as thermal hydrolysis and staged digestion—encompass pretreatment methods and system modifications that boost biogas yields and enhance bio-waste processing. Hundreds of biomethane production facilities have been established and are successfully operating in many countries,

integrating it into their national energy systems using advanced digestion technologies to achieve energy neutrality – or even positive energy. A solar ground-source heat pump system featuring a vertical borehole heat exchanger was developed and experimentally tested under the climatic conditions of Almaty and Astana [10, 11]. Modern 3D numerical models of heat and mass transfer and fluid dynamics were created and verified using experimental data, enabling a detailed analysis of the system's performance. Experimental studies demonstrated that the system achieves a coefficient of performance in the range of 2.11–2.76, confirming its energy efficiency.

Due to its vast land resources and favorable climatic conditions, Kazakhstan possesses significant potential for the development of agriculture and livestock farming. Biomass generated during grain harvesting—specifically large volumes of straw—can be viewed as a potential substrate for biogas production. Livestock waste complements these plant-based residues. As the global community strives for a cleaner and more sustainable energy future, the development of sustainable energy innovations must help address global challenges related to the energy transition and the achievement of carbon neutrality. From a practical standpoint, the primary objectives for most farms acquiring a biogas plant are energy savings and waste management. Depending on the characteristics of the biomass being processed, different operating modes are employed to ensure effective anaerobic digestion: mesophilic (temperature range of 35–38°C) or thermophilic (50–55°C) [4, 5]. The biogas production process relies on the anaerobic digestion of organic matter within a sealed vessel (bioreactor) in the absence of oxygen; microorganisms break down the organic material, releasing methane and carbon dioxide [8, 10-13]. The efficiency of the biogas production process depends directly on maintaining a stable temperature within the bioreactor. Clearly, the climatic conditions of Central Kazakhstan necessitate continuous heating of the bioreactor.

Practice shows that the efficiency of the biomass fermentation process and biogas production directly depends on the temperature regime inside the reactor [5, 8, 14]. There are indicated the need to maintain a biomass heating regime within the bioreactor that ensures the efficient extraction of valuable components. For mesophilic processes, the optimal fermentation temperature should be maintained in the 42–48°C range, requiring the bioreactor's thermal regime to be consistently upheld regardless of seasonal ambient temperature fluctuations throughout the year. The biomass inside the bioreactor chamber must be mixed regularly [12].

As shown in an effective solution for maintaining the thermal regime of a bioreactor is the use of a so-called “water jacket” (thermal jacket), consisting of parallel pipes placed inside the lower part of the bioreactor body together with a special bubbling device. A heated fluid circulates through the jacket's pipes within the vessel, maintaining the temperature within the range required for active biomass fermentation. [15] presents experimental results in which the water jacket was heated by burning coal-water slurry in a specially designed unit featuring a radially rotating nozzle. However, despite the efficiency gains achieved by enriching coal-water fuel through electrohydraulic processing, its use as a heat source for biomass remains relatively costly in terms of practical implementation.

Therefore, it is proposed to use more accessible renewable thermal energy sources—specifically, a ground-source heat pump combined with a solar panel system. The GSHP utilizes heat from the ground and is supplemented, as needed, by electrical units powered by the solar panels.

The proposed overall concept for the bioreactor heating system comprises three main components:

1) A ground-source heat pump (GSHP) that extracts heat from deep soil layers;
2) An electricity generation system using solar photovoltaic panels;
3) A controlled heating system designed to distribute thermal energy throughout the bioreactor volume to ensure uniform heating of the biomass.

At this stage, the implementation of a ground-source heat pump is being considered, along with the determination of the thermal capacity required to maintain the bioreactor's thermal regime, taking into account the specified volume of biomass to be processed.

2. Methodology of experimental research

The object of the study is the thermal control system for a cylindrical bioreactor designed to produce biogas through the processing of organic agricultural waste. The design layout and operating principle of the bioreactor are described in detail in [16]. The technical result of the solution is improved energy efficiency through connection to renewable energy sources; enhanced quality of biogas and fertilizers due to uniform mixing and temperature control; and reduced operating costs combined with a simplified design. The stated technical result is achieved by a proposed bioreactor for processing organic waste, comprising a cylindrical

body, pipes for loading, unloading, and draining, a sparging channel, heating elements, a pressure gauge, a thermometer, and a mechanical stirrer connected to a reduction gear.

The heating elements are positioned in the lower part of the bioreactor along its perimeter, the sparging channel is also located in the lower part of the body, and the bioreactor's power supply system is connected to a renewable electricity source.

2.1 Design and operating principle of a ground source heat pump

The ground-source heat pump system comprises three circuits: an external circuit located in the ground that collects thermal energy; a second circuit consisting of the heat pump itself, where the heat-transfer fluid enters the evaporator and its temperature is raised to the required level; and a third circuit that directly serves the bioreactor heating system. Let us consider the external circuit of the bioreactor's thermal control system, which utilizes a ground-source heat pump (GSHP). The GSHP operates on a principal inverse to that of a standard refrigerator: it extracts low-grade heat from the environment (soil, water, or air), raises its temperature, and transfers it to the heating system. In this instance, the GSHP utilizes heat from the ground at a depth where the temperature is far more stable than at the surface. At depths of approximately 20 meters or more, the soil does not freeze, even when surface temperatures drop to between –35°C and –40°C. The Earth's subsurface layer acts as a thermal reservoir with virtually unlimited capacity. This phenomenon is successfully employed in numerous technologies for both residential heating and the support of various industrial processes.

The GSHP operates by transferring low-temperature heat from the deep soil (a stable heat source) to the end-user via a closed-loop system utilizing a refrigerant and a compressor [16]. The pump extracts low-grade heat from the ground through a heat-transfer fluid circuit (using antifreeze), evaporates the refrigerant, compresses it to raise its temperature, and transfers the heat to the heating system; the cooled refrigerant then returns to the evaporator. To implement the GSHP, preparatory work was carried out at the experimental site, resulting in the drilling of four boreholes, each 21 meters deep and spaced 5 meters apart (Fig. 1).



a) b)

Fig.1. Ground-source heat pump experimental site:
a) general view of borehole drilling; b) blue markers indicate boreholes along the trench.

U-shaped copper pipes with a diameter of 32 mm are installed in the drilled boreholes; each is encased in an outer plastic casing pipe with a diameter of 150 mm (Fig. 2). The U-shaped copper pipes are completely filled with heat-transfer fluid, leaving no voids. At the top, the vertically installed U-shaped pipes are connected in series. In the lower section of the borehole, the space between the vertical pipes inside the plastic casing is filled with groundwater from a depth of 4 m to 20 m below the surface — meaning the so-called groundwater zone spans 16 m. The outer pipe is hermetically sealed at the top. The upper space inside the plastic casing between the copper pipes is filled with air; thus, the air zone extends from 0 to 4 m below the surface.

A powerful pump circulates the heat transfer fluid (an ethylene glycol solution/antifreeze) under pressure through all four boreholes: it flows first into the outermost copper U-shaped pipe of the first borehole, then passes under pressure from the top into the adjacent second borehole, and so on. Upon exiting the fourth borehole, the heated fluid passes through a heat exchanger assisted by a compressor into a secondary circuit, where it transfers heat to a "water jacket" system to warm the organic mass within the bioreactor. The spent, cooled fluid is then pumped back into the geothermal boreholes. No additional cooling equipment is required to return the fluid to the primary geothermal circuit in the ground and prepare it to absorb heat again; this occurs naturally due to the physics of the refrigeration cycle and the inherent properties of the soil. Thus, the heat transfer fluid continuously circulates counter-clockwise through the geothermal piping.

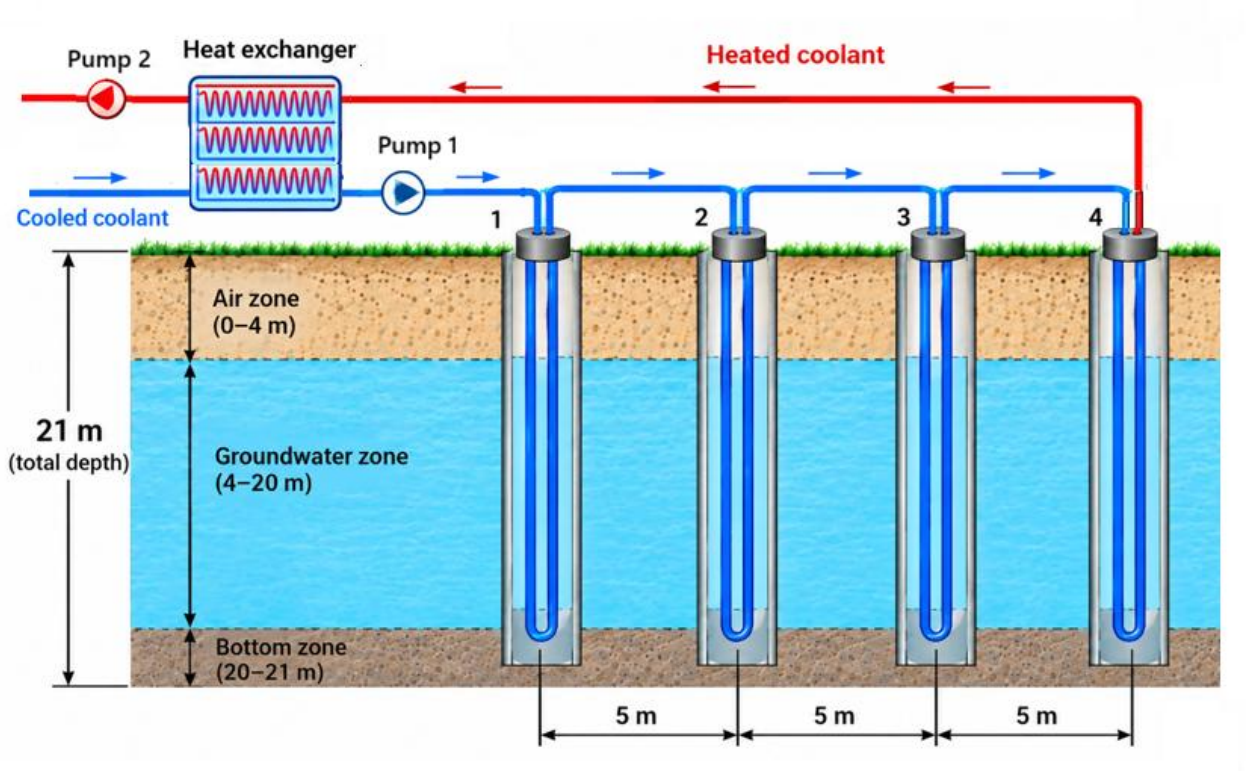


Fig.2. Scheme of a ground-source heat pump system consisting of four boreholes.

Preliminary tests have shown that the heat transfer fluid (antifreeze) can heat up to 60°C or higher during compression. Further temperature increases are undesirable, as the fluid does not have sufficient time to return to the groundwater temperature after cooling. To prevent further heating and accelerate the recovery time, it is necessary to install an automatic control system to adjust the pump pressure, thereby regulating the flow rate of the heat transfer fluid through the circuit.

3. Estimation of the thermal output of a ground source heat pump

Let us determine the amount of heat required to heat a given quantity of biomass. The bioreactor is a cylindrical vessel with a length of 2 m and a diameter of 1.44 m. The steel wall thickness is 4 mm [15, 16]. In practice, the bioreactor vessel is filled to approximately two-thirds of its volume with an organic mixture of cattle manure and water.

The volume of the biomass to be processed, accounting for the wall thickness of the cylindrical bioreactor vessel, is

$V_w = 3{,}14 \times 0{,}68^2 \times 1{,}92 \times 2/3 = 1{,}86\ m^3$

The amount of heat required to heat the given quantity of biomass is determined using the standard formula:

$Q = Vw \times \rho w \times c \times \Delta t = 1.86 \times 10^3 \times 4200 \times 30 \approx 23.436 \times 10^9\ J = 6{,}510\ kWh$

where ρ_w is the density of the heat carrier and c is the specific heat capacity of water is 4,200 J/(kg·°C).

Thus, the objective is to maintain nearly 2 tons of biomass within a specified temperature range. The target heating temperature for the bioreactor's "water jacket" is +42°C, even if the ambient temperature drops to –30°C. It is common practice to use a non-freezing heat transfer fluid—ethylene glycol (ethanediol, chemical formula $C_2H_6O_2$)—in sub-zero temperatures. This is the simplest dihydric alcohol; it appears as a clear, odorless liquid with an oily consistency and a sweet taste. While the substance is highly miscible with water, it is highly toxic to humans and animals and is classified as a moderately hazardous substance (Hazard Class 3). Its key property is that it significantly lowers the freezing point of aqueous mixtures, preventing the fluid from freezing in cold conditions. The proposed technology leverages the stable temperature of groundwater (+3 to +8°C). Therefore, it is crucial to accurately calculate the parameters of the ground-loop heat exchanger's primary circuit to prevent the borehole from freezing. To determine the limiting pressure and temperature values, the thermal capacity of the ground heat exchanger based on fundamental heat balance principles, accounting for heat losses will be calculate.

In a ground-source heat pump system, the cooling of the heat transfer fluid occurs automatically as part of the system's operation. The cooling process within the expansion valve works as follows: after the fluid in the internal circuit has transferred its heat to the storage heat exchanger (at +42°C) and condensed, it passes through a thermostatic expansion valve (TXV) or throttle. At this point, the fluid pressure drops sharply, causing its temperature to plummet instantly to below-freezing levels (e.g., -2°C to -5°C). Next, thermal regeneration takes place in the ground: the "super-cooled" fluid (at 0°C) is circulated back underground to a depth of 20 meters. Since the temperature of the surrounding groundwater remains stable at +3°C or +8°C, the earth acts as a constant, reliable heat source. As the fluid flows through the underground piping, it absorbs heat from the earth, warming back up to its initial +3°C to +8°C range before returning to the pump, thereby completing the cycle.

The length of the circuit - specifically, the length of the pipes carrying the heat transfer fluid—must strictly correspond to the required heat extraction rate. In this instance, the ground-source heat pump (GSHP) circuit consists of copper U-tubes with a diameter of 32 mm, arranged in series across four boreholes 20 meters deep and filled with the heat transfer fluid (see Fig. 2).

Heat transfer per meter of pipe depends on numerous factors, such as soil type, installation depth, and the thermal conductivity of the soil and groundwater. The designed GSHP system utilizes geothermal heat from a depth of 20 meters, where the temperature is more stable than at the surface. Calculating the parameters of the GSHP primary circuit requires determining the ethylene glycol flow rate and the thermal power output needed to supply sufficient heat to warm the specified volume of biomass.

An ethylene glycol solution with a freezing point of -13°C is used as the heat transfer fluid in the primary circuit. The specific heat capacity of an aqueous ethylene glycol solution depends on its concentration and temperature, typically ranging from 3.1 to 4.1 kJ/(kg·°C). Pure water has the highest heat capacity (4.2 kJ/(kg·°C)), whereas pure ethylene glycol is approximately 2.4 kJ/(kg·°C).

For the calculation, the solution properties at 0°C are used: density is 1050 kg/m³ (1.05 g/cm³) and heat capacity is 3.94 kJ/(kg·K). When using an ethylene glycol solution, the pressure loss within the pipe is 1.5 times higher than with water. To calculate the parameters of the heat pump unit's primary circuit, it is necessary to determine the ethylene glycol flow rate.

The temperature difference is assumed to be: $\Delta T = 30$ °C. The loop length of each U-shaped copper pipe is 40 m, the distance between the pipes is 5 m, hence the total length of the copper pipeline with coolant is

L = 40m*4+15 = 175m;

Volume of pumped coolant: $V_t = 3{,}14 \times 0{,}16^2 \times 175 = 14{,}07$ m^3

When compressed, the coolant heats up; the amount of heat it transfers per unit time is equal to:

$$Qt = V_t \times \rho \times c_t \times \Delta T = 14{,}07\ \text{m}^3 \times 1050\ \text{kg/m}^3 \times 3{,}94\ \text{kJ/(kg·°C)} \times (30°\text{C}) \approx 1745.81\ \text{kJ} \approx 0.489\ \text{kWh}$$

Depending on the soil type and condition (dry sand, clay, or water-saturated soil), a U-shaped geothermal probe extracts an average of 30 to 50 W of thermal energy per linear meter. The total thermal power extracted from the ground for the geothermal heat pump will be 175 m × 40 W/m ≈ 7 kW (low-potential heat). To determine the volume of a 50% ethylene glycol solution that can be heated, we compare the thermal power of the heat pump with the flow rate of the coolant.

4. Results and discussion

For a circuit thermal output of 7 kW, the heat carrier flow rate must be very low is only about 160 liters per hour (0.044 L/s). The fluid velocity in a 32 mm pipe would then be approximately 0.07 m/s (this speed corresponds to laminar flow, which impairs heat exchange; therefore, it is more efficient to use a high-flow circulation pump while heating the system cyclically). The total length is 175 m. Assuming a heat yield q of approximately 40–50 W per linear meter of the borehole, the external circuit circulation pump speed must be adjusted so that the temperature difference (delta) between the outgoing and returning heat carrier is about 3°C–5°C. To set the circulation pump speed to achieve a temperature difference (ΔT) within the 3°C–5°C range, the required volumetric flow rate (V) of the coolant is calculated. Clearly, maintaining the required temperature involves costs associated with compensating for heat losses through the walls and via exhaust gases, as well as the energy required to heat the contents, etc. Heat losses through the walls and ventilation losses must be taken into account; approximately 30% should be added to the calculated value. Since there is a closed-loop ground-source heat pump (GSHP) circuit consisting of copper U-tubes filled with heat transfer fluid, the calculation is based on the thermal power that this circuit can consistently extract from the ground.

1) *Calculation of the circuit's thermal power*. Given that the total length of piping in the boreholes is 175 meters, and assuming a heat extraction rate of (40–50) W per linear meter, the total thermal power (Q) extracted from the ground by the external circuit is:

Minimum: Q1 = 175 m × 40 W/m = 7,000 W (7.0 kW)

Maximum: Q2 = 175 m × 50 W/m = 8,750 W (8.75 kW)

2) Calculation of required flow rate. For a propylene glycol-based heat transfer fluid (average specific heat capacity Cp≈3.8kJ/(kg·°C) and density ρ =1030 kg/m^3, the required flow rate is calculated using the formula:

$$V = \frac{Q}{C_p \cdot \rho \cdot \Delta T}$$

Depending on the required temperature difference for each borehole, the circulation pump must provide the following flow rates:

Target temperature difference, (ΔT_g)	With specific heat dissipation q = 40 W/m (7.0 kW)	With specific heat dissipation q = 50 W/m (8.75 kW)
at $\Delta T_g = \mathbf{3}\,^\circ\mathbf{C}$ (max flow)	~35,8 liters per minute	~74,52 liters per minute
at $\Delta T_g = 5\,^\circ\mathbf{C}$ (min flow)	21,42 liters per minute	~44, 70 liters per minute

Calculations show that the circulation pump must circulate the heat transfer fluid at a rate ranging from 21.42 to 44.7 liters per minute. In the experiments, flow meters were used to regulate pump operation within the GSHP system. Flow regulators were installed on the ground-loop distribution manifold, where the pipelines from all four boreholes converge. Since the boreholes are connected to the manifold in series, the flow meters had to be adjusted to ensure an equal volume of heat transfer fluid flowed through each of the four boreholes (approximately 5.3–11.2 l/min per borehole). Additionally, the strength limitations of the GSHP system's copper piping had to be taken into account. Copper pipes with a 32 mm diameter (commonly used in heating and air conditioning systems) have the following characteristics: operating pressure typically does not exceed 2.5–4.0 MPa (25–40 bar), whereas the burst pressure (maximum) ranges from approximately 15 to 30 MPa (150–300 bar), depending on wall thickness (1–1.5 mm) and copper hardness.

It is also necessary to consider the system's hydraulics—specifically, pressure losses. This is because, at a temperature of -8°C, a 50% ethylene glycol solution becomes highly viscous; its kinematic viscosity increases by approximately four to five times compared to water. Consequently, the flow of the heat transfer fluid through the pipes is impeded, resulting in high friction losses (dynamic pressure).

When using a standard three-speed pressure-boosting pump, in this case, a LEO dry-rotor circulation pump with a power rating of 1500 W—the system first switches to speed 2, and the heat pump compressor starts up. After 20–30 minutes of continuous compressor operation, readings are taken from the external circuit temperature sensors (at the ground loop outlet and inlet).

If the temperature difference exceeds 5°C, the pump speed must be increased. Conversely, if the temperature difference is less than 3°C, the flow rate of the heat transfer fluid can be reduced to save electricity.

This adjustment makes it possible to ensure that the length of 175 meters of the circuit through 4 wells completely covers the needs of the system without the risk of freezing of the coolant. And it helps prevent the risk of unwanted overcooling of the coolant.

4. Conclusion

Biogas production from biomass offers potential as an alternative energy source, particularly given the abundance of biomass resources in Kazakhstan. The study analyzes biogas production technologies—focusing on their results and innovative aspects—specifically for regions remote from traditional energy sources. While biogas represents an environmentally beneficial alternative for reducing emissions and managing waste, it is crucial to implement advanced technologies incorporating methane sensors and to rigorously address environmental controls within these processes. Such measures will minimize potential harm to local populations while ensuring the long-term sustainability of biogas and biomethane production and promoting the adoption of these clean energy sources.

An assessment of the thermal energy output, accounting for the efficiency characteristic of the external circuit of a ground-source heat pump is shown. Comparing the calculation results with test measurements leads to the conclusion that the capacity of the designed ground-source heat pump system comprising four 20-meter-deep boreholes is sufficient to reliably meet the requirements for cooling or heating the heat transfer fluid within the specified temperature range.

Monitoring data of the developed system operation and results of measuring its performance indicators during extended experimental testing under autumn-winter climatic conditions will be obtained. Subsequently, a more detailed analysis of heat transfer for each borehole is planned, utilizing modern software suites to determine the optimal operating parameters of the developed geothermal heat pump system.

Conflict of interest statement
The authors declare that they have no conflict of interest in relation to this research, whether financial, personal, authorship or otherwise, that could affect the research and its results presented in this paper.

CRediT author statement
Sakipova S.E.: supervision, writing – review & editing**; Smagulov Zh.:** methodology, validation**; Bekturganov Zh.S., Ismailov Zh.T.:** cconceptualization, investigation; **Kartbayeva, Gulnaz T.**: data curation, writing-original draf**; Duisenbayeva, M.S., Ospanova D.A**.: formal analysis, visualization. The final manuscript was read and approved by all authors.

Statement on the use of Artificial Intelligence.
The authors declare that no artificial intelligence tools were used to generate scientific content, results, or conclusions of this article.

Data Availability Statement
The data are available upon reasonable request from the authors.

Funding
This research is funded by the Science Committee of the Ministry of Science and Higher Education of the Republic of Kazakhstan (AP26102107).

References

1 Kadam, R., Jo, S., Lee, J., Khanthong, K., Jang, H., & Park, J. (2024). A Review on the Anaerobic Co-Digestion of Livestock Manures in the Context of Sustainable Waste Management. *Energies*, *17*(3), 546. https://doi.org/10.3390/en17030546

2 Pilarska, A. A., Pilarski, A., Pilarski, K., Pietrzak, M. B., Przybył, K., & Kałuża, T. (2026). Biogas Plants in the Sustainable Energy Transition: Environmental Performance, Public Health Implications and Socio-Economic Trade-Offs. *Sustainability*, *18*(19), 9876. https://doi.org/10.3390/su18199876

3 Wang, W., Chang, J.-S., & Lee, D.-J. (2023). Anaerobic digestate valorization beyond agricultural application: Current status and prospects. *Bioresource Technology*, *373*, Article 128742. https://doi.org/10.1016/j.biortech.2023.128742

4 Rowan, M., Umenweke, G.C., Epelle, E.I.; Christianah, I., Okoye, P.U., Gunes, B., Okolie, J.A. (2022) Anaerobic co-digestion of food waste and agricultural residues: An overview of feedstock properties and the impact of biochar addition. *Digit. Chem. Eng.*, 4. https://doi.org/10.1016/j.dche.2022.100046

5 Liu, Z., Gao, X., Li, Z., Yang, X., & Hu, Y. (2023). Evaluation of Biogas and Solar Energy Coupling on Phase-Change Energy-Storage Heating Systems: Optimization of Supply and Demand Coordination. *Buildings*, *13*(11), 2712. https://doi.org/10.3390/buildings13112712

6 Tetteh, F., Safo, D., Laari, P. Y., Berko, M., & Osafo, L. (2025). Enhancing Biogas Production Using Organic Waste as Clean Energy for Sustainable Development. *Engineering Proceedings*, 117(1), 59. https://doi.org/10.3390/engproc2025117059

7 Sharipov, M., Majitov J., Ergashev S., Shodiyev E., Narzullayeva Z. (2025). Substitution of thermal-technical and geometrical parameters of a small-scale biogas plant. *Eurasian phys. tech. j.*, *22*(3 (53), 84–90. https://doi.org/10.31489/2025N3/84-90

8 Xue, X., Lv, J., Chen, H., Xu, G., Li, Q. (2022). Thermodynamic and economic analyses of a new compressed air energy storage system incorporated with a waste-to-energy plant and a biogas power plant. *Energy*, 261, 125367. https://doi.org/10.1016/j.energy.2022.125367

9 Arslan, M., Kunt, M., & Yılmaz, C. (2023). Design and optimization of a computer simulation model for green hydrogen production by waste heat recovery from Afyon biogas plant. *International Advanced Researches and Engineering Journal*, *7*(3), 157-164. https://doi.org/10.35860/iarej.1271925

10 Belyayev, Ye., Kaltayev, A., Aliuly A., Mohanraj, M., Singh, R.M. (2019). The innovation of the Republic of Kazakhstan. IP name: Hybrid solar-ground source heat pump; IP number: №33382. https://journal.kaznaru.edu.kz/index.php/research/article/view/721 [in Russian]

11 Amanzholov, T., Seitov, A., Aliuly, A., Yerdesh, Y., Murugesan, M., Botella, O., Feidt, M., Wang, H. S., Belyayev, Y., & Toleukhanov, A. (2022). Thermal Response Measurement and Performance Evaluation of Borehole Heat Exchangers: A Case Study in Kazakhstan. *Energies*, *15*(22), 8490. https://doi.org/10.3390/en15228490

12 Yessenzhol, D., Sakipov, K., Sharipov, M., Majitov, J., Akhmetov, S., & Imomov, S. (2026). Comparative analysis of mixing regimes in biogas plants for optimization of the stirring process. *Eurasian phys. tech. j.*, *23*(2 (56), 47–56. https://doi.org/10.31489/2026N2/47-56

13 Cao, Y., Dhahad, H.A., Togun, H., Haghghi, M.A., Anqi, A.E., Farouk, N., Rosen, M.A. (2021). Seasonal design and multi-objective optimization of a novel biogas-fueled cogeneration application. *Int. J. Hydrogen Energy, 46(*42), 21822–21843. https://doi.org/10.1016/j.ijhydene.2021.04.044

14 Kartbayeva, G.T., Nusupbekov, B.R., Khasenov, A.K., Nusupbekov, U.B., Karabekova, D.Zh., Zholdasbek, E.A. (2022). Installation for biogas and biofertilizer from certain waste. Patent for utility model No. 6971, 4 p. Published 01.04.2022. [in Russian] https://gosreestr.kazpatent.kz/Utilitymodel/Details?docNumber=354140

15 Sakipova, S., Smagulov, Z., Nussupbekov, B., Ismailov, Z., Duisenbayeva, M., Nussupbekov, U., & Turlybekova, R. (2026). Improvement of a Combined Heating System for a Bioreactor Designed for Biogas Production Using Coal–Water Fuel. *Energies*, *19*(14), 3408. https://doi.org/10.3390/en19143408.

16 Smagulov, Zh.K., Bekturganov, Zh.S., & Ismailov, Zh.T. (2026). Bioreactor for processing organic waste using renewable energy sources. Patent 2025/1858.2, Bulletin 7, 5. Published 20.02.2026. [in Russian] https://gosreestr.kazpatent.kz/Utilitymodel/Details? docNumber=442842

AUTHORS' INFORMATION

Sakipova, Saule E. – Candidate of Phys.& Math. Sciences, Professor, Department of Engineering Thermophysics named after professor Zh.S. Akylbayev, Buketov Karaganda National Research University, Karaganda, Kazakhstan**;** Scopus Author ID: 6504154211; https://orcid.org/0000-0002-7505-8413; sakipova1607@gmail.com;

Smagulov, Zhanaidar K. – Candidate of Phys.& Math. Sciences, Professor, Department of Radiophysics and Electronics, Buketov Karaganda National Research University, Karaganda, Kazakhstan; Scopus Author ID: 6506808882; https://orcid.org/0000-0002-3412-973X**;** smagul@mail.ru

Bekturganov, Zhanaly S. – Doctor of Chemical Sciences, Professor, Department of Radiophysics and Electronics, Buketov Karaganda National Research University, Karaganda, Kazakhstan; Scopus Author ID: 6507538959; https://orcid.org/0000-0002-6487-7835; zhbekturganov@gmail.com

Ismailov, Zharaskan T. – Candidate of Phys.& Math. Sciences, Professor, Department of Radiophysics and Electronics, Buketov Karaganda National Research University, Karaganda, Kazakhstan; Scopus Author ID: 25025774800; https://orcid.org/0009-0002-6245-7690; Zhismailov@yandex.kz;

Kartbayeva, Gulnaz T. – Candidate of Biological Sciences, **Assoc. Professor**, Buketov Karaganda National Research University, Karaganda, Kazakhstan**;** Scopus Author ID: 57197772178 ; https://orcid.org/0000-0003-1860-3734; gulnaz_kartbayeva@mail.ru

Duisenbayeva, Moldir – Ph.D., Head of the Department of Physics, Abylkas Saginov Karaganda Technical University, Karaganda, Kazakhstan; Scopus Author ID: 60761103800; https://orcid.org/0000-0003-3733-7662**;** m_o_l_d_i_r_89@mail.ru

Ospanova, Didar A. **–** Ph.D., Senior Lecture, Department of Engineering Thermophysics named after professor Zh.S. Akylbayev, Buketov Karaganda National Research University, Karaganda, Kazakhstan**;** Scopus Author ID: 56286193500; https://orcid.org/0000-0001-7243-4965; bota_didar@mail.ru

EURASIAN PHYSICAL TECHNICAL JOURNAL

2026, Volume 23, No. 3 (57)

https://doi.org/10.31489/2026N3/94-102

Received: 18/06/2026 Revised: 15/08/2026 Accepted: 28/09/2026 Published online: 30/09/2026

Original Research Article

Open Access under the CC BY -NC-ND 4.0 license

UDC 539.1.06; 539.128.53

MODERNIZATION OF A THERMAL DESORPTION SPECTROSCOPY SETUP FOR HIGH-SENSITIVITY ANALYSIS OF HYDROGEN AND HELIUM ISOTOPES

Kulsartov T.[2], Akhanov A.[1], Askerbekov S.[1,2], Shaimerdenov A.[1], Chikhray Ye.[2], Bugybay Zh.[1]*

[1] Institute of Nuclear Physics ARKAE, Almaty, Kazakhstan
[2] Institute of Experimental and Theoretical Physics, al-Farabi Kazakh National University, Almaty, Kazakhstan
*Corresponding author: zh.bugybay@inp.kz

Abstract. *This paper presents the results of an engineering and technical development aimed at modernizing a thermal desorption spectroscopy (TDS) system to enhance the sensitivity of gas-phase mass spectrometry analysis. The measurement system was integrated with a high-sensitivity DLS-20 mass spectrometer operating in conjunction with an RGA-100 quadrupole residual gas analyzer. A vacuum circuit separation scheme utilizing an adjustable leak valve was implemented, providing precise gas flow control and ensuring the stable operation of the DLS-20 analyzer in the low-pressure regime. The relevance of this work stems from the investigation of processes and the determination of gas release mechanisms from tritium-breeding materials, where hydrogen isotopes (primarily as HT molecules) and helium are generated simultaneously. During mass spectrometry analysis, their signals overlap at the mass-to-charge ratio of m/z≈4, which complicates the interpretation of TDS experimental data. It is demonstrated that adjusting the opening degree of the mechanical leak valve allows for a more than 30-fold reduction in the gas flow entering the analyzer. The system was calibrated using helium-deuterium mixtures, revealing that the detection sensitivity for deuterium is approximately 2.7 times higher than that for helium. Reliable resolution of the helium, HT, and D_2 peaks was achieved. The obtained results demonstrate the feasibility of utilizing the modernized setup for high-sensitivity investigations of tritium, hydrogen isotope, and helium release processes, as well as for improving the reliability of TDS spectra interpretation.*

Keywords: thermal desorption spectroscopy (TDS), mass spectrometry, tritium-breeding materials, gas evolution mechanisms.

1. Introduction

The method of thermal desorption spectroscopy (TDS) is widely applied to investigate the processes of gas retention and release from solid materials [1,2]. This method provides comprehensive information on the mechanisms of gas diffusion, trapping, and detrapping, as well as the energetic characteristics of gas atom interactions with crystal lattice defects [3,4]. TDS studies acquire particular relevance when examining materials intended for use in nuclear and thermonuclear power plants. In such materials, neutron irradiation simultaneously generates hydrogen isotopes, including tritium, alongside helium produced via nuclear reactions [5,6]. Investigating the retention and release processes of these gases represents a pivotal task in evaluating the performance and operational lifetime of materials under service conditions [7-9]. One of the primary challenges in the mass spectrometry analysis of gas evolution is the overlap of signals from different gases with close mass numbers. Specifically, in studies of tritium-breeding materials, tritium release frequently occurs in the form of HT molecules, which are detected at the mass-to-charge ratio of m/z≈4. Since the helium

signal is recorded in the exact same region, interpreting the results using standard quadrupole mass spectrometers becomes significantly hindered. An additional complexity arises from the presence of background hydrogen in vacuum systems, which can substantially exceed the flux of hydrogen isotopes evolving from the investigated sample. This constrains the sensitivity of the method and reduces the reliability of analyzing gas release processes. Consequently, there is a clear need to enhance the sensitivity of TDS measurement systems and develop approaches for a more accurate analysis of the gas phase composition, particularly in cases involving overlapping signals of helium and hydrogen isotopes. From an engineering perspective, this problem can be addressed by modernizing the TDS setup through the integration of high-sensitivity mass spectrometers and the implementation of managed gas flow separation schemes between different components of the vacuum system. The objective of the present work is to upgrade the existing thermal desorption spectroscopy system by integrating a DLS-20 high-resolution mass spectrometer, and to investigate the capabilities of the proposed measurement scheme for registering low-intensity gas flows and analyzing hydrogen isotopes and helium, including tasks associated with tritium release.

2. Methods

Experimental Setup

The key concept behind modernizing the thermal desorption spectroscopy (TDS) setup was to expand the existing measurement scheme by integrating an additional high-sensitivity DLS-20 mass spectrometer. The upgraded system comprises two mass spectrometers: an RGA-100 quadrupole residual gas analyzer [10] (Stanford Research Systems) and a DLS-20 mass spectrometer (Hiden Analytical Limited) [11], each connected to its own vacuum system equipped with independent turbomolecular pumps. This configuration ensures optimal operating conditions for each analyzer and enhances measurement stability across a wide pressure range. The connection between the TDS chamber and the DLS-20 mass spectrometer chamber is established via an adjustable leak valve (L1, serving as a throttling element), which allows for precise control of the gas flow entering the high-sensitivity analyzer. The implementation of independent vacuum circuits and the adjustable leak valve represents a key element of the modernization, enabling the DLS-20 mass spectrometer to operate in the low-pressure regime regardless of the pressure level inside the TDS chamber. This feature is of paramount importance for registering low-intensity gas flows and performing high-sensitivity measurements. The RGA-100 mass spectrometer is capable of recording gas spectra in the mass range from 1 to 100 amu. The principle of gas detection is based on the ionization of a small fraction of gas molecules; the resulting positive ions are subsequently separated by mass and measured using a Faraday cup as the detector.

The DLS-20 is a quadrupole mass spectrometer featuring ultra-high mass resolution (up to $\Delta m \approx 0.005$ amu) and an increased quadrupole rod diameter of 20 mm (which provides enhanced sensitivity). It offers two operational modes:

1. RGA (Zone 1): a wide mass range mode (up to ~200 amu);
2. zhRGA (Zone H): an ultra-high-resolution mode (up to ~22.5 amu).

The instrument utilizes an ion-counting secondary electron multiplier (SEM) as a detector, which ensures high sensitivity combined with a low background noise level. Since the recommended maximum operating pressure for the SEM detector is 5×10-6 Torr, the pressure within the DLS-20 mass spectrometer chamber was maintained below this threshold throughout the experiments. To achieve this operating regime, a gas flow regulation scheme between the setup chambers was implemented.

The vacuum system comprised the following components:

- RGA-100 quadrupole mass spectrometer;
- DLS-20 quadrupole mass spectrometer;
- Turbomolecular pumps (assigned to each vacuum circuit);
- Scroll (roughing) pump;
- Ionization vacuum gauges;
- Diaphragm vacuum gauge;
- Gas inlet system.

A schematic diagram of the modernized setup is depicted in Figure 1. The newly integrated elements associated with the DLS-20 mass spectrometer and its corresponding vacuum system are highlighted in red.

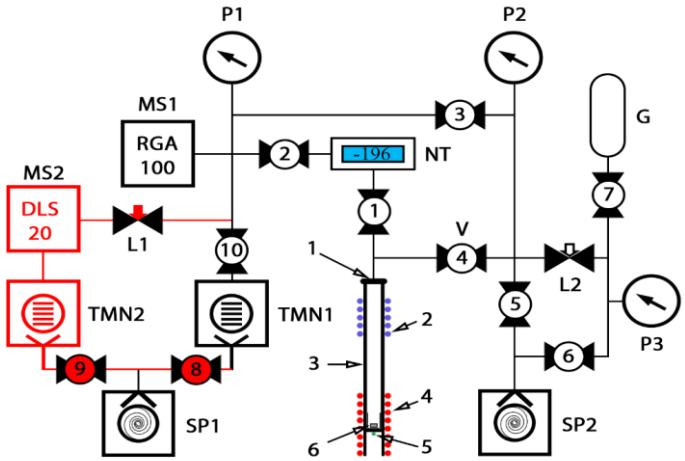


Fig 1. Schematic diagram of the modernized TDS setup integrated with the high-sensitivity DLS-20 mass spectrometer: MS1 – RGA-100 mass spectrometer; MS2 – DLS-20 mass spectrometer; TMN1 – turbomolecular pump of the RGA-100 vacuum circuit; TMN2 – turbomolecular pump of the DLS-20 vacuum circuit; SP1 – scroll (roughing) pump of the RGA-100 vacuum circuit; SP2 – scroll (roughing) pump of the DLS-20 vacuum circuit; NT – nitrogen trap; P1 – ionization vacuum gauge in the mass spectrometer chamber; L1 – leak valve between the TDS and DLS-20 chambers; L2 – leak valve for the controlled inlet of gas (atmospheric air or the helium-deuterium mixture) into the TDS chamber; P2 – ionization vacuum gauge in the experimental device chamber; P3 – diaphragm vacuum gauge; V – vacuum valves; G – replaceable gas cylinder; 1 – loading flange; 2 – cooling system; 3 – experimental device; 4 – heating element; 5 – thermocouple; 6 – crucible with the sample."

3. Results

Investigation of the Leak Valve Opening Influence on Gas Flow

At the first stage of the work, experiments were performed to evaluate the feasibility of regulating gas flows from the TDS + RGA-100 chamber into the chamber of the high-sensitivity DLS-20 mass spectrometer operating in the wide-range (RGA) mode. Mass spectrometry measurements were conducted at various opening degrees of the adjustable leak valve (L1) connecting the chambers of the setup.

The following operating modes were considered:

1. Leak valve fully open;
2. Leak valve fully closed;
3. Leak valve open by one turn;
4. Leak valve open by a half turn;
5. Leak valve open by a quarter turn.

At an initial system pressure of approximately 1.3×10^{-6} Torr, the mass spectra of the main gas-phase components were recorded. The dependence of the gas partial pressures within the setup chambers on the various opening degrees of the leak valve is shown in Figure 2.

The quasi-equilibrium readings of the mass spectrometers are summarized in Table 1. Data for signals with low intensity and high noise levels (m/z = 2 and m/z = 44) were omitted, as they were not utilized in the subsequent analysis. During the experiments, a controlled inlet of atmospheric gases into the TDS chamber was established via a mechanical leak valve (L2). This approach ensured a quasi-stationary composition of the gas phase, which was then used to analyze the changes in gas flows between the setup chambers. Consequently, further evaluations of the reduction coefficients for gas flows from the TDS chamber to the DLS-20 mass spectrometer chamber were carried out for the atmospheric components.

Nitrogen N_2 was selected as the primary tracer gas because it provided the lowest error in determining the flow reduction coefficients. Water vapor exhibited a prolonged stabilization time to reach a quasi-equilibrium state, which led to an increase in measurement error. In the case of oxygen at a small leak valve opening degree (1/4 turn), the recorded flow was insufficiently high, causing a significant increase in the relative error (Table 2). Thus, it is demonstrated that adjusting the opening degree of the leak valve allows for a more than 30-fold reduction in the gas flow entering the DLS-20 mass spectrometer chamber. This operating mode can be utilized when the pressure inside the TDS chamber increases, thereby ensuring stable operating conditions for the high-sensitivity analyzer.

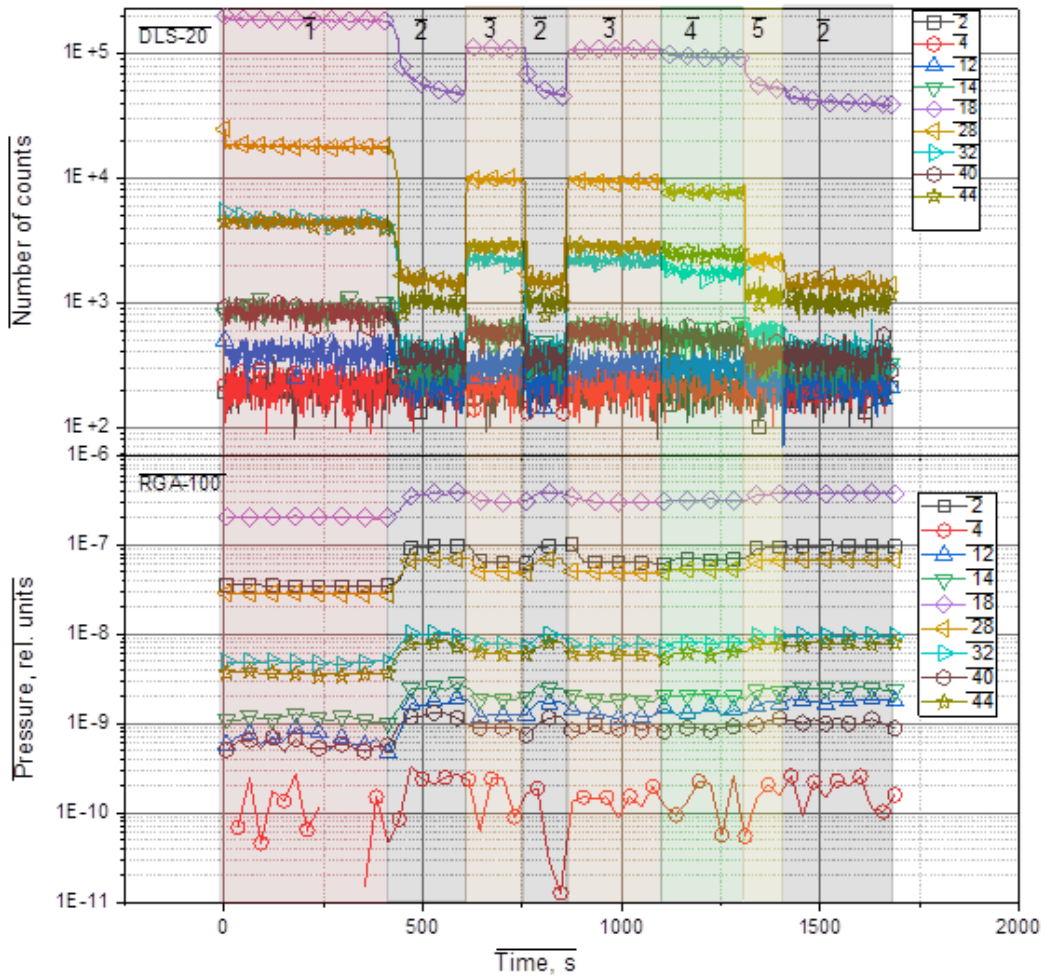


Fig 2. Diagram of changes in the partial pressures of various gases within the setup chambers at different positions of the valve between them.

Table 1. Quasi-equilibrium readings of the mass spectrometers at different stages of the experiment.

M	2	18	28	32	44
Gas	H2	H2O	N2	O2	CO2
RGA-100 (1)	3,55E-08	1,97E-07	2,79E-08	4,93E-09	3,70E-09
RGA-100 (2)	1,02E-07	3,81E-07	6,90E-08	9,88E-09	7,90E-09
RGA-100 (3)	6,40E-08	3,03E-07	4,90E-08	7,60E-09	5,00E-09
RGA-100 (4)	6,90E-08	3,15E-07	5,30E-08	8,11E-09	6,30E-09
RGA-100 (5)	9,30E-08	3,72E-07	6,72E-08	9,76E-09	7,80E-09
DLS-20 (1)	-	1,87E+05	1,71E+04	4,45E+03	-
DLS-20 (2)	-	3,90E+04	1,40E+03	4,00E+02	-
DLS-20 (3)	-	1,10E+05	1,00E+04	2,50E+03	-
DLS-20 (4)	-	9,30E+04	7,75E+03	1,50E+03	-
DLS-20 (5)	-	5,30E+04	1,92E+03	6,00E+02	-

Table 2. Flow reduction factors (k) from the TDS chamber to the DLS-20 chamber at different positions of the connecting valve.

Gas type	28	32	28		32	
	N2	O2	N2		O2	
	Flow into the system, rel. units (during registration)		k	Error %	k	Error %
1-the system is open	1,57E+04	4,15E+03	1,000	1,3	1,000	4,8
3 system is open by 1 turn of the valve	8,60E+03	2,20E+03	0,548	2,3	0,530	9,1
4 the system is open by half a turn of the valve	6,35E+03	1,45E+03	0,405	3,1	0,349	13,8
5 the system is open by ¼ turn of the valve	5,20E+02	2,00E+02	0,033	38,5	0,048	100,0

In the considered mode, the measurement noise level was approximately 200 arbitrary units (arb. u.), which corresponds to a pressure of the order of 2×10^{-10} Torr according to the RGA-100 readings. Meanwhile, the minimum detectable signal that provides an acceptable measurement accuracy is around 1000 arb. u., corresponding to a pressure of about 1×10^{-9} Torr. It should be noted that as the opening degree of the leak valve decreases, the pressure detection sensitivity in the TDS chamber drops proportionally to the flow attenuation factor k. For instance, when the leak valve is open by 1/4 turn, the flow reduction factor is $k \approx 30$, which corresponds to the effective signal recording by the DLS-20 mass spectrometer at pressures above 3×10^{-8} Torr in the RGA-100 chamber. The operational parameters of the DLS-20 mass spectrometer in this mode are shown in Table 3.

Table 3. Operational parameters of the DLS-20 mass spectrometer in the wide-range (RGA) mode during the experiment.

Group	Parameter	Value	Units
Detector	discriminator	–10	%
	multiplier	1700	V
Filter	focus	–90	V
Quad	delta-m	0	%
	pre-post-bias	0.0	V
	resolution	0	%
Source	cage	3.0	V
	electron-energy	70.0	V
	emission	1.0	μA
Other	CRV_range	7	–
	CRV_resolution	6	bit
	DeadBandTime	0	ms
	mass	30.0	amu
	mode-change-delay	1000	ms

Experiments with Helium-Deuterium Mixtures

RGA-100 partial pressures in Torr are obtained by multiplying the raw registered (relative-unit) signal by the gas-specific ionization coefficient, and giving an approximate, order-of-magnitude comparison between the DLS-20 raw count rate and the corresponding RGA-100 partial pressure under the reported operating conditions. At the next stage of the work, calibration experiments for the DLS-20 mass spectrometer operating in the ultra-high resolution zhRGA mode were performed using pre-prepared helium-deuterium mixtures. Gas mixtures with a specified component ratio were prepared in volumes V1 and V1+V2 (with a volume ratio of $V2/V1\approx1.75$) and subsequently transferred into the replaceable gas cylinder (G). Further experiments were conducted using this cylinder as the source of the working gas. The gas was supplied to the vacuum chamber of the setup via a mechanical leak valve (L2) in a controlled continuous inlet mode. During the experiments, the signals from both the RGA-100 and DLS-20 mass spectrometers were recorded simultaneously, allowing for a comparison of the readings from the two analyzers and an evaluation of the gas-phase composition in the system. Typical mass spectra of helium and deuterium recorded in the setup chamber are shown in Figure 3.

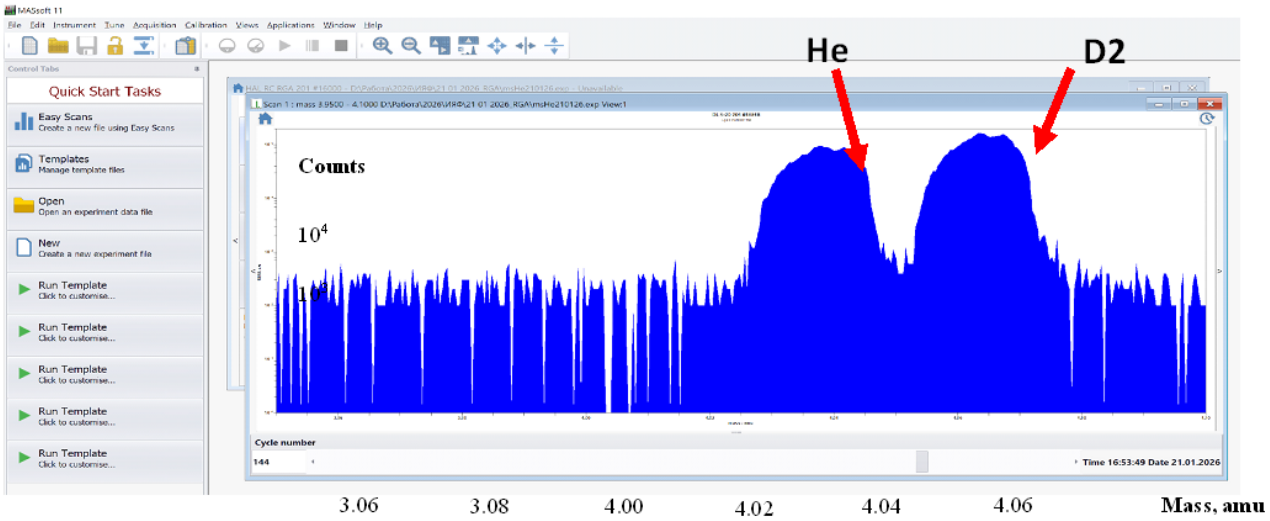


Fig 3. Typical mass spectra of helium and deuterium within the setup chamber.

According to the recorded mass numbers, when the helium-deuterium mixture is supplied to the setup chamber, the following values are obtained via the DLS-20: m/z (He)≈4.038 and m/z (D2)≈4.068.

During the calibration of the DLS-20, the ultra-high resolution zhRGA mode differs from the standard wide-range RGA mode (see Figure 3) only by the following parameters:

– delta-m (0→20 %):: Determines the effective mass peak width (Δm) and its narrowing degree (decreasing this value enhances the resolution and improves the separation of close masses);

– pre-post-bias (0→15 V):: Sets the potentials before and after the quadrupole to adjust ion energy, which influences transmission efficiency and detection sensitivity;

– resolution (0→50 %): A tuning parameter for the quadrupole resolution; increasing this value improves mass separation but may reduce signal intensity;

– mass (46→5.5 amu):

The mass scanning range in the zhRGA mode, optimized for the analysis of light gases and isotopes; emission (1→100 μA): The emission current of the electron gun in the ion source, which determines ionization intensity; increasing the current elevates the signal but accelerates cathode degradation. The experimental diagram along with a qualitative description of the stages are presented in Fig.4 and Table 4.

Table 4. Measured helium and deuterium flow into the system for various inlet modes.

	Inlet pressure He, Torr	Pressure D2 at the inlet	He-D2 ratio	Chamber pressure P	M4 RGA Pressure	M6 RGA Pressure	He (DLS20)	D_2 (DLS20)	He-D2 ratio (according to DLS-20)	Note Working with:
1	707-672	0	1-0	1,7E-5	1.2E-5	Back-ground	37970	200 (Background)	1-0	pure He.
	707~672	0	1-0	3,6E-5	~3E-5	Back-ground	44050-38540	200 (Background)	1-0	
	247	0	1-0	9,1E-6	~8,6E-6	Back-ground	12360	200 (Background)	1-0	
2	90	440	0.17-0.83	6,2E-5	~5.6E-5	~5.25E-7	4690	57110	0.076-0.924	a mixture of He-D2 gases.
3	0	690	0-1	-	9,5E-5	1,61E-6		102990	0-1	pure D2.
		251	0-1	-	2.7E-5	1.52E-7		28890	0-1	
4	440	89	0,83-0,17		2.81E-5	3.65E-8	20300	12690	0.61-0.39	a mixture of He-D2 gases.
	158	31	0,83-0,17		6.26E-6	4.37E-9	6160	4280	0.59-0.41	

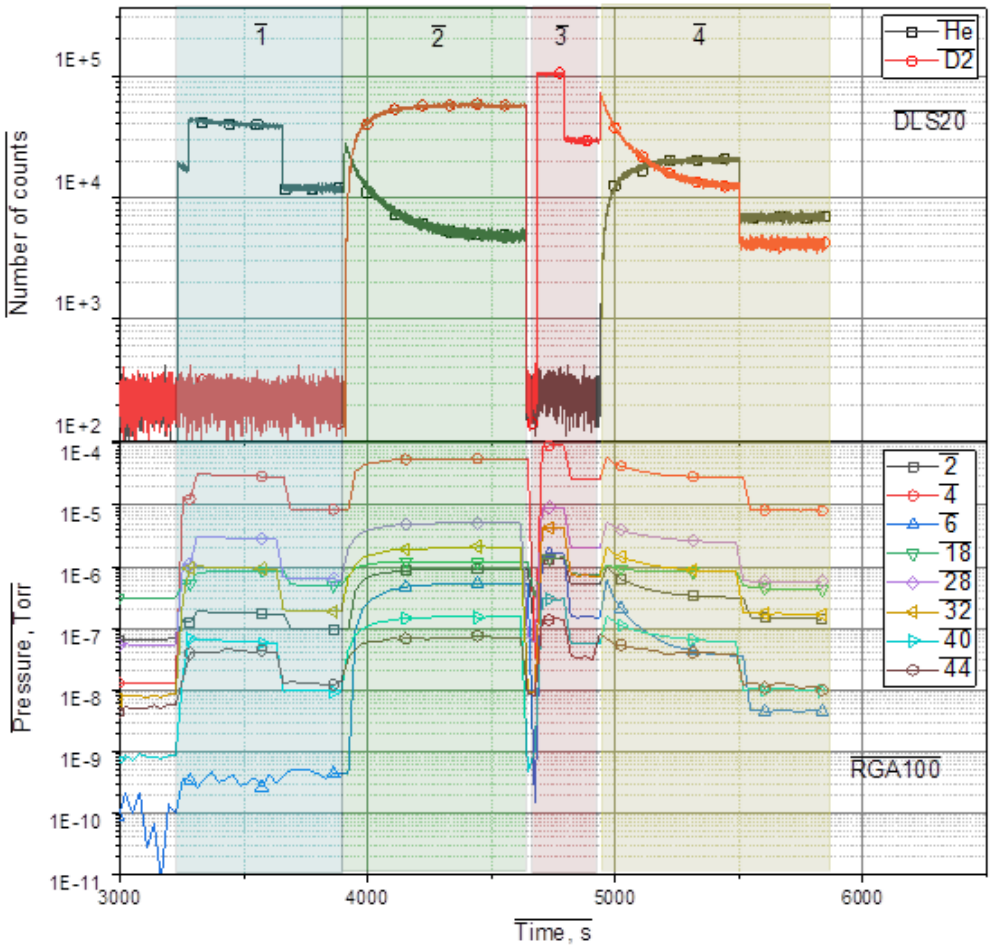


Fig 4. Diagram of experiments with the inlet of helium-deuterium mixtures into the setup chamber.

Based on the obtained data (Table 4), the intensities of the helium and deuterium mass spectrometry signals recorded by the DLS-20 mass spectrometer were plotted as a function of the inlet pressure of the corresponding gases (Figure 5). Analysis of the results revealed that both the sensitivity and the calibration factor for deuterium exceed those for helium by approximately 2.67 times.

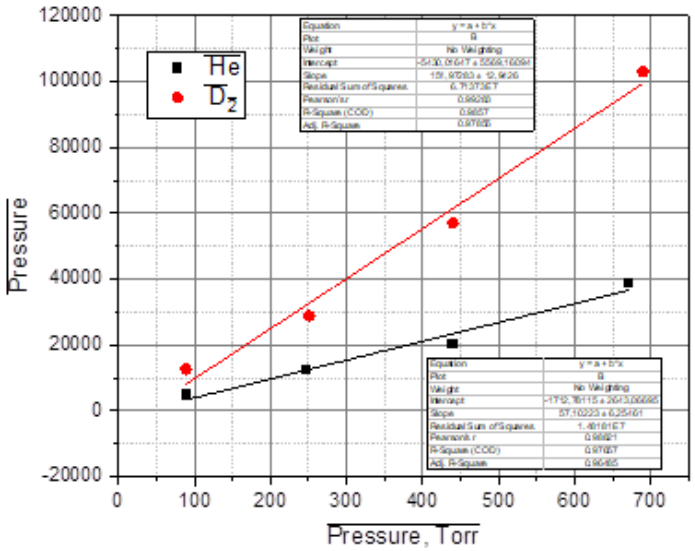


Fig 5. Peak intensities for helium and deuterium measured by the DLS-20 as a function of the inlet pressure of the corresponding gases.

This discrepancy must be taken into account during the quantitative interpretation of mass spectrometry data. The experiments were conducted with the leak valve opening degree corresponding to 1/4 turn.

4. Discussion

The conducted experiments demonstrated that the use of an adjustable leak valve allows for effective control over the gas flow entering the chamber of the high-sensitivity DLS-20 mass spectrometer from the investigated sample. It was established that decreasing the opening degree of the leak valve can reduce the gas flow by a factor of more than 30. This ensures stable operation of the analyzer within its optimal pressure range and prevents its overload during pressure increases inside the TDS chamber.

Calibration experiments with helium-deuterium mixtures indicated that the intensities of the helium and deuterium mass spectrometry signals recorded by the DLS-20 depend linearly on the inlet pressure of the corresponding gases. The obtained relationships confirm the validity of the proposed measurement scheme and the feasibility of performing a quantitative analysis of the gas-phase composition. A comparison of the detection sensitivities for different gases revealed that the calibration factor for deuterium is approximately 2.67 times higher than that for helium. This result must be taken into account during the quantitative interpretation of mass spectrometry data, particularly when analyzing mixtures containing hydrogen isotopes.

The proposed measurement scheme can be employed in studies of materials exhibiting simultaneous release of helium and hydrogen isotopes, including tritium. Under conditions where signals overlap in the mass-to-charge ratio region of $m/z \approx 4$, the modernized system enhances the reliability of gas-phase analysis and reduces uncertainty in the interpretation of TDS experimental results.

5. Conclusion

The thermal desorption spectroscopy setup was modernized by integrating a high-sensitivity DLS-20 mass spectrometer and implementing a vacuum circuit separation scheme using an adjustable leak valve. The proposed solution expands the range of detectable gas flows and enhances measurement stability. The conducted studies confirmed the performance of the proposed scheme and the feasibility of its application for the quantitative mass spectrometry analysis of the gas phase. It is demonstrated that the upgraded setup enables the detection of low-intensity gas flows and allows for sensitivity calibration across various components. The practical significance of this work lies in the applicability of the developed measurement scheme to investigate gas evolution processes from materials characterized by the simultaneous release of hydrogen isotopes and helium (e.g., beryllium-containing materials). Under conditions where signals overlap in the mass-to-charge ratio region of $m/z \approx 4$, the proposed approach improves the reliability of TDS experimental data interpretation.

Conflict of interest statement
The authors declare that they have no conflict of interest in relation to this research, whether financial, personal, authorship or otherwise, that could affect the research and its results presented in this paper.

CRediT author statement
Kulsartov T.V.: Conceptualization, Methodology, Writing Original Draft; **Akhanov A.M.:** Data Curation, Investigation; Software; **Askerbekov S.K.:** Methodology, Resources, Formal analysis; **Shaimerdenov A.A.:** Funding acquisition, Project administration, Supervision; **Chikhray Ye.V.:** Methodology, Validation, Data curation; **Bugybay Zh.T.:** Visualization, Writing – review & editing. The final manuscript was read and approved by all authors.

Statement on the use of Artificial Intelligence.
During the preparation of this manuscript, artificial intelligence tools were used solely for language editing and grammatical improvement. No AI tools were used to generate scientific content, analysis, results, or conclusions.

Data Availability Statement
The data that support the findings of this article are openly available.

Funding
The research has been funded by the Science Committee of the Ministry of Science and Higher Education of the Republic of Kazakhstan under Program BR24993119.

References

1 Tal-Gutelmacher, E., Eliezer, D., & Abramov, E. (2007). Thermal desorption spectroscopy (TDS)–Application in quantitative study of hydrogen evolution and trapping in crystalline and non-crystalline materials. *Materials Science and Engineering:* A, 445–446, 625–631. https://doi.org/10.1016/j.msea.2006.09.089

2 Askerbekov, S., Aitkulov, M., Shaimerdenov, A., Kulsartov, T., Akhanov, A., Bugybay, Z., & Sairanbayev, D. (2025). Gas release kinetics from neutron irradiated Li2TiO3 samples. *Fusion Eng. Des*., 216, Article 115060. https://doi.org/10.1016/j.fusengdes.2025.115060

3 Ma, H.-Z., Li, Y.-H., Niu, Y.-Z., Hua, Y.-C., Kong, X.-S., Cheng, L., Zhou, H.-B., Lu, G., Gao, F., & Lu, G.-H. (2025). Thermal desorption of hydrogen in damaged materials and its implication for defect characterization. *Acta Materialia,* 294, 121130. https://doi.org/10.1016/j.actamat.2025.121130

4 Kulsartov, T. V., Zaurbekova, Zh. A., & Chikhray, E. V. (2018). Development of a technique for TDS experiments with induction heating of hydrogen-pre-saturated samples. *Vestn. NNC (J. NNC*), (4), 129–133. https://doi.org/10.52676/1729-7885-2018-4-129-133 [in Russian]

5 Chikhray, Y., Askerbekov, S., Knitter, R., Kulsartov, T., Shaimerdenov, A., Aitkulov, M., Akhanov, A., Sairanbayev, D., Bugybay, Z., Nessipbay, A., Kisselyov, K., Kizane, G., & Zarins, A. (2024). Studies of irradiated two-phase lithium ceramics Li4SiO4/Li2TiO3 by thermal desorption spectroscopy. *Nucl. Mater. Energy,* 38, Article 101621. https://doi.org/10.1016/j.nme.2024.101621

6 Kozlovskiy, A.L., Abyshev, B., Zhumadilov, K.Sh., & Shlimas, D.I. (2022). Influence of phase formation processes in lithium zirconate ceramics on strength and thermal properties. *Eurasian Physical Technical Journal*, 19, 2(40), 13–18. https://doi.org/10.31489/2022No2/13-18

7 Causey, R. A. (2012). Studies of hydrogen retention and release in fusion materials, IAEA, 17–26. http://www-pub.iaea.org/MTCD/Publications/PDF/apid15_web.pdf.

8 Federici, G., Skinner, C. H., Brooks, J. N., Coad, J. P., Grisolia, C., Haasz, A. A., Hassanein, A., Philipps, V., Pitcher, C., Roth, J., Wampler, W. R., & Whyte, D. G. (2002). Plasma-material interactions in current tokamaks and their implications for next step fusion reactors. *Nuclear Fusion*, 41(12), 1967. https://doi.org/10.1088/0029-5515/41/12/218

9 Roth, J., Tsitrone, E., Loarte, A., Loarer, T., Counsell, G., Neu, R., Philipps, V., Brezinsek, S., Lehnen, M., Coad, P., Grisolia, C., Schmid, K., Krieger, K., Kallenbach, A., Lipschultz, B., Doerner, R., Causey, R., Alimov, V., Shu, W., & Kukushkin, A. (2009). Recent analysis of key plasma wall interactions issues for ITER. *Journal of Nuclear Materials*, 390–391, 1–9. https://doi.org/10.1016/j.jnucmat.2009.01.037

10 Hiden Analytical. (2020). Mass spectrometers for residual gas analysis (RGA) [Brochure]. https://www.hiden.fr/wp-content/uploads/2020/11/TDS-188-7-RGA-Catalogue_High-Res.pdf

11 Hiden Analytical. (2026). DLS-20: *Quadrupole Mass Spectrometer.* https://www.hidenanalytical.com/products/residual-gas-analysis/dls-20/

AUTHORS' INFORMATION

Kulsartov, Timur – Candidate of Physical and Mathematical Sciences, Senior Researcher, Institute of Experimental and Theoretical Physics, al-Farabi Kazakh National University, Almaty, Kazakhstan, SCOPUS Author ID: 8423886500**,** Web of Science ResearcherID: B-4888-2015, ORCID iD: 0000-0003-3890-8172**,** tima@physics.kz

Akhanov, Assyl – Institute of Nuclear Physics ARKAE, Almaty, Kazakhstan, SCOPUS Author ID; 57224822200, Web of Science ResearcherID: HWX-3320-2023, ORCID iD: 0000-0001-5704-1514, aakhanov@inp.kz

Askerbekov, Saulet – PhD, Associate Professor, Institute of Experimental and Theoretical Physics, al-Farabi Kazakh National University, Almaty, Kazakhstan, Institute of Nuclear Physics ARKAE, Almaty, Kazakhstan, SCOPUS Author ID: 57191892035, Web of Science ResearcherID: N-7501-2017, ORCID iD: 0000-0001-7204-4887**,** askerbekov@physics.kz

Shaimerdenov, Asset – PhD, Associate Professor, Institute of Nuclear Physics ARKAE, Almaty, Kazakhstan, SCOPUS Author ID: 56177879200, Web of Science ResearcherID: AAM-6960-2021, ORCID iD: 0000-0003-0304-2049, ashaimerdenov@inpkz

Chikhray, Yevgen – Candidate of Technical Sciences, Senior Researcher, Institute of Experimental and Theoretical Physics, al-Farabi Kazakh National University, Almaty, Kazakhstan, SCOPUS Author ID: 6506943153, Web of Science ResearcherID: A-7226-2012, ORCID iD: 0000-0001-6623-4596, chikhray@physics.kz

Bugybay, Zhanar - PhD student, Institute of Nuclear Physics ARKAE, Almaty, Kazakhstan, SCOPUS Author ID: 57445836700, Web of Science ResearcherID: JRY-0700-2023, ORCID iD: 0000-0002-0195-7969, zh.bugybay@inp.kz

EURASIAN PHYSICAL TECHNICAL JOURNAL

2026, Volume 23, No. 3 (57)

https://doi.org/10.31489/2026N3/103-114

Received: 31/03/2026 Revised: 15/08/2026 Accepted: 28/09/2026 Published online: 30/09/2026

Original Research Article

Open Access under the CC BY -NC-ND 4.0 license

UDC 539.3.6

MODERNIZATION OF THE METHODOLOGY AND INSTALLATION OF TRIAXIAL COMPRESSION FOR THE STUDY OF RHEOLOGICAL PROPERTIES OF DISPERSED MEDIA

Kazhikenova S.[1]*, Akhmetova S.[1], Belomestny D.[2]

[1] A. Saginov Karaganda Technical University, Karaganda, Kazakhstan

[2] University of Duisburg-Essen, Duisburg, Germany

*Corresponding author: sauleshka555@mail.ru

Abstract. *The article discusses the determination of rheological and deformation characteristics of dispersed materials, specifically sand-clay molding mixtures. The authors present the design of a triaxial compression apparatus developed on the basis of a standard stabilometer, incorporating the principles of similarity theory. The study reveals that the presence of residual plastic deformations causes nonlinearity in the material layer formation process. Particular attention is paid to the analysis of the deformation modulus and its dependence on medium density, particle diameter and the internal friction coefficient. The results obtained allow for a more accurate prediction of the behavior of cohesive and non-cohesive bulk media under load, which is essential for optimizing technological processes in foundry production and related industries.*

Keywords: dispersed materials, rheology, stabilometer, triaxial compression, deformation modulus, molding mixture.

1. Introduction

When processing dispersed and lump materials, both cohesive (such as molding mixtures) and non-cohesive (such as coke and limestone), their physical, mechanical, and rheological properties, including elasticity, plasticity, and strength, are crucial. One of the key parameters that determines the deformation behavior of dispersed media under load (including compression in the absence of lateral expansion) is the deformation modulus.

According to the literature data [1, 2], the value of the deformation modulus M is determined by the density of the material δ, the particle diameter s, the coefficient of internal friction γ, and a number of other factors, among which the three listed indicators have a dominant influence. It is known that an increase in the initial density of the medium naturally increases the deformation modulus. The coefficient of internal friction, which reflects the resistance of the medium to shear deformation during fracture, also increases as the packing of particles becomes denser, leading to an increase in the deformation modulus [3]. Conversely, the effect of dispersion (particle size) is the opposite: an increase in the average particle diameter causes a decrease in the deformation modulus.

Due to the multidirectional and interconnected nature of these factors, it is difficult to analytically predict their complex impact, which is critical for theoretical calculations and practical applications. Based on this, a plan was developed for experimental studies to quantify the dependence of the deformation modulus on key physical and mechanical characteristics of the medium.

2. Materials and Methods

To solve the research problems, a modernized experimental triaxial compression setup was assembled (Fig. 1). It allows for independent setting of the two principal stresses vertical τ_z and lateral $\tau_{r,y}$. and measurement of the corresponding principal relative strains j_z and $j_{r,y}$. Axial pressure on the specimen is exerted directly through a piston of the same diameter. As a result, when the specimen is compressed, its lateral expansion is possible only with the corresponding removal of some of the water filling the chamber. This device can be classified as a type stabilometer B, in which the lateral pressure is not simultaneously all-round, the axial pressure can be set independently of the lateral pressure and, in particular, be less than the latter or equal to zero. The stabilometer schematic is shown in Fig. 2. The instrument allows for compression testing, determining the lateral pressure coefficient and deformability characteristics, as well as the strength of the specimen [4].

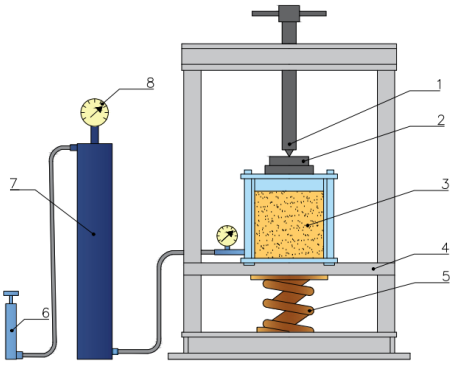


Fig.1. The scheme of the experimental setup: 1-crane; 2-dynamometer; 3-stabilometer; 4-frame for attaching a type B stabilometer; 5-spring; 6-air pump for supplying air to the compensator tank; 7-compensator tank; 8-pressure gauge.

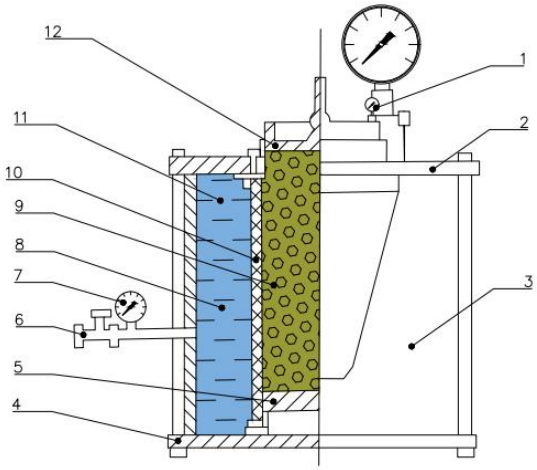


Fig. 2. Scheme of the experimental stabilometer: 1 – TdL 7682-1 dial gauge for measuring vertical deformations; 2 – upper cover; 3 – tap for regulating lateral pressure; 4 – lower cover; 5 – lower piston; 6 – tap for supplying water; 7 – pressure gauge for measuring lateral pressure; 8 – water inside the working chamber; 9 – sample; 10 – rubber cover; 11 – working chamber $H = 300mm, \varnothing = 400mm$; 12 – piston for vertical deepening of the sample $\varnothing = 136mm$.

2.1 Principle of Operation of the Experimental Setup

The design and experimental procedure for the developed testing apparatus (stabilometer) are as follows. The particulate material under study 9, pre-enclosed in an elastic rubber membrane 10 to prevent contact with the working medium, is placed inside the pressure chamber 11. The sealed specimen is rigidly fixed in the vertical direction between the lower 5 and upper 12 pistons (loading plungers). Following specimen installation, the internal volume of the chamber 11 is filled with distilled water. When the stopcock 3 is closed, the hydraulic system becomes completely sealed. Due to the practical incompressibility of water, the lateral (radial) expansion of the particulate material during vertical loading is restricted to zero, ensuring strict confined compression conditions. Consequently, the radial stress $\tau_r = \tau_y$ generated within the closed volume of the fluid due to material lateral pressure is continuously recorded by a standard pressure gauge 7. The measured hydraulic pressure is taken as the true lateral pressure of the medium under study.

2.2 Methodological Features of the Experimental Procedure

During the preparation and execution of the experiments, maintaining two key technological conditions is critical:

– Absolute tightness of the hydraulic circuit. Even minimal leakage of the working fluid from the chamber 11 leads to uncontrolled radial deformation of the specimen, which fundamentally distorts the measured values of the lateral pressure coefficient.

– Complete deaeration of the system. Air trapped within the water, the pressure gauge 7, and the connecting lines must be fully evacuated (via vacuuming or flushing with deaerated water). The presence of gas microbubbles, which possess high compressibility, violates the condition of rigid lateral confinement and significantly reduces the accuracy of deformation characteristics determination.

2.3 Analytical Capabilities of the Method

The developed design of the apparatus enables comprehensive compression testing of particulate media with stable, real-time parameter tracking. Based on the experimental results, the following parameters are determined:

– The coefficient of lateral earth pressure at rest (lateral pressure coefficient of the particulate material) ε;

– Key deformation characteristics (modulus of deformation, coefficient of relative compressibility);

– The shear strength envelope (ultimate shear resistance) of the specimen under specified loading paths.

The limited height of the sample, in the presence of friction at the points of contact between the stamp and the bottom of the device, causes the sample to expand unevenly in height.

To eliminate these shortcomings, the authors [5] recommend that the height of the sample in the experiments be at least twice its diameter.

Taking into account the test methodology [6], compression tests were carried out according to two testing schemes, the difference between which was that at each stage of loading in the first scheme the vertical load was maintained constant, in the second – this load changed.

The experiments were conducted in the following order:

1. The stabilometer was loaded with material at a temperature corresponding to the ambient temperature in the laboratory.

2. The load was applied to the sample smoothly, avoiding impacts, in steps. The average rate of load increase was 30–50 kPa/min.

3. Each pressure step was maintained until the vertical deformation stabilized, not exceeding 0.0001 mm in 15 minutes.

4. Readings from the vertical and lateral pressure measuring devices, as well as the indicator, were recorded in the test log at each pressure stage 15 minutes after the set pressure was established.

5. Testing was terminated when the vertical pressure reached Pb = 480 kPa.

6. After completion of the test, the material sample was unloaded by resetting the vertical and lateral pressures to zero and removed from the stabilometer chamber.

The shear strength study on a triaxial apparatus was also conducted using two schemes. In the first, a fixed, constant lateral pressure was maintained throughout the experiment while the vertical load varied; in the second, after applying the vertical load and holding for ten minutes at the initial stage, the vertical load was increased until the specimen failed [7]. Subsequently, a high lateral pressure was created in the chamber, and

a gradually increasing vertical load was again applied to the specimen. Tests using both schemes were conducted at lateral pressures equal to 20, 40, 60, 80, and 100 kPa. It should be noted that the experiments using the second scheme were considered accelerated, since they were three times faster in duration compared to the tests using the first scheme.

As is known [8], for longitudinal deformations in the direction of the *r, y,* and *z* axes, in the general case of a three-dimensional stress-strain state, these dependencies are as follows:

$$j_r = \frac{\tau_r - u(\tau_y + \tau_z)}{M},\ j_y = \frac{\tau_y - u(\tau_r + \tau_z)}{M}, \qquad j_z = \frac{\tau_z - u(\tau_r + \tau_y)}{M} \tag{1}$$

where parameters *M* and *u* are quantitative characteristics of the deformability of the medium under study.

A compression test involves the vertical deformation (compression) of a cylindrical sample of dispersed materials in a rigid ring (cage). The sample is in a uniform triaxial stress state characterized by normal stresses: $\tau_z = \tau,\ \tau_r = \tau_y = \varepsilon\tau_z$. Considering compression tests as a special case of triaxial deformation, when: $j_r = j_y = 0$, depending on (1) was found:

$$j_z = \frac{\tau}{M} \cdot \frac{1-2u^2}{1-u} \tag{2}$$

$$\varepsilon = \frac{u}{1-u} \tag{3}$$

It is easy to see that, based on the results of measurements of the compression stress Q and compression Δq of the sample, it is impossible to determine *M* and u separately; one can only find the value of the expression that contains both quantities simultaneously:

$$\frac{j_z}{\tau} = \frac{\Delta q}{q_0 \tau} = \frac{\frac{1-2u^2}{1-u}}{M} \tag{4}$$

where j_z – initial relative deformation of the sample before applying the current pressure stage (dimensionless quantity); τ – increment of vertical stress at this stage ($\tau = \tau_i - \tau_h$), kPa; τ_i – final (specified) vertical stress at the fixed loading stage, kPa; τ_h – initial vertical (axial) stress, кPa; Δq – absolute vertical strain (compression displacement) (mm); q_0 – initial height of the specimen (mm); $\frac{1-2u^2}{1-u}$ – lateral constraint coefficient (a coefficient accounting for the constraint of lateral expansion / rigid confinement in a stabilometer); u – Poisson's ratio; M – deformation modulus (elasticity/compaction modulus), кPa.

Usually, Poisson's ratio u is taken from reference data, and then *M* is found from relation (4). For the case of a limited pressure range $\tau = \tau_r - \tau_h$:

$$j_z = \frac{j_h - l_i}{1 + l_h} = \frac{b}{1 + j_h} \cdot (\tau_i - \tau_h) = \frac{b\tau}{1 + j_h} \tag{5}$$

where j_h – initial relative deformation (strain) of the sample before applying the current pressure stage; l_h – initial relative deformation of the sample before applying the current pressure step, (dimensionless quantity); l_i – final relative deformation of the sample at the controlled test stage, (dimensionless value); b – the compaction (compression) coefficient of a dispersed material, which characterizes the compliance of its framework and structural variability under external load, kPa^{-1}. From expressions (2) and (5) we obtain the relationship between *M*, u and *b*:

$$M = \frac{1 + j_h}{b} \cdot \left(\frac{1-2u^2}{1-u}\right). \tag{6}$$

Statistical Analysis

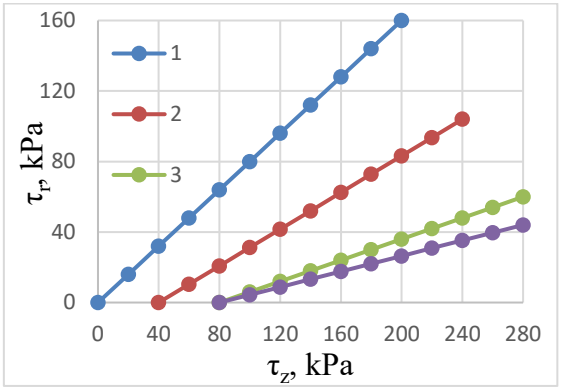
All experiments were performed in at least three independent replicates (*n*=3). The experimental data were statistically analyzed using Microsoft Excel and Origin software. Results are presented as mean ± standard deviation ($\bar{x} \pm SD$) or mean with a 95% confidence interval. The variance (S^2) and standard error of the mean ($SE = \frac{SD}{\sqrt{n}}$) were calculated to verify data reproducibility. Final parameter estimation and functional approximations were performed using the multivariate least squares method.

3. Results

To validate the proposed methodology, a series of triaxial compression experiments was carried out on several dispersed materials. The obtained deformation and strength characteristics are presented below. The experimental results showed that the modulus M, as well as the lateral pressure and Poisson coefficients, largely depend on the porosity of the layer. These difficulties in determining M and u can be avoided by measuring the $\tau_r = \tau_y$ values at each loading stage. Then, from the $\tau_r = f(\tau_z)$ dependence graph (Fig. 3a) approximated by a straight line of the form $y = kx + b$, one can easily obtain the lateral pressure coefficient $\varepsilon = \frac{\tau_r}{\tau_z}$. Then, from the $j_z = f(\tau_z)$ dependence graphs, also approximated by a straight line (Fig. 3 b), one can determine the modulus $M = \frac{\Delta\tau_z}{\Delta j_z} \cdot \alpha$, $\alpha = \frac{1-2u^2}{1-u}$, where α is a coefficient that takes into account the impossibility of lateral expansion. Poisson's ratio can be determined as $u = \frac{\varepsilon}{1+\varepsilon}$. The values of these coefficients for some materials are given in Table1.

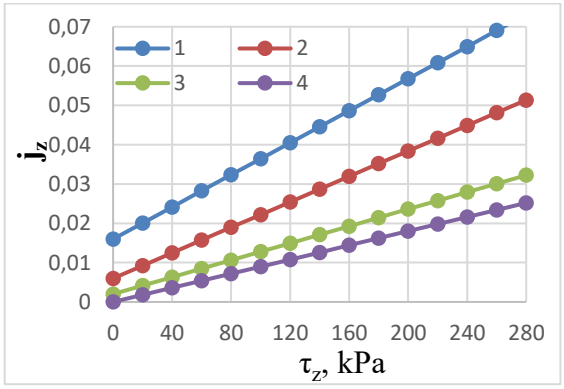
Table 1. MechMechanical properties of the investigated materials (mean ± SD, n = 3).

Parameter	Limestone Scheme 1	Limestone Scheme 2	Sand Scheme 1	Sand Scheme 2	Coke Scheme 1	Coke Scheme 2
Deformation modulus, M, MPa	1.58±0.05	1.54±0.04	1.95±0.06	1.94±0.05	7.67±0.18	7.72±0.21
Lateral pressure coefficient, dimensionless	0.75±0.02	0.73±0.02	0.39±0.01	0.39±0.01	0.25±0.01	0.26±0.01
Poisson's ratio, dimensionless	0.44±0.01	0.42±0.01	0.30±0.01	0.30±0.01	0.18±0.01	0.21±0.01



a)

1 – limestone, Modul 1; 2 – coke, Modul 1;
3 - koksik, Modul 2; 4 – grit, Modul 1



b)

1 – limestone, Modul 1; 2 – sand, Modul 1;
3 – grains, Modul 1; 4 – coke, Modul 1

Fig. 3. The effect of vertical stress on the value of: a) lateral stress and b) relative deformation for different materials.

The primary characteristics of the reference materials used during the experimental validation are systematically presented in Table 2.

Table 2. The primary characteristics of the reference materials

Parameter	Sand	Iron ore concentrate	Coke	Limestone	Iron ore concentrate grit
Equivalent particle diameter, 10^{-3}m	0.16	0.08	2.00	0.63	2.00
Density, kg/m^3	2923	3547	1652	2801	3686
Hovering speed, m/s	2.8	1.6	7.9	5.8	9.2
Internal friction coefficient	1.42	0.92	0.94	0.55	0.51
Layer porosity, m^3/m^3	0.36	0.29	0.56	0.47	0.53

To determine the strength characteristics [9, 10], dependence graphs were constructed $j_z = f(\tau_z - \tau_r)$ at different values of lateral pressure τ_r (Fig. 4). The values were determined from the graphs $(\tau_z - \tau_r)$, corresponding to the moment of specimen destruction. Figure 4 shows the classic deformation curves of a

granular medium at four fixed levels of lateral pressure. The physical meaning of the curves is as follows: the graph clearly demonstrates the nonlinear nature of the medium's deformation. The point where the curve becomes almost vertical corresponds to the moment when the final equilibrium is reached and the sample breaks (shears). The greater the material's bearing capacity, the greater the stress deviation at which failure occurs $\tau_z - \tau_r$. These figures serve as an experimental confirmation that the presence of residual plastic deformations determines the strictly nonlinear nature of the formation and compaction of the layers of dispersed media. The coordinates of the fracture points (τ_z^p and τ_r^p) shown in this figure are directly used by the authors in the article for mathematical analysis.

The angle of internal friction and adhesion were determined as $\tan\gamma = \frac{F-1}{2\sqrt{F}}$, $c = \frac{T}{2\sqrt{F}}$, where F and T are coordinates determined from the expressions:

$$F = \frac{n\sum\tau_r^p\tau_z^p - \sum\tau_r^p \sum\tau_z^p}{n\sum(\tau_r^p)^2 - (\tau_r^p)^2}; \qquad T = \frac{1}{n}\left(\sum\tau_z^p - N\sum\tau_r^p\right) \tag{7}$$

where τ_z^p and τ_r^p are τ_z the τ_r values of and at specimen failure; n is the number of tests.

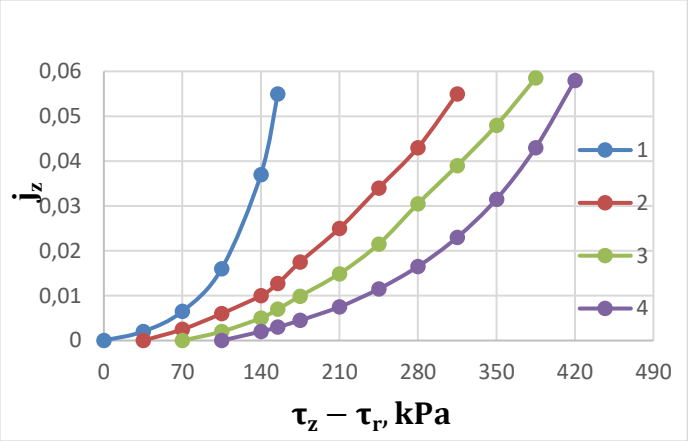


Fig. 4. Dependence of the relative strain of the grit (Modul 2) on the value of $\tau_z - \tau_r$: $1 - \tau_r$ =20 кPa; 2 – 40 кPa; 3 – 60 кPa; 4 – 80 кPa.

The calculated parameter values are presented in Table 3. A comparison of experimental and known from the literature [11] values of the angle of internal friction ($\tan\gamma$) showed that their maximum difference does not exceed 10%, which indicates not only the qualitative but also the quantitative correspondence of the data we obtained to real conditions [12,13]. Based on this information, an experimental plan developed to evaluate the dependence of the deformation modulus on the above-mentioned parameters [14, 15].

Table 3. Strength characteristics of the investigated materials (mean ± SD, n = 3)

Parameter	Coke breeze Scheme 1	Coke breeze Scheme 2	Sand Scheme 1	Sand Scheme 2	Limestone Scheme 1	Limestone Scheme 2
Internal friction angle, φ, deg	43±1.1	44±1.2	31±0.8	32±0.9	35±1.0	34±0.9
Internal friction coefficient, tan φ, dimensionless	0.92±0.03	0.91±0.03	0.61±0.02	0.58±0.02	0.70±0.02	0.68±0.02

The objective was to determine the influence of the main characteristics of the dispersed medium. In other words, the deformation modulus is a parameter. The factors chosen were material density δ, particle diameter s and the coefficient of internal friction γ. The number and values of the levels of the variable factors were determined (Table 4). The factor levels presented in Table 4 were established on the basis of the physical and mechanical properties of the investigated dispersed materials summarized in Table 2. The planning matrix was implemented by varying the density, equivalent particle diameter and internal friction angle within the experimentally observed ranges.

Table 4. Factor levels

Levels	Level 1	Level 2	Level 3	Level 4	Level 5
Particle diameter $(s), mm$	0.2	0.4	0.8	1.6	3.2
Density $(\delta), \frac{kg}{m^3} \cdot 10^{-3}$	1.1	1.2	1.3	1.4	1.5
coefficient of internal friction (γ), deg	22	24	26	28	30

The choice of five levels motivated by the fact that the number of experiments is not very large (only 25) yet sufficient to identify the required pattern of dependence [16]. With three levels identifying the pattern of dependence is difficult due to the limited number of control points. Next, a planning matrix was compiled for the three-factor five-level experiment [17]. The planning matrix is shown in Table 5.

The following difficulty arose when planning the experiment. Since the coefficient of internal friction is related to density, not all levels could be filled with the same values. The experimental results are presented in Table 6. Experiments were conducted using a stabilometer. Each experiment was repeated at least three times. meaning it consisted of at least three trials. The arithmetic mean standard error and variance were determined using standard methods. In subsequent calculations the arithmetic mean values were used as the closest approximation to the actual values. Final data processing and approximation of the empirical relationships were carried out based on the multivariate least squares method [18].

Table 5. Planning matrix

Levels	1	2	3	4	5	6	7	8	9	10	11	12	13	14	15	16	17	18	19	20	21	22	23	24	25
Density $(\delta), \frac{kg}{m^3} \cdot 10^{-3}$	1	1	1	1	1	2	2	2	2	2	3	3	3	3	3	4	4	4	4	4	5	5	5	5	5
Particle diameter $(s), mm$	1	2	2	1	1	1	2	3	1	2	4	2	3	4	3	5	3	3	4	5	5	4	5	4	5
coefficient of internal friction (	1	2	3	4	5	6	1	2	4	5	1	4	3	5	2	5	2	4	3	1	2	3	5	1	4

Table 6. Parameter values (M±SD, MPa)

Level	M_1	M_2	M_3	M_4	$\bar{M} \pm$ SD
1	29.8	29.9	30.1	30	29.95±0.13
2	32.8	32.9	33.2	33	32.98±0.17
3	39.9	40.1	40.2	40	40.05±0.23
4	37.8	37.9	38.1	38	37.95±0.18
5	41.9	42.1	42.2	42	42.05±0.27
6	31.8	31.9	32.2	32	31.97±0.15
7	38.9	39.1	39.2	39	39.05±0.19
8	39.8	39.9	40.1	40	39.95±0.22
9	44.7	44.9	45.2	45	44.95±0.32
10	48.7	48.8	48.9	49	48.85±0.34
11	43.8	43.9	44.1	44	43.95±0.29
12	44.6	44.9	45.2	45	44.92±0.31
13	41.7	41.8	41.9	42	41.85±0.25
14	56.8	56.9	57.1	57	56.95±0.42
15	40.6	40.8	41.2	41	40.90±0.24
16	60.8	60.9	61.1	61	60.95±0.45
17	48.7	48.8	48.9	49	48.85±0.35
18	47.6	47.9	48.2	48	47.92±0.34
19	45.8	45.9	46.1	46	45.95±0.32
20	43.1	43.2	43.3	43	43.15±0.28
21	41.8	41.9	42.1	42	41.95±0.26
22	47.7	47.8	47.2	48	47.67±0.33
23	64.8	64.9	65.1	65	64.95±0.50
24	44.7	44.8	45.2	45	44.92±0.30
25	61.8	61.9	62.1	62	61.95±0.46

Note: Values are represented as mean ± standard deviation for $n \geq 3$ trials.

First paired dependencies were determined by sampling. After sampling the experimental results for each level of each factor five-point paired partial dependencies were obtained between the deformation modulus

and density the angle of internal friction and particle size [19]. The influence of factors on the deformation modulusis shown in Figure 5. Private point dependencies were obtained after ranking the results by increasing each factor and were described mathematically.

The corresponding correlation equations were found using the least squares method. They have the following form: $M_\gamma = 2\gamma\text{-}9$, $M_\delta = 27.3\cdot\delta^{1.8}$, $M_s = 40.1\cdot s^{-0.2}$. These values were then substituted into the empirical multifactorial equation of Protodyakonov [20]:

$$y_n = \frac{\sum_{i=1}^{k} y_i}{y_{av}^{k-1}} \tag{8}$$

where y_n – multifactor equation of M.M. Protodyakonov; y_i – partial functions; y_{av}– average value of all experimental results taken into account; k – number of factors (partial functions).

Thus. we constructed a generalized formula that takes into account all factors:

$$M = \frac{M_\delta \cdot M_\gamma \cdot M_s}{(M_{av})^2} = \frac{27.3 \cdot \delta^{1.8} \cdot 40.1 \cdot s^{-0.2} \cdot (2\gamma - 9)}{2023.2004} = 0.54 \cdot s^{-0.2} \cdot \delta^{1.8} \cdot (2\gamma - 9) \tag{9}$$

where γ – angle of internal friction, *deg*; δ – material density, $\frac{\text{kg}}{m^3} \cdot 10^{-3}$; s – particle diameter, *mm*.

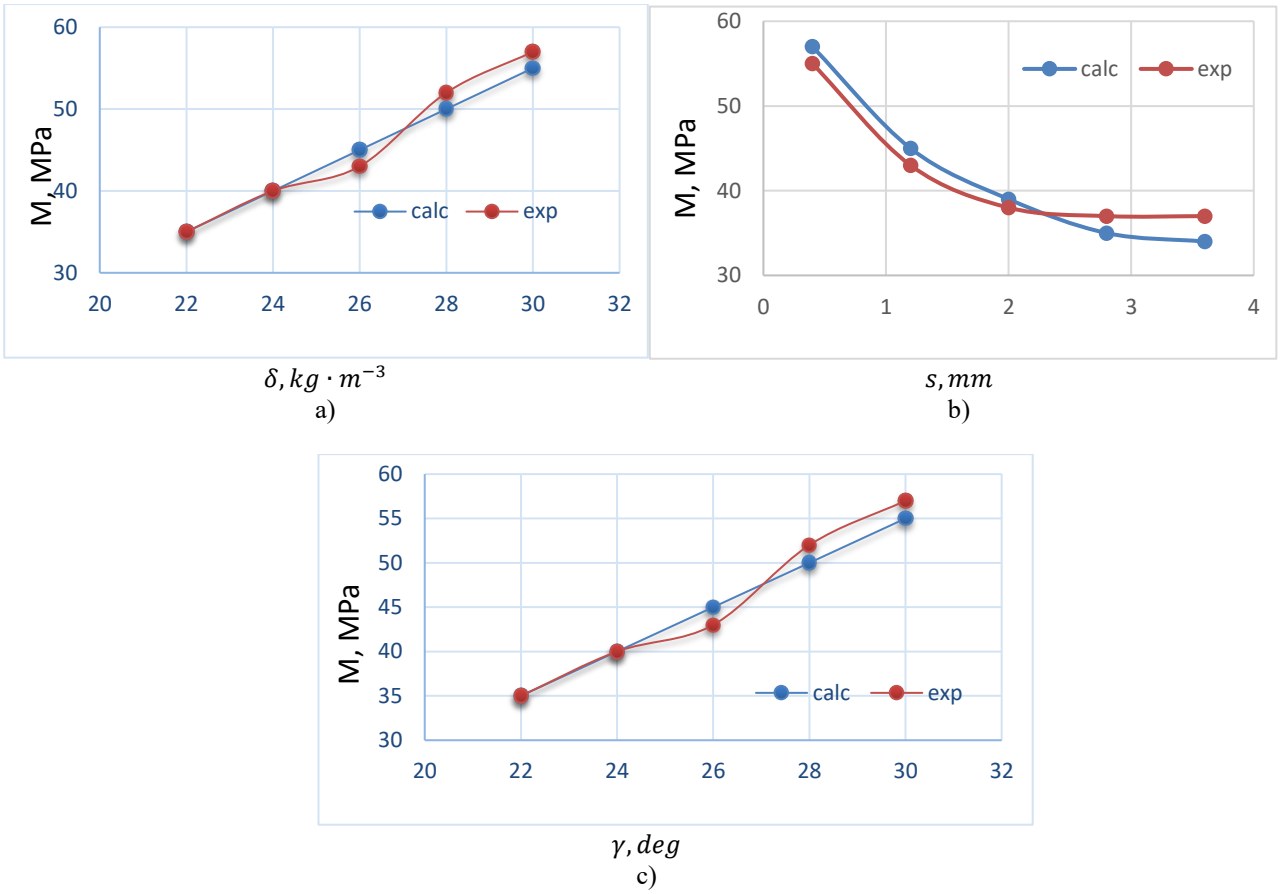


Fig. 5. Effect of deformation modulus:
a) density; b) particle size; c) the internal friction coefficient.

The minus sign indicates that the effect of the corresponding factor is inversely proportional: the greater the factor, the smaller the parameter *M*. An increase in the density of the granular medium leads to an increase in the deformation modulus. The increase in deformation with a decrease in particle size can be explained as follows: the smaller the material, the more densely it packs together, the greater the number of interparticle contacts, and the greater the force required for deformation.

To assess the goodness of fit, the nonlinear multiple correlation coefficient was used [21]:

$$R = \sqrt{1 - \frac{(n-1)\sum_{i=1}^{n}(y_{expi} - y_{thei})^2}{(n-k-1)\sum_{i=1}^{n}(y_{expi} - y_{avei})^2}} \quad (10)$$

where n – number of data points; k – number of active factors (equal to one for partial dependencies); y_{expi} – experimental value of the result; y_{thei} – theoretical (calculated) value; y_{avei} – the average experimental value.

Based on the calculation results, the correlation coefficient was found for n=25 and k=3. It is equal to R=0.8, and the significance is t=10.17>2, which indicates the adequacy of the generalized equation. The error of the equation was calculated using the formula and amounted to 11%:

$$\sigma = \sqrt{\frac{\sum_{i=1}^{n}(y_{expi} - y_{thei})^2}{(n-k-1)}} \quad (11)$$

The experimental results showed that the deformation modulus is significantly influenced by material density, particle size, and the coefficient of internal friction. An increase in density and internal friction coefficient leads to higher stiffness of the medium, whereas an increase in particle diameter causes a decrease in the deformation modulus. The triaxial compression tests also demonstrated the nonlinear character of deformation and compaction processes caused by residual plastic strains. The determined strength and deformation characteristics are in good agreement with published data, with deviations not exceeding 10%, confirming the reliability of the proposed approach.

4. Discussion

The experimental results demonstrate that the deformation behavior of dispersed media under triaxial compression is governed primarily by three interrelated factors: material density, particle size, and the internal friction coefficient. An increase in density leads to a more compact particle arrangement and a larger number of interparticle contacts, resulting in higher resistance to deformation and, consequently, an increase in the deformation modulus. This tendency agrees with the classical concepts of granular media mechanics and soil behavior reported in previous studies [1–3].

The influence of particle size is opposite. As the equivalent particle diameter increases, the deformation modulus decreases because the contact area between particles is reduced and the packing becomes less dense. Similar relationships have been reported in studies devoted to the mechanical behavior of granular soils and particulate materials under compression [9–13]. The obtained results confirm that particle size should be considered together with density rather than as an independent parameter.

The internal friction coefficient also has a significant influence on the deformation characteristics. Materials possessing larger internal friction angles exhibit higher stiffness and greater resistance to irreversible deformation. This observation is consistent with the physical interpretation of shear resistance in granular systems and agrees with the published experimental data on triaxial compression and shear testing [5, 6, 11].

An important result of this study is the experimental confirmation of the nonlinear character of deformation during confined compression. The observed nonlinearity is associated with the accumulation of residual plastic strains and progressive rearrangement of particles inside the granular structure. As loading increases, the contact network evolves continuously, leading to changes in stress redistribution and stiffness. This behavior confirms that linear elastic models are insufficient for describing the deformation of dispersed media over a wide loading range. Unlike many previous investigations that primarily focused on determining mechanical characteristics of soils or granular materials, the present work emphasizes the modernization of the experimental methodology and testing apparatus.

The proposed triaxial compression setup provides independent control of axial and lateral stresses while ensuring continuous measurement of deformation parameters. Such an approach improves the reliability of determining deformation characteristics and extends the applicability of the stabilometer to a wider range of dispersed materials. In contrast to previous studies, the present work combines modernization of the experimental apparatus with a validated methodology for determining both deformation and strength characteristics of dispersed media within a single triaxial testing procedure. The adequacy of the obtained empirical model is supported by the multiple nonlinear correlation coefficient (R=0.8), indicating satisfactory

agreement between the calculated and experimental values. The error of the equation was calculated using the formula and amounted to 11% is acceptable for engineering applications involving heterogeneous granular media, where natural variability of material properties is unavoidable.

The proposed methodology may therefore be used not only for laboratory determination of deformation properties but also for engineering prediction of the mechanical behavior of cohesive and non-cohesive dispersed materials in metallurgical, mining and foundry technologies. Further studies should investigate the influence of moisture content, particle shape, loading rate and cyclic loading on the rheological characteristics of dispersed systems.

5 Conclusions

1. A modernized triaxial compression methodology based on a standard stabilometer has been developed for determining the rheological, deformation and strength characteristics of dispersed media under controlled loading conditions. The proposed experimental setup provides independent control of axial and lateral stresses, thereby improving the reliability and reproducibility of experimental measurements.

2. Experimental investigations demonstrated that the deformation modulus of dispersed materials is primarily governed by material density, equivalent particle diameter, and the internal friction coefficient. An increase in density and internal friction results in higher stiffness of the granular medium, whereas an increase in particle size leads to a reduction in the deformation modulus.

3. The triaxial compression tests confirmed the nonlinear character of deformation caused by progressive particle rearrangement and the accumulation of residual plastic strains. This behavior should be taken into account when describing the mechanical response of cohesive and non-cohesive dispersed materials under compression.

4. An empirical multifactor model describing the dependence of the deformation modulus on the governing parameters was developed using the results of a planned experiment. The adequacy of the model was confirmed by satisfactory agreement between the calculated and experimental data ($R = 0.8$), while the average prediction error did not exceed 11%.

5. The proposed methodology and the modernized experimental apparatus may be used for laboratory determination of deformation characteristics and for engineering prediction of the behavior of dispersed materials in metallurgical, foundry, mining and other technological processes involving bulk media. Further investigations should consider the influence of moisture content, particle shape and loading rate on the rheological behavior of dispersed systems.

Conflict of interest statement
The authors declare that they have no conflicts of interest in this work.

CRediT author statement
Kazhikenova S.: Conceptualisation, Methodology, Software, Data curation, Writing draft preparation. S. Akhmetova, D. Belomestny,: Visualisation, Investigation, Validation, Reviewing and Editing.
The final manuscript was read and approved by all authors.

Statement on the use of Artificial Intelligence.
The authors declare that no artificial intelligence tools were used to generate scientific content, results, or conclusions of this article.

Data Availability Statement
The data are available upon reasonable request from the authors.

Funding

This research was funded by the Science Committee of the Ministry of Science and Higher Education of Kazakhstan Republic (Grant No. AP23486482): «Development of information models for managing technological processes of metallurgical production, monitoring their functioning».

References

1 Mitchell, J.K., & Soga, K. (2005). Fundamentals of soil behavior (3rd ed.). New York: John Wiley & Sons. ISBN 0-471-46302-7

2 Santamarina, J.C., Klein, K.A., & Fam, M.A. (2001). Soils and waves: Particulate materials behavior, characterization and process monitoring. John Wiley & Sons. ISBN 978-0-471-49058-6

3 Tsytovic, N.A. (2014). Soil mechanics (theoretical fundamentals). Librokom. [in Russian] ISBN 978-5-397-04148-5.

4 Lade, P. V. (2016). *Triaxial testing of soils*. Wiley-Blackwell. ISBN: 978-1-119-10662-3. https://doi.org/10.1002/9781119106616

5 Cekerevac, C., Laloui, L., & Vulliet, L. (2005). A Novel Triaxial Apparatus for Thermo-Mechanical Testing of Soils. *Geotechnical Testing Journal*, 28(2), 161-170. https://doi.org/10.1520/GTJ12311

6 Zeng, F., & Shao, L.T. (2016). Unloading Elastic Behavior of Sand in Cyclic Triaxial Tests. *Geotechnical Testing Journal,* 39(3). 1-14. https://doi.org/10.1520/GTJ20150171

7 Sadd, M.H. (2009). *Elasticity: Theory. applications. and numerics* (4th ed.). Academic Press. https://doi.org/10.1016/B978-0-12-374446-3.X0001-6

8 Altenbach, H., & Öchsner, A. (Eds.). (2023). *Encyclopedia of continuum mechanics*. Springer. https://doi.org/10.1007/978-3-662-55771-6

9 Aziz, M., Towhata, I., & Irfan, M. (2016). Strength and deformation characteristics of degradable granular soils. *Geotechnical Testing Journal*, *39*(3). 405 - 421. https://doi.org/10.1520/GTJ20150209

10 Cadet, K., McGregor, F., Perlot, C., & Seco, A. (2026). From rheology to mechanical strength: Methodological and experimental investigation of the fine fraction (<400 μm) of soils for low-carbon earthen construction. *Sustainability,* 18(5), Article 2493. https://doi.org/10.3390/su18052493

11 Seiphoori, A., Duong, T., & Geyin, M. (2025). Comparative analysis of ring shear and direct shear tests for interface friction angle of granular materials. *Geotechnical Frontiers,* 231 - 240. https://doi.org/10.1061/9780784486009.024

12 Akhunov, A., & Tukmakov, D. (2020). Numerical study of the influence of material density of dispersed inclusions on the process of gas-suspension splitting in vacuum. *Bulletin of the Trans-Baikal State University*, 26(3). 6-14. https://doi.org/10.26117/2079-6641-2020-30-1-109-119

13 Andrade, F.A., Al-Qureshi, H.A., & Hotza, D. (2011). Measuring the plasticity of clays: A review. *Applied Clay Science,* 51(1-2), 1-7. https://doi.org/10.1016/j.clay.2010.10.028

14 Morozov, A.V., & Levenson, S.Y. (2021). Ways to increase the efficiency of engineering processes when forming high-density arrays of disperse materials. *Interexpo GEO-Siberia,* 2(3), 295-303. https://doi.org/10.33764/2618-981X-2021-2-3-295-303

15 Morozov, A.V., & Usol'tsev, V.M. (2019). Disperse Material Compression by Attachment with Polyharmonic Source of Oscillations. *International Scientific Conference «Nedropol'zovaniye. Gornoye delo»,* (4), 182-189. https://doi.org/10.33764/2618-981X-2019-2-4-182-189

16 Bjorck, A. (1996). Numerical methods for least squares problems. *Society for Industrial and Applied Mathematics.* https://doi.org/10.1137/1.9781611971484

17 Bulatova, A.Z., Solnyskina, O.A., & Fatkullina, N.B. (2023). Numerical study of the rheological characteristics of dispersed systems in shear flow using the boundary element method. *St. Petersburg Polytechnic University Journal. Physics and Mathematics,* 16(1.1), 288-294. https://doi.org/10.18721/JPM.161.148

18 Bulatova, A.Z., Fatkullina, N.B., & Pityuk, Y.A. (2019). Numerical simulation of the dynamics and calculation of the rheological characteristics of the dispersed systems using BEM. *Journal of Physics: Conference Series,* 1359. 012025. https://doi.org/10.1088/1742-6596/1359/1/012025

19 Heumann, C., Schomaker, M., & Shalabh. (2022). *Introduction to statistics and data analysis: With exercises, solutions and applications in R*. Springer. https://doi.org/10.1007/978-3-031-11833-3

20 Akberdin, A.A., Kim, A.S., & Sultangaziev, R.B. (2019). Planning of numerical and physical experiment when modeling technological processes. *Izvestiya Vysshikh Uchebnykh Zavedenii. Chernaya Metallurgiya*, 61(9), 737-742. https://doi.org/10.17073/0368-0797-2019-9-737-742

21 Bzik, T.J. (2012). Statistical methods for engineers and scientists. *Technometrics*, *39*(2), 229. https://doi.org/10.1080/00401706.1997.10485092

AUTHORS' INFORMATION

Kazhikenova, **Saule Sh. -** Doctor of Technical Sciences, Higher Mathematics Department, Abylkas Saginov Karaganda Technical University, Nazarbayev str., 56, 100000, Karaganda, Kazakhstan. sauleshka555@mail.ru https://orcid.org/0000-0002-6937-1577

Akhmetova, Sandugash - Candidate of Technical Sciences, Associate Professor of the Department of Higher Mathematics at the Karaganda Technical University named after A. Saginov, Kazakhstan, https://orcid.org/0009-0003-7848-4463; s.akhmetova@ktu.edu.kz

Belomestny, Denis – Ph.D., Professor, University of Duisburg-Essen, Forsthausweg 247057 Duisburg, Germany, Scopus ID: 15069577900; https://orcid.org/0000-0002-9482-6430, denis.belomestny@uni-due.de

EURASIAN PHYSICAL TECHNICAL JOURNAL

2026, Volume 23, No. 3 (57)

https://doi.org/10.31489/2026N3/115-124

Received: 30/07/2026 Revised: 03/092026 Accepted: 28/09/2026 Published online: 30/09/2026

Original Research Article

Open Access under the CC BY -NC-ND 4.0 license

UDC: 534.874.1; 629.07;654.9

AUTONOMOUS SEARCH AND RESCUE DRONE WITH REAL-TIME YOLO OBJECT DETECTION AND GPS NAVIGATION USING RASPBERRY PI 4

Turmaganbet U.K.[1], Turlykozhayeva D.A.[1], Akhtanov S.N.[1], Temesheva S.A.[1]*, Ussipov N.M. [1], Tao M.[2]

[1] al-Farabi Kazakh National University, Almaty, Kazakhstan
[2] School of Electronics and Information, Northwestern Polytechnical University, Xian, China
*Corresponding author: temesheva_symbat4@live.kaznu.kz

Abstract. *The development of intelligent unmanned aerial vehicles with onboard computer vision capabilities is increasingly relevant to search and rescue operations. However, real-time human detection on compact UAV platforms remains challenging due to limited computational resources, varying environmental conditions, and the small size of distant targets. This study presents a UAV-based human detection and localization system integrating a Raspberry Pi 4 Model B, YOLOv8, and u-blox NEO-M8N GPS. The system performs onboard processing of the video stream and associates detected targets with the UAV's geographical position. The YOLOv8 model was trained using the VisDrone2019-DET dataset and evaluated through real-world flight experiments under different distances, altitudes, and lighting conditions. The system achieved an average detection confidence of 0.67, with a maximum confidence of 0.81, and a real-time processing speed of 4–8 FPS. Human targets were detected at distances of up to 30 m, while GPS positioning errors ranged from 1.6 to 2.8 m, with a mean error of approximately 2.12 m. The results demonstrate the capability of the proposed UAV platform to perform onboard human detection and GPS-based localization in real-time, providing a basis for UAV-assisted search and rescue applications.*

Keywords: Unmanned aerial vehicles, search and rescue, object detection, computer vision, autonomous navigation, embedded systems, real-time processing.

1. Introduction

Unmanned aerial vehicles (UAVs) have become an important technology for search and rescue (SAR) operations, providing rapid aerial surveillance, efficient coverage of large areas, and direct access to hazardous or inaccessible locations. Compared with traditional ground searches, UAVs can reduce response time and improve situational awareness by transmitting live video and collecting geographic information during flight. These capabilities are especially valuable in forests, mountainous terrain, and disaster-affected areas [1-3].

Recent advances in artificial intelligence have significantly improved the autonomy of UAV systems. Computer vision algorithms, particularly the YOLO family of object detectors, enable drones to identify people in aerial images with high processing speed, making them suitable for real-time applications on embedded platforms. Combined with GPS navigation, onboard detection allows each identified target to be associated with geographic coordinates, providing rescue teams with accurate location information [4,5].

Despite these advances, practical deployment of UAV-based SAR systems remains challenging because human targets often appear as small objects against complex aerial backgrounds, while varying illumination, shadows, and limited onboard computational resources can affect detection performance. Previous studies have addressed lightweight object detection and autonomous navigation; however, practical UAV-based SAR

systems still face challenges in combining real-time onboard inference with GPS-based localization and reliable field operation on resource-constrained embedded platforms [6-11].

This study presents the design and experimental validation of an autonomous FPV UAV based on Raspberry Pi 4 that integrates lightweight YOLO-based human detection with GPS navigation. The proposed system performs onboard real-time video processing, associates detected human targets with GPS coordinates, and records detection data to support search and rescue operations.

The main contributions of this work are:

1) Development and engineering integration of a compact, Raspberry Pi 4-based UAV platform for onboard human target detection;

2) Implementation of real-time YOLOv8 detection synchronized with GPS coordinates using standard, unmodified network architecture;

3) Experimental validation of the complete hardware–software system under real flight conditions, evaluating detection accuracy, processing speed, and GPS positioning error.

The article is organized into five sections. Section II presents related work on UAV-based search-and-rescue systems and deep learning-based object detection. Section III describes the materials and methods, including the proposed UAV system architecture, hardware and software configuration, YOLOv8 training, and experimental methodology. Section IV presents the experimental results, including YOLOv8 detection performance, real-time inference results, and GPS positioning accuracy. Section V concludes the study by summarizing the main findings and outlining directions for future work.

2. Related Works

Recent studies have investigated deep learning-based methods for human and object detection in UAV-assisted search and rescue applications. In [3], the authors developed a drone-based autonomous human identification system for real-time search and rescue missions. The proposed approach combines human detection with UAV-based localization and autonomous operation. In [2], the authors investigated autonomous human detection using a lightweight deep learning model deployed on embedded UAV hardware. In [8], the authors presented a state-of-the-art review of human detection from UAV imagery for search and rescue missions, covering existing detection methods, datasets, and evaluation approaches.

YOLO-based architectures have been widely investigated for real-time detection in aerial imagery. In [1], the authors studied YOLO-based detection for real-time search and rescue and evaluated different architectural modifications, including FPN, BiFPN, PB-FPN, an additional P2 detection head, attention modules, and deconvolution. The experiments were conducted using VisDrone for initial training and the Heridal dataset for SAR-specific fine-tuning. The best-performing configuration achieved a mAP@50 of 0.802 while maintaining real-time inference on Jetson Nano hardware.

In [6], the authors proposed an enhanced YOLO11 model for maritime search and rescue object detection. The architecture incorporates a Space-to-Depth module in the backbone, content-aware upsampling in the neck, and an additional detection head for shallow features. The proposed modifications were designed to improve the detection of small, overlapping, and rarely occurring objects. Experiments on the SeaDronesSee dataset showed improved performance compared with YOLOv8, YOLO11, and MambaYOLO, including under lightweight model configurations. In [7], the authors investigated small-object detection for maritime search and rescue using a virtual testbed developed in Unreal Engine. The study focused on customizing YOLO models and using a simulated environment for training and evaluation. The virtual testbed was used to reproduce different maritime SAR conditions and to investigate the performance of object detection models under controlled scenarios. Model architecture and computational efficiency have also been investigated in UAV-based SAR applications. In [9], the authors evaluated different backbone architectures for YOLOv10 across several model variants, including Nano, Small, Medium, Large, and X-Large configurations. The study compared EfficientNet, GhostNet, MobileNet, ResNet50, and Swin backbones in terms of detection accuracy, inference speed, and computational requirements. The YOLOv10-Nano configuration with a MobileNet backbone achieved 80.5 FPS with a mAP@0.5:0.95 of 0.3945, while larger configurations provided higher detection accuracy at increased computational cost.

Thermal infrared imagery has also been investigated with YOLO-based object detection. In [12], the authors evaluated YOLO models for object detection in thermal infrared images. The study examined the performance of different YOLO architectures on thermal data and investigated their applicability to object detection under conditions where thermal information can provide an alternative to visible-spectrum imagery.

Autonomous UAV navigation has been considered together with computer vision-based detection. In [13], the authors investigated autonomous UAV navigation for search and rescue missions using computer vision and convolutional neural networks. The system combines visual perception with UAV navigation and object tracking. At the multi-UAV level, in [4], the authors proposed an open collaborative platform for multiple drones supporting search and rescue operations. The platform addresses coordination and information exchange between UAVs during SAR missions. In [5], the authors developed an autonomous search and rescue drone integrating onboard computing, flight control, and deep learning-based object detection.

In [10], the authors reviewed smart drone technologies for security surveillance and search and rescue applications, including sensing, artificial intelligence, autonomous operation, and communication technologies. In [11], the authors reviewed metaheuristic algorithms for node placement in UAV communication networks, covering optimization approaches for UAV-assisted communication systems. However, existing approaches still have limitations related to small-object detection, computational complexity, and real-time deployment. Architectural modifications can improve detection accuracy but may increase model complexity, while lightweight models can reduce computational requirements at the cost of detection performance.

3. Materials and Methods

3.1 System Architecture

The proposed UAV system consists of two main components: the flight platform and the ground equipment. The flight platform integrates the propulsion system, flight controller, GPS/compass module, onboard computing unit, camera, battery, and communication receiver. The ground equipment provides remote control and monitoring of the UAV during operation. The flight controller is responsible for real-time flight stabilization, sensor processing, and motor control, while the Raspberry Pi 4 Model B performs onboard image processing and YOLO-based object detection. The camera provides a real-time video stream to the Raspberry Pi, where individual frames are processed to identify objects of interest. The u-blox NEO-M8N GPS module provides the current geographical position of the UAV, which is associated with the detected objects [14]. The separation of flight-control and computational functions allows the flight controller to maintain stable UAV operation independently of the computational load generated by the object detection process. The overall electrical and data connections between the main components of the proposed platform are illustrated in Fig.1.

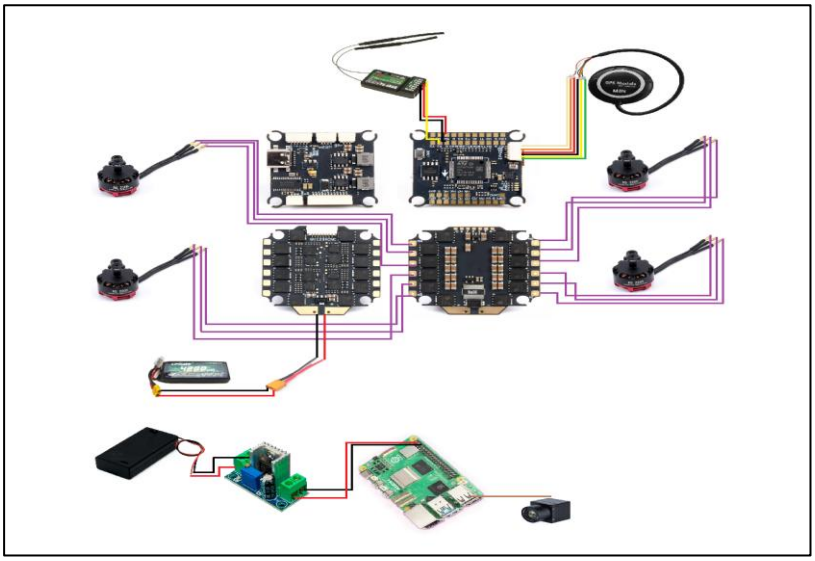


Fig.1. Architecture of the Autonomous Drone System.

Figure 2 presents the functional architecture of the proposed UAV system. The architecture is divided into two main subsystems: flight control and AI-based processing. The flight-control subsystem consists of the flight controller, electronic speed controllers (ESCs), and motors, which provide UAV stabilization and propulsion.

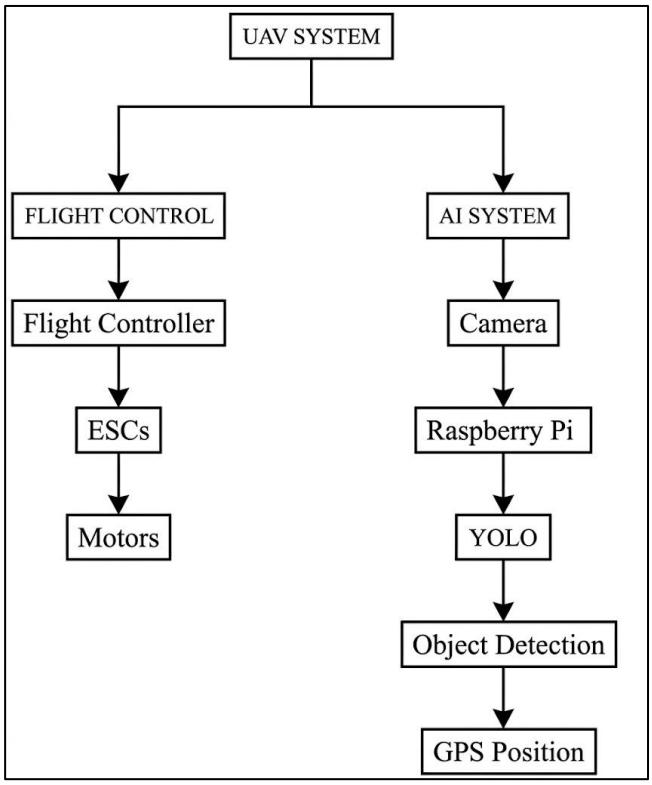


Fig.2. Functional architecture of the proposed UAV-based object detection system.

The AI subsystem includes the camera, Raspberry Pi onboard computer, and YOLO detection model. The camera provides image data to the Raspberry Pi, where YOLO performs real-time object detection. The detected objects are subsequently associated with the UAV's GPS position to obtain their geographical coordinates.

3.2 Hardware Configuration

The UAV platform was assembled using commercial components for flight control, propulsion, navigation, communication, and onboard computing. The main hardware components and their functions are summarized in Table 1. The F405 flight controller with an integrated 65A 4-in-1 ESC serves as the main flight-control unit. It is based on the STM32F405 ARM Cortex-M4 microcontroller and ICM42688P IMU, providing real-time sensor processing, flight stabilization, and motor control. The integrated ESC controls four EMAX RS2205 2300KV brushless motors equipped with HQ5045 BN propellers [15]. Navigation is provided by the u-blox NEO-M8N GPS module with an integrated compass.

Table 1. Hardware configuration of the proposed UAV platform.

Component	*Model / Specification*	*Function*
Flight controller	F405 + STM32F405 + ICM42688P	Flight stabilization and sensor processing
ESC and propulsion	65A 4-in-1 ESC, EMAX RS2205 2300KV ×4, HQ5045 BN	Motor control and propulsion
GPS/Compass	u-blox NEO-M8N	Positioning and orientation
Onboard computing	Raspberry Pi 4 Model B	Image processing and YOLO inference
Power system	4S LiPo, 4200 mAh	UAV and onboard power supply

The module supports multiple GNSS constellations and communicates with the flight controller through UART. The FlySky FS-iA6B receiver provides wireless remote-control communication with the flight controller. The Raspberry Pi 4 Model B is used as the onboard computing platform for image processing and

YOLO-based object detection. The flight controller and Raspberry Pi operate as separate processing units, allowing flight stabilization and AI-based image processing to be performed independently. The UAV is powered by a LiPower 4200 mAh 4S LiPo battery. A DC-DC step-down converter provides a regulated 5 V supply for the Raspberry Pi to ensure stable onboard computing during operation.

3.3 Software Pipeline and YOLO Training Configuration

The YOLOv8 model was trained on the VisDrone2019-DET [16] dataset using an NVIDIA GeForce RTX 4090 GPU. The training pipeline was configured for 100 epochs with a batch size of 16 and an image resolution of 1280 × 720 pixels. Standard data augmentation techniques provided by the Ultralytics [17] framework were applied during training to enhance model robustness under varying illumination and aerial perspectives, including mosaic augmentation, random horizontal flipping, HSV color space jittering (hue, saturation, value), and random scaling. Following training, the optimized weights were deployed directly onto the Raspberry Pi 4 Model B onboard computer for real-time inference using the CPU runtime environment.

For each detected object, the system records the detection information together with the corresponding UAV positional data obtained from the GPS module. The resulting data include the detected class, confidence score, bounding-box coordinates, geographical coordinates, and timestamp. This pipeline enables real-time object detection and provides the information required for subsequent evaluation of the UAV-based detection and localization system.

3.4 Experimental Methodology

The proposed UAV-based object detection system was evaluated through real-world flight experiments using a human target. A total of 5 flight tests were conducted at an approximate flight altitude of 5 m, with the UAV-to-target distance reaching up to 30 m during the experiments. Each test flight evaluated the system localization accuracy over one of five pre-designated ground reference points. Onboard positional telemetry was recorded using the u-blox NEO-M8N GPS module. Reliable positional accuracy was maintained during flights with a 3D fix status, 11 active satellites, and a Position Dilution of Precision (PDOP) of 1.87. Ground truth coordinates for the reference points were measured prior to the flights using a high-precision handheld GNSS receiver with differential correction as a baseline for comparison. The detection capability of the system was evaluated under different environmental and operational conditions, including clear weather, cloudy conditions, direct sunlight, shadowed areas, moving targets, and different flight conditions. During each flight, the camera provided a 1280 × 720 video stream to the Raspberry Pi 4 Model B, where the YOLOv8 model performed onboard real-time inference.

The detection performance was evaluated using precision, recall, F1-score, mAP@0.5, and mAP@0.5:0.95. Precision and recall were calculated as:

$$precision = \frac{TP}{TP+FP}, \tag{1}$$

$$recall = \frac{TP}{TP+FN}, \tag{2}$$

where TP denotes true positive detections, FP denotes false positive detections, and FN denotes false negative detections.

The mAP@0.5 metric was used to evaluate the mean Average Precision at an IoU threshold of 0.5, while mAP@0.5:0.95 represents the mean Average Precision calculated over IoU thresholds from 0.5 to 0.95 with a step of 0.05. The real-time performance of the system was evaluated using the frames per second (FPS) metric:

$$FPS = \frac{N}{T} \tag{3}$$

where N is the number of processed frames and T is the processing time in seconds.

GPS performance was evaluated using the coordinates obtained from the u-blox NEO-M8N module during flight. The localization error was determined by comparing the recorded position with the corresponding reference position.

4. Results

The experimental results demonstrate the performance of the proposed Raspberry Pi-based YOLO detection system under real-world UAV operating conditions. The trained YOLOv8 model was evaluated using the VisDrone2019-DET dataset, which contains aerial images from 10 object classes, including pedestrian and people. A Precision–Recall (PR) curve was used to evaluate the detection performance of the trained model, as shown in Figure 3.

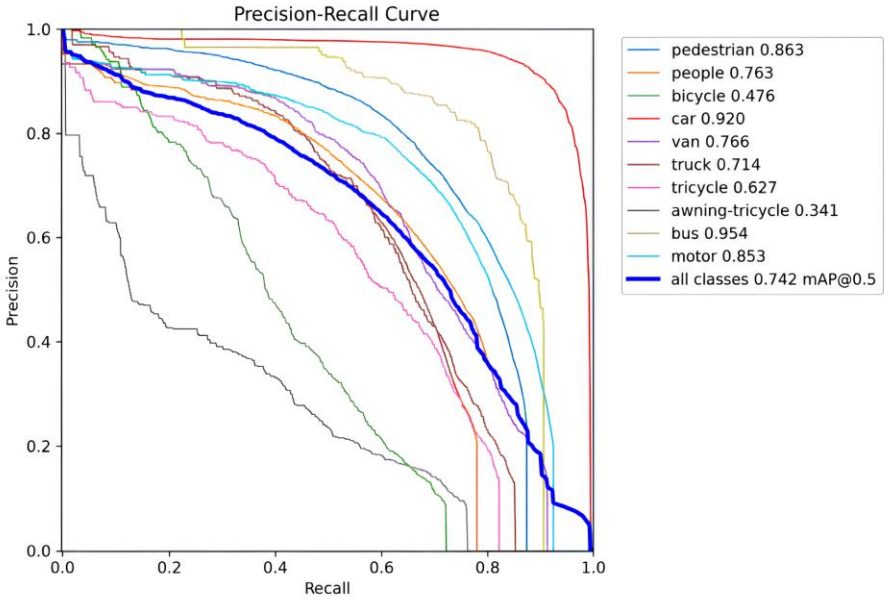


Fig.3. Precision and Recall Curve.

The system achieved an average detection confidence of 0.67, with a maximum confidence of 0.81. The real-time processing speed ranged from 4 to 8 FPS, while human targets were detected at distances of up to 30 m. The GPS-based localization error was approximately 2 m. The class-wise evaluation showed different detection performance across the object categories. Table 2 presents detection performance of YOLOv8 model.

Table 2. Detection performance of YOLOv8 on VisDrone2019-DET dataset.

Class	*AP@0.5*
Bus	0.954
Car	0.920
Pedestrian	0.863
Motor	0.853
Van	0.766
People	0.763
Truck	0.714
Tricycle	0.627
Bicycle	0.476
Awning-tricycle	0.341
All classes (Overall mAP@0.5)	**0.742**

The highest AP was obtained for bus (0.954), followed by pedestrian (0.863), motor (0.853), and people (0.763). The lowest AP was observed for awning-tricycle (0.341). The overall mAP@0.5 was 0.742. The real-world performance of the complete hardware and software architecture was evaluated during field flight operations. The onboard metrics, including processing speed, detection confidence levels, operating range, and positioning accuracy, are detailed in Table 3. The real-time detection results obtained from UAV camera frames are presented in Figure 4, demonstrating the detection of human targets during flight.

Table 3. Performance results.

Experimental Parameter	*Measured Value*
Target Detection Class	Human (Pedestrian / Person)
Onboard Hardware Platform	Raspberry Pi 4 Model B
Video Stream Resolution	1280 × 720 px
Onboard Processing Speed	4–8 FPS
Average Detection Confidence	0.67
Maximum Detection Confidence	0.81
Maximum Detection Distance	Up to 30 m
Mean GPS Localization Error	~2.12 m

As shown in Figure 4, the YOLOv8 model successfully detected human targets in the UAV video frames by generating bounding boxes and confidence scores. The confidence values varied depending on the target distance and apparent object size, with higher confidence observed for closer targets and lower confidence for more distant individuals.

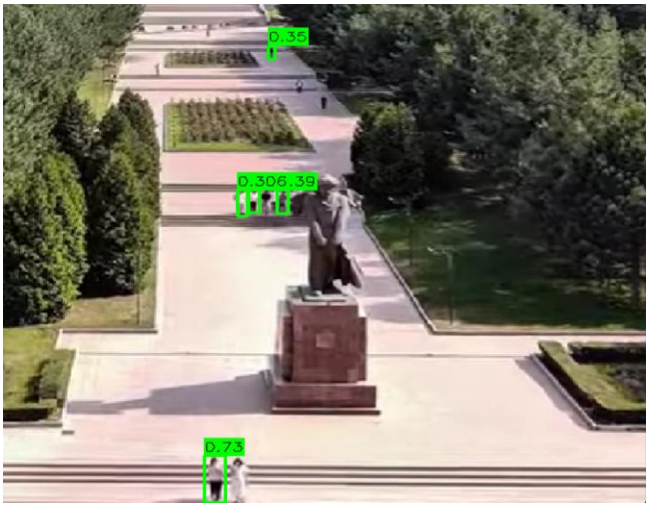


Fig. 4. Real-time human detection using the proposed UAV system.

As shown in Figure 4, the YOLOv8 model successfully detected human targets in the UAV video frames by generating bounding boxes and confidence scores. The confidence values varied depending on the target distance and apparent object size, with higher confidence observed for closer targets and lower confidence for more distant individuals. The UAV demonstrated stable flight and reliable GPS positioning during the experiments. The GPS data obtained during flight were successfully associated with the detected targets for subsequent localization. The UAV position obtained from the satellite navigation system during the experiment is presented in Figure 5.



Fig. 5. GPS position of the UAV during the experimental flight.

The GPS measurements showed positioning errors ranging from 1.6 to 2.8 m across the five reference points. The mean positioning error across all measurement points was 2.12 m, with a standard deviation (SD) of 0.44 m and a Root Mean Square Error (RMSE) of 2.16 m. The lowest error of 1.6 m was obtained at Point 3, while the highest error of 2.8 m was observed at Point 2. These statistical metrics demonstrate consistently positioning repeatability of the onboard navigation system under real flight conditions. The GPS positioning results obtained at the five reference points are presented in Table 4.

Table 4. GPS positioning accuracy at five reference points.

Measurement Point	Reference Coordinates	GPS Measurement	Error (m)
Point 1	43.2381° E, 76.9452° N	43.2383°, 76.9450°	2.1
Point 2	43.2395° E, 76.9468° N	43.2393°, 76.9471°	2.8
Point 3	43.2402° E, 76.9445° N	43.2404°, 76.9446°	1.6
Point 4	43.2378° E, 76.9479° N	43.2376°, 76.9478°	1.9
Point 5	43.2391° E, 76.9461° N	43.2390°, 76.9463°	2.2

The experimental results showed that the detection performance varied depending on target distance, illumination, object motion, and environmental conditions. Higher confidence values were generally obtained for closer targets under favorable lighting conditions, while distant or low-light targets resulted in lower detection confidence and loss of occasional detection. UAV motion and increased computational load also affected the real-time processing performance. Despite these factors, the proposed system successfully combined YOLO-based human detection with GPS positioning, allowing detected targets to be associated with their geographical coordinates during UAV operation. A quantitative comparison with recent related works is summarized in Table 5.

Table 5. Performance comparison with related UAV-based object detection systems.

Ref.	Model	Target / Dataset	Hardware Platform	Accuracy (mAP@0.5)	Speed (FPS)
[1]	Modified YOLO (FPN/BiFPN)	VisDrone / Heridal	NVIDIA	0.802	~15–25
[6]	Enhanced YOLO11	SeaDronesSee	Embedded / GPU	–	–
[9]	YOLOv10-Nano (MobileNet)	VisDrone / Benchmark	Desktop/Workstation GPU	0.394	80.5
Proposed System	Standard YOLOv8	VisDrone / Real Flight	Raspberry Pi 4 Model B (CPU)	0.742	4–8

Compared to high-throughput implementations such as [9], which achieved 80.5 FPS using YOLOv10-Nano on high-performance desktop GPU hardware, the proposed system operates at a lower rate of 4 to 8 FPS. This difference is primarily due to the severe hardware constraints of the Raspberry Pi 4 Model B, which relies exclusively on a quad-core ARM Cortex-A72 CPU without dedicated Neural Processing Units (NPUs) or onboard discrete GPUs.

Despite operating at lower frame rates than GPU-based systems, a processing speed of 4 to 8 FPS remains fully adequate for real-time UAV search and rescue operations. Assuming a standard search flight speed of 2 to 4 m/s at an altitude of approximately 5 m, processing 4 to 8 FPS provides updated target detections and synchronized GPS coordinates every 125 to 250 milliseconds. This spatial and temporal resolution ensures continuous coverage without localization blind spots, confirming the practical real-time applicability of the proposed low-cost, CPU-based system.

5. Conclusion

This study presented a UAV-based real-time human detection and localization system integrating the YOLOv8 model, Raspberry Pi 4 Model B, and u-blox NEO-M8N GPS module. The proposed system was designed to perform onboard object detection while simultaneously obtaining the geographical position of the UAV during flight.

The YOLOv8 model was trained using the VisDrone2019-DET dataset and evaluated under real-world UAV operating conditions. Experimental results showed an average detection confidence of 0.67, with a maximum confidence of 0.81. The onboard system achieved a processing speed of 4-8 FPS and detected human targets at distances of up to 30 m using a 1280 × 720 video stream. The GPS evaluation demonstrated positioning errors ranging from 1.6 to 2.8 m, with a mean error of approximately 2.12 m across five reference points. The obtained results indicate that the system can combine real-time human detection with GPS-based positional information during UAV operation. The main limitations were related to the computational resources of the Raspberry Pi 4, reduced detection confidence for distant or low-light targets, and variations caused by object motion and environmental conditions.

Future work will focus on improving real-time inference efficiency, enhancing detection performance for small and distant targets, and integrating more accurate localization and tracking methods for autonomous search-and-rescue missions.

Conflict of interest statement
The authors declare that they have no conflict of interest in relation to this research, whether financial, personal, authorship or otherwise, that could affect the research and its results presented in this paper

CRediT author statement
Turmaganbet U.K.: Conceptualization, Supervision, Writing-Original Draft**; Turlykozhayeva D.A.:** Writing-Review & Editing; **Akhtanov S.N.: Data** Curation, Writing-Original Draft; **Temesheva S.A.:** Writing-Review & Editing; **Ussipov N.M.:** Data Curation, Writing-Original Draft; **Tao M.:** Writing-Review & Editing. The final manuscript was read and approved by all authors.

Statement on the use of Artificial Intelligence.
During the preparation of this manuscript, artificial intelligence tools were used solely for language editing and grammatical improvement.

Data Availability Statement
The data that support the findings of this article are available upon reasonable request from the authors.

Funding
This work was supported by the Ministry of Science and Higher Education of the Republic of Kazakhstan (grant number AP32320585).

References

1 Ciccone, F., & Ceruti, A. (2025). Real-Time Search and Rescue with Drones: A Deep Learning Approach for Small-Object Detection Based on YOLO. *Drones*, *9*(8), 514. https://doi.org/10.3390/drones9080514

2 Vaman Ravi Prasad, D. A. S. U., & Reddy, P. (2025). Autonomous Human Detection Using Drones in Search and Rescue Operations. SSRN. https://dx.doi.org/10.2139/ssrn.5232204

3 Jayalath, K., & Munasinghe, S. R. (2021). Drone-based autonomous human identification for search and rescue missions in real-time. In *2021 10th Intern. Conference on Information and Automation for Sustainability (ICIAfS)* (pp. 518-523). IEEE. https://doi.org/10.1109/ICIAfS52090.2021.9606048

4 Ho, Y.-H., & Tsai, Y.-J. (2022). Open Collaborative Platform for Multi-Drones to Support Search and Rescue Operations. *Drones*, *6*(5), 132. https://doi.org/10.3390/drones6050132

5 Lyu, M., Zhao, Y., Huang, C., & Huang, H. (2023). Unmanned aerial vehicles for search and rescue: A survey. *Remote Sensing*, *15*(13), 3266. https://doi.org/10.3390/rs15133266

6 Zhao, B., Zhao, J., Song, R., Yu, L., Zhang, X., & Liu, J. (2025). Enhanced YOLO11 for lightweight and accurate drone-based maritime search and rescue object detection. *PLOS ONE*, *20*(7), e0321920. https://doi.org/10.1371/journal.pone.0321920

7 Vaidya, S. K., Sakthivel, V., Majumdar, R., Gupta, P., Jeevan, S., Prakash, P., & Selvamuthukumaran, T. (2026). A virtual testbed for maritime search and rescue: Customizing YOLO for small object detection in unreal engine. *Journal of Ocean Engineering and Science*. https://doi.org/10.1016/j.joes.2025.12.018

8 Abdelnabi, A. A. B., & Rabadi, G. (2024). Human detection from unmanned aerial vehicles' images for search and rescue missions: A state-of-the-art review. *IEEE Access*, *12*, 152009-152035. https://doi.org/10.1109/ACCESS.2024.3479988

9 Mishra, A., Narendra, M., Sinha, A., & Kumar, A. (2025). Dynamic Backbone Optimization of YOLOv10 for Real-Time Object Detection in UAV-Based Search and Rescue Missions. *IEEE Access*, *13*, 195975-195986. https://doi.org/10.1109/ACCESS.2025.3633379

10 Khashush, N. A., Radif, M. J., & Abdalrdha, Z. K. (2025). A review of smart drone technologies for security surveillance and search and rescue. *Journal of Al-Qadisiyah for Computer Science and Mathematics*, *17*(4), 155-173. https://doi.org/10.29304/jqcsm.2025.17.42549

11 Temesheva, S. A., Turlykozhayeva, D. A., Akhtanov, S. N., Ussipov, N. M., Zhunuskanov, A. A., Sun, W., & Tao, M. (2026). A Comprehensive Review of Metaheuristic Algorithms for Node Placement in UAV Communication Networks. *Sensors (Basel, Switzerland)*, *26*(3), 869. https://doi.org/10.3390/s26030869

12 Turmaganbet, U., Zhexebay, D., Turlykozhayeva, D., Skabylov, A., Akhtanov, S., Temesheva, S., & Tao, M. (2025). Thermal infrared object detection with yolo models. *Eurasian Physical Technical Journal*, *22*(2), 121–132. https://doi.org/10.31489/2025N2/121-132

13 Šiktar, L., Ćaran, B., Šekoranja, B., & Švaco, M. (2025, June). Autonomous uav navigation for search and rescue missions using computer vision and convolutional neural networks. In *International Conference on Robotics in Alpe-Adria Danube Region* (pp. 661-669). Springer Nature Switzerland. https://doi.org/10.1007/978-3-032-02106-9_73

14 Tran, H. K., Le, V. T., Tran, T. T., & Nguyen, V. D. (2025). Low-Cost Remotely-Operated Vehicle Navigation with GPS and RF Lora Integration. *Archives for Technical Sciences*, *2*(33), 297-306. http://dx.doi.org/10.70102/afts.2025.1833.297

15 Schedl, D. C., Kurmi, I., & Bimber, O. (2021). An autonomous drone for search and rescue in forests using airborne optical sectioning. *Science Robotics*, *6*(55), eabg1188. https://doi.org/10.1126/scirobotics.abg1188

16 Du, D., Zhu, P., Wen, L., Bian, X., Lin, H., Hu, Q., & Liu, Z. (2019). VisDrone-DET2019: The vision meets drone object detection in image challenge results. In *2019 IEEE/CVF International Conference on Computer Vision Workshop (ICCVW),* 213-226. *IEEE*. https://doi.org/10.1109/ICCVW.2019.00030

17 Jocher, G., Chaurasia, A., & Qiu, J. (2023). Ultralytics yolo. *Zenodo*. https://github.com/ultralytics/ultralytics

AUTHORS' INFORMATION

Turmaganbet, Ulpan - PhD student, Department of Physics and Technology, al-Farabi Kazakh National University, Almaty, Kazakhstan; https://orcid.org/0009-0002-3782-425X ; uturmaganbet@gmail.com

Turlykozhayeva, Dana - PhD, Researcher, Lecturer, Department of Physics and Technology, al-Farabi Kazakh National University, Almaty, Kazakhstan; https://orcid.org/0000-0002-7326-9196; turlykozhayeva.dana@kaznu.edu.kz

Akhtanov, Sayat - PhD, Researcher, Senior Lecturer, Department of Physics and Technology, al-Farabi Kazakh National University , Almaty, Kazakhstan; https://orcid.org/0000-0002-9705-8000; akhtanov.sayat@kaznu.edu.kz

Temesheva, Symbat - PhD student, Department of Physics and Technology, al-Farabi Kazakh National University, Almaty, Kazakhstan; https://orcid.org/0009-0000-2795-9586; temesheva_symbat4@live.kaznu.kz

Ussipov, Nurzhan – PhD, Researcher, Lecturer, Department of Physics and Technology, al-Farabi Kazakh National University, Kazakhstan; https://orcid.org/0000-0002-2512-3280; ussipov.nurzhan@kaznu.kz

Mingliang, Tao - PhD, Researcher, Professor, School of Electronics and Information, Northwestern Polytechnical University, Xian, China, https://orcid.org/0000-0002-0329-7124; mltao@nwpu.edu.cn

EURASIAN PHYSICAL TECHNICAL JOURNAL

2026, Volume 23, No. 3 (57)

https://doi.org/10.31489/2026N3/125-137

Received: 05/05/2026 Revised: 26/08/2026 Accepted: 28/09/2026 Published online: 30/09/2026

Original Research Article

Open Access under the CC BY -NC-ND 4.0 license

UDC 539.1

SPECTROSCOPY AND STRUCTURAL PROPERTIES OF HEAVY QUARKONIUM SYSTEMS

Osang J.E.[1], Inyang E.P.[2]*, Valentine N.H.[3], Mopta S.E.[4], William E.S.[5], Amajama J.[4], Ekechukwu C.C.[4]

[1] Department of Physics, University of Cross River State, Calabar, Nigeria
[2] Department of Physics, Faculty of Science, National Open University of Nigeria, Jabi-Abuja, Nigeria
[3] Department of Science Laboratory Technology, University of Calabar, Calabar, Nigeria
[4] Department of Physics, Faculty of Physical Sciences, University of Calabar, Calabar, Nigeria
[5] Department of Physics, School of Pure and Applied Sciences, Federal University of Technology, Ikot Abasi, Nigeria
Corresponding author: etidophysics@gmail.com

Abstract. *The spectroscopy and structural properties of heavy quarkonium systems are investigated within the Varshni–Hellmann potential model. The radial Schrödinger equation is solved analytically using the Nikiforov–Uvarov method to obtain the energy eigenvalues and normalized wavefunctions of charmonium and bottomonium states. The calculated mass spectra are compared with available experimental data and results from previous theoretical studies. The present model yields sum of absolute deviations (SADs) of 0.002 GeV and 0.003, with corresponding mean absolute errors of 0.00029 GeV and 0.00038 GeV for bottomonium and charmonium, respectively. The corresponding wavefunctions are examined to characterize the spatial structure of the bound states. In addition, the wavefunctions at the origin are used within the Van Royen–Weisskopf formalism to calculate the leptonic decay widths and vector decay constants of the J/ψ(1S) and Y(1S) states. The calculated leptonic widths are 4.467 keV for J/ψ(1S) and 1.190 keV for Y(1S)), compared with the experimental values of 5.55 keV and 1.340 keV, respectively. The results demonstrate that the Varshni–Hellmann potential provides an analytically tractable framework for describing heavy quarkonium mass spectra, wavefunctions, and selected decay properties. The framework may provide a basis for future investigations of exotic hadronic systems and quarkonium behaviour in extreme quantum chromodynamics environments.*

Keywords: Heavy Mesons; Varshni–Hellmann Potential; Quark–antiquark interactions; Schrödinger Equation; Quarkonium Spectroscopy.

1. Introduction

Quark–antiquark interactions lie at the foundation of hadron physics and quantum chromodynamics (QCD), providing the fundamental mechanism responsible for binding quarks into mesons and baryons. Heavy mesons, which are bound states of a heavy quark and its antiquark such as charmonium and bottomonium [1], serve as particularly insightful probes of the non-perturbative regime of QCD. The relatively large masses of the constituent quarks result in low internal velocities, enabling the application of non-relativistic quantum mechanics to their dynamics. This allows theoretical models based on the Schrödinger equation to capture key features of heavy mesons, including their energy spectra, decay properties, spatial structures, and transition rates [2]. Accurate modeling of these systems not only deepens our understanding of QCD in the strong-

coupling regime but also provides essential benchmarks for interpreting experimental results from high-energy physics facilities. Historically, traditional potential models have formed the backbone of quarkonium spectroscopy. Among these, the Cornell potential has been particularly influential due to its simple yet effective form, combining a Coulomb-like term at short distances with a linear confining term at long ranges [3,4]. This formulation successfully reproduces ground-state masses and low-lying excitations of charmonium and bottomonium while capturing the essential feature of confinement in QCD.

However, recent high-precision experiments at LHCb, Belle II, BESIII, and other facilities have revealed a variety of new meson states, including exotic configurations such as tetraquarks, pentaquarks, and other multiquark systems. These discoveries challenge the explanatory power of conventional potentials and highlight the need for more flexible models capable of incorporating medium effects, screening phenomena, and complex inter-quark interactions [5–7]. To address these challenges, several alternative potentials have been proposed. The Varshni potential, originally developed in molecular physics, introduces a tunable interplay between attractive and repulsive forces, making it particularly suitable for modeling intermediate-range interactions [8]. In the context of quarkonium, it captures the delicate balance between binding and repulsive effects that influence radial excitations and level spacings. The Hellmann potential, on the other hand, combines a Coulomb term with a Yukawa-type screening component, effectively describing quark–antiquark interactions in environments where screening, thermal fluctuations, or density effects modify the effective potential [9]. Both potentials extend the flexibility of conventional models, incorporating phenomena such as finite-range screening, medium-induced weakening of confinement, and modifications to excited-state energy levels. Extensive theoretical studies have demonstrated the efficacy of these exponential potentials when applied to quarkonium systems. Purohit *et al.* [10] employed the Linear plus Modified Yukawa Potential with the Nikiforov–Uvarov (NU) method to study heavy–light meson spectra, reporting good agreement with experimental data, particularly for low-lying states. Rai and Rathaud [11] employed the Hellmann potential with relativistic and one-pion exchange corrections to compute dimesonic molecular mass spectra and decay widths, reporting good agreement with experimental states. Inyang et al. [12] applied the Nikiforov–Uvarov (NU) method to derive analytical energy spectra for several mesonic systems, extending the approach to exponential-type potentials and reinforcing the versatility of semi-analytical methods in quarkonium spectroscopy [2,13]. Complementary calculations using Dyson–Schwinger equations by Yin et al. [14] provided independent evaluations of ground-state meson and baryon masses, serving as reliable benchmarks for potential-based models. Hybrid approaches, such as the modified Kratzer plus screened Coulomb potential studied by Ibekwe et al. [15], further demonstrated that analytical methods can produce spectra consistent with experimental observations.

The investigation of thermodynamic and medium-dependent effects has also been an active area of research. Abu-Shady and Fath-Allah [16] employed generalized fractional Klein–Gordon and Schrödinger equations to explore the influence of temperature, plasma anisotropy, topological defects, and baryonic chemical potential on charmonium and bottomonium binding energies and wavefunctions. Their results indicate that increasing temperature generally reduces binding energies, while anisotropy and topological defects can enhance binding. Fractional models consistently yield lower binding energies and suppressed wavefunctions relative to classical cases, demonstrating the potential of fractional calculus in capturing complex medium effects. Additionally, screened potentials have been widely used to study quarkonium dissociation and medium modifications, with methods such as the NU method and the Asymptotic Iteration Method (AIM) providing accurate predictions for mass spectra under varying physical conditions [17,18]. Despite these advances, a combined potential that integrates the strengths of both Varshni and Hellmann forms has not yet been systematically explored. The Varshni–Hellmann potential (VHP) [19] merges the intermediate-range flexibility of the Varshni form with the short-range Coulomb binding and long-range Yukawa screening of the Hellmann potential. This combination provides a framework to model quark confinement more accurately across all distance scales while retaining analytical tractability. Although similar hybrid potentials have been applied in information-theoretic analyses [20], their systematic application to heavy meson spectroscopy remains novel. The primary objective of this study is to investigate the Varshni–Hellmann potential (VHP) as a unified framework for describing heavy quarkonium systems. The non-relativistic radial Schrödinger equation is solved analytically using the Nikiforov–Uvarov method to obtain energy eigenvalues and wavefunctions, which are used to calculate the mass spectra, wavefunctions at the origin, leptonic widths, and vector decay constants of charmonium and bottomonium states. The results are compared with experimental data and selected theoretical predictions to assess the model's predictive capability.

The novelty lies in the systematic application of the combined VHP to both charmonium and bottomonium spectroscopy and related S-wave decay observables. Although the Varshni and Hellmann potentials have been studied separately, and their combination has been applied to selected quantum and molecular systems, its unified application to heavy quarkonium remains limited. This study therefore provides a consistent assessment of the VHP for describing the spectroscopic and structural properties of heavy quarkonium.

The sections that follow introduce the formalism of the Varshni–Hellmann potential and outline the implementation of the NU method for deriving analytical solutions. Computed mass spectra and structural observables are subsequently presented and compared with experimental data and theoretical predictions. The work concludes with an analysis of the results and a summary of the key findings.

The VHP is of the form [19]:

$$V(r) = A_0 - \frac{A_0 B_0 e^{-\alpha r}}{r} - \frac{C_0}{r} + \frac{D_0 e^{-\alpha r}}{r} \quad , \tag{1}$$

where $A_0, B_0, C_0, and\ \mathrm{D}_0$ are potential strength parameters, r is inter nuclear distance, and α is the screening parameter.

To model the potential describing the quark–antiquark interaction, we perform a series expansion of the exponential terms in Eq. (1) up to third order, which yields:

$$V(r) = -\frac{\beta_a}{r} + \beta_b r - \beta_c r^2 + \beta_d \tag{2}$$

where

$$\left.\begin{aligned} &\beta_a = A_0 B_0 + C_0 - D_0, \quad \beta_b = -\frac{A_0 B_0 \alpha^2}{2} + \frac{\alpha^2 D_0}{2} \\ &\beta_c = -\frac{A_0 B_0 \alpha^3}{6} + \frac{D_0 \alpha^3}{6}, \quad \beta_d = A_0 + \alpha A_0 B_0 - \alpha D_0 \end{aligned}\right\} \tag{3}$$

2. Analytical Treatment of the Varshni–Hellmann Potential

The Schrödinger equation (SE), which describes the quantum dynamics of a particle subject to a potential, provides the framework for calculating the energy eigenvalues and corresponding wave functions of the system. In the present study, the SE is expressed as [2]

$$\frac{d^2\psi_{nl}(r)}{dr^2} + \left[\frac{2\mu}{\hbar^2}\left(E_{nl} - V(r)\right) - \frac{l(l+1)}{r^2}\right]\psi_{nl}(r) = 0 \tag{4}$$

Here, ℓ and μ represent the angular momentum quantum number and the reduced mass of the quarkonium system, respectively, while r denotes the inter-particle distance and $\hbar$ is the reduced Planck constant. Substituting Eq. (2) into Eq. (4), we obtain:

$$\frac{d^2\psi_{nl}(r)}{dr^2} + \left[\zeta + \frac{\alpha_0}{r} - \alpha_1 r + \alpha_2 r^2 - \frac{\gamma}{r^2}\right]\psi_{nl}(r) = 0 \tag{5}$$

where,

$$\left.\begin{aligned} &\zeta = \frac{2\mu}{\hbar^2}\left(E_{nl} - \beta_d\right), \ \alpha_0 = \frac{2\mu\beta_a}{\hbar^2} \\ &\alpha_1 = \frac{2\mu\beta_b}{\hbar^2}, \ \alpha_2 = \frac{2\mu\beta_c}{\hbar^2}, \ \gamma = l(l+1) \end{aligned}\right\} \tag{6}$$

By performing a coordinate transformation in Eq. (5), we set $x = \frac{1}{r}$. Differentiating accordingly, simplifying, and substituting back into Eq. (5) yields

$$\frac{d^2\psi_{nl}(x)}{dx^2} + \frac{2}{x}\frac{d\psi_{nl}}{dx} + \frac{1}{x^4}\left[\zeta + \alpha_0 x - \frac{\alpha_1}{x} + \frac{\alpha_2}{x^2} - \gamma x^2\right]\psi_{nl}(x) = 0 \tag{7}$$

We now introduce an appropriate approximation scheme for the terms $\frac{\alpha_1}{x}$ and $\frac{\alpha_2}{x^2}$, in order to facilitate analytical treatment of the equation. Let us assume that the meson possesses a characteristic radius r_0. Based on this, we employ an approximation scheme by expanding the relevant terms in a power series about r_0, i.e., around the point $\delta_o \equiv \frac{1}{r_0}$, up to second order. At this stage, the series expansion is carried out around a characteristic radius r_0, which corresponds to the most probable interquark separation in the bound state. For heavy quarkonium systems, the large quark masses and the confining interaction lead to a strong spatial localization of the radial wavefunctions around r_0. As a result, the dominant contributions to bound-state observables arise from this region. Consequently, it remains reliable over the physically relevant domain of the bound state. This procedure follows the Pekeris approximation, which deforms the centrifugal term into a solvable form and enables the application of the Nikiforov–Uvarov method [21]. In the present calculation, the same value of (δ_o=0.1000) was used for both charmonium and bottomonium, as indicated in Table 1, to maintain consistency in the Pekeris approximation.

By setting $y = x - \delta_0$ and expanding around $y = 0$, the function can be expressed as a power series in x, given by:

$$\frac{\alpha_1}{x} = \alpha_1 \left(\frac{3}{\delta_0} - \frac{3x}{\delta_0^{\,2}} + \frac{x^2}{\delta_0^{\,3}} \right) \tag{8}$$

Analogously,

$$\frac{\alpha_2}{x^2} = \alpha_2 \left(\frac{6}{\delta_0^{\,2}} - \frac{8x}{\delta_0^{\,3}} + \frac{3x^2}{\delta_0^{\,4}} \right) \tag{9}$$

Inserting Eqs. (8) and (9) into Eq. (7) yields:

$$\frac{d^2\psi(x)}{dx^2} + \frac{2x}{x^2}\frac{d\psi(x)}{dx} + \frac{1}{x^4}\left[-\varepsilon + \alpha_3 x - \beta x^2 \right]\psi(x) = 0 \tag{10}$$

Such that

$$-\varepsilon = \left(\zeta + \frac{6\alpha_2}{\delta_0^{\,2}} - \frac{3\alpha_1}{\delta_0} \right),\ \alpha_3 = \left(\frac{3\alpha_1}{\delta_0^{\,2}} + \alpha_0 - \frac{8\alpha_2}{\delta_0^{\,3}} \right),\ \beta = \left(\gamma + \frac{\alpha_1}{\delta_0^{\,3}} - \frac{3\alpha_2}{\delta_0^{\,4}} \right) \Bigg\} \tag{11}$$

A comparison between Eq. (10) and Eq. (A1) gives

$$\left.\begin{aligned} &\tilde{\tau}(x) = 2x,\ \sigma(x) = x^2 \\ &\tilde{\sigma}(x) = -\varepsilon + \alpha_3 x - \beta x^2 \\ &\sigma'(x) = 2x,\ \sigma''(x) = 2 \end{aligned}\right\} \tag{12}$$

Inserting Eq. (12) into Eq. (A9) yields

$$\pi(x) = \pm\sqrt{\varepsilon - \alpha_3 x + (\beta + k)x^2} \tag{13}$$

The value of k is obtained by computing the discriminant of the radicand, resulting in

$$k = \frac{\alpha_3^2 - 4\beta\varepsilon}{4\varepsilon} \tag{14}$$

Inserting Eq. (14) into Eq. (13) yields:

$$\pi(x) = \pm\left(\frac{\alpha_3 x}{2\sqrt{\varepsilon}} - \frac{\varepsilon}{\sqrt{\varepsilon}} \right) \tag{15}$$

The negative branch is selected to satisfy the NU bound-state condition $\tau'(x) < 0$ and to ensure physically acceptable, normalizable solutions.

Differentiation then gives:

$$\pi'_{-}(x) = -\frac{\alpha_3}{2\sqrt{\varepsilon}} \tag{16}$$

Inserting Eqs. (12) and (16) into Eq. (A7) yields:

$$\tau(x) = 2x - \frac{\alpha_3 x}{\sqrt{\varepsilon}} + \frac{2\varepsilon}{\sqrt{\varepsilon}} \tag{17}$$

Taking the derivative of Eq. (17) yields

$$\tau'(x) = 2 - \frac{\alpha_3}{\sqrt{\varepsilon}} \tag{18}$$

With the aid of Eq. (A10), we arrive at:

$$\lambda = \frac{\alpha_3^2 - 4\beta\varepsilon}{4\varepsilon} - \frac{\alpha_3}{2\sqrt{\varepsilon}} \tag{19}$$

By proceeding with Eq. (A11), we obtain the following result

$$\lambda_n = \frac{n\alpha_3}{\sqrt{\varepsilon}} - n^2 - n \tag{20}$$

Upon equating Eqs. (19) and (20), and using Eqs. (3) and (6), the expression for the energy eigenvalue becomes Eq. (21). The total radial wavefunction is written as $\psi(x) = \phi(x) y(x)$, where $\phi(x)$ is obtained from the logarithmic derivative relation in Eq. (A4), and the polynomial solutions $y(x)$ are generated using the Rodrigues formula in Eq. (A5), leading to the normalized wavefunction given in Eq. (22).

$$E_{nl} = A_0 + \alpha A_0 B_0 - \alpha D_0 + \frac{A_0 B_0 \alpha^3}{{\delta_0}^2} - \frac{D_0 \alpha^3}{{\delta_0}^2} - \frac{3A_0 B_0 \alpha^2}{2\delta_0} + \frac{3D_0 \alpha^2}{2\delta_0}$$

$$-\frac{\hbar^2}{8\mu}\left[\frac{\frac{2\mu}{\hbar^2}\left(A_0 B_0 + C_0 - D_0\right) + \frac{3\mu}{\hbar^2 {\delta_0}^2}\left(-A_0 B_0 \alpha^2 + \alpha^2 D_0\right) - \frac{16\mu}{6\hbar^2 {\delta_0}^3}\left(-A_0 B_0 \alpha^3 + D_0 \alpha^3\right)}{n + \frac{1}{2} + \sqrt{\left(l + \frac{1}{2}\right)^2 + \frac{\mu}{\hbar^2 {\delta_0}^3}\left(-A_0 B_0 \alpha^2 + \alpha^2 D_0\right) - \frac{\mu}{\hbar^2 {\delta_0}^4}\left(-A_0 B_0 \alpha^3 + \alpha^3 D_0\right)}}\right]^2 \tag{21}$$

The solution for the wavefunction, involving Laguerre polynomials, takes the form

$$\psi_{nl}(x) = N_{nl} x^{-\frac{\alpha}{2\sqrt{\varepsilon}}} e^{-\frac{\varepsilon}{x\sqrt{\varepsilon}}} L_n^{\frac{\alpha}{\sqrt{\varepsilon}}}\left(\frac{2\varepsilon}{x\sqrt{\varepsilon}}\right) \tag{22}$$

The constant N_{nl} is the normalization factor, derived using the following condition

$$\int_0^\infty \psi_{nl}(r)\psi_{nl}^*(r)dr = 1 \tag{23}$$

To evaluate the mass spectra of heavy quarkonium systems (e.g., charmonium and bottomonium), composed of quark–antiquark pairs of the same flavor, we employ the following relation [22]:

$$M = 2m + E_{nl} \tag{24}$$

In this framework, m denotes the quark mass, while E_{nl} represents the corresponding energy eigenvalues. Substituting Eq. (21) into Eq. (24), we obtain the expressions for the mass spectra of the VHP:

$$M = 2m + A_0 + \alpha A_0 B_0 - \alpha D_0 + \frac{A_0 B_0 \alpha^3}{{\delta_0}^2} - \frac{D_0 \alpha^3}{{\delta_0}^2} - \frac{3A_0 B_0 \alpha^2}{2\delta_0} + \frac{3D_0 \alpha^2}{2\delta_0}$$

$$-\frac{\hbar^2}{8\mu}\left[\frac{\frac{2\mu}{\hbar^2}\left(A_0 B_0 + C_0 - D_0\right) + \frac{3\mu}{\hbar^2 {\delta_0}^2}\left(-A_0 B_0 \alpha^2 + \alpha^2 D_0\right) - \frac{16\mu}{6\hbar^2 {\delta_0}^3}\left(-A_0 B_0 \alpha^3 + D_0 \alpha^3\right)}{n + \frac{1}{2} + \sqrt{\left(l + \frac{1}{2}\right)^2 + \frac{\mu}{\hbar^2 {\delta_0}^3}\left(-A_0 B_0 \alpha^2 + \alpha^2 D_0\right) - \frac{\mu}{\hbar^2 {\delta_0}^4}\left(-A_0 B_0 \alpha^3 + \alpha^3 D_0\right)}}\right]^2 \tag{25}$$

3. Decay Constants and Transition Rates

The predictive power of a potential model for heavy quarkonia extends beyond the mass spectrum to observables such as leptonic widths and vector decay constants. These quantities depend on the short-distance behaviour of the quarkonium wavefunction and, for an S-wave state, specifically on the finite radial wavefunction at the origin, (R(0)). It is therefore important to distinguish between the reduced radial function and the physical radial function. These observables are sensitive to the wavefunction at the origin, $\left|\psi_{no}\left(0\right)\right|^2$, which encapsulates the short-distance behavior of the quark–antiquark system [23]. From Eq. (22), the radial wavefunction can be further expressed as

$$\psi_{nl}(r) = N_{nl} r^s e^{-k_1 r} L_n^{(2s)}\left(2k_1 r\right) \tag{26}$$

where $L_n^{(2s)}$ are the associated Laguerre polynomials, s and k_1 are the parameters determined by the NU procedure and N_{nl} is the normalization constant defined in Eq. (23)

For S-wave states (ℓ=0), the radial wavefunction obtained in Eq. (26) becomes

$$\psi_{n,0}(r) = N_{nl} r^s e^{-k_1 r} L_n^{(2s)}\left(2k_1 r\right) \tag{27}$$

Evaluating this at the origin gives

$$\psi_{n,0}(0) = \lim_{r\to 0} N_{nl} r^s e^{-k_1 r} L_n^{(2s)}\left(2k_1 r\right) \tag{28}$$

Since $e^{-k_1 r} \to 1$ as $r \to 0$ and the associated Laguerre polynomial satisfies

$$L_n^{(\Omega)}\left(0\right) = \frac{\Gamma\left(n+\Omega+1\right)}{\Gamma\left(\Omega+1\right)n!} \tag{29}$$

Putting $\Omega = 2s$ into Eq. (29) gives

$$L_n^{(2s)}\left(0\right) = \frac{\Gamma\left(n+2s+1\right)}{\Gamma\left(2s+1\right)n!} \tag{30}$$

Hence, $\psi_{n,0}\left(0\right) = N_{n,0}\dfrac{\Gamma\left(n+2s+1\right)}{\Gamma\left(2s+1\right)n!}\lim_{r\to 0} r^s$ (31)

The probability density at the origin is given as

$$\left|\psi_{n,0}\left(0\right)\right|^2 = \left|N_{n,0}\right|^2 \left(\frac{\Gamma\left(n+2s+1\right)}{\Gamma\left(2s+1\right)n!}\right)^2 \lim_{r\to 0} r^{2s} \tag{32}$$

3.1 Leptonic widths

For heavy quarkonium systems, leptonic decay widths are governed by the short-distance behavior of the quark–antiquark wavefunction. The total wavefunction is written as $\psi(r) = R(r)Y_{lm}(\theta,\varphi)$,where the radial function satisfies $R(r) = \chi(r)/r$ with $\chi(r)$ denoting the reduced radial wavefunction. For S-wave states (ℓ = 0), the spherical harmonic reduces to $Y_{00} = 1/\sqrt{4\pi}$,and therefore the wavefunction at the origin is given by $\psi(0) = \left.\dfrac{\chi(r)}{r}\right|_{r=0} \dfrac{1}{\sqrt{4\pi}}$ .Consequently, the physically relevant quantity entering leptonic decay widths is $\left|\psi\left(0\right)\right|^2 = \left|\chi\left(0\right)\right|^2/\left(4\pi\right)$. Accordingly, the Van Royen–Weisskopf formula for the leptonic decay width of a vector meson, including the leading-order QCD radiative correction, is written as [24].

$$\Gamma_{ee}\left(V \to e^+e^-\right) = \frac{16\pi\alpha_f^2 e_Q^2}{M_V^2}\left|\psi\left(0\right)\right|^2\left(1-\frac{16\alpha_s}{3\pi}\right), \tag{33}$$

where $\alpha_f \simeq 1/137.036$ is the fine-structure constant, e_Q is the heavy-quark charge, M_V is the vector meson mass, and α_s is the QCD running coupling.

3.2 Vector decay constants

The leptonic decay constant f_V is defined through the matrix element of the vector current and is related to the leptonic width by [24]:

$$\Gamma_{ee}\left(V \to e^+e^-\right) = \frac{4\pi\alpha_f^2 e_Q^2}{3M_V} f_V^2 \left[1-\left(16/3\pi\right)\alpha_s\right] \tag{34}$$

leading to

$$f_V^2 = \left(\frac{12}{M_V}\right)\left|\psi\left(0\right)\right|^2, \tag{35}$$

Equations (33) and (35) together allow the extraction of decay constants directly from the normalized wavefunctions obtained with the Varshni–Hellmann potential. Experimental reference values for leptonic widths are available in the Particle Data Group listings [26], enabling direct comparison with theoretical predictions.

The mean absolute error (MAE) is given as

$$\frac{1}{N}\sum\left|M_i^{\,T} - M_i^{\,E}\right| \tag{36}$$

The variables appearing in this expression are defined as follows: N denotes the number of available experimental data points, ME represents the experimental values, and M^T corresponds to the theoretically calculated values.

4. Discussion of results

The mass spectra of charmonium and bottomonium states, from 1S to 1F, were computed using Eq. (25). The potential parameters were determined simultaneously from the experimentally established (1S), (2S), (3S), and (4S) mass levels for each quarkonium system, subject to the physical constraints given in Table 1. Reference values were taken from Refs. [27,28].

Table 1. Parameters of the Varshni–Hellmann potential and the corresponding properties of the heavy mesons.

Parameters	Charmonium	Bottomonium
A_0	1.3400 GeV	1.6100 GeV
B_0	4.9675 GeV^{-1}	4.6513 GeV^{-1}
C_0	0.9217	5.4212
D_0	6.6565	7.4885
α	0.0100 GeV	0.0100 GeV
δ_0	0.1000	0.1000
μ	0.6045 GeV	2.4115 GeV

Constituent quark masses of 1.209 GeV for charmonium and 4.823 GeV for bottomonium yield reduced masses of 0.6045 GeV and 2.4115 GeV, respectively [29]. The results, summarized in Tables 2 and 3, demonstrate the effectiveness of the Varshni–Hellmann potential, which combines a short-range Coulomb-like term with a long-range screened interaction, capturing essential QCD features such as asymptotic freedom at short distances and confinement at intermediate ranges. For bottomonium, the calculated masses show an agreement with experimental data across all states, from the tightly bound 1S to higher excitations such as 4S and 1D. The model reproduces fine spectral structures arising from the strong binding of the heavy quark, which leads to compressed spatial configurations, sharper wavefunctions, and wider level spacings, characteristic features of the heavy-quark regime in QCD.

Table 2. Mass spectra of bottomonium (GeV) for Varshni–Hellmann potential

State	Present work (PW)	[22]	[18]	Experiment [27,28]	Error (PW)	Error [22]	Error [18]
1S	9.460	9.460	9.462	9.460	0.000	0.000	0.002
2S	10.023	10.023	10.027	10.023	0.000	0.000	0.004
1P	9.899	9.619	9.963	9.899	0.000	0.280	0.064
2P	10.260	10.114	10.299	10.260	0.000	0.146	0.039
3S	10.356	10.355	10.361	10.355	0.001	0.000	0.006
4S	10.580	10.567	10.624	10.580	0.000	0.013	0.044
1D	10.165	9.864	10.209	10.164	0.001	0.300	0.045
2D	10.307	-	-	-	-	–	–
1F	10.210	-	-	-	–	–	–

Note: "—" indicates that no corresponding experimental or reference value is available; the present-work value is therefore a model prediction.

Table 3. Mass spectra of charmonium (GeV) for Varshni–Hellmann potential

State	Present work (PW)	[22]	[18]	Experiment [27,28]	Error (PW)	Error [22]	Error [18]
1S	3.096	3.096	3.096	3.096	0.000	0.000	0.000
2S	3.686	3.686	3.672	3.686	0.000	0.000	0.014
1P	3.525	3.255	3.521	3.525	0.000	0.270	0.004
2P	3.773	3.779	3.951	3.773	0.000	0.006	0.178
3S	4.040	4.040	4.085	4.040	0.000	0.000	0.045
4S	4.264	4.269	4.433	4.263	0.001	0.006	0.170
1D	3.771	3.504	3.800	3.770	0.001	0.266	0.030
2D	4.160	-	-	4.159	0.001	–	–
1F	3.962	-	-	-	–	–	–

Note: "—" indicates that no corresponding experimental or reference value is available; the present-work value is therefore a model prediction.

For bottomonium, the present work (PW) shows good agreement with the experimental value, with a sum of absolute deviations (SAD) of 0.002 GeV and a mean absolute error (MAE) of 0.00029 GeV, compared with 0.204 GeV and 0.02914 GeV, respectively, for Ref. [18], and 0.739 GeV and 0.10557 GeV for Ref. [22]. Similarly, for charmonium, PW gives a sum of absolute deviations (SAD) of 0.003 GeV and a mean absolute error (MAE) of 0.00038 GeV, substantially lower than those of Ref. [18] (0.441 GeV, 0.06300 GeV) and Ref. [22] (0.548 GeV, 0.07829 GeV). These results demonstrate the accuracy of the Varshni–Hellmann potential in reproducing the observed heavy-quarkonium mass spectra. Using established values of the wavefunction at the origin $\left|R_{J/\psi}(0)\right|^2 = 0.81 GeV^3 and \left|R_{\Upsilon(1S)}(0)\right|^2 = 6.48 GeV^3, \alpha_S(m_c) = 0.26, \alpha_S(m_b) = 0.18$ together with the Van Royen–Weisskopf formula and the one-loop QCD correction in Eq. (33), the leptonic widths and vector decay constants listed in Table 4 were evaluated. The results in Table 4 show that the calculated leptonic widths provide reasonable, although not exact, agreement with the experimental values. For J/ψ(1S), the calculated width of 4.467 keV differs from the experimental value of (5.55±0.145) keV by approximately 20%. For Υ(1S), the calculated width of 1.190 keV differs from the experimental value of (1.340±0.018) keV by approximately 11%.

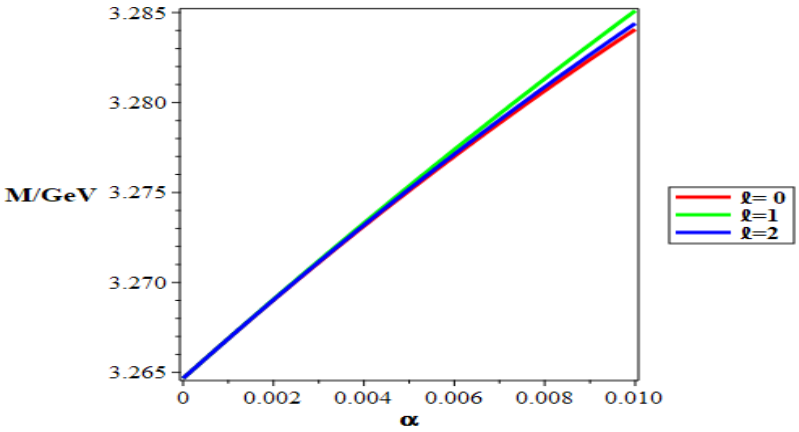


Fig.1 Mass spectra as a function of the screening parameter for different angular quantum numbers

These deviations indicate that, although the present non-relativistic treatment captures the dominant short-distance contribution, the decay observables remain sensitive to effects not explicitly included in the present model, including higher-order QCD radiative corrections, relativistic corrections, and uncertainties associated with the chosen strong-coupling scale. Therefore, the decay-width results should be regarded as an additional validation of the model rather than as a precision determination of the leptonic widths.

Table 4: Leptonic widths (Γee) and vector decay constants (fV)for S-wave heavy mesons.

State	$\Gamma_{ee}(KeV)$	$f_V(MeV)$	$PDG\ \Gamma_{ee}(KeV)$ [26]
$J/\psi(1S)$	4.467	374	5.550 ± 0.140
$\Upsilon(1S)$	1.190	674	1.340 ± 0.018

Figure 1 illustrates the dependence of the calculated mass spectrum on the screening parameter (α) for orbital angular quantum numbers ℓ = 0, 1, and 2. The parameter (α) controls the exponential screening of the long-range component of the Varshni–Hellmann interaction and therefore determines the effective range over which the corresponding attractive interaction remains significant. As (α) increases, the long-range interaction becomes more strongly screened, modifying the effective binding between the quark and antiquark and producing a systematic shift in the energy eigenvalues and meson masses. The approximately linear increase in the calculated masses with (α) over the range considered indicates that screening produces a smooth modification of the quark–antiquark interaction for the parameter values investigated. States with higher angular momentum are additionally affected by the centrifugal contribution, which leads to differences in their spectral response to changes in (α). The observed dependence therefore reflects the combined effects of short-distance binding, screened long-range interaction, and the centrifugal contribution.

Wavefunction profiles in Figs. 2 and 3 reveal further structural features. For charmonium (Fig. 2), the wavefunctions exhibit radial nodes and spatial broadening with increasing excitation, consistent with weaker binding. In contrast, bottomonium wavefunctions (Fig. 3) remain sharply localized near the origin, reflecting the strong binding and compact size characteristic of systems dominated by a heavy quark mass. These results demonstrate the robustness of the Varshni–Hellmann potential as a reliable and analytically tractable framework for modeling heavy quark–antiquark systems. Its success in reproducing experimental spectra and capturing key spatial and dynamical features highlights its value for studying not only charmonium and bottomonium but also exotic hadronic states and quarkonium behavior under extreme QCD conditions such as those probed in heavy-ion collisions.

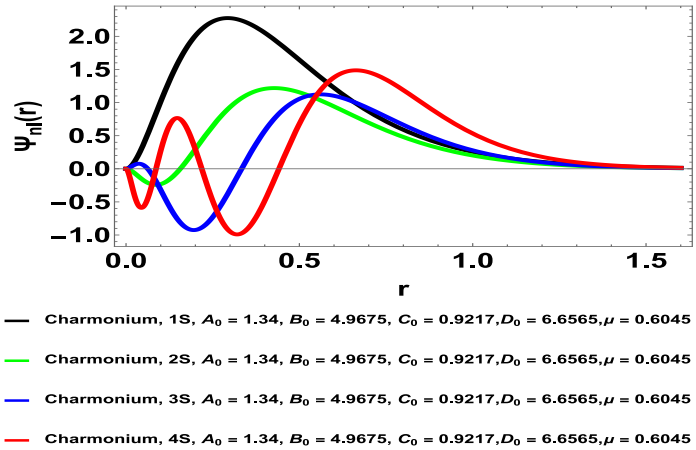


Fig.2. Wavefunctions of charmonium for different S states.

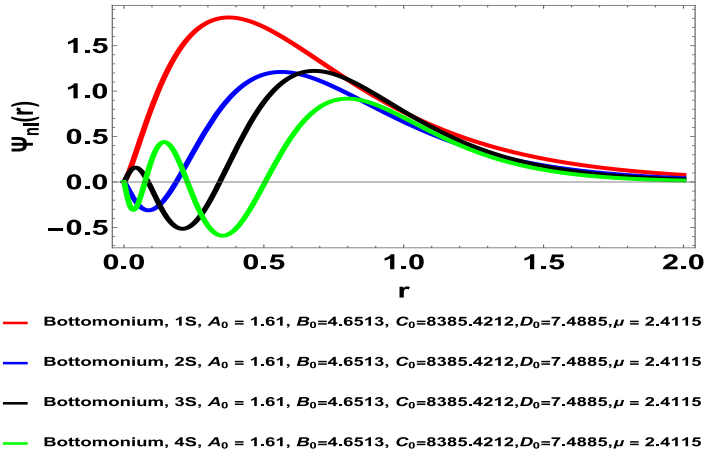


Fig.3 Wavefunctions of bottomonium for different S states.

4. Conclusion

In this study, the Varshni–Hellmann potential was employed to investigate the spectroscopy and structural properties of heavy quark–antiquark systems. The Schrödinger equation was solved analytically using the Nikiforov–Uvarov method, yielding energy spectra and corresponding wavefunctions for different orbital states. The model reproduces the experimental mass spectra with high accuracy, with a sum of absolute deviations (SAD) of 0.002 GeV and a mean absolute error (MAE) of 0.00029 GeV for bottomonium, and SAD of 0.003 GeV and MAE of 0.00038 GeV for charmonium. This close agreement demonstrates the effectiveness of the combined Coulomb-like short-range and screened long-range components of the potential, together with the fitted model parameters.

The calculated leptonic widths and decay constants of the S-wave states, obtained within the Van Royen–Weisskopf framework, show reasonable agreement with the Particle Data Group values and results from phenomenological and lattice QCD studies. Predictions for the P- and D-wave states provide an additional assessment of the model beyond the S-wave states used for parameter determination. Overall, the Varshni–Hellmann potential provides an analytically tractable and effective framework for describing heavy quarkonium spectra and related decay observables. Future studies may extend this framework to exotic hadronic systems and medium-dependent quarkonium properties in extreme QCD environments, including screening and dissociation phenomena.

Conflict of interest statement
The authors declare that they have no conflict of interest in relation to this research, whether financial, personal, authorship or otherwise, that could affect the research and its results presented in this paper.

CRediT author statement
Inyang E. P.: Conceptualization, Methodology, Investigation; Writing – original draft; **Valentine, N. H.** and **Osang J.E.:** Data Curation, Writing Original Draft; ***William E.S.*** and **Mopta S.E:** Methodology, Resources, Validation; **Amajama J. and Ekechukwu C.C.:** Resources. The final manuscript was read and approved by all authors.

Statement on the use of Artificial Intelligence.
During the preparation of this manuscript, artificial intelligence tools were used solely for language editing and grammatical improvement. No AI tools were used to generate scientific content, analysis, results, or conclusions.

Data Availability Statement
No external datasets were used in this study. All data were generated numerically from the analytical solutions.

Funding
This research was funded by the 2026 TETFund Institutional Based Research (IBR) grant of the National Open University of Nigeria with grant number NOUN/TETFIBR26/FACSCIENCES/053

Acknowledgements
This work is reverently dedicated to Professor Olufemi Peters, with thanksgiving to God for his visionary leadership, wisdom, and enduring contributions to research and open and distance education at the National Open University of Nigeria.

References

1. Litvinov, A., & Meshcheriakov, P. (2025). Meson mass spectrum in QCD2 ’t Hooft's model. *Nuclear Physics B, 1010*, 116766. https://doi.org/10.1016/j.nuclphysb.2025.116766

2. Inyang, E.P., Ali, N., Endut, R., Rusli, N., & Aljunid S.A. (2025). The radial scalar power potential and its application to quarkonium systems. *Indian Journal of Physics, 99*,715-724. https://doi.org/10.1007/s12648-024-03335-9

3.. Ali, M. S, Hassan, G. S., Abdelmonem, A. M., Elshamndy, S. K., Elmasry, F., & Yasser, A. M. (2020). The spectrum of charmed quarkonium in non-relativistic quark model using matrix Numerov’s method. *Journal of Radiation Research and Applied Sciences, 13*, 226–233. https://doi.org/10.1080/16878507.2020.1723949

4. Inyang, E. P., Ali, N., Endut, R., Rusli, N., Aljunid, S. A., Ali, N. R., & Asjad M. M. (2024). Thermal properties and mass spectra of heavy mesons in the presence of a point-like defect. *East European Journal of Physics, 1*, 156–166. https://doi.org/10.26565/2312-4334-2024-1-14

5. Matvienko, D. (2018). The Belle II experiment: Status and physics program. *EPJ Web of Conferences, 191*, 02010. https://doi.org/10.1051/epjconf/201819102010

6. Mistry, R., Shah, M., & Majethiya, A. (2024). Mass spectra, Regge trajectories and decay properties of heavy-flavour mesons. *Revista Mexicana de Física, 70*, 010801. https://doi.org/10.31349/RevMexFis.70.010801

7. Inyang, E. P., Nwachukwu, I. M., Ekechukwu, C. C., Ekong, I. B., William, E. S., Lawal, K. M., Momoh, K. O., & Oyelami, O. A. (2024). Analytical solution of the class of inversely quadratic Yukawa potential with application to quantum mechanical systems. *Eurasian Physical Technical Journal, 21*(4), 118–130. https://doi.org/10.31489/2024No4/118-130

8. Varshni, Y. P. (1957). Comparative study of potential energy functions for diatomic molecules. *Reviews of Modern Physics, 29*, 664–669. https://doi.org/10.1103/RevModPhys.29.664

9. Hellmann, H. (1935). A new approximation method in the problem of many electrons. *The Journal of Chemical Physics, 3*, 61. https://doi.org/10.1063/1.1749559

10. Purohit, K. R., Rai, A. K., & Parmar, R. H. (2024). Spectroscopy of heavy-light mesons (D, Ds, B, Bs) for the linear plus modified Yukawa potential using Nikiforov–Uvarov method. *Indian Journal of Physics, 98*, 1109–1121. https://doi.org/10.1007/s12648-023-02852-3

11. Rai, A. K., & Rathaud, D. P. (2015). The mass spectra and decay properties of dimesonic states, using the Hellmann potential. *European Physical Journal C, 75*, 462. https://doi.org/10.1140/epjc/s10052-015-3695-z

12. Inyang, E. P., Inyang, E. P., William, E. S., & Ibekwe, E. E. (2021). Study on the applicability of Varshni potential to predict the mass spectra of the quark–antiquark systems in a non-relativistic framework. *Jordan Journal of Physics, 14*(4). https://doi.org/10.47011/14.4.8

13. Inyang, E. P., Obisung, E. O., Iwuji, P. C., Ntibi, J. E., Amajama, J., & William, E. S. (2022). Masses and thermal properties of a charmonium and bottomonium mesons. *Journal of the Nigerian Society of Physical Sciences, 4*(3), 884. https://doi.org/10.46481/jnsps.2022.884

14. Yin, P. L., Chen, C., Krein, G., Roberts, C. D., Segovia, J., & Xu, S. S. (2019). Masses of ground-state mesons and baryons, including those with heavy quarks. *Physical Review D, 100*, 034008. https://doi.org/10.1103/PhysRevD.100.034008

15. Ibekwe, E. E., Emah, J. B., Inyang, E. P., & Akpan, A. O. (2022). Mass spectrum of heavy quarkonium for combined potentials (modified Kratzer plus screened Coulomb potential). *Iranian Journal of Science and Technology*, 46,1748. https://doi.org/10.1007/s40995-022-01264-2

16. Abu-Shady, M., & Fath-Allah, H. M. (2025). Thermodynamic analysis and mass spectra of heavy mesons via the generalized fractional Klein–Gordon equation. *Revista Mexicana de Física, 71*, 030801. https://doi.org/10.31349/RevMexFis.71.030801

17. Abu-Shady, M., & Fath-Allah, H. M. (2025). Investigating heavy quarkonia binding in an anisotropic-dense quark–gluon plasma with topological defects in the framework of fractional non-relativistic quark model. *Scientific Reports, 15*, 1875. https://doi.org/10.1038/s41598-025-01875-2

18. Ciftci, H., & Kisoglu, H. F. (2018). Non-relativistic arbitrary l-states of quarkonium through asymptotic iteration method. *Advances in High Energy Physics, 2018*, 4549705. https://doi.org/10.1155/2018/4549705

19. William, E., Inyang, E., Ntibi, J. E., Obu, J. A., & Inyang, E. P. (2022). Solutions of the non-relativistic equation interacting with the Varshni-Hellmann potential model with some selected diatomic molecules. *Jordan Journal of Physics, 15*, 179–193. https://doi.org/10.47011/15.2.9

20. Inyang, E. P., Aouami, A. E. L., Ali, N., Endut, R., Ali, N. R., & Aljunid, S. A. (2024). Information entropies with Varshni–Hellmann potential in higher dimensions. *Physics Open, 20*, 100220. https://doi.org/10.1016/j.physo.2024.100220

21. Nikiforov, S. K., & Uvarov, V. B. (1988). *Special functions of mathematical physics*. Birkhäuser, Basel. https://doi.org/10.1007/978-1-4757-1595-8

22. Abu-Shady, M., Abdel-Karim, T. A., & Ezz-Alarab, Y. (2019). Masses and thermodynamic properties of heavy mesons in the non-relativistic quark model using the Nikiforov–Uvarov method. *Journal of the Egyptian Mathematical Society, 27*, 145. https://doi.org/10.1186/s42787-019-0022-2

23. Van Royen, R., & Weisskopf, V.F. (1967). Hadron decay processes and the quark model. *Il Nuovo Cimento A (1965–1970), 50*(3), 617–645. https://doi.org/10.1007/BF02823542

24. Olavo, L. S. F. (1999). Foundations of quantum mechanics: Non-relativistic theory. *Physica A: Statistical Mechanics and its Applications, 262*(1–2), 197–214. https://doi.org/10.1016/S0378-4371(98)00395-1

25. Wittig, H. (2020). QCD on the lattice. In *Particle Physics Reference Library, Vol. 1: Theory and Experiments* (pp. 137–262). Springer, Cham. https://doi.org/10.1007/978-3-030-38207-0_5

26. Navas, S., Amsler, C., Gutsche, T., Hanhart, C., Hernández-Rey, J. J., Lourenço, C., Masoni, A., Mikhasenko, M., Mitchell, R. E., & Particle Data Group. (2024). Review of particle physics. *Physical Review D, 110*(3), 030001. https://doi.org/10.1103/PhysRevD.110.030001

27. Tanabashi, M., Carone, C. D., Trippe, T. G., Wohl, C. G., & Particle Data Group. (2018). Review of particle physics. *Physical Review D, 98*, 030001. https://doi.org/10.1103/PhysRevD.98.030001

28. Olive, K. A., Groom, D. E., Trippe, T. G., & Particle Data Group. (2014). Review of particle physics. *Chinese Physics C, 38*, 090001. https://doi.org/10.1088/1674-1137/38/9/090001

29. Barnett, R. M., Carone C. D., Groom, D. E., Trippe, T. G., Wohl, C. G., & Particle Data Group. (2012). Review of particle physics. *Physical Review D, 86*, 010001. https://doi.org/10.1103/PhysRevD.86.010001

AUTHORS' INFORMATION

Inyang, Etido Patrick. – Dr. (Sci.), Department of Physics, Faculty of Science, National Open University of Nigeria, Abuja, Nigeria; SCOPUS Author ID: 16175170000; https://orcid.org/0000-0002-5031-3297; etidophysics@gmail.com

Osang, Jonathan Eyire. **–** Dr. (Sci.), *Department of Physics, University of Cross River State, Calabar, Nigeria,*; SCOPUS Author ID: 7221839733; https://orcid.org/0000-0001-6895-3332; jonathanosang@yahoo.com

Ekechukwu, Christopher Chinasa- Mr. (Sci.), Department of Physics, Faculty of Physical Science, University of Calabar, Calabar, Nigeria; SCOPUS Author ID**:** 57190218952; https://orcid.org/0000-0001-7559-4112; ekehmore@gmail.com

Mopta, Samuel Eyeh. - Dr. (Sci.), Department of Physics, Faculty of Physical Science, University of Calabar, Calabar, Nigeria; SCOPUS Author ID: 57927014600; https://orcid.org/0009-0007-3114-9843; samuelmopta@unical.edu.ng

William, Eddy Sunday- Dr. (Sci.), Department of Physics, School of Pure and Applied Sciences, Federal University of Technology, Ikot Abasi, Nigeria; SCOPUS Author ID: 57221313665, https://orcid.org/0000-0002-5247-5281; williameddyphysics@gmail.com

Amajama, Joseph - Dr. (Sci.), Department of Physics, Faculty of Physical Science, University of Calabar, Calabar, Nigeria; SCOPUS Author ID: 58091457900, https://orcid.org/0000-0002-8475-9457; joeamajama@unical.edu.ng

Valentine, Ndianabasi Henry. -Dr. (Sci.), Depart*ment of Science Laboratory Technology, University of Calabar, Calabar, Nigeria*; SCOPUS Author ID: 57224817629, https://orcid.org/0009-0001-8978-9997; ndianabasivalentine@ unical.edu.ng

APPENDIX A: Review of Nikiforov-Uvarov (NU) method

The NU method was proposed by Nikiforov and Uvarov [33] to transform Schrödinger-like equations into a second-order differential equation via a coordinate transformation $x = x(r)$, of the form

$$\psi''(x) + \frac{\tilde{\tau}(x)}{\sigma(x)}\psi'(s) + \frac{\tilde{\sigma}(x)}{\sigma^2(x)}\psi(x) = 0 \tag{A1}$$

where $\tilde{\sigma}(x),$ and $\sigma(x)$ are polynomials, at most second degree and $\tilde{\tau}(x)$ is a first-degree polynomial. The exact solution of Eq.(A1) can be obtain by using the transformation.

$$\psi(x) = \phi(x)y(x) \tag{A2}$$

This transformation reduces Eq.(A1) into a hypergeometric-type equation of the form

$$\sigma(x)y''(x) + \tau(x)y'(x) + \lambda y(x) = 0 \tag{A3}$$

The function $\phi(x)$ can be defined as the logarithm derivative

$$\frac{\phi'(x)}{\phi(x)} = \frac{\pi(x)}{\sigma(x)} \tag{A4}$$

With $\pi(x)$ being at most a first-degree polynomial. The second part of $\psi(x)$ being $y(x)$ in Eq.(A2) is the hypergeometric function with its polynomial solution given by Rodrigues relation as

$$y(x) = \frac{B_{nl}}{\rho(x)}\frac{d^n}{dx^n}\left[\sigma^n(x)\rho(x)\right] \tag{A5}$$

Where B_{nl} is the normalization constant and $\rho(x)$ the weight function which satisfies the condition below;

$$(\sigma(x)\rho(x))' = \tau(x)\rho(x) \tag{A6}$$

where, also

$$\tau(x) = \tilde{\tau}(x) + 2\pi(x) \tag{A7}$$

For bound solutions, it is required that

$$\tau'(x) < 0 \tag{A8}$$

The eigenfunctions and eigenvalues can be obtained using the definition of the following function $\pi(x)$ and parameter λ, respectively:

$$\pi(x) = \frac{\sigma'(x) - \tilde{\tau}(x)}{2} \pm \sqrt{\left(\frac{\sigma'(x) - \tilde{\tau}(x)}{2}\right)^2 - \tilde{\sigma}(x) + k\sigma(x)} \tag{A9}$$

And

$$\lambda = k_- + \pi'_-(x) \tag{A10}$$

The value of k can be obtained by setting the discriminant in the square root in Eq. (A9) equal to zero. As such, the new eigenvalues equation can be given as

$$\lambda + n\tau'(x) + \frac{n(n-1)}{2}\sigma''(x) = 0, (n = 0,1,2,...) \tag{A11}$$

EURASIAN PHYSICAL TECHNICAL JOURNAL

2026, Volume 23, No.3 (57)

https://doi.org/10.31489/2026N3/138-143

Received: 22/04/2026 Revised: 15/08/2026 Accepted: 28/09/2026 Published online: 30/09/2026

Original Research Article Open Access under the CC BY -NC-ND 4.0 license

UDC 53.01

PHOTOMETRIC VARIABILITY OF DO LEO BASED ON TESS DATA

Achkassova S.E., Vaidman N.L., Khokhlov S.A., Agishev A.T.*, Azhikenova A.S.

al-Farabi Kazakh National University,
Data Science in Astrophysics Research Center named after Z.Zhanabayev, Almaty, Kazakhstan
*Corresponding author: agishev.aldiyar@kaznu.kz

Abstract. *This article presents a photometric analysis of the cataclysmic variable star DO Leo. The main focus is on TESS observational data, in particular sector 72. The main focus of this work is the analysis of TESS data. This work investigates the TESS light curve of DO Leo obtained in Sector 72, which has not been previously analyzed in detail. This data set allows us to examine cycle-to-cycle variability and characteristic photometric modulation. The analysis reveals pronounced short-period variability with a period of approximately 5.6 hours, consistent with the previously reported orbital period of DO Leo. At the same time, cycle-to-cycle amplitude variations were identified, indicating that the shape of the light curve and the depth of the modulation vary. To further estimate the period, the Lomb–Scargle method was applied, confirming the derived period. Bootstrap resampling was used to estimate the period uncertainty. Ultimately, the obtained results confirm the nature of DO Leo and highlight the importance of this object for studying instability processes in cataclysmic variable stars.*

Keywords: CVS, eclipsing binary systems, photometric variability, light curves, TESS.

1. Introduction

Cataclysmic variables (CVs) are interacting binary systems in which one of the components, a white dwarf, accretes matter from a low-mass compagnon orbiting it. The observed variability of such systems is due to several physical processes, such as instability of the accretion disk, magnetic control of the mass flux in magnetic systems, and thermonuclear flares on the surface of a white dwarf in novae [1].

In the evolution of cataclysmic variables, special attention is paid to the relationship between the observed variability and the accretion regime, the evolution of the orbital period due to the loss of angular momentum. Great importance is still attached to the problem of period discontinuity and the discrepancy between the theoretically predicted and observed spatial density of such systems [2].

In recent studies of eclipsing cataclysmic variables, it has been noted that their variability is influenced by changes in the structure of the accretion flow and the physical condition of the disk, as well as changes in the rate of mass transfer. For example, in the work of Kara et al. [3] analysis of the AY Psc system of the Z Cam type showed that the rate of mass transfer varies between different states, which affects changes in the accretion disk. Similarly, Medina Rodriguez et al. [4], observing the VY Scl SDSS J154453.60+255348.8 type system, found that the photometric behavior depends on the accretion regime, while the accretion disk is present in the high state and more suppressed in the low state. It can be concluded that the observed variability is due not only to orbital motion in the binary system, but also to changes in the accreting flow.

Recent TESS observations have significantly expanded the possibilities for studying cataclysmic variables due to the availability of long and nearly continuous light curves. Bruch [5] demonstrated the effectiveness of TESS data for detecting periodic variability and determining or refining orbital periods in

cataclysmic variables. Ellaqany et al. [6] analyzed TESS photometry of eclipsing CVs to determine orbital periods and eclipse epochs and to investigate possible orbital-period changes. More recently, Dağ et al. [7] performed a systematic analysis of TESS observations of a large sample of cataclysmic variables and candidates using Lomb–Scargle periodograms to identify coherent periodic signals. These studies demonstrate the effectiveness of TESS photometry for investigating orbital and short-term variability in cataclysmic systems.

One of the most prominent representatives of the CVs class is DO Leo (TIC 61285257). In the work of Abbott et al. [8], spectroscopic and photometric analysis showed that the observed eclipse is approximately $1^m.5$ deep and the period ≈ 5.63 hours. More recently, Subebekova et al. [9] included DO Leo in a catalog of eclipsing cataclysmic variables based on TESS observations, reporting an orbital period of approximately 5.62 hours. The DO Leo spectrum contains emission lines of hydrogen, He I, and a pronounced He II-line λ4686, which indicates a high degree of gas ionization and makes this object particularly interesting from the point of view of its classification [8]. According to modern Gaia DR3 data, DO Leo has a brightness of G ≈ 16.87 and a parallax of about 0.805±0.075 wt, which corresponds to a distance of 1.18 ± 0.10 kpc [2]. Additional opportunities for studying this object are provided by the TESS (Transiting Exoplanet Survey Satellite) observations, which provide continuous photometric time series suitable for studying the stability of periodic signals and the detailed shape of the light curve [10].

In this paper, the photometric variability of DO Leo is analyzed using TESS data, with a focus on Sector 72. The aim of this study is to characterize short-term modulation, evaluate its cycle-to-cycle stability, and investigate variations in the shape and amplitude of the light curve.

2. Observations and data analysis.

Photometric data used in this work were obtained with TESS. Sector 72 was selected, and SPOC data for TIC 61285257 (DO Leo) with a frequency of 200s was used. This sector has not been analyzed before and the choice is due to the presence of a homogeneous and almost continuous time series suitable for studying the short-term photometric variability of an object. The data was uploaded and initially processed using the Barbara A. Mikulski Archive for Space Telescopes (MAST) [11] and the lightkurve package in the Python environment. The processing also included removing invalid values (NaN) and normalizing the flow for further analysis. To study the object, the light curve of sector 72 was divided into local maxima and minima. Since the observed signal contains both relatively deep brightness dips and smaller local modulations, using all the identified minima would introduce an additional error in determining the cycle. Therefore, local minima located close to the maxima were used to determine individual cycles. This provides a more uniform description of the signal in a short time interval by suppressing false long intervals caused by deeper minima, that is, large drops in brightness. The cycle was determined by the distance between successive local minima.

For additional verification, an independent search was performed for the period along the light curve for sector 72 using the Lomb-Scargle method. The uncertainty of the Lomb-Scargle period was estimated using an initial resampling procedure that was applied to the original time series. In each implementation, the light curve was resampled and replaced. And the final period was taken as the median of the resulting deviation of this distribution.

3. Results

At the first stage, the TESS light curve for DO Leo in sector 72 was studied. Figure 1 shows that the observed signal has a complex structure and represents a short-period component of variability. Since the purpose of this analysis was to trace local short-period modulation, only the last minima were used to determine individual cycles of variability. This avoids misidentification of cycles caused by deep drops in brightness. Based on the identified maxima and selected local minima, the light curve was divided into cycles. The boundaries of individual cycles were determined by minima associated with short-period modulation.

After dividing the light curve of DO Leo into cycles, a period was determined for each cycle and is presented in Figure 2. Looking at the figure, it is clear that the periods fluctuate around a single average value about 5.6 hours. However, slight deviations are also observed in the first and last approximately ten cycles. These deviations may be attributed to variations in the light curve itself and to changes in the orbital motion of the system from cycle to cycle. This indicates the presence of repetitive modulation, a constant short-term component in the variability of the system.

.

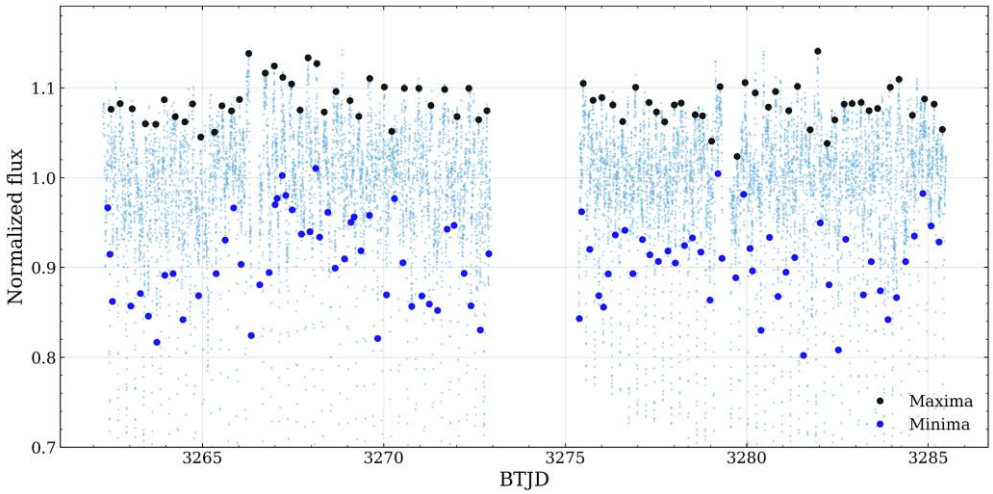


Fig. 1. The light curve of DO Leo in sector 72. The black dots correspond to the maxima, while blue dots - to the minima. BTJD = BJD - 2457000.

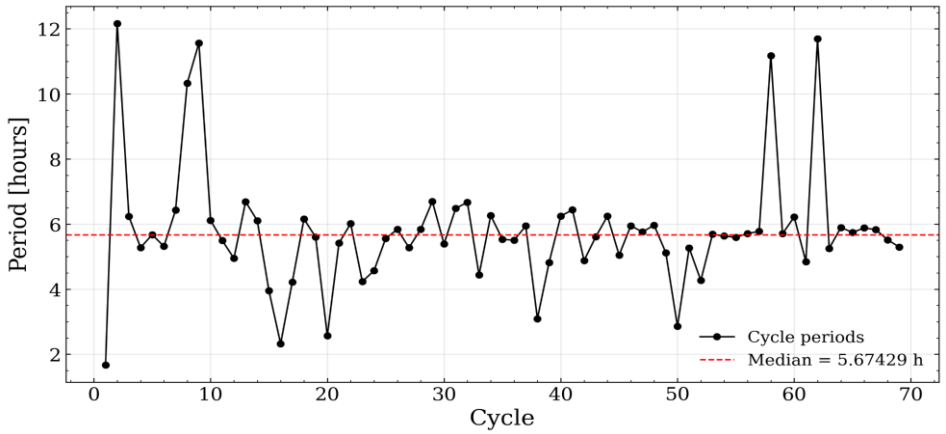


Fig. 2. Dependence of the period on the cycle. The red dashed line indicates the average value of the period ~ 5.6 h.

After that, an additional check was carried out to determine the period using the Lomb-Scargle method. Figure 3 shows a periodogram where a prominent peak indicates a period value of about 5.63 hours, which confirms the cycle-based analysis and the repeating signal.

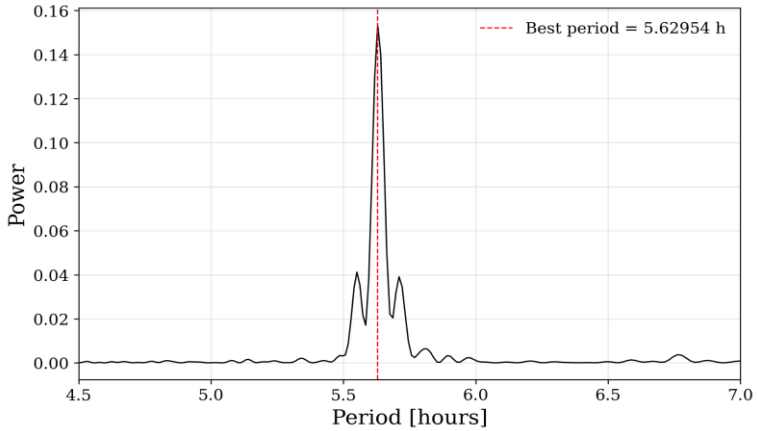


Fig. 3. Lomb-Scargle periodogram of DO Leo in sector 72.

However, it should be borne in mind that the two methods used should be considered as separate approaches, since the cycle-based method is sensitive to selected local minima, while the Lomb-Scargle method considers the complete structure of the light curve. The uncertainty of the period calculated by the

Lomb-Scargle method was determined using an initial re-sampling of the light curve. The resulting distribution of periods gives the total value of the period. This provides a reliable statistical estimate of the observed signal.

The results obtained were collected and presented in Table 1. The photometric variability of the object is non-permanent and may indicate changes in the light curve due to the contribution of components in the system. It may also be related to the geometry and physical component of the accreting substance.

Table 1. Comparison of periods of DO Leo with different methods.

Method	Period (h)
Cycle-based analysis	5.67
Lomb-Scargle	5.63
Bootstrap Lomb-Scargle	5.63 ± 0.001

At the next stage, each cycle was phased out, and Figure 4 shows the overall light curve. Superimposing the light curves on top of each other allows us to study the average shape of the modulation, and it can be seen that most of the data describes a certain profile of the light curve. This result indicates the presence of constant short-period modulation and is consistent with the results of the cycle analysis. A light curve with an average period of 5.6 hours was also highlighted.

At the same time, noticeable differences remain from cycle to cycle, both in amplitude and in the detailed shape of the profile. These deviations are expressed in changes in the depth of the minima, the height of the maxima, and minor phase-dependent distortions of the folded profiles. This behavior indicates that although the system exhibits repetitive short-term modulation, the detailed photometric response is not strictly stationary.

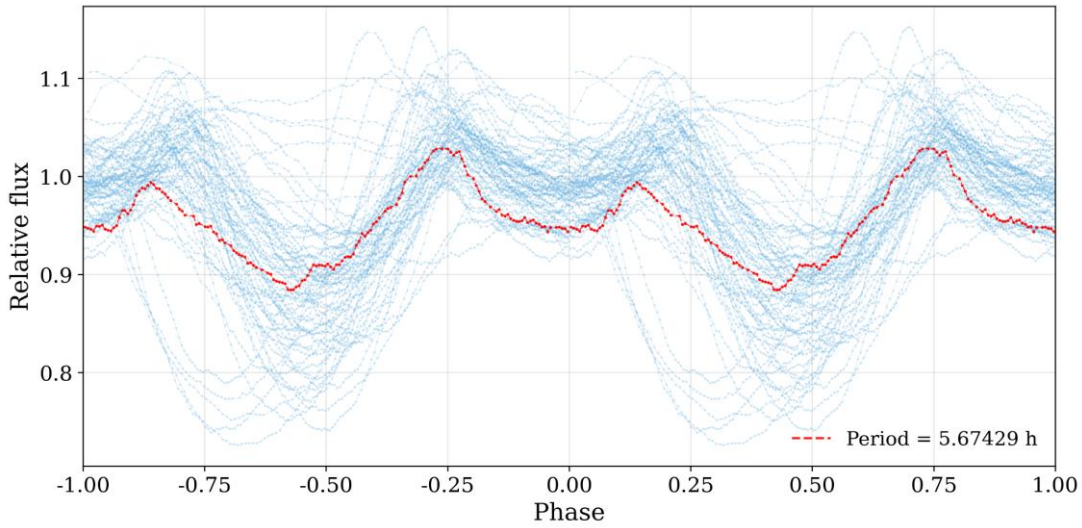


Fig. 4. The light curves of individual cycles of DO Leo.
The red dashed line highlights the modulation combined with a period of 5.67 h.

In addition, for each selected cycle, the oscillation amplitude was calculated as the difference between the maximum and neighboring minima. This analysis makes it possible to assess how stable the modulation depth changes from cycle to cycle. It also allows you to check whether its intensity remains constant.

The resulting amplitude value is shown in Figure 5. It is noticeable that the amplitude value between maxima and minima of the light curve fluctuates within a range of 0.18. These cycle-to-cycle variations exhibit pronounced modulation. This behavior is consistent with our findings, which show that despite the presence of a stable periodic component, the shape of the light curve of DO Leo and amplitude vary. That is, they do not remain strictly constant.

.

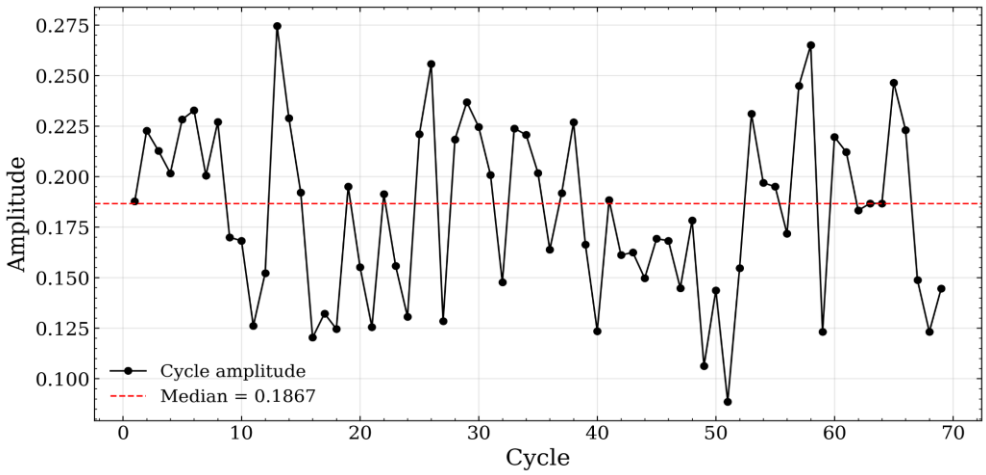


Fig. 5. Dependence of the amplitude on the sector cycle 72.
The red dashed line corresponds to the average value of 0.1867.

4. Conclusion

This work was based on an analysis of DO Leo photometric variability using TESS data. The main analysis was based on the determination of the period by cycles; an additional check was the Lomb-Scargle analysis. As a result, a persistent short-term modulation with a characteristic period of about 5.6 hours was detected. Repeated bootstrap resampling was used to estimate the uncertainty of the derived period.

The obtained light curves show that there is a general modulation scheme, but the shape and depth of the variability is not strictly constant. Therefore, the photometric behavior of the object is not strictly stable, but involves a change in amplitude from cycle to cycle. This confirms the assumption that the detected signal is at least partially related to the variability of the system's orbit.

With catastrophic variables, this behavior is naturally expected if the accretion disk evolves over time. In this context, cycle-based analysis, the Lomb-Scargle periodogram, and initial uncertainty estimates provide additional information about the repetitive and non-stationary components of the observed signal.

Taken together, these results indicate that the DO Leo variability is determined by the interaction between a recurring short-term component and unsteady processes most likely related to the accretion disk and its evolving structure.

Conflict of interest statement
The authors declare that they have no conflict of interest in relation to this research, whether financial, personal, authorship or otherwise, that could affect the research and its results presented in this paper.

CRediT author statement
Achkassova S.E.: Formal analysis, Software, Visualization, Writing - Original Draft; **Vaidman N.L.:** Conceptualization, Resources; **Khoklov S.A.:** Validation, Methodology, Project administration; **Agishev A.T.:** Investigation, Data curation, Writing - Review & Editing, Supervision; **Azhikenova A.S.:** Visualization, Investigation. The final manuscript was read and approved by all authors.

Statement on the use of Artificial Intelligence.
The authors declare that no artificial intelligence tools were used to generate scientific content, results, or conclusions of this article.

Data Availability Statement
The data that support the findings of this article are openly available.

Funding

This research was funded by the Science Committee of the Ministry of Science and Higher Education of the Republic of Kazakhstan (Grant No. AP23484898).

References

1 Knigge, C. (2006). The donor stars of cataclysmic variables. *Monthly Notices of the Royal Astronomical Society*, 373(2), 484-502. https://doi.org/10.1111/j.1365-2966.2006.11096

2 Canbay, R., Bilir, S., Özdönmez, A., & Ak, T. (2023). Galactic model parameters and spatial density of cataclysmic variables in the Gaia era: New constraints on population models. *The Astronomical Journal*, 165(4), 163. https://doi.org/10.3847/1538-3881/acbead

3 Kára, J., Zharikov, S., Wolf, M., Amantayeva, A., Subebekova, G., Khokhlov, S., Agishev, A., & Merc, J. (2023). The Z Camelopardalis-type Star AY Piscium: Stellar and Accretion Disk Parameters. *The Astrophysical Journal*, 950(1), 47. https://doi.org/10.3847/1538-4357/accd63

4 Medina Rodriguez, A.L., Zharikov, S., Kára, J., Wolf, M., Agishev, A., & Khokhlov, S. (2023.) VY Scl-type cataclysmic variable SDSS J154453.60+255348.8: stellar and disc parameters. *Monthly Notices of the Royal Astronomical Society*, 521(4), 5846-5859. https://doi.org/10.1093/mnras/stad881

5 Bruch, A. (2022). TESS light curves of cataclysmic variables – I – Unknown periods in long-known stars. *Monthly Notices of the Royal Astronomical Society*, 514(4), 4718-4735. https://doi.org/10.1093/mnras/stac1650

6 Ellaqany, M.M., Garcia-Lopez, V., Hatten, E.S., Agarwal, M., & Moffett, D.A. (2025). Period Analysis of Eclipsing Cataclysmic Variable Stars. *Journal of the American Association of Variable Star Observers*, 53.

7 Dağ, M.K., Scaringi, S., O'Brien, K., Veresvarska, M., Rawat, N., Tampo, Y., Hernández-Díaz, S., et al. (2026). A catalogue of orbital periods of cataclysmic variables and candidates from TESS observations. *Monthly Notices of the Royal Astronomical Society*, 548(1), stag514. https://doi.org/10.1093/mnras/stag514

8 Abbott, T.M.C., Shafter, A.W., Wood, J.H., Tomaney, A.B., & Haswell, C.A. (1990). DO Leonis: A new eclipsing cataclysmic variable. *Publications of the Astronomical Society of the Pacific*, 102, 558-564. https://doi.org/10.1086/132669

9 Subebekova, G., Adil, M., Khokhlov, S., & Agishev, A. (2025) A List of the Most Prospective Eclipsing Cataclysmic Variables According to the TESS. *Galaxies,* 13(4), 92. https://doi.org/10.3390/galaxies13040092

10 Ricker, G.R., Winn, J.N., Vanderspek, R., Latham, D.W., Bakos, G.Á., et al. (2015). Transiting Exoplanet Survey Satellite (TESS). *Journal of Astronomical Telescopes, Instruments, and Systems*, 1(1), 014003. https://doi.org/10.1117/1.JATIS.1.1.014003

11 Barbara, A. Mikulski Archive for Space Telescopes (MAST) (2023). Space Telescope Science Institute. Available online: https://archive.stsci.edu

---

AUTHORS' INFORMATION

Achkassova Snezhana – BSc student, Al-Farabi Kazakh National University, Almaty, Kazakhstan, ORCID: 0009-0003-5247-4275, snezhanachkasova29@gmail.com

Vaidman, Nadezhda – MSc, Al-Farabi Kazakh National University, Almaty, Kazakhstan, Scopus: 58554640500, ORCID: 0000-0002-7449-0108, nva1dmann@gmail.com

Khoklov, Serik – PhD, Al-Farabi Kazakh National University, Almaty, Kazakhstan, Data Science in Astrophysics Research Center named after Z.Zhanabayev, Almaty, Kazakhstan, Scopus: 57193160477, ORCID: 0000-0001-5163-508X, skhokh88@gmail.com

Agishev, Aldiyar – PhD, Al-Farabi Kazakh National University, Almaty, Kazakhstan, Data Science in Astrophysics Research Center named after Z.Zhanabayev, Almaty, Kazakhstan, Scopus:57201661110, ORCID: 0000-0001-9788-7485, agishev.aldiyar@kaznu.kz

Azhikenova, Alina – MSc student, Al-Farabi Kazakh National University, Almaty, Kazakhstan, ORCID: 0009-0009-8360-1226, alina40021071@gmail.com

.

EURASIAN PHYSICAL TECHNICAL JOURNAL

2026, Volume 23, No. 3 (57)

https://doi.org/10.31489/2026N3/144-153

Received: 10/06/2026 Revised: 21/08/2026 Accepted: 28/09/2026 Published online: 30/09/2026

Original Research Article

Open Access under the CC BY -NC-ND 4.0 license

UDC 53.01; 524.8

COSMOLOGICAL EVOLUTION DYNAMICS AND OM(Z) DIAGNOSTIC IN A SCALAR–FERMION MODEL WITH A GENERALIZED SCALE FACTOR

Ratbay A.*, Razina O., Tsyba P., Satbekova E.

L.N. Gumilyov Eurasian National University, Astana, Kazakhstan
*Corresponding author: aisara.ratbay@gmail.com

Abstract. *A cosmological model of an expanding Universe with scalar–fermion interactions is considered.Our model is based on the interaction of scalar and fermion fields via a Yukawa-type coupling, which influences the development of cosmological expansion in its late stages. The generalized scale factor is used to study the evolution and dynamics of the system. This approach allows us to explore various expansion regimes and analyze the contribution of fields, namely, the scalar and fermion components, to the total energy density and pressure. The viability of the cosmological evolution model is studied using the dimensionless Hubble parameter and the Om(z) diagnostic.The behavior obtained differs from the standard ΛCDM case, where the parameter* $Om(z)$ *remains constant. Our results show that the effective component of dark energy dynamically evolves as the Universe expands. Our analysis demonstrates that the interaction of scalar and fermion fields can significantly influence the history and evolution of the expansion and lead to stable cosmological behavior. The proposed model can be used for further studies of dark energy interaction scenarios.*

Keywords: Scalar–fermion interaction, Yukawa coupling, cosmic acceleration, dark energy models, Om(z) parameter.

1. Introduction

The physical nature of the accelerating expansion of the Universe remains one of the central open problems in modern cosmology [1–3]. Observational data indicate that the expansion rate increases in the late stages, while within the standard formulation of general relativity, such behavior cannot be explained without introducing an additional component. This motivates us to consider extended cosmological scenarios in which the effective energy content of the Universe changes and does not remain constant. In this context, scalar field models have proven particularly effective, as they offer a flexible framework capable of describing various evolutionary regimes of our Universe [4–6]. At the same time, we can usefully consider interactions between scalar and fermionic fields [7–13]. Coupling with fermionic matter makes additional contributions to the total energy density and pressure, thereby influencing the overall dynamics and evolution of the expansion [7,8]. Yukawa-type interactions represent one of the simplest and most consistent ways to account for such effects [12,13]. To analyze the expansion history in a model-independent manner, we typically use diagnostic quantities. One of the most informative tools is the parameter $Om(z)$, defined as [14,15]

$$Om(z) = \frac{E^2(z) - 1}{(1+z)^3 - 1}, \tag{1}$$

where the dimensionless Hubble function is given by

$$E(z) = \frac{H(z)}{H_0}. \quad (2)$$

This diagnostic parameter allows us to track the evolution of the expansion rate and distinguish between different dark energy scenarios without specifying a specific cosmological model. A cosmological model with scalar-fermion interactions is considered within a framework that uses a generalized form of the chosen scale factor. Our goal is to investigate how the interaction term influences the expansion dynamics so that we can analyze the resulting behavior using the diagnostic parameter $Om(z)$.

2.Theoretical Framework and Research Methods

2.1. Field equations and Cosmological Dynamics

A cosmological model in which a scalar field is coupled to a fermionic sector is considered.Here we will work only with the scalar-fermionic system and neglect any additional contribution of matter. Our system dynamics are described by the action [7,8,12,13]

$$S = \int d^4x\sqrt{-g}\left[\frac{1}{2}R + \frac{1}{2}g^{\mu\nu}\,\partial_\mu\phi\,\partial_\nu\phi - U(\phi) - \lambda\bar{\psi}\phi\psi + \frac{i}{2}\left(\bar{\psi}\Gamma^\mu D_\mu\psi - (D_\mu\bar{\psi})\Gamma^\mu\psi\right) - V(\bar{\psi}\psi)\right] \quad (3)$$

where, ϕ is the scalar field, ψ is the fermionic spinor field, and ψ is its Dirac conjugate.

The function $U(\phi)$ denotes the scalar field potential, while $V(\bar{\psi}\psi)$ describes the fermionic self-interaction potential. The parameter λ characterizes the interaction between the scalar and fermionic sectors. To do this, we use the Friedman-Lemaitre-Robertson-Walker spatially flat metric [4]

$$ds^2 = dt^2 - a^2(t)(dx^2 + dy^2 + dz^2), \quad (4)$$

where, $a(t)$ is the cosmological scale factor describing the expansion dynamics of the Universe.

The effective Lagrangian takes the form

$$L = -3a\dot{a}^2 + a^3\left[\frac{1}{2}\dot{\phi}^2 - U(\phi) - \lambda\bar{\psi}\phi\psi + \frac{i}{2}\left(\bar{\psi}\gamma^0\dot{\psi} - \dot{\bar{\psi}}\gamma^0\psi\right) - V(\bar{\psi}\psi)\right], \quad (5)$$

here, the dot denotes differentiation with respect to the cosmic time t. Together with the Friedmann–Robertson–Walker metric (4), the equations of motion derived from the action (3) take the following form

$$3H^2 = \rho, \quad (6)$$

$$-2\dot{H} - 3H^2 = p, \quad (7)$$

$$\ddot{\phi} + 3H\dot{\phi} + \frac{dU}{d\phi} + \lambda\bar{\psi}\psi = 0, \quad (8)$$

$$\dot{\psi} + \frac{3}{2}H\psi + i\gamma^0\frac{\partial V}{\partial\bar{\psi}} + i\lambda\gamma^0\psi\phi = 0, \quad (9)$$

$$\dot{\bar{\psi}} + \frac{3}{2}H\bar{\psi} - i\frac{\partial V}{\partial\psi}\gamma^0 - i\lambda\phi\bar{\psi}\gamma^0 = 0 \quad (10)$$

The effective energy density and pressure are given by

$$\rho = \frac{1}{2}\dot{\phi}^2 + U(\phi) + \lambda\phi\psi\bar{\psi} + V(\bar{\psi}\psi), \quad (11)$$

$$p = \frac{1}{2}\dot{\phi}^2 - U(\phi) + \bar{\psi}\psi\frac{dV}{d(\bar{\psi}\psi)} - V(\bar{\psi}\psi). \quad (12)$$

First, the Dirac equations are solved, and the evolution equation for the fermionic bilinear invariant is then obtained:

$$\frac{d}{dt}(\bar{\psi}\psi) + 3H(\bar{\psi}\psi) + i\left(\bar{\psi}\gamma^0\frac{\partial V}{\partial\bar{\psi}} - \frac{\partial V}{\partial\psi}\gamma^0\psi\right) = 0. \quad (13)$$

For the nonlinear fermionic self-interaction [7,8]

$$V = \delta_0(\bar{\psi}\psi)^n, \quad (14)$$

here, δ_0 is a constant parameter and n determines the power-law form of the fermionic self-interaction potential. This equation gives

$$\bar{\psi}\psi = \frac{C}{a^3}, \quad (15)$$

where C is an integration constant. Therefore, the fermionic potential becomes to

$$V = \delta_0\left(\frac{C}{a^3}\right)^n = \frac{\delta_0 C^n}{a^{3n}}. \quad (16)$$

Substituting Friedmann equations, we get

$$3H^2 = \frac{1}{2}\dot{\phi}^2 + U(\phi) + \frac{C\lambda\phi}{a^3} + \frac{\delta_0 C^n}{a^{3n}}, \quad (17)$$

$$-2\dot{H} - 3H^2 = \frac{1}{2}\dot{\phi}^2 - U(\phi) + (n-1)\frac{\delta_0 C^n}{a^{3n}}. \quad (18)$$

2.2. Reconstruction of the Scalar-Fermion System

The generalized scale factor [9] is used in the analysis.

$$a(t) = \alpha + \beta e^{\gamma t^2} t^{2\delta}, \quad (19)$$

where the constants α, β, γ and δ control the dynamical behavior of the expansion.

This combination of the exponential and power-law scale factor goes beyond simple power-law models and allows for a richer set of evolutionary modes. At the same time, the exponential has the property of a super-de Sitter solution due to t^2, characterized by faster dynamics. Figure 1 illustrates the dynamical evolution of the generalized scale factor with cosmic time.

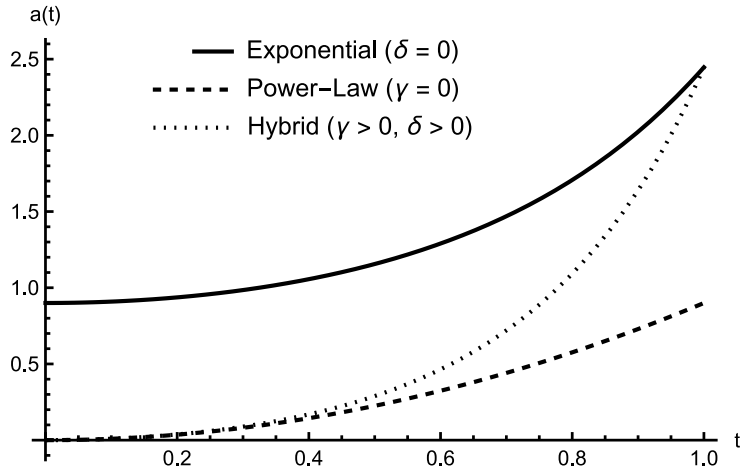


Fig.1. Evolution of the hybrid scale factor $a(t)$ for different parameter values: the exponential expansion regime ($\delta = 0$), the power-law expansion regime ($\gamma = 0$, dashed curve), and the hybrid expansion regime ($\gamma = 0, \delta = 0$, dotted curve).

For all considered parameter sets, the scale factor increases monotonically, describing an expanding Universe. Larger values of the parameter β lead to a more rapid growth of $a(t)$, indicating an enhanced expansion rate. At later stages, the expansion becomes significantly accelerated due to the exponential contribution in the chosen parametrization.

The corresponding Hubble parameter is

$$H = \frac{2\beta e^{\gamma t^2} t^{2\delta-1}(\gamma t^2 + \delta)}{\alpha + \beta e^{\gamma t^2} t^{2\delta}} \tag{20}$$

The derivative of the Hubble parameter follows directly from the explicit form of $H(t)$:

$$\dot{H} = \frac{\beta e^{\gamma t^2} t^{2\delta-2}\left[4\gamma^2 t^4 + 2\gamma(4\delta+1)t^2 + 2\delta(2\delta-1)\right]\left(\alpha+\beta e^{\gamma t^2} t^{2\delta}\right) - 4\beta^2 e^{2\gamma t^2} t^{4\delta-2}(\delta+\gamma t^2)^2}{\left(\alpha+\beta e^{\gamma t^2} t^{2\delta}\right)^2}. \tag{21}$$

To obtain an explicit expression for the scalar field, we define the form of self-interaction potential as

$$U(\phi) = \frac{1}{2} m^2 \phi^2. \tag{22}$$

For convenience, we combine the Friedmann equations by subtracting the pressure equation from the energy density equation, which leads to

$$\rho - p = 6H^2 + 2\dot{H}. \tag{23}$$

Using the previously obtained expressions for ρ and p, we rewrite the left-hand side as

$$\rho - p = m^2\phi^2 + \frac{C\lambda}{a^3}\phi + (2-n)\frac{\delta_0 C^n}{a^{3n}}. \tag{24}$$

By equating both expressions, we obtain the following algebraic equation for the scalar field

$$m^2\phi^2 + \frac{C\lambda}{a^3}\phi + (2-n)\frac{\delta_0 C^n}{a^{3n}} - (6H^2 + 2\dot{H}) = 0. \tag{25}$$

The corresponding solution for the scalar field is [13]

$$\phi = \frac{-\frac{C\lambda}{a^3} \pm \sqrt{\frac{C^2\lambda^2}{a^6} - 4m^2\left[(2-n)\frac{\delta_0 C^n}{a^{3n}} - (6H^2+2\dot{H})\right]}}{2m^2}. \tag{26}$$

Substituting the obtained the scalar field solution into the potential yields

$$U(\phi) = \frac{1}{8m^2}\left(-\frac{C\lambda}{a^3} \pm \sqrt{\frac{C^2\lambda^2}{a^6} - 4m^2\left[(2-n)\frac{\delta_0 C^n}{a^{3n}} - (6H^2+2\dot{H})\right]}\right)^2. \tag{27}$$

3.Results and Discussion

3.1. Observational constraints

To work with observational data, a transition to redshift terms is required. The cosmological time t is not tied to a specific scale, which makes it difficult to determine the exact time intervals. The redshift z, on the contrary, allows for an accurate determination of the moment of an event. The transition to redshift terms is made according to the formula

$$a(t) = \frac{1}{1+z}. \tag{28}$$

The transition to redshift terms leads to a dimensionless Hubble parameter of the form

$$E(z) = \frac{2\beta\sqrt{\gamma\delta}e^{\delta\mathcal{W}}(1+\mathcal{W})}{\left(\beta e^{\delta\mathcal{W}}+\alpha\left(\sqrt{\frac{\delta}{\gamma}}\mathcal{W}\right)^{-2\delta}\right)\sqrt{\mathcal{W}}}, \quad (29)$$

where $\mathcal{W} = \mathrm{W}\left(\frac{\gamma}{\delta}\left(\frac{(1+z)^{-1}-\alpha}{\beta}\right)^{\frac{1}{\delta}}\right)$ is the Lambert function.

However, working with observational data requires dimensional calibration of the Hubble parameter, so E(z) is transformed using the formula $H(z) = H_0E(z)$, where H_0 is the value of the Hubble parameter in the modern era at $z = 0$. The following sets of observational data are used to verify the model and select parameters:

1. *Cosmic Chronometers* (CC) [16] is a set of model-independent measurements of the Hubble $H(z)$ function obtained from the differential ages of passive galaxies in the range up to about $z \sim 2$.

2. *Baryonic Acoustic Oscillations* (BAO) datasets SDSS and DESI [17] contain measurements of the characteristic scale of baryon acoustic oscillations in the distribution of galaxies and quasars, usually in the form of combinations of distances (angular and radial) and the Hubble scale at different redshifts. They provide geometric constraints on cosmological parameters through the standard BAO ruler.

3. *Pantheon+ with SH0ES* [18] is a combined data set of type Ia Pantheon+ supernovae with local calibration of distances from SH0ES, providing measurements of the distance module in a wide range of redshifts and direct reference to the Hubble H0 scale.The likelihood formula is used for calculations:

$$\ln\mathcal{L} = -\frac{1}{2}\chi^2 = -\frac{1}{2}\sum_i\left(\frac{H_{\mathrm{mod}}(z_i)-H_{obs}}{\sigma_{H_{obs}}}\right)^2, \quad (30)$$

where H_{mod} is the Hubble function of the model, H_{obs} is the observational Hubble parameter and $\sigma_{H_{obs}}$ is the error of observations.

The Cobaya MCMC Bayesian analysis code with the Gelman-Rubin convergence criterion $R - 1 < 0.01$ was used to analyze the parameter values. The calculation results are shown in Figure 2 and Table 1.

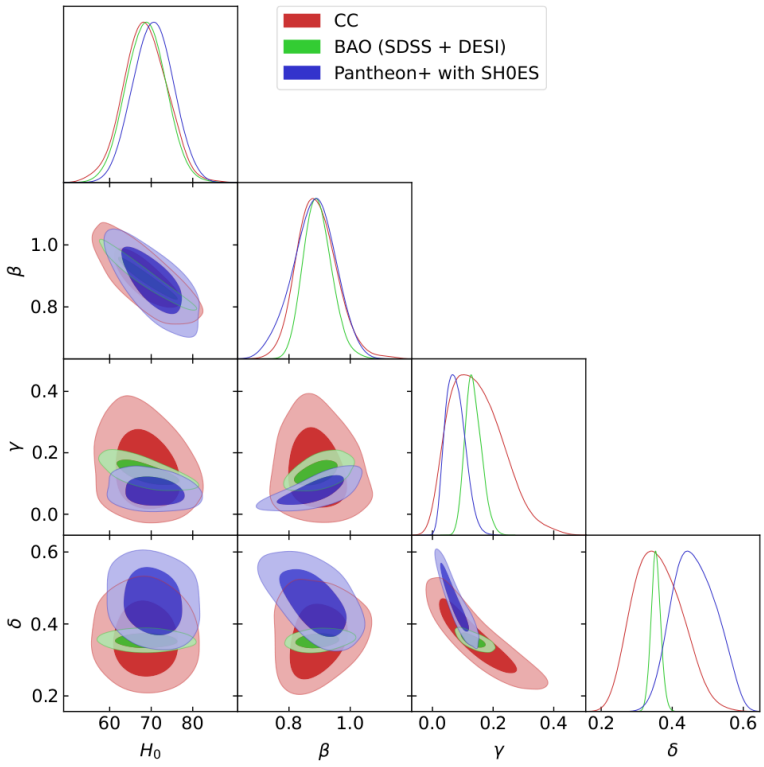


Fig.2. Constraints on cosmological parameters obtained from three independent datasets: CC (red), BAO (green) and Pantheon+ with SH0ES calibration (blue) with confidence levels 1σ and 2σ.

Table 1. Parameter values in the 1σ confidence interval

Dataset	H_0, m s^{-1} Mpc^{-1}	β	γ	δ
CC	$68.608^{+5.435}_{-5.241}$	$0.892^{+0.064}_{-0.064}$	$0.146^{+0.089}_{-0.090}$	$0.359^{+0.072}_{-0.070}$
BAO (SDSS+DESI)	$68.793^{+4.743}_{-4.885}$	$0.894^{+0.046}_{-0.046}$	$0.135^{+0.028}_{-0.027}$	$0.354^{+0.014}_{-0.013}$
Pantheon+ with SH0ES	$70.472^{+4.836}_{-4.929}$	$0.882^{+0.071}_{-0.070}$	$0.075^{+0.032}_{-0.033}$	$0.463^{+0.066}_{-0.061}$

3.2. Scalar-Field Evolution

Since the values of the scale factor parameters are known, the next step is to study the dynamics of the scalar field [9–13], the results of which are shown in Figure 3.

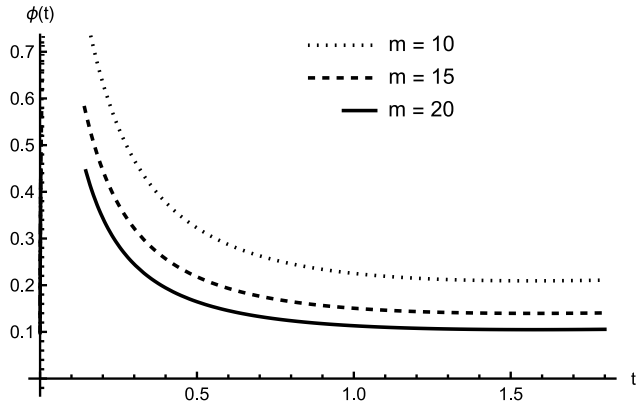


Fig.3. Evolution of the scalar field for different values of the parameter m: $m = 10$ (dotted), $m = 15$ (dashed), and $m = 20$. The scale-factor parameters are determined from the mean values reported in Table 1. The remaining model parameters are fixed at $C = 0.5$, $\lambda = 0.8$, $n = 2$, and $\delta_0 = 0.3$.

Figure 3 shows the time evolution of the scalar field. The field changes more rapidly at early stages, while at later times its variation becomes smoother, indicating a transition toward a more stable dynamical regime.

3.3. Energy Density and Pressure Evolution

The total energy density is given by the Friedmann equation

$$\rho = 3H^2. \tag{31}$$

Using Eq. (20), the total energy density becomes

$$\rho = 3\left[\frac{2\beta e^{\gamma t^2} t^{2\delta-1}(\delta+\gamma t^2)}{\alpha+\beta e^{\gamma t^2} t^{2\delta}}\right]^2. \tag{32}$$

The bosonic energy density is

$$\rho_b = \frac{1}{2}\dot{\phi}^2 + \frac{1}{2}m^2\phi^2, \tag{33}$$

where the scalar field $\phi(t)$ is given by (26).

The Yukawa interaction contribution to the energy density is

$$\rho_{Yukawa} = \frac{C\lambda}{a^3}\phi. \tag{34}$$

Using Eqs. (19) and (26), the Yukawa contribution becomes

$$\rho_{Yukawa} = \frac{-\frac{C^2\lambda^2}{a^6} \pm \frac{C\lambda}{a^3}\sqrt{\frac{C^2\lambda^2}{a^6} - 4m^2\left[(2-n)\frac{\delta_0 C^n}{a^{3n}} - (6H^2 + 2\dot{H})\right]}}{2m^2} \tag{35}$$

This expression is obtained by substituting the scalar-field solution into the Yukawa interaction term, which explicitly reveals how the interaction contribution is governed by the scalar-field dynamics and its coupling to the fermionic sector [12,13]. The fermionic energy density is

$$\rho_{fermion} = \frac{\delta_0 C^n}{a^{3n}}. \tag{36}$$

Using Eq. (19), we obtain

$$\rho_{fermion} = \frac{\delta_0 C^n}{(\alpha+\beta e^{\gamma t^2} t^{2\delta})^{3n}}. \tag{37}$$

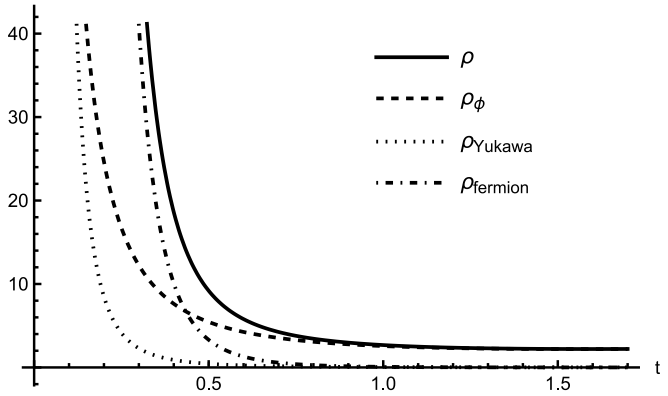


Fig.4 The time evolution of the energy density $\rho(t)$ and its components: ρ_ϕ (dashed), ρ_{Yukawa} (dotted) and $\rho_{fermion}$ (dot-dashed) with constant values: $C = 0.5, \lambda = 0.8, n = 2, m = 20$, and $\delta_0 = 0.3$.

Figure 4 shows how the total energy density and its components evolve with cosmic time. All curves decrease with increasing *t*, indicating a decrease in the effective energy density due to cosmic expansion and the gradual suppression of interaction terms in the late stages of the Universe. The Yukawa and fermion terms decrease rapidly and become almost negligible at later stages.

In contrast, the boson part changes more slowly and largely determine the characteristic behavior of the total energy density. This indicates that the contribution of the scalar field dominates the dynamics at later stages, while the other terms primarily influence the early stages of evolution rather than the later ones [4–6]. The pressure of the scalar field is

$$p_\phi = \frac{1}{2}\dot{\phi}^2 - \frac{1}{2}m^2\phi^2. \tag{38}$$

where $\phi(t)$ is defined by Eq. (26).

The fermionic pressure is

$$p_{fermion} = (n-1)\frac{\delta_0 C^n}{a^{3n}}. \tag{39}$$

Using Eq. (19), the following expression is obtained:

$$p_{fermion} = (n-1)\frac{\delta_0 C^n}{\left(\alpha+\beta e^{\gamma t^2} t^{2\delta}\right)^{3n}}. \tag{40}$$

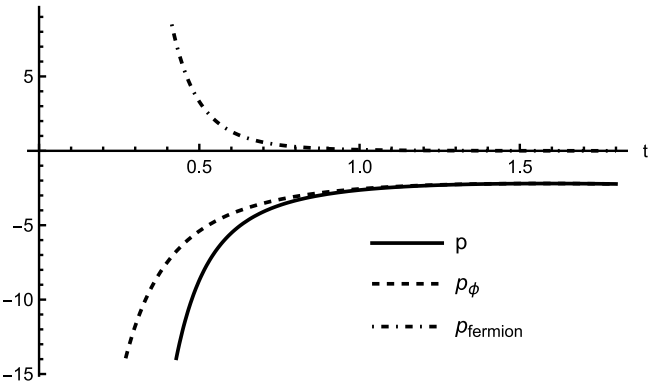


Fig.5. The time evolution of the energy density $p(t)$ and its components: p_ϕ (dashed), and $p_{fermion}$ (dot-dashed) with constant values $C = 0.5, \lambda = 0.8, n = 2, m = 20$, and $\delta_0 = 0.3$.

Figure 5 shows how the pressure component behaves in the model under consideration. In the early stages, we can see that the total pressure takes negative values and then gradually approaches zero as the system evolves. The scalar sector determines the overall dynamics, while the fermion contribution is secondary and rapidly diminishes. This behavior reflects the diminishing role of material structures during the cosmic expansion of the Universe.

3.4. Om(z) Diagnostic Analysis

In this section, we analyze the evolution of the proposed cosmological model using the diagnostic function *Om*(*z*), which provides a convenient tool for examining the expansion dynamics and distinguishing between different dark energy scenarios without specifying a particular model [14,15]. Using the Hubble parameter given in Eq. (20), the dimensionless Hubble function can be written as (29).The obtained expressions make it possible to study the evolution of *E*(*z*) and compare it with the standard ΛCDM cosmology. The Om diagnostic parameter is defined as (1)

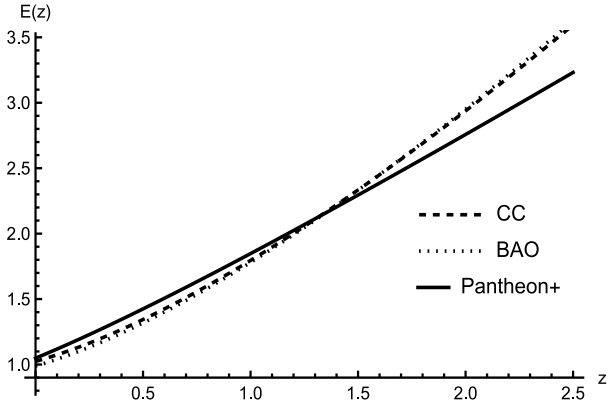


Fig.6. The function $E(z)$ as a function of the redshift z in the interval $0 < z \leq 2.5$

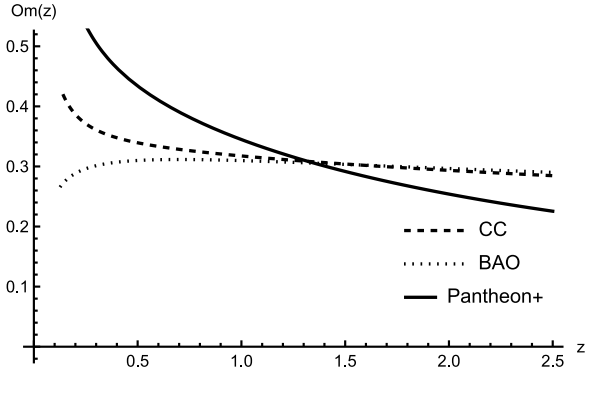


Fig.7. The function *Om*(*z*) as a function of the redshift z in the interval $0 < z \leq 2.5$

It is observed that the curves exhibit a pronounced variation at small values of z, indicating an active dynamical regime at late times. As z increases, the behavior gradually transitions toward a nearly constant and stable profile. Such a trend suggests that the considered model deviates from the standard ΛCDMscenario, for which the *Om*(*z*) parameter remains constant over redshift. The behavior of the parameter *Om*(*z*) gives us important insight into the phenomenon of dark energy within the framework of our proposed model [14]. We observed deviations from constant behavior, indicating a deviation from the constant ΛCDM scenario, suggesting the presence of a dynamic component to dark energy [14,15].

4.Conclusions

Using a generalized scale factor, we analyzed a cosmological model with scalar-fermion interactions. This approach allowed us to describe a broader class of expansion regimes without imposing any restrictive assumptions on the dynamics of our Universe.

The field equations of the model are obtained, and the corresponding expressions for the energy density and pressure of all relevant components are derived. Our results show that the interaction between the scalar and fermion sectors leads to a nontrivial modification of cosmological evolution, especially in the late stages of the Universe.

Our reconstructed Hubble function $E(z)$ exhibits smooth and physically consistent behavior over the redshift range under consideration. However, we discovered that the diagnostic parameter $Om(z)$ does not remain constant, indicating a clear deviation from the standard ΛCDM scenario. The results obtained indicate the dynamical nature of the effective dark energy component in the model. The behavior we obtained suggests that the scalar field makes the dominant contribution to the overall dynamics in the late stages of evolution, while the fermionic component becomes secondary as the Universe expands.

The proposed model provides a consistent phenomenological description of cosmic evolution and can serve as an alternative approach to modeling dark energy using interacting fields [9–13].

Conflict of interest statement.
The authors declare that there are no conflicts of interest regarding the publication of this paper.

CRediT author statement.
Ratbay A.: Conceptualization, Investigation, Formal analysis, Writing – original draft; **Razina O.:** Methodology, Supervision, Validation, Writing – review & editing; **Tsyba P.:** Theoretical framework development, Formal analysis, Interpretation of results; **Satbekova E.:** Literature review, Data curation, Visualization. The final manuscript was read and approved by all authors.

Statement on the use of Artificial Intelligence.
Artificial intelligence tools were used only for language editing and formatting assistance. All scientific derivations, calculations, interpretations, and conclusions were obtained and verified by the authors.

Data Availability Statement
The data that support the findings of this article are openly available.

Funding
This research was funded by the Science Committee of the Ministry of Science and Higher Education of the Republic of Kazakhstan (Grant No. AP26194585).

References

1 Planck Collaboration. (2020). Planck 2018 results. VI. Cosmological parameters. *Astronomy & Astrophysics*, 641, A6. https://doi.org/10.1051/0004-6361/201833910

2 Riess, A.G., Filippenko, A.V., Challis, P., Clocchiatti, A., Diercks, A., Garnavich, P.M., Gilliland R.L., Hogan C.J., Jha S., Kirshner R.P., Leibundgut B., Phillips M.M., Reiss D., Schmidt B.P., Schommer R., Smith R.C., Spyromilio J., Stubbs C., Suntzeff N.B., Tonry J. (1998). Observational evidence from supernovae for an accelerating universe and a cosmological constant. *Astronomical Journal*, 116, 1009–1038. https://doi.org/10.1086/300499

3 Perlmutter, S., Aldering, G., Goldhaber, G., Knop, R.A., Nugent, P., Castro, P.G., Deustua, S., Fabbro, S., Goobar, A., Groom, D.E., Hook, I.M., Kim, A.G., Kim, M.Y., Lee, J.C., Nunes, N.J., Pain, R., Pennypacker, C.R., Quimby, R., Lidman, C., Ellis, R.S., Irwin, M., McMahon, R.G., Ruiz-Lapuente, P., Walton, N., Schaefer, B., Boyle, B.J., Filippenko, A.V., Matheson, T., Fruchter, A.S., Panagia, N., Couch, W.J., Sutherland, R. (1999). Measurements of Ω and Λ from 42 high-redshift supernovae. *Astrophysical Journal*, 517, 565–586. https://doi.org/10.1086/307221

4 Copeland, E.J., Sami, M., Tsujikawa, S. (2006). Dynamics of dark energy. *International Journal of Modern Physics D*, 15, 1753–1936. https://doi.org/10.1142/S021827180600942X

5 Ratra, B., Peebles, P.J.E. (1988). Cosmological consequences of a scalar field. *Physical Review D*, 37, 3406–3427. https://doi.org/10.1103/PhysRevD.37.3406

6 Caldwell, R.R., Dave, R., Steinhardt, P.J. (1998). Cosmological imprint of dark energy. *Physical Review Letters,* 80, 1582–1585. https://doi.org/10.1103/PhysRevLett.80.1582

7Saha, B. (2001). Spinor field cosmology. *Physical Review D,* 64, 123501. DOI:10.1103/PhysRevD.64.123501

8 Ribas, M.O., Devecchi, F.P., Kremer, G.M. (2005). Fermions as sources of accelerated regimes in cosmology. Physical Review D, 72, 123502. https://doi.org/10.1103/PhysRevD.72.123502

9 Razina, O.V., Tsyba, P.Yu., Altayeva, G., Myrzakulova, S. (2023). Power law solution of a cosmological model with non-minimal coupled the fermionic field. *AIP Conference Proceedings*, 2872(1), 060004. https://doi.org/10.1063/5.0162898

10 Tsyba, P.Yu., Razina, O.V., Suikimbayeva, N.T. (2021). Analysis of cosmological tachyon and fermion model and observation data constraints. International *Journal of Modern Physics D,* 30(15), 2150114. https://doi.org/10.1142/S0218271821501145

11 Razina, O.V., Tsyba, P.Yu., Suikimbayeva, N.T. (2021). Tachyonization Cosmological Model in the Framework of Linear Form-Invariance Transformations. *Eurasian Physical Technical Journal,* 18(3), 93–100. https://doi.org/10.31489/2021No3/93-100

12 Chakrabarti, S., Lahiri, A. (2022). Scalar–fermion interaction as the driver of cosmic acceleration. Physics of the Dark Universe, 37, 1–15. https://doi.org/10.1016/j.dark.2022.101121

13 Razina, O.V., Myrzakulov, Y.M., Serikbayev, N.S., Nugmanova, G., Myrzakulov, R. (2011). G-essence cosmologies with scalar-fermion interactions. *European Physical Journal Plus,* 126(9), 85. https://doi.org/10.1140/epjp/i2011-11085-9

14 Sahni, V., Shafieloo, A., Starobinsky, A.A. (2008). Two new diagnostics of dark energy. *Physical Review D,* 78, 103502. https://doi.org/10.1103/PhysRevD.78.103502

15 Alcaniz, J.S. (2004). Some observational consequences of dark energy cosmologies. *Physical Review D,* 69, 083521. https://doi.org/10.1103/PhysRevD.69.083521

16 Moresco, M., Pozzetti, L., Cimatti, A., Jimenez, R., Maraston, C., Verde, L., Pozzetti, L., Tojeiro, R., Bolzonella, M., Zucca, E., et al. (2016). A 6% measurement of the Hubble parameter at z≈0.45: direct evidence of the epoch of cosmic re-acceleration. *Journal of Cosmology and Astroparticle Physics*, 2016(05), 014. https://doi.org/10.1088/14757516/2016/05/014

17 DESI Collaboration. (2024). DESI 2024 results: *Cosmological constraints from baryon acoustic oscillations*. https://arxiv.org/abs/2404.03002

18 Brout, D., Scolnic, D., Popovic, B., Riess, A.G., Riess, A.G., Jones, D.O., et al. (2022). The Pantheon+ Analysis: Cosmological Constraints. *Astrophysical Journal*, 938(2), 110. https://doi.org/10.3847/1538-4357/ac8e04

AUTHORS' INFORMATION

Ratbay, Aisara — PhD student, Department of General and Theoretical Physics, L.N. Gumilyov Eurasian National University, Astana, Kazakhstan; https://orcid.org/0009-0008-1031-9177; aisara.ratbay@gmail.com

Razina, Olga — PhD, Professor, Department of General and Theoretical Physics, L.N. Gumilyov Eurasian National University, Astana, Kazakhstan; Scopus ID: 52364540700; https://orcid.org/0000-0002-4400-4789; olvikraz@mail.ru

Tsyba, Pyotr – PhD, Associate Professor, Department of General and Theoretical Physics, L.N. Gumilyov Eurasian National University, Astana, Kazakhstan; Scopus ID: 36946423600; https://orcid.org/0000-0003-4928-0392; pyotrtsyba@gmail.com

Satbekova, Enilik — Master's student, Department of General and Theoretical Physics, L.N. Gumilyov Eurasian National University, Astana, Kazakhstan; https://orcid.org/0009-0008-0985-5343; satbekova.enilik@bk.ru

EURASIAN PHYSICAL TECHNICAL JOURNAL

2026, Volume 23, No. 3 (57)

https://doi.org/10.31489/2026N3/154-163

Received: 04/06/2026 Revised: 15/08/2026 Accepted: 28/09/2026 Published online: 30/09/2026

Received: 04/06/2026 Open Access under the CC BY -NC-ND 4.0 license

UDC 53.01; 519.6, 521.1, 524.4

COULD GLOBULAR CLUSTERS IN THE VICINITY OF THE GALACTIC CENTRE HAVE CONTRIBUTED STARS TO THE NUCLEAR STAR CLUSTER IN THE PAST?

Kalambay M.[1,2]*, Kuvatova D.[1,3], Ishchenko M.[4,5,1], Berczik P.[1,4], Omarov Ch.[1], Kusakin A.[1]

[1] Fesenkov Astrophysical Institute, Observatory 23, Almaty, Kazakhstan
[2] K. Zhubanov Aktobe Regional University, Aktobe, Kazakhstan
[3] Al-Farabi Kazakh National University, Almaty, Kazakhstan
[4] Main Astronomical Observatory, National Academy of Sciences of Ukraine, Kyiv, Ukraine
[5] National university of life and environmental sciences of Ukraine, Kyiv, Ukraine
*Corresponding author: kalambay@fai.kz

Abstract. *The results of direct N-body simulations of three Milky Way bulge globular clusters – Terzan 2, Terzan 4, and Terzan 5 – evolving in a time-varying galactic potential derived from the IllustrisTNG-100 cosmological database over 8 Gyr are presented. Incorporating full stellar evolution and compact remnant formation, we quantify the probability and efficiency of stellar accretion onto the Galactic nuclear star cluster (NSC) during close pericentre passages of these three clusters. To parametrize the effect of dynamical friction in the dense central environment, we introduce a velocity reduction factor (V_{red}) ranging from 1.00 to 0.10. It was found that all three clusters contribute stars to the NSC even in the absence of velocity reduction, with a combined bound stellar count of ~730 stars and a total accreted mass of ~278 $M_\odot$ at V_{red} = 1.00, growing to ~5420 stars and ~1175 $M_\odot$ at V_{red} = 0.10. Terzan 4 is the dominant contributor across all velocity reduction factors, reflecting its more frequent and closer pericentre passages near the Galactic centre. The mass distribution of accreted stars reveals a bimodal structure: a low-mass component below ~1 $M_\odot$ whose capture is independent of V_{red}, and a prominent high-mass tail extending to ~20 $M_\odot$ corresponding to neutron stars and black holes, which grows with decreasing V_{red}. Notably, Terzan 4 is the only cluster for which white dwarfs are also captured by the NSC at every V_{red} value. Our results suggest that the Terzan family represents a more significant source of compact remnants for the Galactic NSC than previously studied clusters, while confirming that tidal stripping of surviving globular clusters alone cannot account for the total NSC mass.*

Keywords: Globular Cluster, Nuclear Star cluster, Dynamical evolution, Milky Way, Time-variable galactic potential, N-body modelling, star accretion.

1. Introduction

Nuclear star clusters (NSCs) are among the densest and most massive stellar systems and are found in the centers of most late-type galaxies [1]. In the case of the Milky Way (MW), the mass of the NSC is estimated to be ~107 $M_\odot$ [2]. Its stellar population includes both old and relatively young components, indicating a complex formation history [3]. One of the proposed formation mechanisms for NSCs is the migration and subsequent dissolution of globular clusters (GCs) due to dynamical friction, leading to their accretion onto the

Galactic Centre (GalC) [4, 5]. Numerical models show that this process can proceed efficiently on cosmological timescales [6]. However, a number of studies suggest that the contribution of this mechanism is likely limited and can account for only a fraction of the NSC mass, while the remaining portion is formed through in situ star formation or gas accretion [7, 8]. An additional growth channel for NSCs can be associated not with the complete disruption of clusters, but with partial stellar mass loss during close passages through the GalC. In this case, even surviving clusters may contribute to the stellar population of the NSC [9]. It should be noted that the efficiency of this mechanism strongly depends on the orbital parameters of the clusters, their internal structure, and their evolutionary history [10].

In our previous works [6, 11], we investigated the dynamical evolution of six MW GCs (NGC 6401, NGC 6642, Palomar 6, NGC 6681, NGC 6981, and HP 1) selected based on a high probability of close passages to the GalC, using direct N-body simulations in a time-dependent potential derived from the cosmological database IllustrisTNG-100 [12, 13]. We showed that most of these clusters, which are predominantly bulge clusters, lose up to 70–90% of their mass over ~8 Gyr. A significant fraction of the stripped stars may potentially contribute to the formation of the NSC. However, only one GC - NGC 6642 exhibits a contribution to the NSC (primarily stars with masses < 1 $M_\odot$) of less than 0.1% of the current NSC mass, highlighting the strong dependence of the process on specific GC's orbital and structural properties.

At the same time, several bulge GCs, including Terzan 2, Terzan 4, and Terzan 5, were not included in the previous analysis, despite their proximity to the GalC and their potentially important dynamical role. These objects are of particular interest because, in addition to their close proximity to the GalC, they show signs of strong gravitational interactions with other clusters [14], which may significantly affect both their internal evolution and orbital dynamics. Terzan 5 occupies a special place, as its nature remains under debate. Unlike typical GCs, it exhibits a complex chemical and stellar structure, which has led to hypotheses that it may be the remnant of a protogalactic fragment or the product of mergers between multiple systems [15, 16]. This makes it a potentially non-standard source of stars for the NSC and warrants separate consideration. These three clusters were selected as a direct continuation of our previous study [6], in which we examined stellar accretion from clusters with close pericentre passages near the Galactic Centre but with apocentres located far from it (4–20 kpc). In the present work, we extend this analysis to clusters that evolve entirely within the central region of the Galaxy: Terzan 2, Terzan 4, and Terzan 5 all have apocentric distances of only 1–2 kpc, making them a natural sample for probing the accretion efficiency of clusters permanently confined to the Galactic Centre environment.

In this work, we focus on these three GCs, Terzan 2, Terzan 4, and Terzan 5, to assess their possible contribution to the formation and growth of the MW NSC. To this end, we perform direct N-body simulations of their evolution in a time-dependent galactic potential, including stellar evolution and the formation of compact remnants. This approach allows us to quantitatively evaluate the transfer of stars into the central region and its dependence on the properties of individual systems.

2. Initial conditions for physical models, modelling and mass loss

The initial conditions for each of the three selected Terzan-family clusters were chosen individually in order to reproduce the evolution of their masses and spatial characteristics. The initial stellar masses in each cluster were sampled from the Kroupa initial mass function [17] in the range 0.08-100 $M_\odot$. The individual metallicity of each cluster was taken into account in the subsequent stellar-evolution treatment [18]. To construct equilibrium initial models, we used King models [19] characterised by two free parameters: the half-mass radius r_{hm} and the dimensionless concentration parameter W_0. Thus, for each cluster, three key initial parameters – the mass M, r_{hm}, and W_0 – were selected at t = –8 Gyr relative to the present day. Their values were chosen so that, by the present epoch, the model clusters reproduced the observed properties of their real counterparts. The details of the fitting procedure are given in our earlier work [6], whereas a more complete description of the numerical setup is presented in our recent article [20]. The initial masses, half-mass radii, King concentration parameters, and metallicities adopted for the Terzan 2, Terzan 4, and Terzan 5 models at (t = –8 Gyr) Gyr are summarised in Table 1.

In addition, a scaling approach in which one numerical particle represents ten real stars of the same type was used. A detailed justification and description of this method are provided in [21]. The full N-body simulations were carried out using the parallel high-order φ-GPU code[1] [22], into which a time-dependent MW-like galactic potential was incorporated.

Table 1. Initial physical characteristics at -8 Gyr for the Terzans.

GC	M, 10^6 M $_\odot$	N	r_{hm}, pc	W_0	Z_m, 10^{-3}
Ter2	1.1	1 916 827	5.0	9.0	3.17
Ter4	1.3	2 265 341	5.0	9.0	0.50
Ter5	2.3	4 007 900	5.0	3.0	3.17

A model with ID 411321 from the IllustrisTNG-100 cosmological database was aaccepted [12, 13], whose properties are close to those of the MW at zero redshift. In addition, a single-star evolution prescription [23] was implemented in the code. Together, these components allowed us to improve the physical realism of our simulations. The mass evolution of Terzan 2, Terzan 4, and Terzan 5 over 8 Gyr is shown in Fig. 1. Terzan 2 and Terzan 4 exhibit similar mass-loss histories, each losing approximately 75% of its initial mass by the present day, whereas Terzan 5 loses about 45%. In Fig. 2 we present the large-scale view of today's density distributions for Terzans family after the 8 Gyr of dynamical evolution, which was calculated based on Equation (1) from our previous article [6].

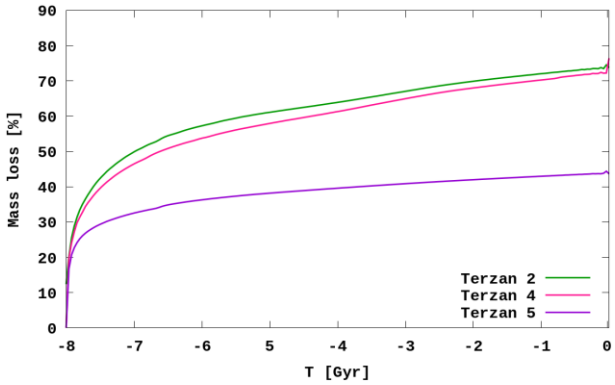


Fig.1. Evolution of the mass loss in the Terzan 2, 4 and 5 in percent due to stellar evolution and orbital type.

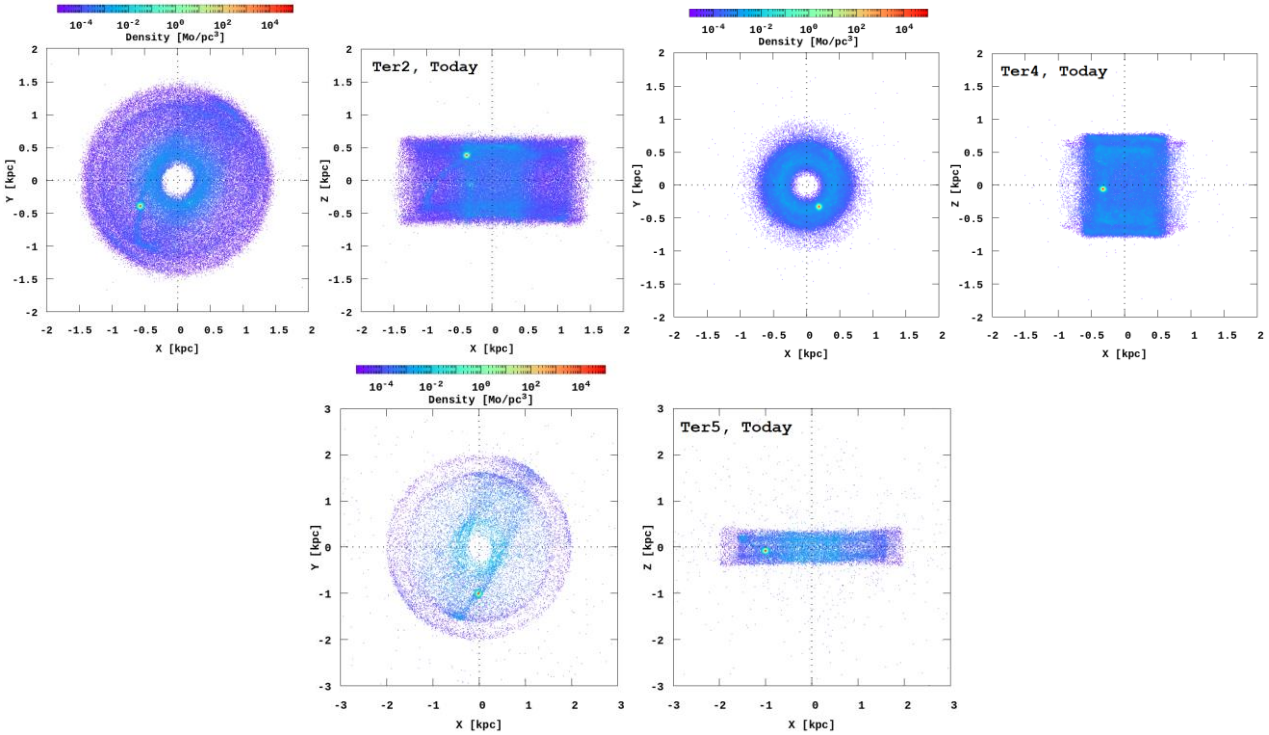


Fig.2. The stellar density distributions of Terzan 2, Terzan 4, and Terzan 5 after 8 Gyr of modelling is illustrated through two projections: (X, Y) and (X, Z).

It should be noted that based on applied Kroupa mass function for our stellar single generation prescription, we obtain the following total numbers of proto-stellar remnants — black holes (BH), neutron stars (NS), and white dwarfs (WD) — for each cluster: Terzan 2: BH = 3190, NS = 12030, WD = 172720; Terzan 4: BH = 3890, NS = 17070, WD = 218280; Terzan 5: BH = 5840, NS = 22630, WD = 321700. Due to the implementation of up-to-date natal kick prescription for BH and NS in our dynamical modelling, after 8 Gyr of evolution we obtain the next amount of the BH and NS which are still bound to their host GCs: Terzan 2: BH = 1780, NS = 840, WD = 93130; Terzan 4: BH = 2280, NS = 1460, WD = 101730; Terzan 5: BH = 3980, NS = 2930, WD = 315720. As expected, almost all of them are located in the central region of the GCs, less than GC's tidal radii.

3. Results and discussion

To evaluate the probability of stellar accumulation onto the Galactic NSC from Terzan 2, Terzan 4, and Terzan 5, we followed individual stellar trajectories throughout the full 8 Gyr of dynamical evolution and started to record each event in which a star entered the inner GalC zone within D < 100 pc. After that, we identified the closest approach (minimum distance) to the NSC and calculated the status of the star in relation to the NSC — whether it was bound or not. Following the approach of Ishchenko et al. (2024) [6], we introduced a relative velocity reduction factor V_{red} to account for the effect of dynamical friction in the dense central environment, which is not explicitly modelled in our N-body simulations. The bound status of each star during its closest passage near the NSC potential was evaluated using the energy criterion:

$$E^*_{bound} = -\frac{(M_{NSC}+m_*)}{R_*} + V_{red} \cdot 0.5 \cdot V_*^2, \quad (1)$$

where MNSC is the NSC mass, R_* is the separation between the NSC and the star, and V_* is the relative velocity between them. Stars with $E^*_{bound} < 0$ are considered bound to the NSC. This parameterisation allows us to explore a range of dynamical friction scenarios from the no-friction limit (V_{red} = 1.00) to strong deceleration (V_{red} = 0.10).

Fig. 3 shows the cumulative number distributions of NSC-bound stars as a function of their orbital parameters – pericentric distance r_{per} and orbital eccentricity ecc for the combined Terzans. As V_{red} decreases, the maximum pericentric distance of bound stars shifts to larger values, reflecting the artificial velocity reduction applied in the energy estimate (Eq. 1). The bound particles generally exhibit high orbital eccentricities (≳0.8), and consequently large semimajor axes.

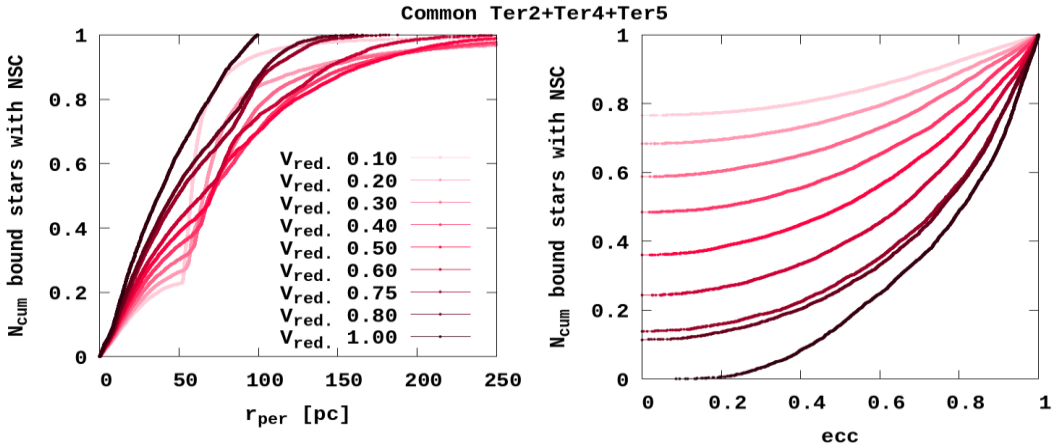


Fig. 3. Cumulative number distributions of particles bound to the NSC as a function of the orbital parameters — pericentric distance r_{per} and orbital eccentricity ecc - shown for different velocity reduction factors for the three Terzan clusters.

The total number of bound stars and their accumulated masses for all V_{red} values are summarised in Table 2. The total present-day masses of the three clusters are: Terzan 2 – 6.70×104 $M_\odot$, Terzan 4 – 8.19×10^4 $M_\odot$, and Terzan 5 – 1.25×10^5 $M_\odot$, giving a combined mass of 2.74×10^5 $M_\odot$.

Table 2. Total number of the bound particles with the NSC and their masses with different velocity reduction.

V_{red}	Ter2		Ter4		Ter5		Ter2+Ter4+Ter5	
	$M_\odot$, %	N, %	$M_\odot$, %	N, %	$M_\odot$, %	N, %	$M_\odot$, %	N, %
V_{red} 1.00	4.643e+01, 0.06926	130, 5.18	2.032e+02, 0.2481	470, 1.72	2.793e+01, 0.02234	130, 1.96	2.775e+02, 0.1013	730, 2.00
V_{red} 0.80	7.577e+01, 0.1130	220, 3.69	2.346e+02 0.2865	630, 1.81	3.917e+01, 0.03134	160, 1.65	3.496e+02, 0.1276	1010, 2.00
V_{red} 0.75	9.022e+01, 0.1346	250, 3.12	2.393e+02, 0.2921	670, 1.81	7.477e+01, 0.05983	220, 1.96	4.042e+02, 0.1476	1140, 2.03
V_{red} 0.60	1.199e+02, 0.1789	350, 2.71	2.838e+02, 0.3465	820, 1.86	1.453e+02, 0.1163	400, 2.17	5.490e+02, 0.2004	1570, 2.08
V_{red} 0.50	1.367e+02, 0.2039	430, 2.67	3.314e+02, 0.4047	970, 2.01	1.834e+02, 0.1467	480, 1.98	6.515e+02, 0.2379	1880, 2.12
V_{red} 0.40	1.490e+02, 0.2223	530, 2.75	3.682e+02, 0.4496	1130, 2.14	2.222e+02, 0.1778	580, 1.99	7.394e+02, 0.27	2240, 2.21
V_{red} 0.30	1.683e+02, 0.2510	690, 3.12	4.169e+02, 0.5091	1450, 2.5	2.381e+02, 0.1905	710, 2.22	8.232e+02, 0.3006	2850, 2.54
V_{red} 0.20	1.930e+02, 0.288	900, 3.51	4.918e+02, 0.6005	1860, 2.93	2.785e+02, 0.2229	1000, 2.69	9.633e+02, 0.3517	3760, 2.98
V_{red} 0.10	2.318e+02, 0.3458	1210, 4.38	6.017e+02, 0.7347	2710, 4.03	3.416e+02, 0.2733	1500, 3.71	11.75e+02, 0.4290	5420, 4.00

* M, % — accreted mass as a percentage of the cluster's total present-day mass; N, % — number of unique bound stars as a percentage of the total number of bound-star records (repeated close passages of the same star counted separately).

Even in the absence of velocity reduction (V_{red} = 1.00), all three clusters contribute stars to the NSC: Terzan 2 contributes ~130 stars (~46 $M_\odot$, 0.069% by mass), Terzan 4 ~470 stars (~203 $M_\odot$, 0.25%), and Terzan 5 ~130 stars (~28 $M_\odot$, 0.022%). The combined system delivers ~730 stars with a total mass of ~278 $M_\odot$ at V_{red} = 1.00. As V_{red} decreases to 0.10, this grows to ~5420 stars and ~1175 $M_\odot$ for the combined system, with Terzan 4 consistently providing the largest absolute contribution across all reduction factors.

Fig. 4 shows the cumulative stellar mass distributions as a function of individual stellar mass at the moment of closest approach to the GalC for V_{red} = 1.00, 0.75, 0.50, and 0.20 (combined Ter2 + Ter4 + Ter5). The number of low-mass stars (below 1 $M_\odot$) bound to the NSC remains constant across all four velocity reduction factors: 160 stars with a total mass of ~3.82 $M_\odot$. This value is the same for all V_{red}, indicating that the capture of low-mass stars is entirely independent of velocity deceleration and is governed purely by the orbital dynamics during close pericentre passages. However, given that 160 stars represents a statistically small sample relative to the total bound population, this low-mass component is not shown in Fig. 4 to avoid misleading visual impressions at this scale; it is reported here in the text for completeness. The distributions in Fig. 4 therefore begin at ~1 $M_\odot$ and are dominated by the high-mass tail corresponding to NSs and BHs, which grows progressively with decreasing V_{red}, reflecting the increasing efficiency of compact remnant capture under stronger velocity deceleration. This is consistent with the findings of Ishchenko et al. (2024) [6] for NGC 6642, where the vast majority of accreted objects are low-mass stars – in our case, however, the Terzan family shows a much more prominent compact remnant contribution even at realistic V_{red} values.

The relative efficiency with which each cluster contributes stars and remnants to the NSC can be understood in terms of which stars actually reach the central region: these are predominantly stars that have become unbound from their host cluster and populate its tidal tails, rather than stars still gravitationally bound to the cluster core. Terzan 5 retains an unusually dense core even after 8 Gyr of evolution, owing to its compact

initial half-mass radius (~2 pc) and high initial concentration parameter (W0 = 8; see Fig. 1), which limits the fraction of stars lost into tidal tails and therefore available for capture by the NSC — accounting for its comparatively low contribution relative to its total mass despite being the most massive of the three clusters.

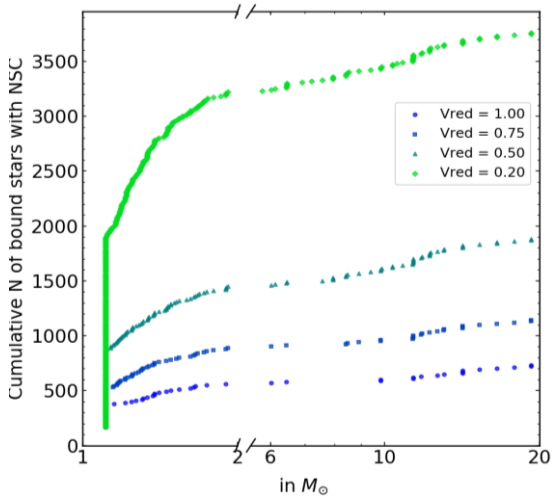


Fig. 4. Cumulative number of stars bound to the NSC as a function of individual stellar mass (in $M_\odot$) for Ter2 + Ter4 + Ter5 at the moment of closest approach to the GalC, shown for four velocity reduction factors (V_{red} = 1.00, 0.75, 0.50, and 0.20). Note: the low-mass component (< 1 M⊙) is omitted for clarity and reported separately in the text.

Terzan 2 and Terzan 4, by contrast, lose a comparable fraction of their mass into tidal tails over the same period; the larger accreted population from Terzan 4 therefore reflects its orbit, whose pericentre lies closer to the Galactic Centre, rather than a difference in mass-loss efficiency between the two clusters.

The fraction of compact stellar remnants – BHs and NSs – captured by the NSC is presented in Fig. 5, separately for each cluster and their combined contribution. These fractions increase substantially with decreasing V_{red}: at 0.10, Terzan 4 reaches 6.94% bound BHs and 13.42% bound NSs (270 BHs, 2290 NSs), the highest values in the sample. Terzan 2 reaches 2.82% bound BHs and 9.23% bound NSs (90 BHs, 1110 NSs), and Terzan 5 reaches 3.25% bound BHs and 5.79% bound NSs (190 BHs, 1310 NSs) at the same reduction factor.

Notably, Terzan 4 is the only cluster in our sample for which compact remnants of all three types – BHs, NSs, and WDs – are captured by the NSC. Specifically, 10 WDs are bound to the NSC from Terzan 4 consistently across all V_{red} values, while no WDs are captured from Terzan 2 or Terzan 5 at any V_{red}. This can be attributed to the particularly dense and frequent dynamical interaction of Terzan 4 with the NSC, which makes it the most strongly coupled cluster to the GalC environment among the three. Despite the always-high natal kick velocities associated with NS formation, the number of NSC-bound NSs is comparable to – and in many cases exceeds – the number of bound BHs. This behaviour is consistent with findings in Ishchenko et al. (2024) [6] and reflects the large total number of NSs formed relative to BHs, which compensates for their lower retention probability. The contribution of the captured NSs to the NSC and their implications for the gamma-ray flux from the GalC are discussed in detail in Kalambay et al. (2026) [24].

In [20], the long-term dynamical evolution of Terzan 2, Terzan 4, and Terzan 5 was studied in detail through high-resolution direct N-body simulations over 8 Gyr. It was demonstrated that all three clusters undergo substantial mass loss: Terzan 2 and Terzan 4 each lose approximately 75% of their initial mass, while Terzan 5 loses about 45%. Multiple close encounters between the clusters were identified, with the most significant interactions occurring between the Ter2-Ter4 and Ter4-Ter5 pairs, in some cases with separations smaller than the sum of their tidal radii. Terzan 4 was found to be the most dynamically active cluster, driving triaxial deformations in Terzan 2 and Terzan 5 through repeated gravitational perturbations. In the present work, the analysis is extended by focusing on the second key aspect: the probability and efficiency of stellar and compact remnant accretion onto the Galactic NSC during close pericentre passages of these three clusters. These three clusters were selected as representatives of the GC population located closest to the GalC, making them natural candidates for NSC mass growth through tidal stripping. The contribution of each cluster to the stellar population and compact object content of the Galactic NSC was quantified using the velocity reduction factor V_{red} to parametrise the effect of dynamical friction in the dense central environment.

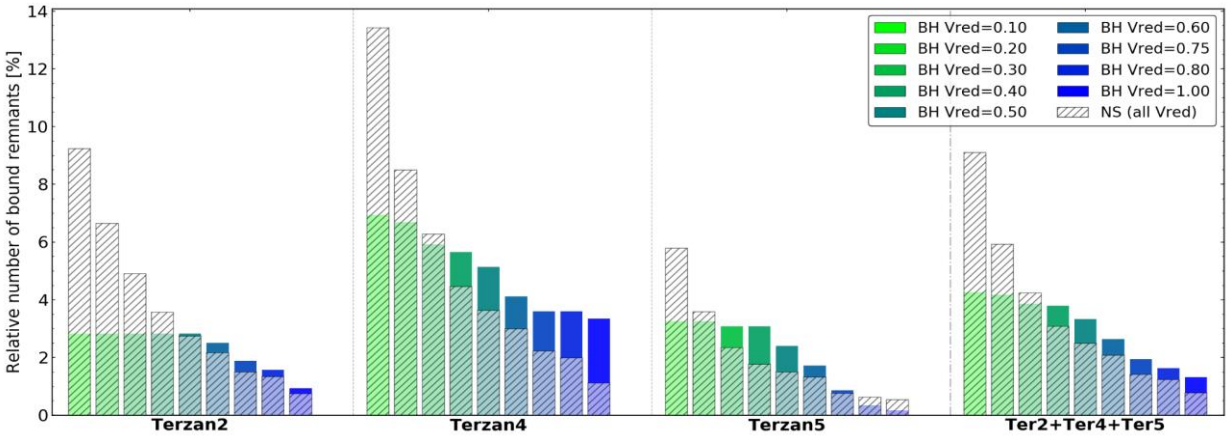


Fig. 5. Fraction of compact stellar remnants (BHs and NSs) bound to the NSC for Terzan 2, Terzan 4, Terzan 5, and their combined contribution (Ter2 + Ter4 + Ter5), shown across ten velocity reduction factors (Vred = 0.10–1.00); BHs and NSs are distinguished by different colours and symbols.

The mass distribution of the accreted stellar population reveals a clear bimodal structure (Fig. 4). The number of low-mass stars (below 1 $M_\odot$) bound to the NSC remains constant across all four velocity reduction factors: 160 stars (scaled from 16 simulation particles) with a total mass of ~3.82 $M_\odot$. This indicates that the capture of low-mass stars is independent of V_{red} and is governed purely by orbital dynamics during close pericentre passages. Due to the small size of this low-mass sample relative to the total bound population, it is not shown in Fig. 4 but is reported here for completeness. The distributions in Fig. 4 are therefore dominated by the high-mass tail extending up to ~20 $M_\odot$, corresponding to NSs and BHs, which grows progressively with decreasing V_{red}. This behaviour is qualitatively different from what was found for NGC 6642 in Ishchenko et al. (2024) [6], where the accreted population was dominated by low-mass stars with negligible compact remnant contribution at realistic V_{red} values. The Terzan clusters, particularly Terzan 4, thus represent a potentially more significant source of compact remnants for the Galactic NSC.

Compact remnants are captured by the NSC across all V_{red} values. At V_{red} = 0.10, Terzan 4 contributes 270 BHs (6.94%) and 2290 NSs (13.42%), the highest fractions in the sample; Terzan 2 contributes 90 BHs (2.82%) and 1110 NSs (9.23%); and Terzan 5 contributes 190 BHs (3.25%) and 1310 NSs (5.79%). Additionally, Terzan 4 is the only cluster for which 10 WDs are captured by the NSC consistently at every V_{red} value, attributable to its uniquely dense and frequent dynamical coupling with the GalC environment. Despite the always-high natal kick velocities associated with NS formation, the number of NSC-bound NSs is comparable to or exceeds that of BHs in all three clusters, owing to the much larger total number of NSs formed over the course of cluster evolution. This disproportionate remnant contribution may locally enhance the BH and NS content of the Galactic NSC relative to a standard stellar population. The implications of the captured NSs for the gamma-ray flux from the GalC are discussed in detail in Kalambay et al. (2026) [24].

4. Conclusion

The main results of this study are as follows. Terzan 2 provides a moderate but consistent contribution across all V_{red} values, reaching ~1210 stars and ~232 $M_\odot$ at V_{red} = 0.10. While its absolute contribution is lower than that of Terzan 4, it remains significant across the full range of velocity reduction factors, reflecting its relatively compact orbit and frequent pericentre passages near the GalC. At V_{red} = 1.00, Terzan 2 already delivers ~130 stars (~46 $M_\odot$), confirming that stellar capture occurs even without any velocity deceleration. Only BHs and NSs are captured from Terzan 2; no WDs are bound to the NSC at any V_{red} value.

Terzan 4 is the dominant contributor across all V_{red} values, both in stellar number and total accreted mass, reaching ~2700 stars and ~602 $M_\odot$ at V_{red} = 0.10. Its higher contribution compared to the other two clusters reflects its orbital properties – in particular more frequent and closer pericentre passages near the GalC – and is further evidenced by the unique capture of compact remnants of all three types (BHs, NSs, and WDs) at every V_{red} value, which is not observed for Terzan 2 or Terzan 5. Terzan 5 contributes ~1500 stars and ~342

$M_\odot$ at $V_{red} = 0.10$, making it the second largest contributor by stellar number in the sample. Despite being the most massive cluster of the three — with a present-day mass of ~1.25×10^5 $M_\odot$ — its contribution as a fraction of its total mass remains the smallest among the three clusters, reflecting the lower orbital coupling of Terzan 5 with the NSC compared to Terzan 4. At $V_{red} = 1.00$, Terzan 5 contributes ~130 stars (~28 $M_\odot$), comparable in number to Terzan 2. Similar to Terzan 2, no WDs are captured from Terzan 5 at any V_{red} value, and the captured remnant population consists exclusively of BHs and NSs.

Taken together, these results indicate that all three members of the Terzan family are capable of contributing stars and compact remnants to the Galactic NSC, with Terzan 4 being the most efficient contributor across all remnant types. The efficiency of this process depends critically on the degree of velocity deceleration experienced by stars during their closest passages through the NSC potential. A significant contribution even at $V_{red} = 1.00$ distinguishes the Terzan clusters from several of the clusters studied in Ishchenko et al. (2024) [6], where NSC-bound stars only appeared at lower V_{red} values, and underlines the importance of the specific orbital configurations of Terzan 2, Terzan 4, and Terzan 5.

An additional contribution may originate from clusters that were disrupted early in the Galaxy's history and are therefore absent from the present-day GC population. In work [25], we investigated this channel using 150 theoretical GC models evolved in a time-dependent Milky Way-like potential from 10 to 5 Gyr ago, including stellar evolution. Accretion onto the proto-NSC was most efficient during the first billion years of evolution, with the most compact models providing the largest total contribution. The accreted stellar population was dominated by low-mass stars (~ 0.33 $M_\odot$). The total accreted mass from these models reached approximately 4×10^5 $M_\odot$, corresponding to about 2% of the present-day NSC mass of 2×10^7 $M_\odot$) adopted in that study. An extended estimate incorporating higher-mass cluster models, under the assumption of the same frequency distribution as for the lower-mass population, yielded a contribution of approximately 6%. This estimate was interpreted as a conservative lower limit within the adopted modelling framework. These findings indicate that early cluster disruption can provide an additional contribution beyond that inferred from surviving GCs, although the populations considered in that study do not reproduce the entire present-day NSC mass.

The present results, together with those of Ishchenko et al. (2024) & Kuvatova et al. (2026) [6, 25], consistently show that individual surviving MW GCs do not provide substantial stellar accretion to the NSC under realistic dynamical friction conditions. Even in the most favourable cases – such as Terzan 4 and NGC 6642 – the accreted mass represents only a small fraction of the NSC total mass of ~10^7 $M_\odot$. This confirms that the inspiral and tidal stripping of surviving clusters alone cannot account for the formation of the Galactic NSC, and that other channels – such as the complete dissolution of now-defunct clusters or in situ star formation – must have played a dominant role in its assembly. Thus, summarizing the results obtained in this study and the two preceding papers, we can conclude that, based on the N-body modeling, the current mass of the NSC could not have formed solely through the accretion of stars from globular clusters—whether those observed today or those that may have been disrupted by now. Most likely, both mechanisms are involved in such a process, including formation of stars from gas that has previously migrated to the galactic center.

Conflict of interest statement

The authors declare that they have no conflict of interest in relation to this research, whether financial, personal, authorship or otherwise, that could affect the research and its results presented in this paper.

CRediT author statement

M. Kalambay: Formal analysis, Data curation, Writing – original draft. **D. Kuvatova:** Formal analysis, Data curation, Writing – original draft. **M. Ishchenko:** Conceptualization, Software, Investigation, Visualization, Writing – original draft. **P. Berczik:** Conceptualization, Methodology, Software, Supervision, Writing – review & editing. **Ch. Omarov:** Writing – review & editing. **A. Kusakin:** Writing – review & editing.The final manuscript was read and approved by all authors.

Statement on the use of Artificial Intelligence.

During the preparation of this manuscript, artificial intelligence tools were used solely for language editing and grammatical improvement.

Data Availability Statement

The data are available upon reasonable request from the authors.

Funding

This research was supported by the Ministry of Science and Higher Education of the Republic of Kazakhstan under Project No. AP26100669, "Galactic Archaeology of Gaia-Enceladus Globular Clusters as Indicators of the Formation History of the Milky Way Disk", and by the Aerospace Committee of the Ministry of Artificial Intelligence and Digital Development of the Republic of Kazakhstan under Program No. BR34836926, "Research and Monitoring of Near-Earth Space and Deep Space Based on the Development and Scaling of the Kazakhstan Network of Optical Telescopes".

Acknowledgements

Authors gratefully acknowledge the Polish high-performance computing infrastructure PLGrid (HPC Center: ACK Cyfronet AGH) for providing computer facilities and support within computational grant No. PLG/2026/019243.

References

1 Neumayer, N., Seth, A., & Böker, T. (2020). Nuclear star clusters. *The Astronomy and Astrophysics Review*, 28(1), 4. https://doi.org/10.1007/s00159-020-00125-0

2 Feldmeier-Krause, A., Zhu, L., Neumayer, N., van de Ven, G., de Zeeuw, P. T., & Schödel, R. (2017). Triaxial orbit-based modelling of the Milky Way nuclear star cluster. *Monthly Notices of the Royal Astronomical Society*, 466(4), 4040-4052. https://doi.org/10.1093/mnras/stw3377

3 Pfuhl, O., Fritz, T. K., Zilka, M., Maness, H., Eisenhauer, F., Genzel, R., Ott, T., Dodds-Eden, K., & Sternberg, A. (2011). The star formation history of the Milky Way's Nuclear Star Cluster. *The Astrophysical Journal*, 741(2), 108. https://doi.org/10.1088/0004-637X/741/2/108

4 Tremaine, S. D., Ostriker, J. P., & Spitzer, L. (1975). The formation of the nuclei of galaxies. I. M31. *The Astrophysical Journal*, 196, 407-411. https://ui.adsabs.harvard.edu/abs/1975ApJ...196..407T

5 Fahrion, K., Leaman, R., Lyubenova, M., & van de Ven, G. (2022). Disentangling the formation mechanisms of nuclear star clusters. *Astronomy & Astrophysics*, 658, A172. https://doi.org/10.1051/0004-6361/202039778

6 Ishchenko, M., Berczik, P., Panamarev, T., Kuvatova, D., Kalambay, M., Gluchshenko, A., Veles, O., Sobolenko, M., Sobodar, O., & Omarov, C. (2024). Dynamical evolution of Milky Way globular clusters on the cosmological timescale-I. Mass loss and interaction with the nuclear star cluster. *Astronomy & Astrophysics*, 689, A178. https://doi.org/10.1051/0004-6361/202450399

7 Antonini, F., Capuzzo-Dolcetta, R., Mastrobuono-Battisti, A., & Merritt, D. (2012). Dissipationless formation and evolution of the Milky Way nuclear star cluster. *The Astrophysical Journal*, 750(2), 111. https://doi.org/10.1088/0004-637X/750/2/111

8 Aharon, D., & Perets, H. B. (2015). Formation and evolution of nuclear star clusters with in situ star formation: nuclear cores and age segregation. *The Astrophysical Journal*, 799(2), 185. https://doi.org/10.1088/0004-637X/799/2/185

9 Gao, Y., Li, H., Zhang, X., Su, M., & Ng, S. C. Y. (2024). Globular clusters contribute to the nuclear star clusters and galaxy centre γ-ray excess, moderated by galaxy assembly history. *Monthly Notices of the Royal Astronomical Society,* 527(3), 7731-7742. https://ui.adsabs.harvard.edu/abs/2024MNRAS.527.7731G

10 Gnedin, O. Y., Lee, H. M., & Ostriker, J. P. (1999). Effects of tidal shocks on the evolution of globular clusters. *The Astrophysical Journal*, 522(2), 935-949. https://ui.adsabs.harvard.edu/abs/1999ApJ...522..935G

11 Ishchenko, M., Sobolenko, M., Kuvatova, D., Panamarev, T., & Berczik, P. (2023). Milky Way globular clusters on cosmological timescales-II. Interaction with the Galactic center. *Astronomy & Astrophysics*, 674, A70. https://doi.org/10.1051/0004-6361/202245753

12 Pillepich, A., Nelson, D., Hernquist, L., Springel, V., Pakmor, R., Torrey, P., Weinberger, R., Genel, S., Naiman, J. P., Marinacci, F., & Vogelsberger, M. (2018). First results from the IllustrisTNG simulations: the stellar mass content of groups and clusters of galaxies. *Monthly Notices of the Royal Astronomical Society*, 475(1), 648-675. https://doi.org/10.1093/mnras/stx3112

13 Nelson, D., Springel, V., Pillepich, A., Rodriguez-Gomez, V., Torrey, P., Genel, S., Vogelsberger, M., Pakmor, R., Marinacci, F., Weinberger, R., Kelley, L., Lovell, M., Diemer, B., & Hernquist, L. (2019). The IllustrisTNG simulations: public data release. *Computational Astrophysics and Cosmology*, 6(1), 2. https://doi.org/10.1186/s40668-019-0028-x

14 Ishchenko, M., Sobolenko, M., Berczik, P., Omarov, C., Sobodar, O., Kalambay, M., & Yurin, D. (2023). Milky Way globular clusters on cosmological timescales-III. Interaction rates. *Astronomy & Astrophysics*, 678, A69. https://doi.org/10.1051/0004-6361/202346553

15 Ferraro, F. R., Dalessandro, E., Mucciarelli, A., Beccari, G., Rich, R. M., Origlia, L., Lanzoni, B., Rood, R. T., Valenti, E., Bellazzini, M., Ransom, S. M., & Cocozza, G. (2009). The cluster Terzan 5 as a remnant of a primordial building block of the Galactic bulge. *Nature,* 462(7272), 483-486. https://ui.adsabs.harvard.edu/abs/2009Natur.462..483F

16 Origlia, L., Rich, R. M., Ferraro, F. R., Lanzoni, B., Bellazzini, M., Dalessandro, E., Fabbri, S., & Beccari, G. (2011). Spectroscopy unveils the complex nature of Terzan 5. *The Astrophysical Journal Letters*, 726(2), L20. https://doi.org/10.1088/2041-8205/726/2/L20

17 Kroupa, P. (2001). On the variation of the initial mass function. *Monthly Notices of the Royal Astronomical Society*, 322(2), 231-246. https://doi.org/10.1046/j.1365-8711.2001.04022.x

18 Hurley, J. R., Pols, O. R., & Tout, C. A. (2000). Comprehensive analytic formulae for stellar evolution as a function of mass and metallicity. *Monthly Notices of the Royal Astronomical Society*, 315(3), 543-569. https://doi.org/10.1046/j.1365-8711.2000.03426.x

19 King, I. R. (1966). The structure of star clusters. III. Some simple dynamical models. *The Astronomical Journal,* 71, 64. https://ui.adsabs.harvard.edu/abs/1966AJ.....71...64K

20 Ishchenko, M., Berczik, P., & Kuvatova, D. (2026). Dynamical evolution of Milky Way globular clusters on the cosmological timescale II. Terzan 2, 4, and 5 mass loss and collision tracking. *Astronomy & Astrophysics*, 710, A58. https://doi.org/10.1051/0004-6361/202659137

21 Panamarev, T., Just, A., Spurzem, R., Berczik, P., Wang, L., & Arca Sedda, M. (2019). Direct N-body simulation of the Galactic centre. *Monthly Notices of the Royal Astronomical Society*, 484(3), 3279-3290. https://doi.org/10.1093/mnras/stz208

22 Berczik, P., Nitadori, K., Zhong, S., Spurzem, R., Hamada, T., Wang, X., Berentzen, I., Veles, A., & Ge, W. (2011, October). High performance massively parallel direct N-body simulations on large GPU clusters. *In International conference on High Performance Computing* (pp. 8-18). https://ui.adsabs.harvard.edu/abs/2011hpc..conf....8B

23 Banerjee, S., Belczynski, K., Fryer, C. L., Berczik, P., Hurley, J. R., Spurzem, R., & Wang, L. (2020). BSE versus StarTrack: implementations of new wind, remnant-formation, and natal-kick schemes in NBODY7 and their astrophysical consequences. *Astronomy & Astrophysics*, 639, A41. https://doi.org/10.1051/0004-6361/201935332

24 Kalambay, M., Ishchenko, M., Kuvatova, D., Panamarev, T., & Berczik, P. (2026). The contribution to Galactic Centre γ-ray excess from cluster-born millisecond pulsars: constraints from direct N-body simulations. *Astronomy & Astrophysics*, 708, A89. https://doi.org/10.1051/0004-6361/202557963

25 Kuvatova, D., Ishchenko, M., Berczik, P., Veles, O., Sobodar, O., & Panamarev, T. (2026). How our proto-nuclear star cluster formed and grew due to early globular cluster disruption – I. Case of low masses. *Astronomy & Astrophysics*, 706, A220. https://doi.org/10.1051/0004-6361/202556182

AUTHORS' INFORMATION

Kalambay, Mukhagali – PhD, researcher, Fesenkov Astrophysical Institute, Almaty, Kazakhstan; Associate professor, Heriot-Watt International Faculty, K. Zhubanov Aktobe Regional University, Aktobe, Kazakhstan. Scopus Author ID: 59365823900; ORCID: 0000-0002-0570-7270; kalambay@fai.kz

Kuvatova, Dana – PhD student, Al-Farabi Kazakh National University, Fesenkov Astrophysical Institute, Almaty, Kazakhstan; Scopus Author ID: 57980506300; ORCID: 0000-0002-5937-4985; kuvatova@fai.kz

Ishchenko, Maryna – Dr., Leading Researcher, Main Astronomical Observatory, National Academy of Sciences of Ukraine, Kyiv, Ukraine; Fesenkov Astrophysical Institute, Almaty, Kazakhstan; Scopus Author ID: 55348120800; ORCID: 0000-0002-6961-8170; marina@mao.kiev.ua

Berczik, Peter – Dr (Sci)., Leading Researcher, Fesenkov Astrophysical Institute, Almaty, Kazakhstan; Main Astronomical Observatory, NAS of Ukraine, Kyiv, Ukraine; Scopus Author ID: 8681718700; ORCID: 0000-0003-4176-152X; berczik@mao.kiev.ua

Omarov, Chingis – Dr., Professor, Fesenkov Astrophysical Institute, Almaty, Kazakhstan; Scopus Author ID: 8655858100; ORCID: 0000-0002-1672-894X; chingis.omarov@fai.kz

Kusakin, Anatoly – Dr., Leading Researcher, Fesenkov Astrophysical Institute, Almaty, Kazakhstan; Scopus Author ID: 6603251549; ORCID: 0000-0002-7756-546X; kusakin@fai.kz